UNIVERSITY COLLEGE LONDON

DEPARTMENT OF CHEMICAL ENGINEERING

ELECTROCHEMICAL INNOVATION LAB

PhD

Jia Di YANG

PhD Thesis

Developing Cell-Level Testing Protocols and Mass Estimation Models for Fuel Cell Hybrid Electric Vehicles

Supervisors: Dr. James Robinson, Dr. Jason Millichamp

Abstract

With an increasing focus on decarbonisation of the transport sector, it is imperative to consider routes to electrify ground vehicles beyond the use of Li-ion technology. This thesis presents a comprehensive analysis of tools and experimental systems of Proton Exchange Membrane Fuel Cell (PEMFC) and lithium-ion battery (LiB) systems integrated into fuel cell hybrid electric vehicles (FCHEVs), focusing on component sizing, synergy between PEMFC and LiBs, electrochemical degradation characterisation, and degradation analysis using X-Ray computed tomography (CT). Both parallel and fuel cell range extender (FCREx) architecture were taken into consideration.

Through the collection and analysis of electrochemical degradation data, such as polarisation curves, cyclic voltammetry (CV), linear sweep voltammetry (LSV), capacity fade, and electrochemical impedance spectroscopy (EIS), the study identifies degradation modes under various operating scenarios and their implications for long-term performance and durability. X-ray CT techniques were used to further probe the LiB degradation as a form of physical characterisation. To stress-test the PEMFCs and LiBs under realistic driving behaviour, a drive cycle endurance testing protocol was formulated for both the PEMFC and LiB counterparts.

Additionally, the thesis explores the effect of hybridisation degree on system mass and performance across different vehicle types, including light-duty vehicles, Class 8 heavy goods vehicles, and buses. By modelling these scenarios and varying the operating conditions such as hybridisation degree and cell operating power of the PEMFC stack and battery pack, the research highlights the benefits and potential hindrances of hybridisation in terms of weight, packaging, durability, and cost-effectiveness. A vehicle sizing tool was programmed in MATLAB Simulink from the ground up to achieve this. The model has a novel system weight feedback loop that enhances accuracy in vehicle mass and performance estimation, offering a valuable tool for vehicle design. This model focuses more on sizing, weight analysis, and hybridisation degree, rather than energy management systems (EMS), which is already abundant in the literature.

By combining insights on electrochemical degradation, physical degradation, hybridisation impacts, and the application of drive cycles, this research helped develop tools and experimental systems to improve the optimisation of FCHEVs, contributing to the advancement of sustainable ground-vehicle transportation.

Impact Statement

The research conducted during my PhD helps to advance the field of Fuel Cell Hybrid Electric Vehicles (FCHEVs), addressing research gaps in testing protocols, simulation tools, and device-level endurance testing methodologies. The work not only focuses on FCHEVs for light-duty vehicles (LDVs) but also heavy goods vehicles (HGVs) and buses, covering a wide range of vehicle scenarios.

One major contribution is the development of updated drive cycle testing protocols and testing methods tailored for modern FCHEVs. Traditional modal drive cycles, such as the New European Driving Cycle (NEDC), which was released in the 1990s, are outdated and fail to represent real-world vehicle operation's transient and dynamic conditions. If cell-level testing is subject to outdated standards, the reliability of such testing protocol needs to be questioned. This research used more modern transient drive cycles, including the Worldwide Harmonized Light Vehicles Test Procedure (WLTP), released in 2017, to create simulation and experimental protocols that reflect contemporary and realistic driving conditions. These protocols provide a more accurate depiction of realistic FCHEV usage, ensuring improved relevance and applicability for current and future FCHEV designs.

An FCHEV-specific MATLAB modelling tool, HybeMass, was also developed. The tool covers different categories of road-going FCHEVs such as LDVs, HGVs, and buses. Unlike existing models that are often designed for broader use of conventional internal combustion engine vehicles (ICEVs), HybeMass addresses the specific mass complications of FCHEV systems, incorporating fuel cells, batteries, and hybrid configurations across diverse operational scenarios. By offering this precision and adaptability, HybeMass enables manufacturers and researchers to optimize vehicle design for performance and efficiency, contributing to the transition into the age of electrochemical power and the next generation of sustainable vehicles.

Drive cycle endurance testing was also conducted to evaluate possible degradation in proton exchange membrane fuel cells (PEMFCs) and lithium-ion batteries in hybrid vehicle scenarios. Traditional testing methods, such as constant current, constant voltage (CC-CV) approaches, do not capture the complexities of real-world conditions. While some literature incorporates drive cycles, these are predominantly simulation or computational based. Most experimental-based literature uses older drive cycle testing standards, which are less realistic to real-world driving. This work bridges this gap by combining experimental endurance testing with modern transient drive cycles like WLTP and drive cycles designed for HGVs and buses, providing a realistic assessment of FCHEV components' performance and durability under dynamic load conditions.

In conclusion, this PhD research addresses significant limitations in FCHEV testing and design, enhancing the field's ability to develop vehicles that meet the challenges of modern transportation. By updating outdated testing methodologies, creating an FCHEV-specific modelling tool, and integrating experimental and simulation-based approaches, this work contributes to the broader adoption of FCHEVs. These advancements represent an essential step toward more efficient testing, design, and validation of FCHEVs.

Table of Contents

Table of Figures

List of Tables

List of Abbreviations

Abbreviation	Definition
APC	Advanced Propulsion Centre
BE	Battery-electric
BEV	Battery electric vehicle
CATC	Contemporary Amperex Technology Co.
CC	Constant-current
CD	Charge-depleting
CT	Computed tomography
CV	Cyclic voltammetry
dc	Drive cycle
DOE	Department of Energy
ECSA	Electrochemical surface area
EIS	Electrochemical impedance spectroscopy
EMS	Energy management system
EPA	Environmental protection agency
EV	Electric vehicle
FC	Fuel cell
FCE	Fuel cell electric
FCEV	Fuel cell electric vehicle
FCH	Fuel Cells and Hydrogen Joint Undertaking
FCHEV	Fuel cell hybrid electric vehicle
FCREx	Fuel cell range extender
FCV	Fuel cell vehicle
FTP	Federal Test Procedure
GDL	Gas diffusion layer
GVM	Gross vehicle mass
HD	Hybrid degree
HGV	Heavy goods vehicle
ICEV	Internal combustion engine vehicle
LCO	Lithium cobalt oxide
LDV	Light-duty vehicle
LFP	Lithium iron phosphate
LiB	Lithium ion battery
LMO	Lithium manganese oxide
LSV	Linear sweep voltammetry
MEA	Membrane electrode assembly
MP	Maximum PEMFC
MPML	Maximum PEMFC maximum lithium-ion battery
NCA	Nickel cobalt aluminium oxide
NEDC	New European Drive Cycle
NMC	Nickel manganese cobalt oxide

NP	Nominal PEMFC
NPML	Nominal PEMFC maximum lithium-ion battery
NPNL	Nominal PEMFC nominal lithium-ion battery
PEIS	Potentiostatic electrochemical impedance spectroscopy
PEM	Proton exchange membrane
PEMFC	Proton exchange membrane fuel cell
PTFE	Polytetrafluoroethylene
RPM	Revolutions per minute
SSB	Solid state battery
SUV	Sport utility vehicle
UDDS	Urban dynamometer driving schedule
USD	United States Dollar
WHVC	World Harmonised Vehicle Cycle
WLTP	Worldwide Harmonised Light Vehicle Test Procedure

Acknowledgements

First, I would like to thank all the academics and university staff who have supervised me throughout this PhD, including Dr. James Robinson, Prof. Paul Shearing, Dr. Jason Millichamp, Prof. Dan Brett, and Dr. Michael Whiteley. There is no doubt that the regular meetings we’ve had have contributed immensely to the completion of this thesis.

I would also like to thank my parents, who have provided me with the mental support needed to complete this PhD project.

In addition, I would like to thank Dr. Theo Suter for his support as a laboratory and research mentor. You’ve been helpful not only in the scientific field, but also in giving general advice on how to be a successful PhD student and candidate. Furthermore, thanks to Mr. Toby Neville for guidance on how to use and diagnose lab equipment.

I would also like to thank my colleagues Alexander Dimitrijevic, Alessia Matruglio, Alexander Marinov, Renier Arabolla Rodriguez, Shangwei Zhou, Wenjia Du, Linlin Xu, Keenan Smith, and Emanuele Magliocca for the insightful scientific discussions we’ve had.

List of Publications

1. Di Yang, J., et al., *An adaptive fuel cell hybrid vehicle propulsion sizing model.* iEnergy, 2024. **3**(1): p. 59-72.
2. Yang, J.-D., et al., *PEMFC Electrochemical Degradation Analysis of a Fuel Cell Range-Extender (FCREx) Heavy Goods Vehicle after a Break-In Period.* Energies, 2024. **17**(12).
3. Yang, J.D., et al., *A Review of Drive Cycles for Electrochemical Propulsion.* Energies, 2023. **16**(18).
4. Zhou, S., et al., *Water content estimation in polymer electrolyte fuel cells using synchronous electrochemical impedance spectroscopy and neutron imaging.* Cell Reports Physical Science, 2024. **5**(9).
5. Xu, L., et al., *A Scalable and Robust Water Management Strategy for PEMFCs: Operando Electrothermal Mapping and Neutron Imaging Study.* Adv Sci (Weinh), 2024. **11**(36): p. e2404350.
6. Andrade, T.S., et al., *Energy efficiency of hydrogen for vehicle propulsion: On- or off-board H2 to electricity conversion?* International Journal of Hydrogen Energy, 2024. **92**: p. 1493-1499.
7. Wu, Y., et al., *Water management and mass transport of a fractal metal foam flow-field based polymer electrolyte fuel cell using operando neutron imaging.* Applied Energy, 2024. **364**.

Conference Presentations

09/2023: Presentation, Trade-offs between Degradation and Vehicle Weight in PEMFC and Lithium-Ion Battery Hybrid Vehicles across Different Vehicle Scenarios and Drive Cycles, 30th Society of Chemical Industry (SCI) Conference, London

06/2022: Presentation, Hybridisation – The Future of the Electrochemical Engine, 241st Electrochemical Society (ECS) Conference, Vancouver

UCL Research Paper Declaration Form Referencing the Doctoral Candidate's Own Published Work(s)

Please use this form to declare if parts of your thesis are already available in another format, e.g. if data, text, or figures:

- *have been uploaded to a preprint server*
- *are in submission to a peer-reviewed publication*
- *have been published in a peer-reviewed publication, e.g. journal, textbook.*

This form should be completed as many times as necessary. For instance, if you have seven thesis chapters, two of which containing material that has already been published, you would complete this form twice.

For a research manuscript that has already been published (if not yet published, please skip to section 2)

What is the title of the manuscript?

An Adaptive Fuel Cell Hybrid Vehicle Propulsion Sizing Model

Please include a link to or doi for the work

https://doi.org/10.23919/IEN.2024.0008

Where was the work published?

iEnergy

Who published the work? (e.g. OUP)

iEEE

When was the work published?

March 2024

List the manuscript's authors in the order they appear on the publication

Jia Di Yang; Paul R. Shearing; Jason Millichamp; Theo Suter; Dan J.L. Brett; James B. Robinson

Was the work peer reviewed?

Yes

Have you retained the copyright?

No.

Was an earlier form of the manuscript uploaded to a preprint server? (e.g. medRxiv). If 'Yes', please give a link or doi)

Yes, https://doi.org/10.31224/3553.

If ‘No’, please seek permission from the relevant publisher and check the box next to the below statement:

☐

I acknowledge permission of the publisher named under ***1d*** *to include in this thesis portions of the publication named as included in* ***1c****.*

For multi-authored work, please give a statement of contribution covering all authors (if single-author, please skip to section 4)

Conceptualization, J.D.Y., D.J.L.B. and T.S.; methodology, J.D.Y. and J.B.R.; formal analysis, J.D.Y. and J.M.; investigation, J.D.Y.; resources, J.D.Y. and D.J.L.B.; data curation, J.D.Y.; writing—original draft preparation, J.D.Y.; writing—review and editing, all authors.; visualization, J.D.Y.; supervision, D.J.L.B., P.R.S. and J.B.R.; project administration, D.J.L.B.; funding acquisition, D.J.L.B., P.R.S. and J.B.R. All authors have read and agreed to the published version of the manuscript.

In which chapter(s) of your thesis can this material be found?

Chapter 3

e-Signatures confirming that the information above is accurate (this form should be co-signed by the supervisor/ senior author unless this is not appropriate, e.g. if the paper was a single-author work)

Candidate

Jia Yang

Date:

04/10/2024

Supervisor/ Senior Author (where appropriate)

Date: 16/12/2024

UCL Research Paper Declaration Form Referencing the Doctoral Candidate's Own Published Work(s)

Please use this form to declare if parts of your thesis are already available in another format, e.g. if data, text, or figures:

- *have been uploaded to a preprint server*
- *are in submission to a peer-reviewed publication*
- *have been published in a peer-reviewed publication, e.g. journal, textbook.*

This form should be completed as many times as necessary. For instance, if you have seven thesis chapters, two of which containing material that has already been published, you would complete this form twice.

For a research manuscript that has already been published (if not yet published, please skip to section 2)

What is the title of the manuscript?

PEMFC Electrochemical Degradation Analysis of a Fuel Cell Range-Extender (FCREx) Heavy Goods Vehicle after a Break-In Period

Please include a link to or doi for the work

https://doi.org/10.3390/en17122980

Where was the work published?

Energies

Who published the work? (e.g. OUP)

MDPI

When was the work published?

June 2024

List the manuscript's authors in the order they appear on the publication

Jia Di Yang; Theo Suter; Jason Millichamp; Rhodri E. Owen; Wenjia Du; Paul R. Shearing; Dan J.L. Brett; James B. Robinson

Was the work peer reviewed?

Yes

Have you retained the copyright?

Yes

Was an earlier form of the manuscript uploaded to a preprint server? (e.g. medRxiv). If 'Yes', please give a link or doi)

No

If ‘No’, please seek permission from the relevant publisher and check the box next to the below statement:

☒
*I acknowledge permission of the publisher named under **1d** to include in this thesis portions of the publication named as included in **1c**.*

For a research manuscript prepared for publication but that has not yet been published (if already published, please skip to section 3)

What is the current title of the manuscript?

Click or tap here to enter text.

Has the manuscript been uploaded to a preprint server? (e.g. medRxiv; if ‘Yes’, please give a link or doi)

Click or tap here to enter text.

Where is the work intended to be published? (e.g. journal names)

Click or tap here to enter text.

List the manuscript’s authors in the intended authorship order

Click or tap here to enter text.

Stage of publication (e.g. in submission)

Click or tap here to enter text.

For multi-authored work, please give a statement of contribution covering all authors (if single-author, please skip to section 4)

Conceptualization, J.-D.Y., P.R.S., D.J.L.B., J.B.R. and J.M.; methodology, J.-D.Y., J.M., T.S. and R.E.O.; software, J.-D.Y.; validation, J.-D.Y., P.R.S., D.J.L.B. and J.B.R.; formal analysis, J.-D.Y.; investigation, J.-D.Y. and W.D.; resources, J.-D.Y., T.S. and W.D.; data curation, J.-D.Y.; writing—original draft preparation, J.-D.Y.; writing—review and editing, all authors; visualization, J.-D.Y.; supervision, D.J.L.B., P.R.S. and J.B.R.; project administration, J.B.R.; funding acquisition, D.J.L.B., P.R.S. and J.B.R..

In which chapter(s) of your thesis can this material be found?

Chapter 2

e-Signatures confirming that the information above is accurate (this form should be co-signed by the supervisor/ senior author unless this is not appropriate, e.g. if the paper was a single-author work)

Candidate

Jia Yang

Date:

04/10/2024

Supervisor/ Senior Author (where appropriate)

Date: 16/12/2024

UCL Research Paper Declaration Form Referencing the Doctoral Candidate's Own Published Work(s)

Please use this form to declare if parts of your thesis are already available in another format, e.g. if data, text, or figures:

- *have been uploaded to a preprint server*
- *are in submission to a peer-reviewed publication*
- *have been published in a peer-reviewed publication, e.g. journal, textbook.*

This form should be completed as many times as necessary. For instance, if you have seven thesis chapters, two of which containing material that has already been published, you would complete this form twice.

For a research manuscript that has already been published (if not yet published, please skip to section 2)
What is the title of the manuscript?

A Review of Drive Cycles for Electrochemical Propulsion

Please include a link to or doi for the work

https://doi.org/10.3390/en16186552

Where was the work published?

Energies

Who published the work? (e.g. OUP)

MDPI

When was the work published?

12 September 2023

List the manuscript's authors in the order they appear on the publication

Jia Di Yang; Jason Millichamp; Theo Suter; Paul R. Shearing; Dan J.L. Brett; James Robinson

Was the work peer reviewed?

Yes

Have you retained the copyright?

Yes

Was an earlier form of the manuscript uploaded to a preprint server? (e.g. medRxiv). If 'Yes', please give a link or doi)

No

If ‘No’, please seek permission from the relevant publisher and check the box next to the below statement:

☒

*I acknowledge permission of the publisher named under **1d** to include in this thesis portions of the publication named as included in **1c**.*

For a research manuscript prepared for publication but that has not yet been published (if already published, please skip to section 3)

What is the current title of the manuscript?

Click or tap here to enter text.

Has the manuscript been uploaded to a preprint server? (e.g. medRxiv; if ‘Yes’, please give a link or doi)

Click or tap here to enter text.

Where is the work intended to be published? (e.g. journal names)

Click or tap here to enter text.

List the manuscript’s authors in the intended authorship order

Click or tap here to enter text.

Stage of publication (e.g. in submission)

Click or tap here to enter text.

For multi-authored work, please give a statement of contribution covering all authors (if single-author, please skip to section 4)

Click or tap here to enter text.

In which chapter(s) of your thesis can this material be found?

Literature review

e-Signatures confirming that the information above is accurate (this form should be co-signed by the supervisor/ senior author unless this is not appropriate, e.g. if the paper was a single-author work)

Candidate

Jia Di Yang

Date

07/10/2024

Supervisor/ Senior Author (where appropriate)

James

Date: 16/12/2024

1 Introduction

The widely legislated requirement for net-zero transport has increased the interest and development of electrochemical power sources including proton exchange membrane fuel cells (PEMFC) and lithium-ion batteries (LiB) for a range of automotive applications. When considered in isolation both power sources have several specific advantages and disadvantages, which, when considered in an appropriate manner allow the technologies to be applied in an application-specific manner to maximise the utility and efficiency of a propulsion system. It is undoubted that most passenger electric vehicles will be powered by LiBs in the coming years. For these vehicles, LiB technology is well suited to deliver sufficient power over appropriate time scales, which when coupled with the higher efficiencies typically observed offer compelling performance and economic benefits. However, there are concerns about the sustainability of these systems which may provide a market opportunity for fuel cell electric vehicles (FCEVs) in this area over longer timeframes. Furthermore, the comparatively high gravimetric energy density and quick refuelling times of fuel cell (FC) systems may provide specific benefits for fleet and heavier vehicles and those primarily designed for extended range.

The challenge in moving towards a widespread electrification of vehicles involves converting existing systems including heavy goods vehicles, buses and beyond which require comparatively high specific energy and power density, adequate transient response times for power delivery and very long range [1]. In these applications, it is clear that there is a need to move beyond the capability of existing LiBs and as a result of this there is a substantial commercial interest in exploring the application of hybridised fuel cell/battery vehicles. These systems often do not have the volumetric constraint associated with electric vehicles which reduces the viability of hybridised systems in passenger EVs. By undertaking a considered hybridisation, it is possible to maximise the benefits of the battery and fuel cell systems on board, delivering long-range propulsion over appropriate lifetimes with acceptable power response. Further, in extending the lifetime of the propulsion system, when compared to a single technology in isolation, it is also possible to amortise the cost of the system over a longer duration reducing the overall operating costs of the vehicle for users [2][3].

In general, there are three main architectures of hybrid vehicles, namely series, parallel, and series-parallel [3][4]. In a series architecture, only one power source propels the wheels of a vehicle, while the other source is used for recharging the main propulsive power source; when using a parallel architecture, both power sources can propel the wheels [3][4]. The series-parallel architecture combines both architectures, in which both sources can provide traction while keeping the capability of one source charging another source. The motor can work in both directions, both as a propelling motor and a generator. Regenerative braking is possible in all architectures, during regen, the motor operates in reverse and acts as a generator, which provides recharge to the battery pack. The powertrain layout modelled in this study is the parallel layout, in which both the PEMFC stack and LiB pack can propel the vehicle independently. There is an industrial term for the series and series-parallel architecture named the range extender vehicle; in hybridisation between PEMFC and LiB, it would be called the fuel cell range extender (FCREx) vehicle. This type of vehicle typically has the fuel cell running at a more constant (minimal transientness) power output when compared to parallel vehicles. The fuel cell has the option to charge the battery (series architecture) and propel the drivetrain (series-parallel architecture). Both the parallel and FCREx architecture will be analysed in this work.

A key aspect of developing a parallel hybridised system is determining an appropriate hybrid degree (HD), a measure of the fuel cell system power output to the total required power of a vehicle. In the most widely popularised FC hybrid vehicle, the Toyota Mirai, the HD is around 0.71 $kW_{FC}/kW_{vehicle}$ [5][6]; however, this will vary significantly when determining the requirements of a vehicle including the size of a system, range, lifetime, and cost. Determining an appropriate operating power for the system is also a significant requirement in the hybridisation of the vehicle as operating at higher powers can reduce the mass at a cost to the lifetime. A MATLAB model was built from the ground-up to examine the synergy of hybrid ratio and mass of FCHEV vehicles of different categories (e.g. LDVs, HGVs, and buses). In a typical automotive engineering V-model shown in Figure 1-1, this HybeMass model helps to simplify and reiterate the detailed design, implementation, and integration, testing, and verification stages of the V-model.

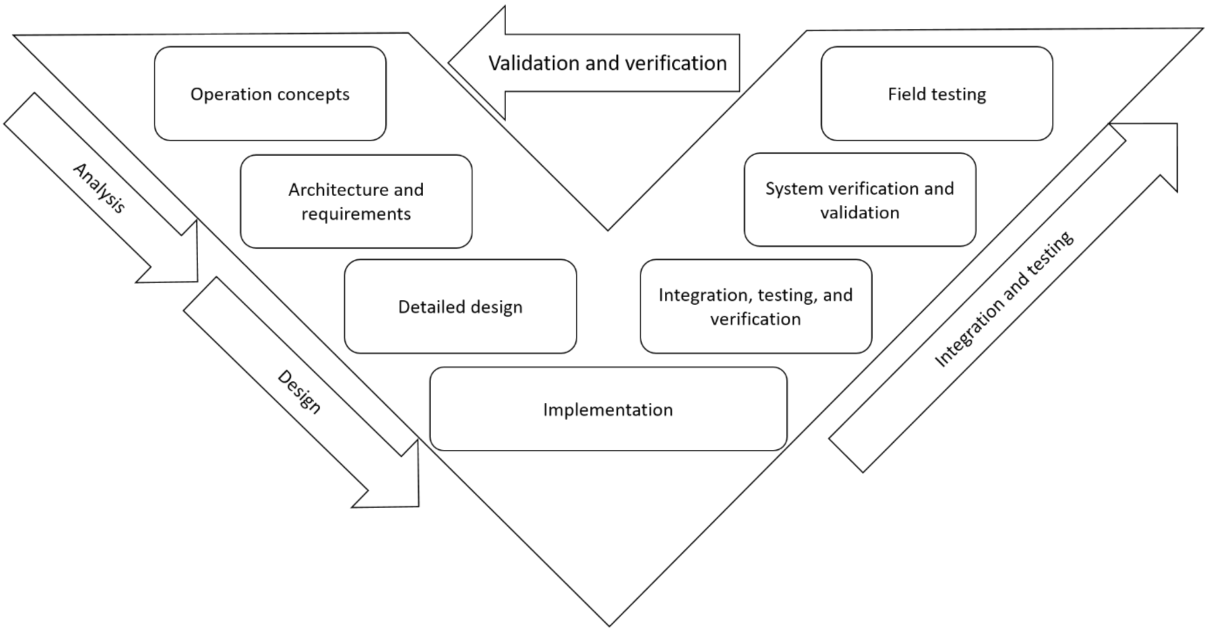

Figure 1-1: Generic automotive engineering V-model. The HybeMass model focuses on detailed design located on the ‘left V’ of the model.

The HybeMass model focuses on the sizing and mass analysis of propulsions systems for FCHEVs of all vehicle classes rather than providing information regarding the required energy split or management strategies (EMS) of such vehicles which is heavily dependent upon use case and therefore unlikely to be generalised for the analysis type detailed here. Literature is abundant on optimising the EMS that a vehicle uses, but such studies tend not to elaborate on how the vehicle was sized before the application of EMSs. Usually, sizing is pre-determined without explanation or selected from a pre-built vehicle.

The laboratory experiments of this PhD work aim to understand the degradation mechanisms and quantification of PEMFCs and LiBs in FCHEV LDV, Class 8 (gross vehicle mass >15,000 kg) heavy goods vehicle (HGV), and bus scenarios. Scaled-down bench testing offers a controlled environment to simulate operating conditions and accelerate degradation processes, replicating the real-life driving dynamics of FCHEVs in a laboratory setting. A key aspect of the project involves the development of drive cycle based bench testing tailored to range-extender FCHEV operation, enabling the characterisation of power division [4]. Power cycles can be computed from drive cycles to estimate the power consumption of a vehicle as a whole. These power cycles can then be divided into two or more separate drive cycles to simulate power division in a hybrid vehicle [4]. These divided power cycles can then be scaled down to a cell level to facilitate cell bench testing in an electrochemical lab [4] using fuel cell testing stations and battery cyclers.

The PEMFC degradation characterisation used in this study focuses on electrochemistry techniques, such as polarisation curves, cyclic voltammetry (CV), linear sweep voltammetry (LSV), and electrochemical impedance spectroscopy (EIS), to characterise degradation. The LiB degradation characterisations focused on capacity fade, EIS, and X-ray computed tomography (CT). These techniques provide invaluable insights into the electrochemical and degradation performance of PEMFCs and LiBs.

2 Literature Review

2.1 Literature Review Chapter Introduction

The literature review covers cell-level fundamentals and current status, to more vehicular-level concepts. In most subsections, both the PEMFC and LiB concepts are discussed simultaneously, instead of being divided into separate subsections; this ensures the overall theme of FCHEV hybridisation is met.

Scientific papers, roadmaps, and textbooks were surveyed by the researcher to conduct this literature review. The fundamental electrochemistry concepts are mostly obtained from scientific papers and textbooks. The current status of PEMFCs and LiBs are mostly obtained from scientific papers and roadmaps. The vehicular-based discussion comes from scientific papers and textbooks.

The cell-level concepts are at the start of the chapter, while the vehicular concepts are at the end of the chapter. There is also a chapter that discusses the possible drive cycles that can be used in electrochemical testing, as well as the complications in using these drive cycles. The aim is to capture an overall snapshop of all the complications and theory of designing cell-level experimental systems and modelling vehicular-level power demands, mass estimation, and synergy between PEMFCs and LiBs.

2.2 Fundamentals of PEMFCs

A polymer electrolyte membrane fuel cell (PEMFC) works by combining hydrogen (H_2) and oxygen (O_2) to generate electricity, producing water (H_2O) and heat as by-products. Unlike batteries, PEMFCs can only produce electricity, whereas batteries can both produce and store electricity. Generally, a PEMFC consists of a cathode, anode, and a polymer electrolyte membrane. Figure 2-1 and Equations (2-1) to (2-3) show the workings and chemical reactions of a PEMFC, respectively. H_2 is pumped into the anode, which then undergoes an oxidation reaction resulting in the presence of protons which migrate through the polymeric membrane, shown in Equation (2-1); O_2 or air is pumped into the cathode, which then undergoes a reduction reaction, shown in Equation (2-2) [7], [8]. Either pure O_2 or air can be used as a fuel for the cathode; although when air is used, only oxygen gas is used to react with H_2 on the anode side to generate electricity, the other gases, such as nitrogen, argon, and carbon dioxide, are not involved in the reaction. O_2 or air can either be supplied from compressed gas cylinders or from the ambient air, which is a popular choice in automotive scenarios. During PEMFC operation, protons travel from the anode to the cathode through the polymer electrolyte membrane (e.g. Nafion), this membrane is capable of only allowing protons to pass through but restricts the flow of electrons. The protons come from the oxidation of hydrogen from the anode, this half-reaction is shown in Equation (2-1). PEMFC membranes, such as Nafion, are usually made out of materials containing sulfonic acid groups [8]. Sulfonic acid groups are beneficial in providing proton conduction [8]. In addition, water molecules present in the membrane facilitate proton hopping, also known as the Grotthuss mechanism [9][10]. Protons come from hydrogen splitting at the anode. Electrons travel from the anode to the cathode through the external circuit. The pathways of PEMFC operation are shown in Figure 2-1 and half-reactions are shown in Equation (2-1), which depicts an oxidation reaction at the anode, and Equation (2-2), which depicts a reduction reaction at the cathode [8]. Together, the half-reactions make up the full chemical reaction of a working PEMFC, as shown in Equation (2-3) [8]. The physical components of a PEMFC consist of a polymer electrolyte membrane, platinum carbon (Pt/C) catalyst, gas diffusion layer (GDL), flow field plates, polytetrafluoroethylene (PTFE) gaskets, and metallic end plates. While the above-listed components are required for a generic PEMFC, some manufacturers, such as Intelligent Energy, are looking into removing the need for certain components such as metallic end plates to reduce production costs [7]. The components and assembly of a PEMFC will be discussed more in the Methodology section.

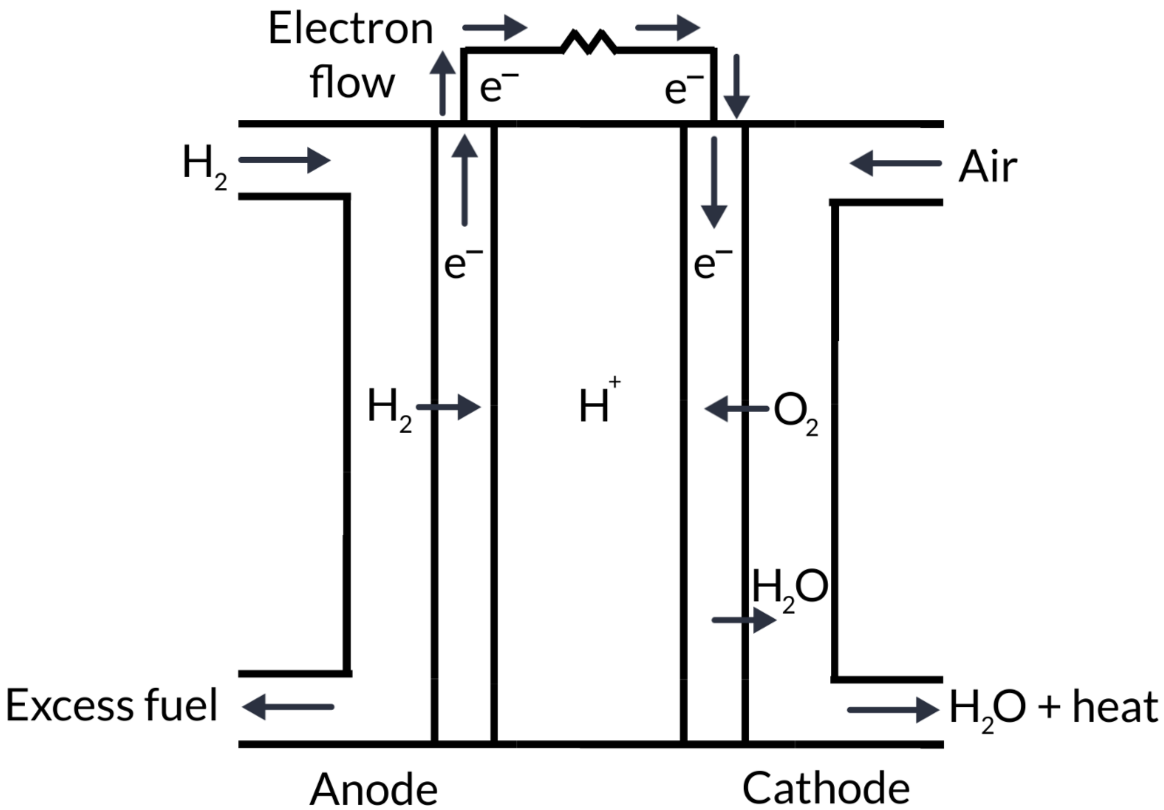

Figure 2-1: PEMFC fundamentals and operation showing the distribution of hydrogen towards the anode of the cell, through the gas diffusion layer where it dissociates. Protons travel from the anode to the cathode through the membrane, which consists of sulfonic acid groups, while electrons travel through the outer circuit.

$$H_2 \rightarrow 2H^+ + 2e^-$$

(2-1)

$$\frac{1}{2}O_2 + 2H^+ + 2e^- \rightarrow H_2O$$

(2-2)

$$H_2 + \frac{1}{2}O_2 \rightarrow H_2O + \text{electric energy} + \text{heat}$$

(2-3)

The theoretical voltage of a PEMFC can be calculated using the Nernst equation. The reversible voltage (E_r) needs to be calculated first using Equation (2-4) [8]:

$$E_r = \frac{\Delta G}{nF}$$

(2-4)

Where ΔG is the change in Gibb's free energy for the overall PEMFC equation outlined in Equation (2-3), which is −237.3 kJ mol^{-1} under standard-state conditions (25 °C, 1 atm), n is the number of electrons involved (2), and F is the Faraday constant (96485 C mol^{-1}). Inserting the corresponding values, E_r equates to 1.229 V for a Hydrogen PEMFC.

Equation (2-5) sums up the Nernst equation for hydrogen-based PEMFCs [8]:

$$E = E_r - \frac{RT}{nF}\ln\frac{\alpha_{H_2O}}{\alpha_{H_2}\alpha_{O_2}^{\frac{1}{2}}}$$

(2-5)

Where R is the universal gas constant ($8.314\ \mathrm{J\ molK^{-1}}$), T is the absolute temperature in Kelvin (298.15 K), and α is the activity of H_2O (1), H_2 (1), and O_2 (0.21), which can be derived from the ratio between partial pressure and standard pressure.

Inserting corresponding values into the Nernst equation, the theoretical voltage of a hydrogen PEMFC can be calculated, as shown in Equation (2-6) [8].

$$E = 1.229 - \frac{8.314\ \mathrm{J\ molK^{-1}} \times 298.15\ \mathrm{K}}{2 \times 96485\ \mathrm{C\ mol^{-1}}}\ln\frac{1}{1 \times 0.21^{\frac{1}{2}}} = 1.219\ \mathrm{V}$$

(2-6)

The Nernst equation suggests that the theoretical maximum voltage a Hydrogen PEMFC can achieve is 1.219 V in perfect conditions with no losses. In real-life operations or automotive scenarios, it is almost impossible for a PEMFC to reach this voltage; for a pristine cell, the open circuit voltage (OCV) is typically around 1.0 V.

Aside from the Nernst equation, the Butler-Volmer equation can be used to portray the activation overpotential or voltage losses during operation. The equation is shown in Equation (*2-7*).

$$\mathrm{j} = \mathrm{j}_0[\exp\left(\frac{\alpha_\alpha \mathrm{F} \eta_a}{\mathrm{RT}}\right) - \exp\left(\frac{-\alpha_c \mathrm{F} \eta_c}{\mathrm{RT}}\right)]$$

(2-7)

Where j is the current density (A m^{-2}), j_0 is the exchange current density (A m^{-2}), η is the overpotential (V), α_α and α_c are anode and cathode transfer coefficients, respectively, F is the Faraday's constant, R is the gas constant, and T is the temperature.

Equation (2-8) shows the equation that calculates the actual operating voltage of a PEMFC while a load is being applied.

$$\mathrm{V_{cell}} = \mathrm{E_{Nernst}} - (\eta_\mathrm{a} + \eta_\mathrm{c} + \eta_\mathrm{Ohmic} + \eta_\mathrm{concentration})$$

(2-8)

Where η_a and η_c are the anodic and cathodic activation overpotentials, respectively, also known as activation losses or η_{act}, η_{Ohmic} are the Ohmic losses, and $\eta_{concentration}$ are the concentration losses.

The equations to calculate activation losses (η_{act}), Ohmic losses (η_{Ohmic}), and concentration losses (η_{conc}) are shown below in Equations (2-9) to (2-11) [8]. Equation (2-9), the calculation of η_{act}, is a derivation of the Butler-Volmer equation outlined in Equation (2-7) [8]. Equation (2-10), the calculation of η_Ohmic, comes from Ohm's law.

$$\eta_\mathrm{act} = \frac{\mathrm{RT}}{\alpha\mathrm{F}}\ln\frac{\mathrm{i}}{\mathrm{i}_0}$$

(2-9)

$$\eta_\mathrm{Ohmic} = \mathrm{iR_{Ohmic}}$$

(2-10)

$$\eta_\mathrm{conc} = \frac{\mathrm{RT}}{\mathrm{nF}}\ln\left(\frac{\mathrm{i_L}}{\mathrm{i_L} - \mathrm{i}}\right)$$

(2-11)

Where i_0 is the exchange current density, and $\mathrm{R_{Ohmic}}$ is the Ohmic resistance.

2.3 Fundamentals of LiBs

LiBs can be regarded as an energy storage system (ESS) that yields Li-ions and electrons. A lithium-ion battery cell consists of a positive electrode (PE), made of lithium metal oxide, and a negative electrode (NE), typically made of carbon (graphite) and/or silicon [11], a separator, electrolyte, and current collectors. The terminologies PE and NE are used instead of cathode and anode to better describe the workings of a rechargeable Li-ion battery, as both electrodes can undergo both oxidation and reduction depending on whether the cell is charging or discharging [7]. The PE can be made of many alternative types of lithium metal oxides, and each type has its advantages and disadvantages [12]. During charge, Li-ions travel from the PE to the NE through the separator and electrolyte, while electrons travel in the same direction from the positive terminal to the negative terminal around the outer circuit. The electrolyte acts as a conductor in this process, as well as an insulator for the electrons [12]. The opposite happens during discharge, ions travel from the NE to the PE, while electrons travel in the same direction from the negative terminal to the positive terminal [12]. The aforementioned depiction in shown in Figure 2-2. Using the lithium nickel manganese cobalt (NMC) oxide chemistry as an example, the following reversible reactions take place during the aforementioned processes. At the PE, the reversible half-reaction is shown in Equation (*2-12*):

$$\mathrm{Li[Ni_{0.8}Mn_{0.1}Co_{0.1}]O_2} \rightleftharpoons \mathrm{Li}_{1-x}\mathrm{[Ni_{0.8}Mn_{0.1}Co_{0.1}]O_2} + \mathrm{xLi^+} + \mathrm{xe^-} \tag{2-12}$$

At the NE, the reversible half-reaction in Equation (*2-13*) takes place:

$$\mathrm{C_6} + \mathrm{xLi^+} + \mathrm{xe^-} \rightleftharpoons \mathrm{Li}_x\mathrm{C_6} \tag{2-13}$$

Combining the half-reactions, we get the full reaction:

$$\mathrm{Li}_x\mathrm{C_6} + \mathrm{Li}_{1-x}\mathrm{[Ni_{0.8}Mn_{0.1}Co_{0.1}]O_2} \rightleftharpoons \mathrm{C_6} + \mathrm{Li[Ni_{0.8}Mn_{0.1}Co_{0.1}]O_2} \tag{2-14}$$

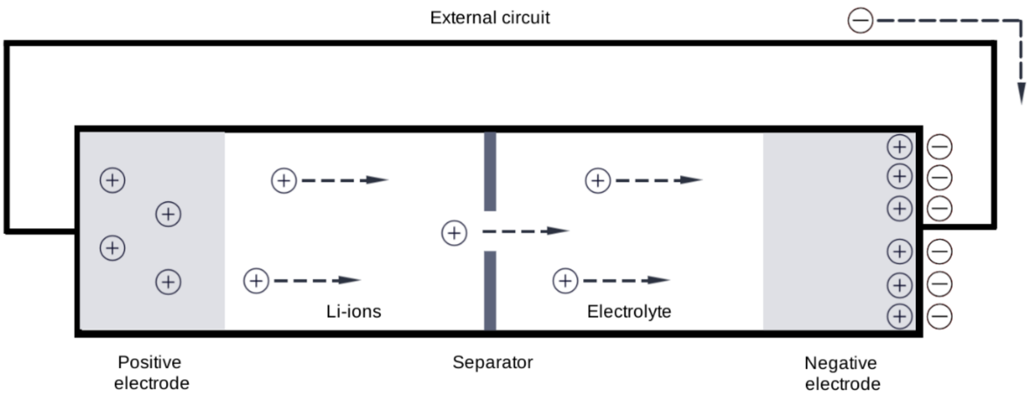

Figure 2-2: LiB fundamentals showcasing positive and negative terminals, electrolyte, and Li-ion flow. The arrows shown for the Li-ions and electrons in the diagram represent the charging process. During charge, the Li-ions move from the positive electrode to the negative electrode through the electrolyte, while the electrons move in the same direction through the external circuit. During discharge, the Li-ions and electrons move in the opposite direction, the Li-ions move from the negative electrode to the positive electrode through the electrolyte, while the electrons move in the same direction through the external circuit. The diagram above shows the charge process.

2.4 Overview of Popular LiB Chemistries for Automotive Applications

There are several types of chemistries of lithium-ion batteries suitable for use in the transportation sector. There is no single best type of cell chemistry for automotive vehicle powertrains. Each has its advantages and disadvantages. Currently, when electrodes are designed right, LiBs can achieve high power density and/or energy density, however, there are often compromises to cycle life and safety [13]. The best cell chemistry depends on what the automotive manufacturer is aiming for, or, specifically, whether the automobile requires more range, more power, or more durability while ensuring the safety of the occupants and being cost-effective.

2.4.1 Lithium Nickel Manganese Cobalt Oxide (NMC)

In an automotive scenario, NMC batteries lessen range anxiety due to their high energy density [12]. NMC batteries can reach gravimetric energy densities of 250 Wh kg^{-1} [14]. The nickel in NMC provides high specific energy. Manganese, however, provides more stability for the battery but provides low specific energy [12][15]. Originally, the PE in NMC cells consisted of an equal amount of nickel, manganese and cobalt, known as the NMC 111 [16]. Different weight ratios of these three metals may also be viable. [17][16]The progression of research and development from the past few decades was from NMC 111 to NMC 523 to NMC 622 to

NMC 811 to NMC 955 (in research) [16][13]. The trend in R&D is to have a higher nickel content to obtain higher energy density; although higher nickel content NMC may be more prone to structural and thermal instability, high capacity fade, and short cycle life [17], [19]

2.4.2 Lithium Iron Phosphate (LFP)

The lithium iron phosphate (LFP) PE chemistry was developed at the University of Texas at Austin by John Goodenough in 1996 [12]. A major benefit of LFP is the reduced cost of production when compared to cobalt-type chemistries [18][19], and is more environmentally and ethics friendly. LFP is also considerately safer in terms of the possibility of thermal runaway and more durable due to its crystal structure [12]. In nail penetration tests, LFP only has a peak temperature rise to 79 °C instead of 549 °C for NMC [18]. In addition, an estimate of three times less heat release rate and toxic carbon monoxide release is to be expected [18]. When implemented into an EV, the capacity retention after two million miles of driving can be as high as 70% [18]. This over-exceeds the 150,000-mile guarantee made by many automotive manufacturers and legislative bodies [20]. The specific power of LFP is shown to be better than that of NMCs; the specific energy is ranked lower, but recent improvements have been made which may allow the specific energy to be equivalent to NMCs [18]. Because of these benefits, this is a common PE chemistry type used in electric buses in China [11]. In addition, Tesla announced in 2021 that all its mid-range models will operate on LFP chemistry [13].

2.4.3 Lithium Nickel Cobalt Aluminium Oxide (NCA)

Nickel-rich PE chemistries typically excel in high energy density and efficiency and have gained popularity [21]. Lithium nickel cobalt aluminium oxide (NCA) or $LiNiCoAlO_2$ is also a type of cell that can be used in EVs. This type of cell is used in some of Tesla's EVs [22]. NCAs provide high specific energy, long lifespan, high power, and low cost [12], [23], [24]. Safety is ranked lower than other chemistry types, due to its structural instabilities [25]. One major safety concern is that the reactions of the electrolyte with oxygen gas evolution can cause thermal runaways [25]. The use of aluminium (Al) improves power performance by stabilising the PE charge transfer impedance. Cycle life performance is moderate but poorer than that of NMCs and LFPs [26], however, NCAs suffer from voltage decay problems [21]. In a study by Omar et al., it is found that NCA-type batteries would likely require an external heater in automotive powertrain scenarios if the vehicle is prone to cold temperatures; its cold-temperature cyclability is not as adequate when compared to the likes of LFP [26]. Starting in 2019, a growing trend is to prioritise NMC instead of NCA [16].

2.5 Current Status of LiBs and PEMFCs Technologies in a Transportation Scenario

2.5.1 Roadmaps

Table 2-1 shows a forecast of key design targets for automotive grade PEMFC systems up to 2040 with substantial improvements in the stack and system costs required, alongside enhanced system durability and efficiency [27]. While FCEVs are currently regarded by some as an overly expensive solution toward net-zero transportation [2], the improvements outlined by this development roadmap outline a path towards more competitive economics. These forecasted developments have a compounding impact when considered in a vehicle with improved system efficiency and durability reducing the cost and requirement for hydrogen generation and extending the potential cradle-to-grave impact of systems. Furthermore, the potential to recycle fuel cell components and systems has been demonstrated suggesting the longer-term sustainability of this technology may be more readily achievable at scale than for LiB technologies [28].

Table 2-1: Roadmap for FCV light-duty vehicles (LDVs), adapted from APC fuel cell roadmaps [29].

	2025	2030	2040
$ kW^{-1} (System)	112	68	40
$ kW^{-1} (Stack)	70	40	20
System Efficiency (%)	65	68	70
Stack Durability (h)	6,000	7,000	8,000

While there are significant benefits expected in fuel cell technology, it is undoubted that battery technology will also continue to develop in the same time frame. These expected improvements in cell and system performance are detailed in Table 2-2 which shows forecasts of battery technology at the cell and pack level [3]. Alongside this, there is an expectation that the higher volumes of production which are expected will result in reduced cell and pack costs, and the significant focus on automotive applications will result in improvements in the charging times for systems. However, even if the projected improvements in battery and fuel cell technologies are realised, applications well suited to hybridisation will remain. This approach allows the benefits of both technologies to be leveraged, with the challenges associated with each individual solution mitigated at a full system level.

Table 2-2: Roadmaps for battery electric vehicle (BEV) LiBs, adapted from APC electrical energy storage roadmaps [29].

	2025	2030	2035
Cell Level Transient Discharge Power Density (W kg^{-1})	1180	1260	1340
Gravimetric Cell Energy Density (Wh kg^{-1})	300	320	340
Volumetric Cell Energy Density (Wh L^{-1})	770	850	900
Cell Cost (\$ kWh^{-1})	70	58	48
Pack Level Transient Discharge Power Density (W kg^{-1})	825	945	1070
Pack C-Rate	2.5	3.5	4
Gravimetric Pack Energy Density (Wh kg^{-1})	210	240	275
Volumetric Pack Energy Density (Wh L^{-1})	540	640	720
Pack Cost (\$ kWh^{-1})	97	77	63

2.5.2 Vehicle Efficiency

For the aim of this project, It is important to consider the well-to-wheel efficiency and powertrain efficiency of the proposed vehicle. The ‘well’ in well-to-wheel efficiency refers to the efficiency of the generation of the energy source or fuel; in the context of a BEV, this usually refers to the efficiency of gathering energy from the electric grid, while in the case of an FCEV, this usually refers to the production of hydrogen [30]. There are a few different methods for hydrogen production, including renewable and non-renewable, the efficiencies and colour codes (associated environmental impact) of these methods are outlined in Table 2-3. Generally, darker colour codes suggest higher CO_2 emissions while brighter colour codes suggest lower CO_2 emissions. Electrolysis, a now popular renewable method of producing hydrogen, also called ‘green hydrogen,’ is around 70% efficiency [31]. Currently, the most common method of hydrogen production in the UK is the non-renewable steam methane reforming method, typically referred to as grey hydrogen, which has an efficiency of 74 to 85% [31], [32]. The government is looking to transition to more renewable methods such as electrolysis [31]. The ‘wheel’ in well-to-wheel efficiency refers to the endpoint of the efficiency calculation, specifically the propulsion of the wheels [30]. Well-to-wheel efficiency is the same for all electrochemical and conventional vehicles. Still, the variables used in calculations may slightly differ because inputs such as powertrain efficiency and energy generation efficiency are defined differently according to powertrain type.

Table 2-3: Methods of hydrogen production and their efficiencies. Both renewable and non-renewable methods are outlined [31], [33], [34], [35].

H_2 Production Method	**Colour**	**Efficiency (%)**
Steam methane reforming	Grey	74 to 85
Gasification	Brown	35
Pyrolysis	Turquoise	42.5
Electrolysis	Green	70
Bio-hydrogen	Green	0.1
Photocatalysis	Green	0.06
Thermochemical cycles	Green	52
Plasmolysis	Green	79.2

The well-to-wheel efficiencies of a vehicle with batteries can be defined using the following equation [30]:

$$\eta_{\mathrm{well\_wheel}} = \eta_{\mathrm{grid}} \times \eta_{\mathrm{C}} \times \eta_{\mathrm{source\_wheel}} \tag{2-15}$$

where $\eta_{\mathrm{well\_wheel}}$ is the well-to-wheel efficiency of a vehicle, η_{grid} is the efficiency of power generation from the electric grid, η_{C} is the charging efficiency, and $\eta_{\mathrm{source\_wheel}}$ is the energy source to wheel efficiency.

A list of well-to-wheel efficiencies and powertrain efficiencies of various electrochemical vehicles is shown in Table 2-4. For BEVs, powertrain efficiency refers to the efficiency from the battery pack to the wheels; for FCEVs, it refers to the efficiency from the booster to the wheels and for ICEVs, it refers to the efficiency from the fuel tank to the wheels [3], [30]. BEVs can have the highest well-to-wheel efficiency, of 66.5% [3], but this depends on how well the system is optimised. For an under-optimised system, the well-to-wheel efficiency can be as low as 21.3% [3], while for FCEVs the lowest well-to-wheel efficiency is 31.2% [3], which is higher than the lowest efficiency of BEVs. It should be noted that the FCEV scenario considered in this case would still require a small battery pack for start-ups and regenerative braking capabilities since a pure FCEV is not yet commercially viable. BEVs typically have higher powertrain efficiencies when compared to FCEVs and ICEVs.

Table 2-4: Well-to-wheel efficiency and powertrain efficiency of vehicles with a single source (non-hybrids). Well-to-wheel efficiency and powertrain efficiency are defined differently for different propulsion categories. FCEV and ICEV efficiency values are calculated by Durkin et al [36].

Propulsion category	Well-to-wheel efficiency (%)	Powertrain efficiency (%)

BEV	21.3 to 66.5	80
FCEV	31.2 to 41.6	45.9
ICEV	12.4 to 15.8	23.2 to 29.0

2.5.3 Energy and Power Density

Generally speaking, lithium-ion batteries have moderate specific energy and relatively high specific power [3]. Shown in the Ragone plot in Figure 2-3, batteries can have estimated specific energy between 10 to 550 Wh kg^{-1}, and estimated specific power between 10 to 550 W kg^{-1}. Although energy density is moderate, range anxiety concerns remain prevalent amongst battery electric vehicle (BEV) drivers [37]. Figure 2-4 shows a Maximum Power vs. Range graph of commercially available BEVs and FCEVs within different vehicle segments. In simplistic terms, power density refers more to the capability of helping a vehicle reach a certain speed, whereas energy density is more closely related to the range of a vehicle. This figure shows that BEVs tend to have less range than their FCEV counterparts, but they can provide more power. A special type of BEV segment popularised by higher-end manufacturers, the performance LDVs and SUVs, referring to vehicles such as the Porsche Taycan and the Tesla Model S P100D, have higher range than 'non-performance' oriented BE (battery electric) LDVs, with a few having similar ranges to FC (fuel cell) LDVs.

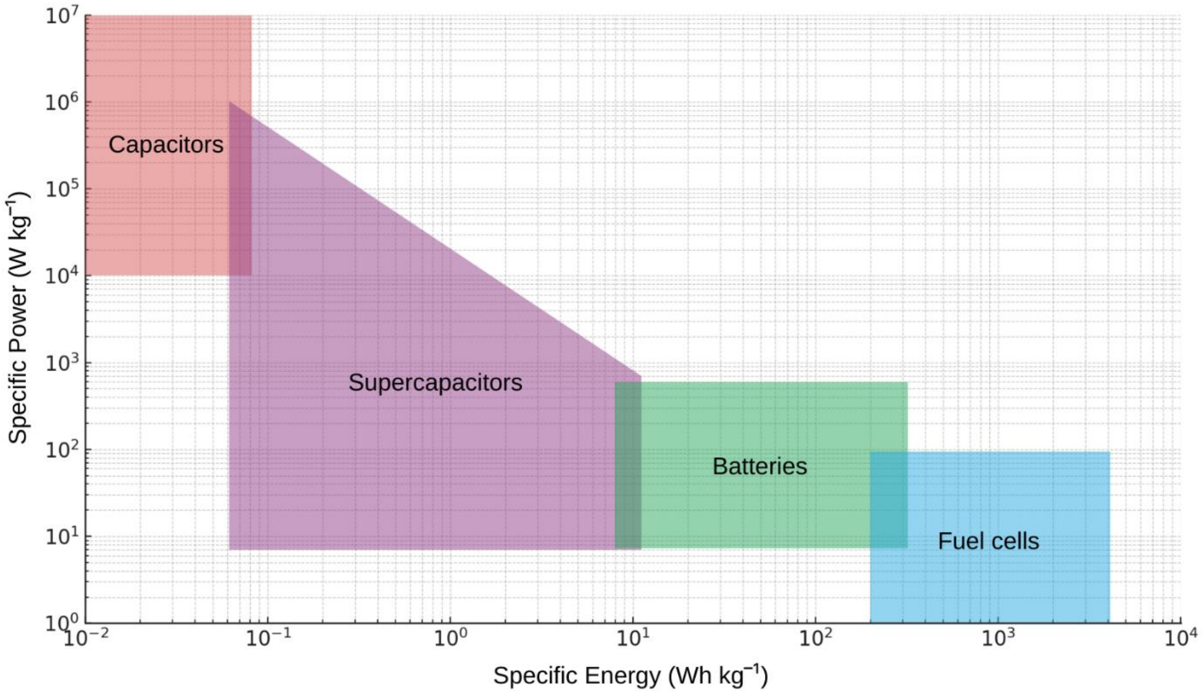

Figure 2-3: Ragone plot of fuel cells, Li-ion batteries, and capacitors [38].

Hydrogen PEMFCs have a high specific energy but low specific power. Shown in the Ragone plot in Figure 2-3, fuel cells have estimated specific energy between 400 to 5500 Wh kg^{-1}, and estimated specific power of 1 to 100 W kg^{-1}. This suggests that PEMFC can provide an optimal driving range capability; this is further verified by Figure 2-4, which shows that commercial FCEVs tend to excel in range while lacking in maximum power. In an electrochemical hybrid vehicle, PEMFCs are best used to provide for base driving, while a battery pack acts as a booster providing for transient and peak power demands. A major disadvantage of PEMFCs is their relatively poor transient performance, especially during low and high output power [39]. If a PEMFC's power output becomes excessively transient, the PEMFC may suffer premature degradation.

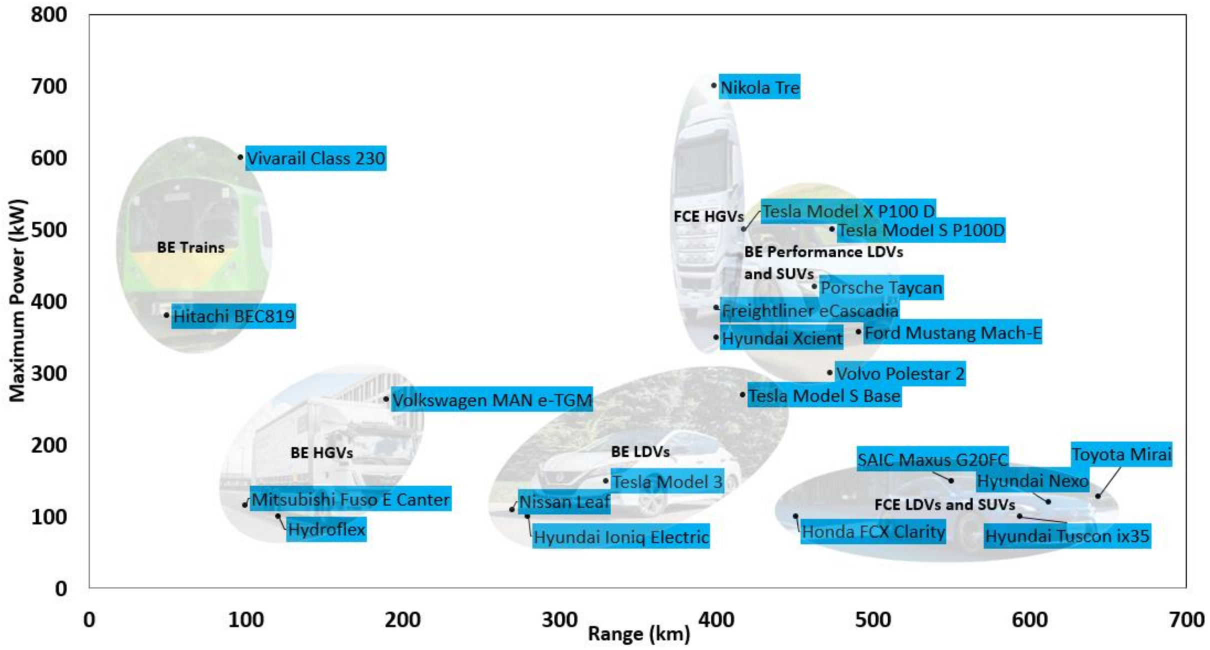

Figure 2-4: Maximum power vs. range graph for single-sourced vehicles. Road vehicles of various purposes are included, namely HGVs, passenger cars and sport utility vehicles (SUV), and trains. BEVs and FCEVs are included but internal combustion engine vehicles (ICEVs) are omitted. The graph is made by the author, the information is gathered based on viewing manufacturer specification sheets and Email exchanges with the manufacturers. BE is the abbreviation for battery electric while FCE is the abbreviation for fuel cell electric.

2.5.4 Durability

Even after years of research and development (R&D), Li-ion batteries suffer from degradation issues caused by frequent charging and discharging [39], due to solid electrolyte interphase (SEI) formation, lithium plating and NE volume changes [40]. A review paper by Pollet *et al.* suggested that an electric car battery should have a lifespan of 10 years or 150,000 miles [3].

Generally, for lithium-ion batteries used in EVs, a cycle life of 2000 to 2500 cycles is suggested before power losses reach 20% [3], [34], [36].

Lithium-ion battery degradation can be divided into three causes or modes: loss of lithium inventory, loss of anode active material, and loss of cathode active material. Table 2-6 categorises the degradation modes and the possible degradation mechanisms corresponding to them. Loss of lithium inventory induces capacity fade [41]. On the other hand, loss of anode and cathode active material can induce both capacity and power fade [41]. Some degradation mechanisms may overlap in degradation mode, such as lithium plating and dendrites formation, which can both affect lithium inventory and anode active material.

Table 2-5: Categorisation of Li-ion degradation modes with degradation mechanisms [41].

	Degradation Mode		
	Loss of Lithium Inventory	**Loss of Anode Active Material**	**Loss of Cathode Active Material**
Degradation Mechanisms	SEI growth SEI decomposition Electrolyte decomposition Lithium plating Dendrites formation	Lithium plating/dendrites Graphite exfoliation Structural disordering Electrode particle cracking Current collector corrosion	Structural disordering Electrode particle cracking Current collector corrosion CEI formation Charge transfer slow down

PEMFCs have suffered from durability issues ever since the introduction of them in 1960s [42], [42]. There are prevalent issues regarding the reliability of a PEMFC, which can include platinum catalyst decay, membrane breaks and internal gas leaks [40]. Wang *et al*. stated that the primary method of degradation in PEMFCs, platinum catalyst decay, poses a challenge for developing longer-lasting FCEVs [43]. Meng *et al.* conducted a study of operating a PEMFC using dynamic cycles for 1700 repetitions, which closely represents PEMFC operation in vehicles, and found that the main degradation modes are voltage decay and ECSA loss [44]. Most of this was caused by the poor dynamic response of PEMFCs which results in gas starvation [44]. Chandran *et al.* also conducted a study of dynamic load testing for PEMFCs. The PEMFCs were stress-tested for 2000 dynamic cycles. It was suggested that both the poor transient loading of PEMFCs and the amount of stop-start operation caused the majority of the degradation in the PEMFC, 56.78% and 33.17%, respectively [45]. Other reasons for degradation include high current density operation [45]. Carbon corrosion and delamination of the MEA could be spotted after stress testing [45]. In 2020, the Advanced Propulsion Centre UK suggested durability of only 5,000 h for a passenger car PEMFC stack [27]. A few government bodies have set targets of 8,000 h for transportation use. Durability is forecast to increase by 60% from 2020 to 2035 (~8,000 h) [27], but this target still lags behind the durability of some current ICEs (~20,000 h) [27].

2.5.5 Safety

Safety concerns are prevalent in lithium-ion batteries, although their use in commercially available vehicles has proved that they can be mitigated with regulatory systems and rigorous testing. These concerns mainly relate to over-charging and over-discharging, which can cause overheating, electrolyte gassing and pressure build-up in casings, inducing risks such as thermal runaway [39]. BEV manufacturers have the challenge of avoiding lithium-ion chemistries that are more prone to thermal runaway. The safer choice, lithium iron phosphate, is becoming more prevalent [3].

There is a growing concern in various news media regarding EVs undergoing thermal runaway, however, a report and study by the US National Fire Protection Association claims that EVs, specifically Tesla's, are 20 times less likely to catch on fire when compared to ICEVs. In addition, in a statistical analysis conducted in Norway in 2016, about 9% of total vehicle fires was related to EVs in the country [46]. In addition, many vehicle fires collected in statistics may not directly correspond to the traction type used in the vehicle, whether it is batteries or ICE, but can be due to external causes such as arson [46].

It is worth mentioning the requirements needed for a Li-ion battery to catch fire or undergo thermal runaway, also known as the battery fire triangle, shown in Figure 2-5. A resting battery already has two components needed to complete the fire triangle, that being fuel from the electrolyte, anode, or separator, and oxygen from several different cathode materials [46]. The only third component needed for the battery to undergo thermal runaway is heat, which can be obtained from a rise in external temperature, charging/discharging the battery beyond its safety limits, or causing physical damage to the battery.

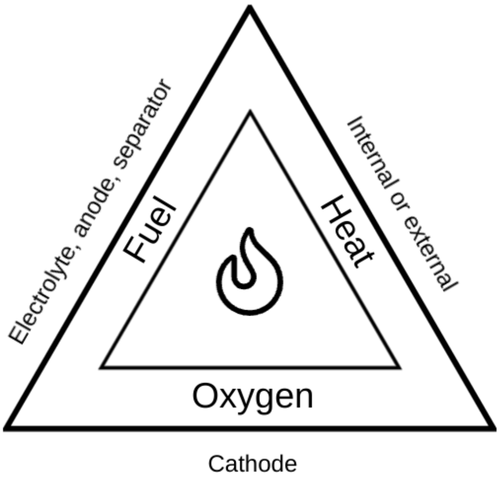

Figure 2-5: Li-ion battery fire triangle. These are the components needed for a battery to undergo thermal runaway [46].

PEMFCs are also subject to safety concerns due to the explosiveness and low ignition point of hydrogen [43]. FCEVs' safety concerns include voltage shock, hydrogen release and the structural integrity of the hydrogen storage tank or FC system [47]. Automotive engineers and designers need to package the fuel cell system (i.e. the hydrogen storage tank, valves, lines, supports) robustly to mitigate these concerns; in addition, rigorous SAE (Society of Automotive Engineers) approved tests need to be conducted [47].

BEVs and FCEVs have existed for many years but are relatively new concepts to first responders. As electrochemical vehicles become the new norm, extra training must be given to paramedics, particularly in 'disarming' the high-voltage system [47]. Typically, it is standard practice for EV manufacturers to keep the voltage to be less than 60 V per battery module [46]. In addition, as per regulations, voltage should not be over 30 V AC or 60 V DC [46]. Together, a passenger EV battery pack can be around 300 to 1000 V [46].

2.5.6 Recharging and Refuelling

A major disadvantage of a BEV is its recharging time. The Tesla supercharger is currently one of the fastest readily available BEV charging stations. It usually takes 30 minutes for a Tesla to be fully charged [37]. For comparison, a FCEV only takes three to five minutes to refuel [48]. When charging a BEV using a fast charger, charging efficiency is only 60% [49]. If charging a BEV at home, charging efficiency is approximately 90% [49], [50]

With hybridisation, the PEMFC system can act as a quick-refuelling alternative energy device upon energy depletion. A driver may have the option to 'refuel' the hybrid vehicle using both a battery charger and a hydrogen refuelling station if the vehicle has a parallel hybrid powertrain layout. Furthermore, with a series-parallel battery and PEMFC architecture, the PEMFC can help charge the battery [50], [51].

2.5.7 Cost

The APC has published a roadmap, from 2025 to 2035, that contains cost figures for automotive batteries; shown in Table 2-2. For a vehicle-based project, it is not enough to consider only the stand-alone battery cost, since the powertrain costs of electrochemical vehicles are also important; these are shown in Table 2-6. Currently, both BEV and FCEV powertrains are more costly than conventional ICE powertrains [52], [53]. The capital cost of BEV powertrains is expected to have a ~70% decrease from 2010 to 2030 [52].

Table 2-6: Capital costs of various vehicle powertrains for light-duty vehicles [52]. The 2030 cost figures are estimates.

Powertrain type	Capital cost in 2030 (£)
BEV	6022
FCEV	8063
ICEV	1888

PEMFCs are costly to manufacture [3]. Currently, the cost of a PEMFC powertrain is estimated to be five times higher than that of an ICE powertrain [42]. One of the main contributors to this high cost is the use of precious metals, especially the use of platinum in the manufacturing of the catalyst. Much research on PEMFC cost-reduction has focused on reducing the platinum loading for catalysts, facilitating better catalyst utilisation, or using non-platinum-based catalysts [54], [55]. Although the cost of PEMFC systems has decreased over the years, (it was 112 $/kW in 2020 for passenger cars), there remains much room for improvement [50]. PEMFC costs are projected to improve from 2020 to 2035, with a decrease of 64% from 2020 to 2035 [50]. The decline of cost targets would accelerate widespread commercialisation and public acceptance of vehicle-use fuel cells.

2.6 Hybrid Vehicle Sizing

There are gaps in research regarding the actual sizing of components for the optimisation of the parameters of an electrochemical hybrid vehicle. This is true for some, but not all, aspects of Hybridisation for X. For example, much research has been carried out into optimising sizing to improve fuel economy, degradation and cost. However, equivalent information on X parameters, such as weight and degradation, appear to be under-represented in the literature. There is an abundance of literature on optimising the EMS that a vehicle uses, but such studies tend not to elaborate on how the vehicle was sized before the application of EMSs. Usually, sizing is pre-determined without explanation or selected from a pre-built vehicle. For example, in a study by Fisher *et al*., pre-determined sizing was taken from a pre-built Microcab H2EV hydrogen-electric vehicle [56]. For reasons related to commercialisation, consumer-available fuel cell hybrid electric vehicles (FCHEVs), such as the Toyota Mirai, tend to have an oversized fuel cell stack and a small battery pack [57]; a scientific gap exists in the optimisation of sizing for these electrochemical hybrid vehicles.

The Society of Automotive Engineers (SAE) has introduced guidelines on the sizing and power delivery requirements of a vehicle [58]. This includes the capability to sustain driving at 120 km h^{-1} with a 0% grade and 80 km h^{-1} with a 6% grade [58]. These two requirements correspond to 30 and 38 kW of average power for a mid-sized FCEV, as simulated in the

Advanced Vehicle Simulator (ADVISOR) by Marx *et al*. [58]. For an electrochemical hybrid vehicle, the norm for sizing is to ensure that the fuel cell system accounts for base driving while the battery system accounts for transient demands. Marx *et al*. studied the hydrogen fuel consumption and degradation of various electrochemical system sizing configurations for a mid-sized passenger vehicle. The EMS used was a state machine strategy paired with a rule-based strategy that was consistent for all sizing variations [58]. Table 2-7 shows the sizing configurations and the motivations on which this study was based. From simulations using ADVISOR, it was found that a mid-sized passenger vehicle would require at least a 40 kW FC and a 60 kW battery or 100 kW in total (Row 2 of Table 2-7) [58], adhering to the SAE protocols. If a standalone battery-only propulsion mode were a design goal, then the battery would need to be at least 100 kW in size (Row 1) [58]. Rows 3 and 4 configure the minimal system into a more fuel cell dominant vehicle, with a 40 kW FC - 60 kW battery and an 80 kW FC - 20 kW battery system, respectively. These two configurations have decreased hybridisation rates. The hybridisation rate can be defined as the ratio of the power of the battery to the total power (battery plus fuel cell power) [59]. Finally, Row 5 illustrates a sizing similar to that of a first-generation Toyota Mirai [58]. It was concluded, from this study, that larger hybridisation rates and component sizes improved the hydrogen consumption and degradation of both the fuel cell and the battery [58].

Table 2-7: System sizing configurations used by Marx et al.[58].

FC sizing (kW)	Battery sizing (kW)	Motivation behind sizing configuration
40	100	Minimal fuel cell sizing, vehicle can be operated under battery-only mode
40	60	Minimal sizing adhering to SAE requirements
60	40	Decreased hybridisation rate
80	20	Decreased hybridisation rate
100	20	Sizing similar to Toyota Mirai first-generation

Kim *et al*. conducted a study of a PEMFC-battery hybrid minibus sizing based on a matrix of different sizes, for both energy sources, to find the most efficient combination [60]. The matrix used is shown in Table 2-8. In this matrix, the battery is in units of cells in series and the fuel cell is in units of kW; the values derived act to describe the efficiency of the system. Each cell has a capacity of 85 Ah [60], but the exact model and specification of the cell were not specified. Efficiency is defined as the power delivery of the PEMFC and the battery [60]. The goal was to test all component sizes listed in the matrix and identify a combination where both the fuel cell and the battery were operating at maximum efficiency. The aim was to ensure that the fuel cell did not operate in the low or high-power ranges and that the battery operated at a desired SOC with minimal power losses. It was concluded that a battery size of 18 cells (equivalent to 30 kW) and a fuel cell power of 40 kW was the most efficient combination, which enabled the efficiency of the system to reach 38% [60].

Table 2-8: PEMFC and battery size matrix by Kim *et al*.[60]. The values within the matrix are the efficiencies of the system.

Sub-Batteries Number	Stack Capacity (kW)				
	30	40	50	60	70
16	11	34	35	34	32
18	28	38	36	35	34
20	32	31	29	33	35
22	32	33	30	31	30
24	22	31	32	32	32
26	16	33	33	33	32
28	22	33	34	34	33
30	24	33	35	34	33

Using a modelling-based approach, Wang *et al*. conducted a study of the impact of different sizing configurations on degradation, fuel economy and cost for a battery-PEMFC bus, using three different drive cycles, namely the UDel[1], Manhattan and Orange County bus drive cycles. Only two battery sizes were compared in this study, namely 5.5 and 11 kWh, but a range of fuel cell sizes was used, from 20 to 160 kW. A rule-based EMS was used for all comparisons [61]. Tests were run using the UDel drive cycle first, which has a higher power demand than the Manhattan and Orange County bus drive cycles. It was found that, while keeping the battery size constant, increasing the size of the fuel cell to above 80 kW shortened the lifetime of the stack, since it operated at a higher potential, with the same power demand as the smaller stacks [61]. The FC stack could not be too small, however, as a 40 kW stack and an 11 kWh battery pack were incapable of supporting the drive cycle demands after only 2,000 h of use [61]. The stack sizes that produced the best degradation performance were 60 and 80 kW stacks when paired with an 11 kWh battery pack [61]. Using the smaller 5 kWh battery pack also induced greater degradation in the FC stack, due to the need for the stack to handle higher power demands; furthermore, the battery was packaged prematurely due

---

[1] The UDel Drive Cycle is a private drive cycle based on data collected by the Centre for Fuel Cells and Batteries, of the University of Delaware, on routes around the university campus, using a Gillig platform PEMFC-battery bus.

to the higher C-rate that it experienced [61]. After further testing, using the other two drive cycles, it was concluded that a battery-dominant hybrid setup was best in terms of degradation of the PEMFC [61]. It was also concluded that PEMFC systems with sizing configurations that produce more than the average power demand of the drive cycle tend to degrade quickly [61].

A typical sizing strategy is to have the PEMFC to take an average load of a load profile and the battery pack accounting for the rest. Cai *et al*. have followed this principle to size an unmanned underwater vehicle (UUV) [62]. This strategy has resulted in a longer range when compared to a UUV with only one energy source. Depending on the power or energy requirements of the vehicle, supercapacitors can also be used in place of batteries, if a more power-dense system is required [62]. This research has focused more on the selection of the types of energy sources used, and the sizing for these sources [62].

2.7 Hybrid Vehicle Classification

There are many ways to categorise hybrid vehicles. Common approaches are based on the degree of hybridisation, architecture and whether passive or active (based on the existence of power electronics). Many hybrid vehicles fall into a number of categories. Figure 2-6 summarises hybrid vehicle classification. This classification system can apply to both conventional battery-ICE hybrid vehicles and electrochemical hybrids. Classification systems can be based on the degree of hybridisation, powertrain architecture, charging strategy and the existence of power electronics. As more research has featured battery-ICE hybrid vehicles than electrochemical ones, many classification schemes identified during this literature review came from articles focused entirely on conventional battery-ICE hybrids. In this Section, the classification systems described are initially based on battery-ICE, but there follows a more in-depth description of methods and the complications of applying the classifications to electrochemical hybrid vehicles. For simplicity, battery-ICE hybrid vehicles are referred to as ‘conventional’, with PEMFC-battery hybrid vehicles referred to as ‘electrochemical’. Certain conventional hybridisation classification methods, such as classification based on the path of energy flow, have been omitted, as most electrochemical hybrids use an electrical power transmission path (EPTP), instead of a mechanical power transmission path (MPTP) like conventional hybrids [63].

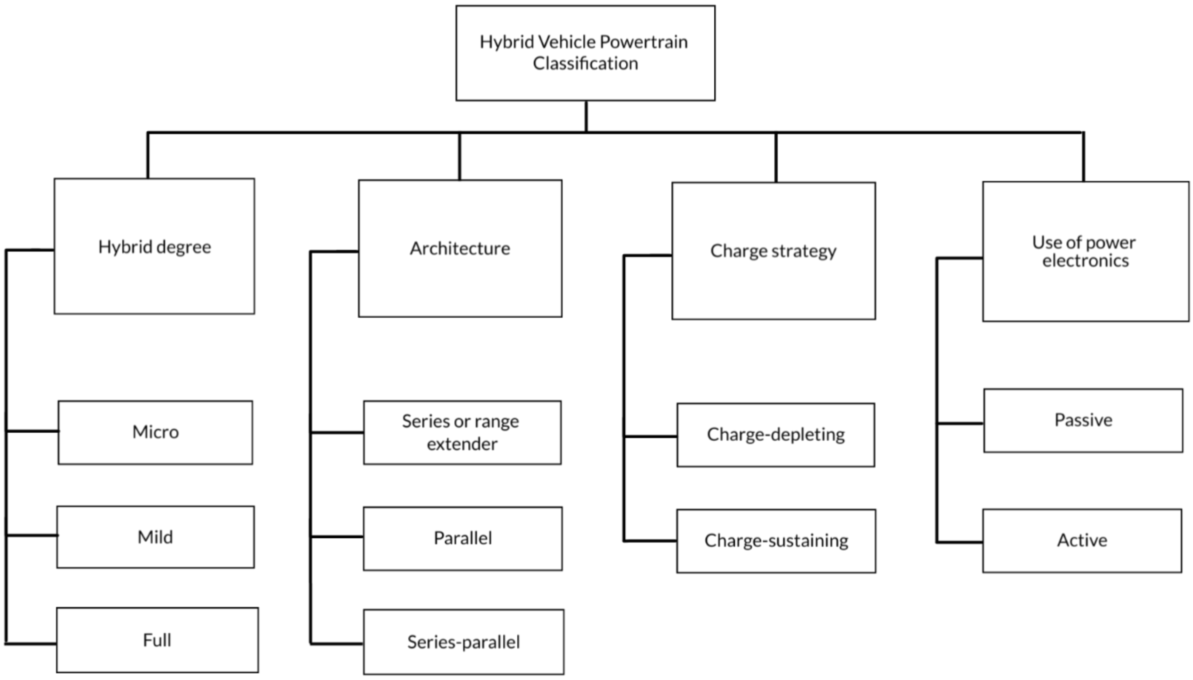

Figure 2-6: Hybrid vehicle classification. Hybrid vehicles can be classified based on degree of hybridisation, architecture, charge strategy and the existence of power electronics.

2.7.1 Hybridisation Degree (HD)

The hybridisation degree (HD) can be either a qualitative or quantitative classification. The qualitative classification is based on the amount of electric motor power, battery size, and the general purpose of the hybridisation [39]. A micro-hybrid vehicle usually refers to a vehicle with start-stop technology. Typically, the electric motor in this type of vehicle is very small. Some experts argue that this type of vehicle should not be categorised as a hybrid vehicle, as the starter motor does not provide propulsion to the wheels [39]. A 'mild hybrid vehicle', on the other hand, contains one power source that has significantly less capacity and volume than the main propulsion source [39]. This low-capacity source is mainly used to provide additional support for vehicle boost, vehicle recuperation and vehicle start-up [39]. A 'full hybrid' refers to the type of vehicle that people usually associate with being a 'conventional hybrid vehicle.' In a conventional hybrid vehicle, the requirement for such a vehicle is that the electrochemical components, specifically the electric motor paired with the battery pack, are able to provide propulsion to the wheels [3], [39]. This propulsion may be aided by other energy sources, such as ICEs or flywheels, but there must be coaxial or wheel-hub motors propelling the vehicle, suggesting the use of electrochemical sources such as batteries, fuel cells, or supercapacitors [39]. Typically, full hybrids have large electric motors [39]. Typically, full hybrids are configured in parallel or series-parallel architectures, which will covered in later sections. The Toyota Prius is an example of a full hybrid vehicle.

Hybrid degrees can also be quantified in terms of ratio or percentage. This concept is useful for evaluating the hybridisation classifications being discussed. For an FCHEV, the hybridisation degree can be calculated using the equation below [39]:

$$\mathrm{HD} = \frac{\mathrm{P_{PEMFC}}}{\mathrm{P_{tot}}} \times 100\% \ (\%)$$

(2-16)

where $\mathrm{P_{PEMFC}}$ is total PEMFC power output and $\mathrm{P_{tot}}$ is total powertrain power (both PEMFC and LiB combined). HD is measured as a percentage (%).

Different authors and researchers may use different terms for hybrid degree, a few common variations are hybrid ratio and hybrid factor. In addition, the term can be defined differently, but all serve a similar purpose. For example, Almeida *et al*. defines hybrid degree as the ratio of the battery's power output to the total output [6]; Partridge *et al*. define hybrid degree as the ratio of PEMFC to the other power source available, which in this case, is a supercapacitor [64]. To keep the data analysis consistent in this thesis, the author has followed the convention of Equation (2-16), on par with Atwood *et al*. and Feng *et al*.'s definition [65], [66].

2.7.2 Classification Based on Architecture

Hybrid architecture can be divided into three main categories: series (range extender), parallel, and series-parallel [67]. With battery and ICE hybridisation, the battery and ICE component sizing varies depending on the architecture used. Figure 2-7 shows a ranking of the electrification levels of typical battery-ICE hybrids. In general, the higher the electrification level, the larger the battery needs to be. The same concept can be adapted to all-electrochemical hybrid vehicles. However, instead of the 'electrification' level, the classification needs to account for the relative balance between the fuel cell and Li-ion battery and the way that they are required to operate together.

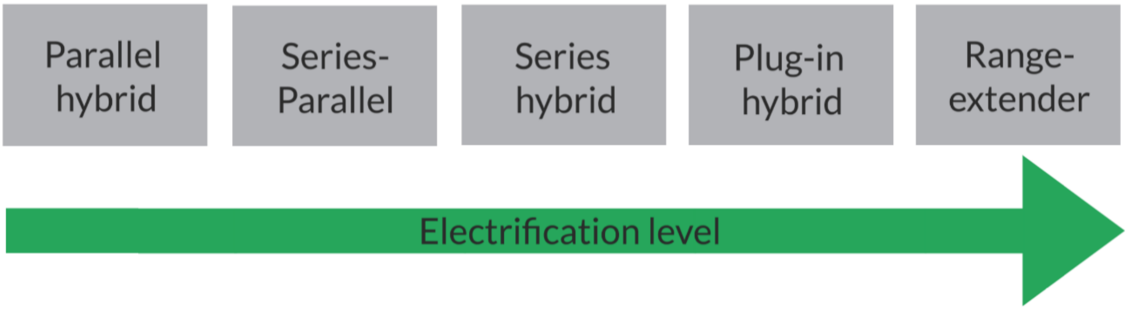

Figure 2-7: Electrification level of battery-ICE vehicles [67]. This diagram can also be adapted for electrochemical hybrid vehicles.

A battery-ICE parallel hybrid vehicle allows the propulsion of the wheels from both the battery and the ICE and is considered as the 'least electrified'. The battery-electric motor and the ICE are in a parallel layout with a mechanical coupling, hence the name. A typical parallel hybrid architecture is shown in Figure 2-8. This architecture would typically require a higher-capacity ICE and a smaller-sized battery compared to other systems. The higher engine capacity is to ensure its wheel propulsion capabilities.

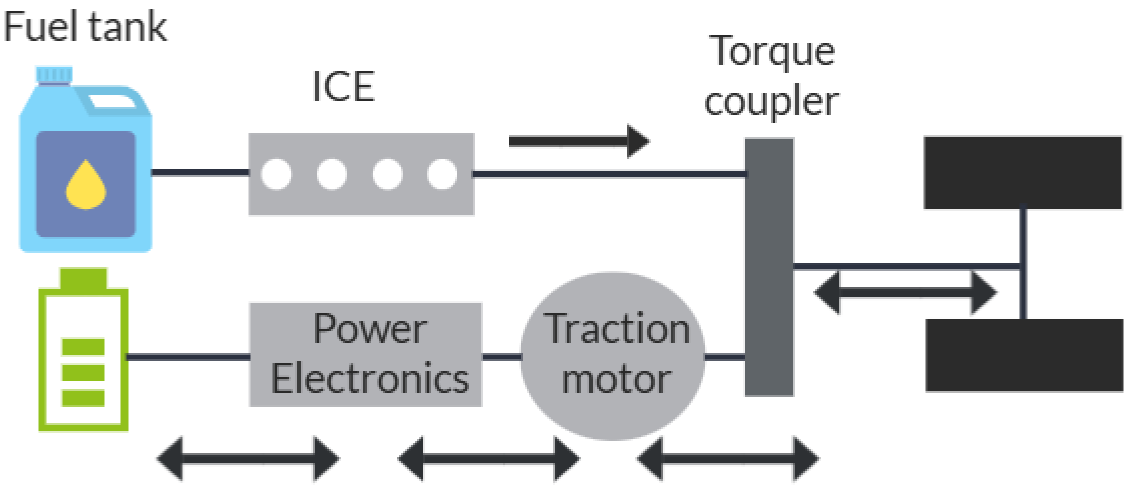

Figure 2-8: Typical parallel architecture. This type of architecture allows propulsion by both the electric motors and ICE [68]. Some manufacturers may steer away from using power electronics to avoid power losses, creating what is known as a passive hybrid system.

The same sizing concept can be applied to a parallel fuel cell–battery hybrid architecture. Another sizing consideration that needs to be considered for this hybrid architecture, or any architecture, is whether the system is active or passive. Active systems are hybrid systems with power electronics, such as DC/DC converters, while passive systems are systems without them [69]. A passive system has the advantage of less power loss but makes it more challenging to implement an energy-management strategy when compared to an active system. The difference in the power output and availability of energy-management strategy creates another complication when sizing in terms of duty cycles.

A 'series hybrid' is one where only the electric motor propels the wheels, and the ICE is only used to charge the battery, having no mechanical connection to the wheels [70]. A typical series hybrid architecture is shown in Figure 2-9a. The ICE is typically downsized and smaller in capacity compared to a parallel architecture [67]. This means, however, that when sizing with duty cycles, the battery and traction motor need to account for the maximum required power. A 'cousin' of the series architecture is the range-extender architecture, where the layout is still in series, but the ICE is even more downsized, paired with a higher-capacity battery pack to lessen the need for charging from the ICE, Figure 2-9b shows a representation of this modified series architecture. This type of architecture is considered more electrified than the series architecture, as the battery has more capacity; it is, therefore, represented at the extreme right of the spectrum in Figure 2-7. A series architecture is sometimes referred to as a range extender or vice versa. There is no strict naming convention, but a requirement is that only one energy system can propel the wheels. Therefore, sizing the propulsive components of these vehicles would need to be done differently for these architectures and between these architectures. For the case of the range extender, once again, the battery and electric motor need to account for 100% of the required power. However, the battery would need to be sized with more capacity than the conventional series architecture as there is less charging capability from the downsized ICE. Electrochemical hybrid vehicles also use configurations like series and range extenders. The Renault Kangoo Z.E. is an example of such a vehicle [71].

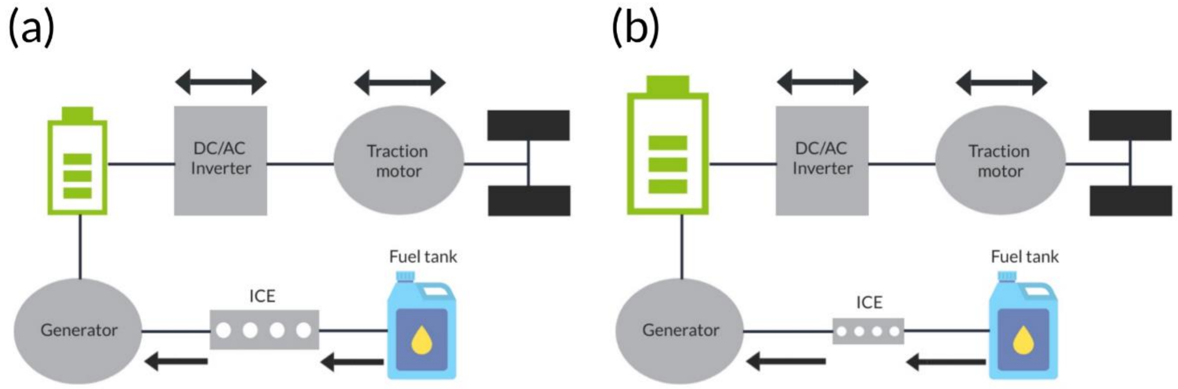

Figure 2-9: Series and range-extender hybrid architecture. (a) Series architecture. In this architecture, only the electric motor paired with the battery is capable of propelling the wheels. The ICE is only used for charging. (b) Range extender.

The series-parallel architecture combines series and parallel architecture to retain the advantages of both types. The said layout is shown in Figure 2-10. The ICE can charge the battery, as well as provide propulsion to the wheels [39]. A power split device helps divide the engine output into separate mechanical and electrical paths [39]. The main benefit of this setup is that more power can be provided for a longer period, without the need to plug the vehicle into an outlet. The disadvantages are that this system is costlier and implies greater system complexity [39]. A control strategy is usually put into place to allow the powertrain to go into parallel mode when there is high power demand, where the engine can aid the electric motor with propulsion. A control strategy is usually put into place to allow the powertrain to go into parallel mode when there is high power demand, when the engine can aid the electric motor with propulsion.

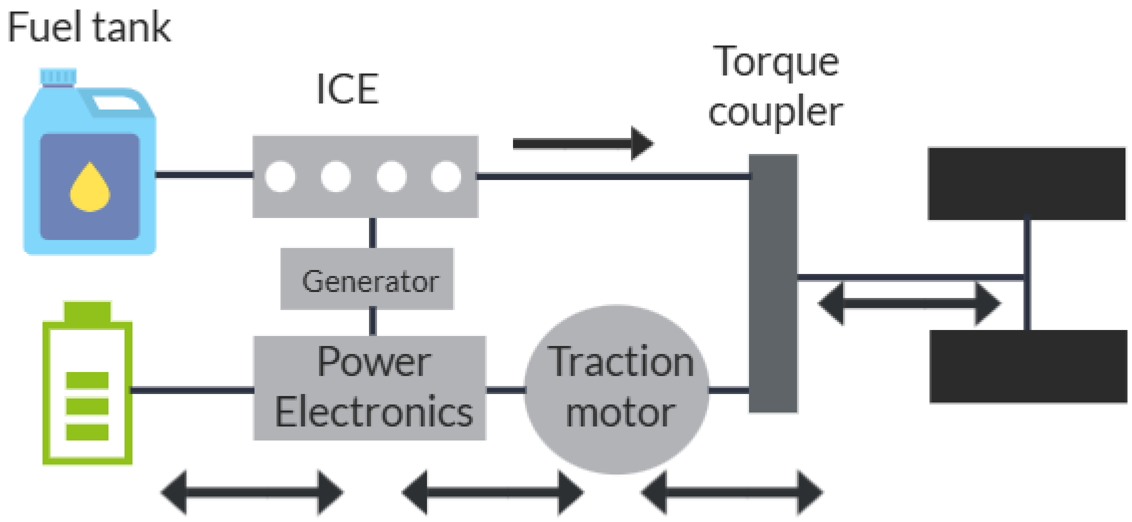

Figure 2-10: Series-parallel architecture.

2.7.3 Classification Based on Charge Strategy

There are two main types of charging strategy for hybrid vehicles: charge-depleting (CD) and charge-sustaining (CS) [72]. A charge-depleting strategy uses the electric motor paired with an electrochemical source, or a combination of electrochemical sources, to propel the vehicle's wheels until the source(s) reaches a minimum threshold state-of-charge (SOC), before causing permanent damage to the sources through, for example, battery over-discharging [72]. When the minimum threshold is reached, the vehicle's other sources, such as an ICE, need to take over, or the depleted source is recharged or refuelled [72]. Charge-sustaining, on the other hand, refers to keeping the SOC of the electrochemical sources within a certain range, to avoid intense depletion [72].

Most current hybrid vehicles use a combination of charge-depleting and charge-sustaining, namely CD-CS and blended modes, and cannot be classified as being solely CD or CS. CD-CS entails first putting the electrochemical source into CD mode along the driving cycle, and then, when the minimum threshold SOC is reached, the EMS directs the vehicle into CS mode, where a minimum SOC range is maintained until the end of the trip The blended mode also has a combination of CD and CS modes, but instead of depleting the electrochemical source to its minimum SOC, CD and CS modes are constantly alternated by the EMS [72]. The blended mode also has a combination of CD and CS modes, but instead of depleting the electrochemical source to its minimum SOC, CD and CS modes are constantly alternated by the EMS [72].

2.7.4 Classification Based on Power Electronics

As Figure 2-6 has shown, hybrid vehicles can be divided into two categories, based on whether power electronics such as DC/DC converters, or DC/AC inverters, are used. A powertrain system with power electronics is called an active system and one without is called a passive system [69]. Nishizawa *et al*. showed that a passive battery-fuel cell system reduces losses due to the lack of conversion efficiency penalty from power electronics [69].In a passive fuel cell supercapacitor system, the supercapacitor pack absorbs the excess power produced from the fuel cell stack [73].

2.8 Drive Cycles

Drive cycles are standardised speed vs. time data profiles used by automotive manufacturers, testers, and researchers for fuel consumption, emissions, and durability testing and validation [74]. Over the years, they have changed from being used solely for emissions and dynamometer testing in internal combustion engine (ICE) applications to also acting as inputs for vehicle simulations, parameterising and powertrain component sizing [74]. In a review paper published in 2002 by Esteves-Booth *et al*., it mentioned the simulation and estimation capabilities of certain drive cycles, and how drive cycles provide more than just emissions testing [75]. This paper was over two decades ago when drive cycles were starting to become more popular for simulations rather than solely emissions testing. Over the past decade, battery electric and fuel cell powered vehicles have initially attracted more interest and increasingly a higher market share due to a range of legislative and environmental factors. These vehicles have the potential to reduce, and indeed remove, combustion emissions including CO_2 and NO_x resulting in improved air quality and a mitigated environmental impact from personal transportation. When studying the performance of these vehicles or energy sources, drive cycles are a crucial tool to simulate realistic driving. These cycles are used by systems designers and researchers for activities as diverse as cell-level degradation studies to pack-level component sizing.

Some countries and regions have also implemented their own specific legislative drive cycles such as The New European Drive Cycle (NEDC) or China Automotive Test Cycle (CATC), while others use a jointly produced worldwide drive cycle [76]. However, all drive cycles have their limitations and are not universally applicable across different vehicle powertrain architectures (ICE, EV, hybrid), vehicle size classification and nature of the application. Other limitations have been identified including not accurately representing real-world driving behaviours, which can include significant differences in energy usage between drive cycles using similar dynamics, locations having different driving dynamics than others and region-specific driving styles and needs [74], [77], [78]. For example, Son *et al*. conducted a driving comparisons study between driving in the United Kingdom (UK) and South Korea using a combustion-powered vehicle (CV). The driving survey was conducted based on similar road conditions in the UK and North Korea, with the UK being slightly higher in driving distance. It was found that the vehicles driven in the UK have resulted a much higher fuel economy; the vehicle used in the UK had a fuel efficiency of 19.52 km L^{-1} while the vehicle used in South Korea had a fuel efficiency of 8.66 km L^{-1} [79]. This was due to different driver characteristics, road environments, and traffic flow between the two regions. This suggests that if a UK-based drive cycle were to be used to design and range estimate a vehicle for the South Korean market, the result would be skewed.

Drive cycles can be divided into two categories: modal and transient. Transient drive cycles are usually collected based on real driving data while modal cycles are not. The introduction of drive cycles in different regions of the world has evolved as summarised in Figure 2-11. In Japan, the first-ever legislative drive cycle, 4-Mode, was introduced in 1966 [80], [81]. Thirty-nine years later, this was succeeded by the JC08 cycle in 2005 [82]. In the United States, the California 7-Mode drive cycle was established in 1968 [80], [81]. The latter cycle was created based on Los Angeles Street conditions and was used as a national drive cycle [80], [81]. The (Environmental Protection Agency) EPA Federal Test Procedure drive cycle was introduced as a legislative test procedure for passenger cars in 1972, hence the naming classification (FTP-72) [80]–[8]. FTP-72 later became FTP-75, in 1975 [82]. In 1970, European countries started with a legislative modal cycle, UN-ECE Regulation Number 15 (ECE-15), which later became a part of the New European Drive Cycle (NEDC); this was later replaced by a cycle known as the Worldwide Harmonised Light Vehicle Test Procedure (WLTP) cycle, in 2017 [84]. In 2019, China introduced its transient drive cycle, China Automotive Test Cycles (CATC), to reflect the country's unique driving dynamics due to extreme congestion resulting from overpopulation [85]. None of the drive cycles in the timeline was built purely for electric vehicles, but as 'general-use' cycles. The electric motor is a major component that makes electric vehicles different from CV driving. Electric vehicles have instant torque from a standstill and produce a speed and acceleration curve different from that of CVs, which should be represented in a drive cycle. Protocols already exist in converting conventional use drive cycles for electrochemical bench testing; for example, Fuel Cell and Hydrogen Joint Undertaking (FCH) has a current control based NEDC drive cycle for fuel cell bench testing [86]. However, NEDC was a modal drive cycle introduced earlier in the 1980s [87], when electrochemical vehicles were far less utilised and researched compared to today. In addition, NEDC was not collected from real-life driving data; instead, was a dynamometer testing cycle better suited for emissions testing rather than vehicle engineering or simulation.

Using a transient drive cycle that mimics real-life driving scenarios and actual vehicle behaviour is crucial for proper design and accurate range estimation of electrochemical vehicles. Jeong *et al*. simulated electric vehicle driving based on conventional drive cycles and concluded that the cycles do not account for the higher acceleration capabilities of electric vehicles [88]. In addition, the importance of developing 'electric-only' drive cycles was emphasised. An electric vehicle transient drive cycle can be collected using techniques such as microtrip clustering technique combined with a CANBUS datalogger. Some electric drive cycle collections have been done in the past, such as in a study conducted by Peng *et al*. for developing a hybrid electric bus cycle in Zhengzhou, China using the Markov chain method [89]. However, none are legislated for widespread use and tend to be city, research facility, or academic institution-dependent. The lack of electric drive cycles is a legislative problem rather than an engineering problem, as collecting one is straightforward but requires organisation, data acquisition, and manpower. As we enter the age of electrochemical propulsion, legislated and dedicated region-specific electric vehicle drive cycles are crucial for the accurate representation of these vehicles.

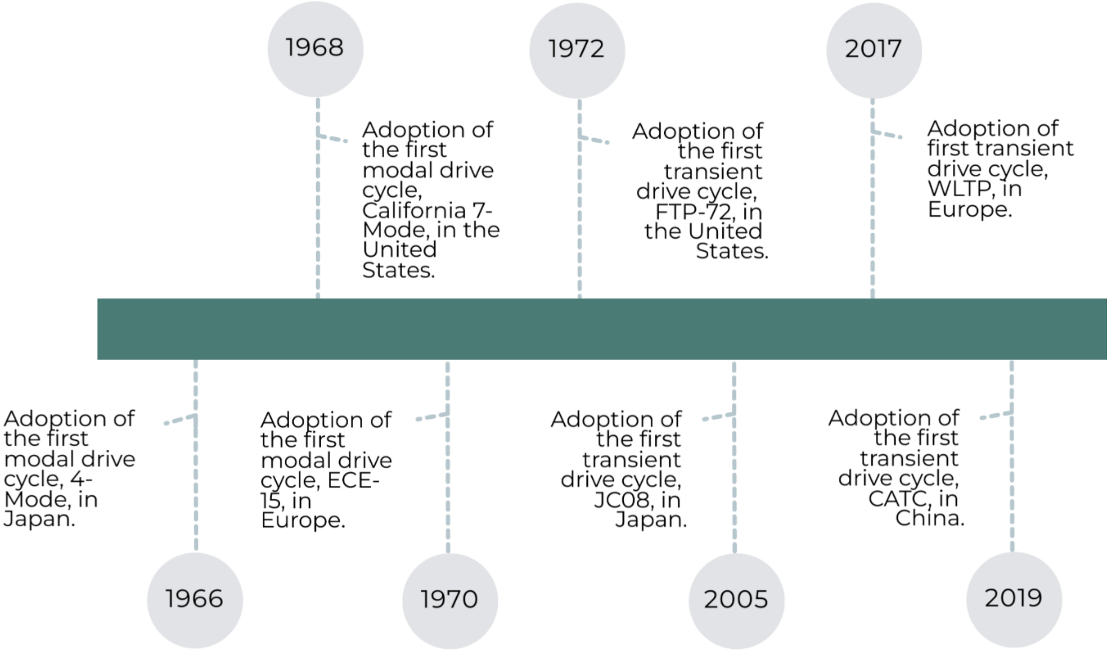

Figure 2-11: Timeline of modal and transient drive cycle adoption between different countries.

There have been review papers regarding drive cycles in previous literature, but very few recent ones, none have gone into depth about the history of the cycles and their adaptability to electrochemical vehicles of the current decade. Esteves-Booth *et al*. published a review paper in 2002 which reviewed developments in drive cycles and broke them down into emission factor, speed, and modal models [75]. Emission factor models only correspond to one type of vehicle and driving route and are not representative of other types of vehicles such as electrochemical vehicles. Average speed models rely on emission functions and are mainly used for emission testing instead of vehicle or device simulations. Modal cycles are described in the paper as the most realistic compared to real-world driving. However, this paper was published in 2002 when very few countries had introduced a legislative transient cycle; only the United States had a transient cycle at the time, FTP-72. Samuel *et al*. emphasised in their review paper that transient cycles should be used for accurate emissions testing and estimation of vehicles [90]. Again, this paper was published in 2002 when electrochemical vehicles were less popularised. In a more recent paper, Tong *et al*. developed a drive cycle for an electric bus operating in Hong Kong and compared characteristics such as velocity and acceleration trends of the drive cycle to other bus cycles [91].

2.8.1 Drive Cycle Classification

Drive cycles can be divided into two categories: modal and transient [77],[78]. Modal drive cycles, such as the New European Drive Cycle (NEDC), are designed for specific regulation testing [74]. Modal drive cycles tend to have sections of linear acceleration and constant velocity, shown in the NEDC example in Figure 2-12, and do not accurately depict realistic driving behaviours [74], [77], [78]. Transient cycles, on the other hand, are collected from real driving data, typically using a global positioning datalogger (GPD) or CAN-BUS readers, such as Advanced Vehicle Location (AVL) [92], OXTS inertial+ [93], or Launch Tech Diagnostic Tools; these tools help determine vehicle location, gradient, and speed data via GPS and CAN messages from a vehicle [74], [77], [78], [94]. Figure 2-12 is a speed vs. time graphical comparison between a modal (NEDC) and transient (WLTP Class 3) drive cycle. As seen in the figure, modal drive cycles appear less varying while transient cycles appear more random. NEDC contains four repetitions of the same profile of the ECE-15 drive cycle, which represents urban driving, and one repetition of the Extra-Urban Driving Cycle (EUDC), which represents highway driving. In contrast, the WLTP cycle is divided into four sections: low, medium, high, and extra high. These sections have increasing average speeds to represent driving on distinct types of roads and traffic conditions. Low represents congested traffic, medium and high represent more free-flowing urban traffic, and extra-high represents highway driving.

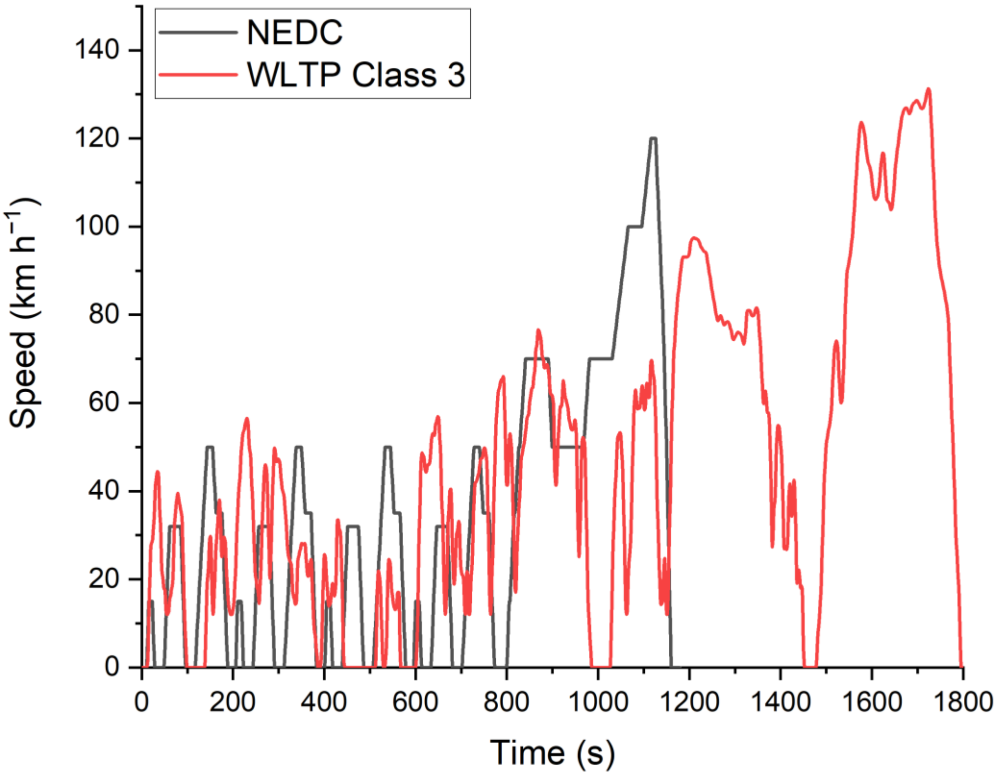

Figure 2-12: Modal (NEDC) vs. transient (WLTP Class 3) drive cycles. The NEDC drive cycle is an 1180 s modal drive cycle with linear acceleration and constant velocity. It contains two sections: city driving and highway driving. The WLTP drive cycle is a 1800 s transient drive cycle that represents real-world driving behaviour.

2.8.2 Overview and History of Legislative Drive Cycles Sorted by Region

2.8.2.1 European Drive Cycles

UN-ECE Regulation Number 15 was introduced in Europe, in 1970, to simulate urban driving [84], [95]. This modal drive cycle later became part of the NEDC, which was introduced in 1980 [87], [96]. There was legislation regarding vehicle emissions before 1970, in the form of the Agreement of 20 March 1958, which concerned the adoption of uniform conditions of approval and reciprocal recognition of approval for motor vehicle equipment and parts, but no actual drive cycle was introduced [95]. This agreement, however, led to the introduction of UN-ECE Regulation Number 15, in 1970 [95]. The UN-ECE Regulation Number 15 Test consists of three separate parts: Type-I, pollutant emission testing for speeds up to 50 km hr^{-1}, Type-II, carbon-monoxide emission testing during idling, and Type-III, crank-case emission testing [84], [95]. The regulation was an attempt to evaluate the emissions of urban driving and was later adopted as a component of the New European Drive Cycle (NEDC).

The NEDC for passenger cars was introduced in 1980, and this was mandated in most of Europe. This NEDC represented urban driving only and included of four repetitions of the pre-existing ECE-15 cycle (Type I test of UN-ECE Regulation Number 15), for a total duration of 780 seconds [87]. Although the Type-I test of UN-ECE Regulation 15 that was used during the 1970s consisted of repeating the ECE-15 cycle four times, it did not have the official cycle name of NEDC until 1980 [96]. In 1992, a new section, named the Extra Urban Drive Cycle (EUDC), was added to the NEDC, to account for non-urban speeds, such as during highway driving. The EUDC has an average and top speed of 62.59 km h^{-1} and 120 km h^{-1}, respectively [87]. With the new addition, the average and top speeds of NEDC became 33 km h^{-1} and 120 km h^{-1}, respectively [87]. After the addition of EUDC, NEDC remained unchanged and stayed as a European legislative cycle the WLTP was mandated, in 2017. The final version of NEDC is shown in Figure 2. Like most modal drive cycles, the NEDC has been criticised for its failure to represent real-world driving behaviour [77]. The drive cycle has an abundance of constant speed travel and idling durations, and this has made it difficult to estimate some vehicle parameters, such as fuel economy and range [77], [85], [97].

2.8.2.2 American Drive Cycles

The US first adopted a modal drive cycle, named 'California 7-Mode', in 1968 [80], [81]. This drive cycle was mainly based off-road, in Los Angeles, but was used to represent US national driving [80], [81]. Even though this drive cycle did not become mandated until 1968, early drive cycle development had been carried out since the 1950s, with the Los Angeles County Air Pollution Control District Laboratory surveying a single Los Angeles route [80], [81]. This survey was later updated and improved, in 1956, by the Automobile Manufacturers Association [80], [81]. The drive cycle had a duration of only 137 seconds, with a maximum and average speed of 80 km h^{-1} and 41.8 km h^{-1}, respectively. As with all modal cycles, this cycle was criticised for not representing real-world driving, especially during rush hour conditions.

In 1972, the US released the EPA Federal Test Procedure for passenger cars, also referred to as the EPA Urban Dynamometer Driving Schedule (UDDS), or FTP-72, which is shown in Figure 2-13(a) [82]. This transient drive cycle was created upon the introduction of the 'gas guzzler' tax, which imposed a tax on users with heavy-emission vehicles [83]. It has a duration, average speed and maximum speed of 1,372 s, 31.5 km h^{-1}, and 91.3 km h^{-1} [98]. FTP-72 is divided into two phases: the cold start phase, which accounts for the first 505 seconds and the stabilised phase, which accounts for the remaining 867 seconds [74], [98], [99], [100]. The cold start phase requires the vehicle to be running at an ambient temperature of 20 to 30°C [99]. FTP-75, shown in Figure 2-13(b), is an extended variant of FTP-72, with the addition of the hot start phase at the end; it is also used in Australia and Sweden but under different names (Australian Design Rules and Constant Volume Sampler) [74], [99]. The hot start phase is a repeat of the cold start transient phase (first 505 seconds) of FTP-72, except that it is tested under different temperature conditions; specifically, the vehicle is 'hot soaked' or kept at a desired operating temperature ('warmed-up' temperature for the vehicle) for 540 to 660 s before the commencement of the phase [82], [99], [101]. FTP-75 has a duration, average speed and top speed of 1,877 s, 34.1 km h^{-1}, and 56.7 km h^{-1}, respectively, when not including the hot soak period [102]. When the hot soak period is included the overall duration of the test is increased from 2,417 to 2,537 s [102]. Some vehicle simulation software and programming plugins, such as ADVISOR and MATLAB Simulink Drive Cycle Source block set, include the hot soak period as a default when the drive cycle sources or functions are used [101], [102], although this can be adjusted according to the simulation needed. Figure 2-13 shows the aforementioned drive cycles.

In 1996, the US Supplemental Federal Test Procedure (SFTP) cycle was developed as an addition to the pre-existing FTP-75 cycle, in the form of SFTP-US06 and SFTP-SC03, shown in Figure 2-13(c) and (d), to account for higher rates of acceleration, higher speeds and the use of climate control functions [99], [103]. SFTP-US06 was added to account for higher velocity driving and has a duration of 596 s, with an average speed and maximum speed of 78 km h^{-1} and 129 km h^{-1}, respectively [99], [104]. The SFTP-SC03 incorporated climate control use [99], [105]. the cycle collects data in the form of speed vs. time data but requires that the vehicle be tested with the air conditioning on, to measure emissions associated with climate control function usage [105]. It has a duration, average velocity and maximum velocity of 596 seconds, 35 km h^{-1}, and 88 km h^{-1}, respectively [105].

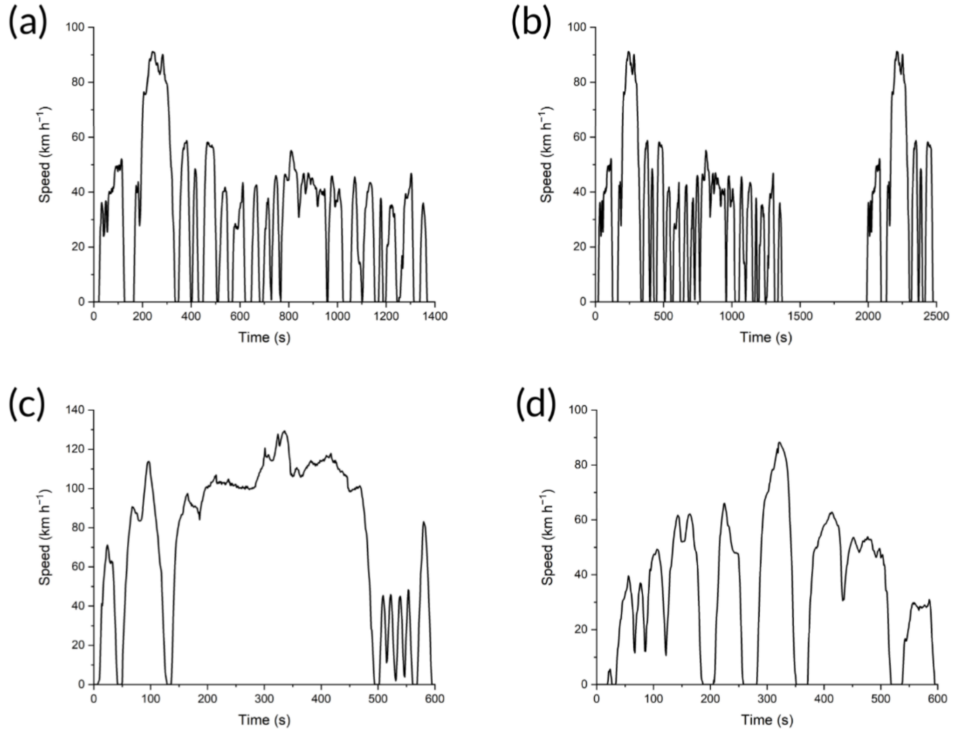

.

Figure 2-13: EPA federal test procedure variations and segments. (a) FTP-72 Urban Dynamometer Driving Schedule. (b) FTP-75 Urban Dynamometer Driving Schedule (UDDS) with a hot start; this is the same as FTP-72, but with an additional hot start phase at the end. (c) SFTP US06 for high-speed driving. (d) SC03 for high-speed driving and climate-control incorporation.

Although US SFTP tests were introduced in 1996, they were not mandated until 2007 [103], [106]. Specified climate control test conditions were administered to newly manufactured light-duty vehicles (LDVs) requiring SFTP-SC03 certification [106]. These conditions simulate hot and cold ambient temperatures, i.e. 35 and −7°C [106]. Climate control systems are turned on to represent realistic driver comfort settings, and the vehicle is run on a dynamometer using the SFTP-SC03 cycle [105], [106].

In 2008, a further drive cycle was added to the US EPA tests, namely the Highway Fuel Economy Test Cycle (HWFET) [99]. This cycle was proposed to simulate highway driving and used in synchronisation with the pre-existing city driving cycle, FTP-75, to identify both highway and urban fuel economy ratings [107]. The EPA released the 5-cycle test method in 2008; this consisted of two tests of the FTP-75 cycle, one with average ambient temperature and one with a cold temperature, the two SFTP tests (SFTP-US06 and SFTP-SC03) and the newly-introduced HWFET [99]. The EPA Federal Test Procedure was unchanged after this addition.

2.8.2.3 Japanese Drive Cycles

Before the first European and United States legislative cycles were introduced, Japan had developed its driving cycle, the 4-Mode, or J4, in 1966 [108]. The 4-Mode is a simple modal cycle, with cruising speed varying from 10 to 70 km h^{-1} in increments of 10 km h^{-1} [80]. 4-Mode has a maximum speed of 70 km h^{-1} [80]. The Japan 10-Mode replaced this drive cycle, in 1973 [80]. Similar to ECE-15, the 10-Mode is a longer driving cycle that simulates urban driving only. Just as EUDC was added to ECE-15 to form NEDC, the 10-Mode was later expanded with a separate drive cycle, named 15-Mode, to represent highway driving, to create a grouped urban and highway driving cycle [80]. The 15-Mode has a top speed of 70 km h^{-1} [80]. The combination, named the 10-15 Mode, consists of three cycles of 10-Mode and one cycle of 15-Mode. The 10-15 Mode has a duration, average speed and top speed of 660 seconds, 22.7 km h^{-1}, and 70 km h^{-1}, respectively [80]. For the same reason as NEDC, the 10-15 has been criticised for not accurately representing real-world driving behaviour, due to it being a modal drive cycle. Because of this, Japan introduced a transient legislative drive cycle, named the JC08, in 2005 [80]. This cycle has a duration, average speed and top speed of 1,204 seconds, 24.4 km h^{-1}, and 81.6 km h^{-1}, respectively [80]. A comparison between 10-15 Mode and JC08 can be found in Figure 2-14. Unlike other legislative drive cycles, mentioned in previous sections, JC08 covers medium-duty vehicles, as well as light-duty vehicles [80].

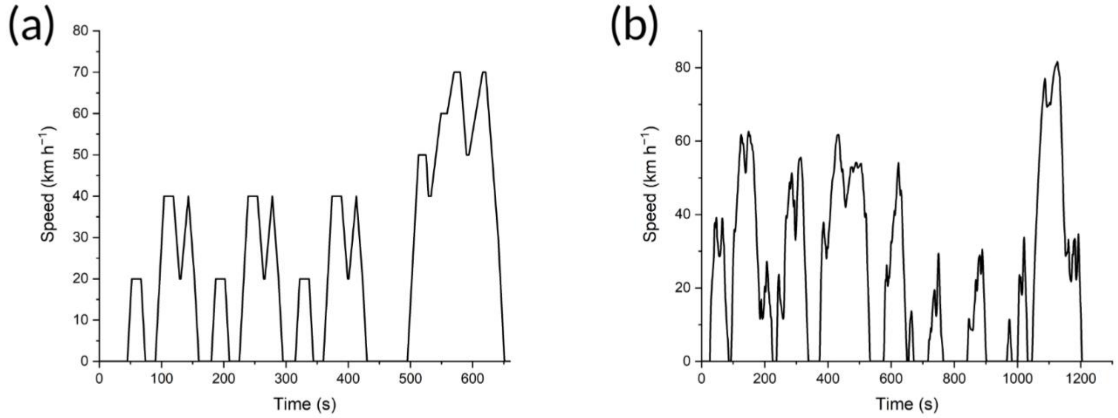

Figure 2-14: Japanese legislative drive cycles. (a) The 10–15 Mode drive cycle was fully developed in 1991. It has a duration, average speed, and top speed of 660 s, 22.7 km h^{-1}, and 70 km h^{-1}, respectively. (b) The JC08 drive cycle was released in 2005. It has a duration, average speed, and top speed of 1204 s, 24.4 km h^{-1}, and 81.6 km h^{-1}, respectively.

2.8.2.4 Chinese Drive Cycles

The Chinese Automotive Test Cycles (CATC) were created in 2019 [109], [110]; they are divided into light-duty (CLTC) and heavy-duty vehicle (CHTC) tests [110], [111]. The tests are further divided according to the specific purposes of these vehicles. This cycle was created based on actual roads in China, using 5,000 vehicles that travelled in 41 Chinese cities [111]. A total of 32 million kilometres of data was collected to develop the drive cycle, which is currently the longest sampling distance of all legislative drive cycles. The complete cycle has a duration of 1,800 s, an average speed of 28.96 km h^{-1}, and an average acceleration of 0.45 m s^{-2} [111].

In 2020, the CATC drive cycle became the primary test cycle in China [111]. Before this, WLTP and NEDC were used [112]. CATC was developed in response to the growing concern that NEDC and WLTP did not accurately represent real-world driving behaviour [109], [110], given the congested traffic conditions in China. NEDC is a modal cycle that has been widely criticised for its lack of real-world representation. China has introduced more stringent and detailed cycles for heavy-duty vehicle testing due to a data collection conducted in 2017; where diesel HGVs produce the majority of vehicle NO_x and particulate matter emissions, with values of 70% and more than 90%, respectively [112], [113]. China’s Limits and Measurement Methods for Pollutant Emissions from Heavy Duty Diesel Vehicles protocol, otherwise known as China's Sixth Phase, has introduced the detailed breakdown of CHTC into different HGV categories, to thoroughly crackdown and inspect the release of new diesel HGVs, aiming to reduce harmful pollutants [112], [113].

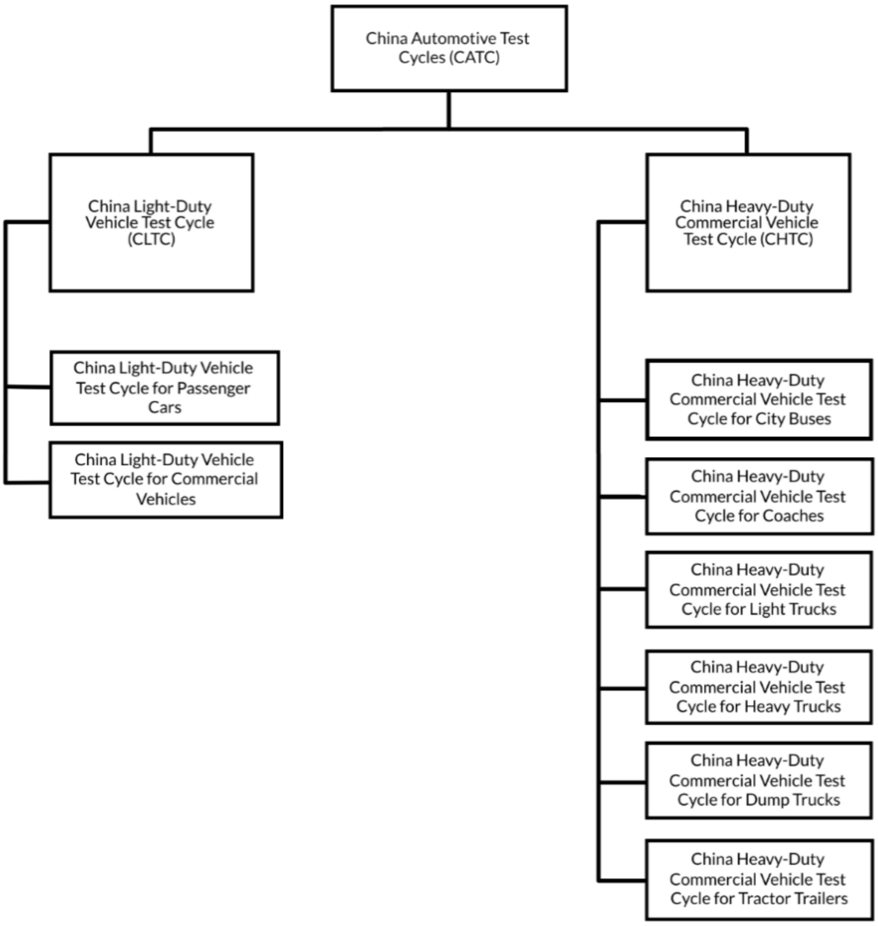

Figure 2-15: Division of China Automotive Test Cycles (CATC) [78], [81].

2.8.2.5 Worldwide Drive Cycles—Worldwide Harmonised Light Vehicle Test Procedure (WLTP)

WLTP is the successor to NEDC, which represents a change from a modal cycle to a transient cycle [74], [77]. The procedure contains three classes, with each class corresponding to vehicles of different power-to-weight ratios (PW_r) [114]. Since September 2017, electric and plug-in hybrid passenger cars in Europe have been required to comply with WLTP for speed requirements; in addition, the emission testing of LDVs is also performed under this cycle [115], [116], [117]. This legislation addresses the concern that drive cycles are not only meant to be used as a profile for emission testing, but also as a tool for internal industrial benchmarking.

Class 1 accounts for all vehicles with a PW_r less than or equal to 22 [114], with power measured in kW and weight in tonnes. This class is widely representative of vehicles in India, where many vehicles have low PW_r [118]. This class has a duration, average speed, and top speed of 1,022 s, 28.5 km h^{-1}, and 64.4 km h^{-1} [102].

Class 2 relates to all vehicles with PW_r of more than 22 and less than or equal to 34 [114] It is widely used in India and Japan, and European countries [118]. This class has a duration, average speed, and top speed of 1477 s, 35.7 km h^{-1}, and 123.1 km h^{-1}, respectively [102].

Class 3 is intended for vehicles with PW_r over 34. Due to the high power-to-weight ratio, this class is mainly representative of vehicles driven in Japan and Europe [118]. Hybrid and electric vehicles also belong to this class. Class 3 is different from the other classes in the way in which there are two sub-categories, Class 3a and 3b. Class 3a is used for vehicles that cannot reach a maximum speed of 120 km h^{-1}, while 3b is used for vehicles that can exceed a speed of 120 km h^{-1} [118].

2.8.3 Comparison of Legislative Drive Cycles

Specific characteristics of standard legislative drive cycles are compared in this section. The comparisons only include LDV drive cycles which account for both urban and highway driving, so standalone urban cycles such as ECE-15 are not included since they will be shown as part of a 'full' drive cycle (NEDC contains ECE-15). US legislative drive cycles are also not included, as they are broken down into separate urban and highway driving cycles.

Shown in Figure 2-16(a), the maximum duration of legislative cycles is 1800 s. WLTP (not including Class 1) and CLTP both have the longest duration. Japan has shown relatively shorter durations for both of its drive cycles, even after introducing its transient cycle, JC08. It is a trend to see transient successors of modal cycles having a longer duration.

Figure 2-16(b) and (c) shows the top speed, average speed, and idling percentage comparison between legislative drive cycles when also accounting for the idling phases. Shown in Figure 2-16(b), WLTP Class 3 has both the highest top and average speed. WLTC is representative of many regions throughout the world, where data was collected in the USA, Korea, Japan, India, and various European countries [85]. There is a trend of drive cycles simulating European roads having a top and average speed higher than that of other countries, namely WLTP and EUDC. This statement is backed up by a study by Son *et al*, where they collected drive cycles both in the UK and South Korea [79]. The drive cycles collected in the UK all have higher maximum and average speeds when compared to South Korea. This is consistent with several European countries having higher speed limits [119]. Both of the two Japanese drive cycles have the slowest top speed; however, as shown in Figure 2-16(c), these cycles also have the highest idling percentage, which is a primary contributor to the low average speed. Both CLTC cycles have lower average speeds, 17.5 km h^{-1} lower than that of WLTP Class 3 in the case of CLTC-P, which accurately reflects the more congested road conditions in major Chinese cities [85]. Wang *et al*. compared the performance of NEDC compared to actual driving comparisons in Beijing, China. It was also concluded that NEDC had higher maximum speeds [120]. It was also suggested that the lower maximum speed in Beijing is due to the more congested driving conditions, and using NEDC as the previous legislative China drive cycle would underestimate emission estimations. As shown in Figure 2-16(c), CLTC-P has a relatively high idle percentage amongst the transient cycles. It is also visible that Asian drive cycles tend to have higher idling percentages than European drive cycles, which correlates to the findings by Son *et al.* and Wang *et al.*.

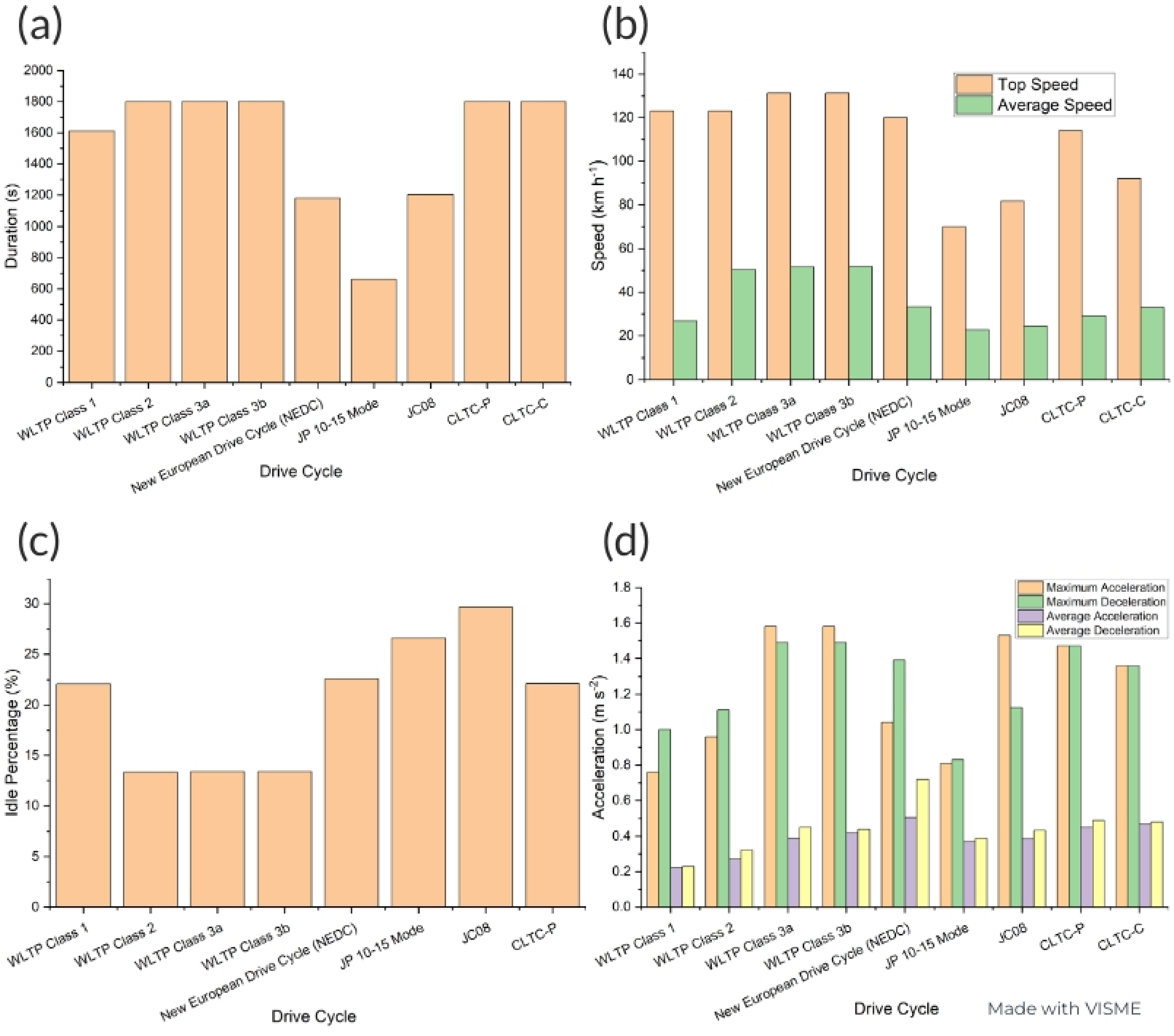

Figure 2-16: Comparisons of legislative drive cycles. (a) Duration comparison. (b) Top and average speed comparisons. (c) Idle percentage comparison. (d) Acceleration and deceleration comparisons.

Figure 2-16 (d) shows a comparison of acceleration and deceleration values for various legislative drive cycles. The comparisons show that transient drive cycles tend to have a higher maximum acceleration than modal ones and are similar to each other in value. For maximum deceleration, worldwide (WLTP), European (NEDC), and Chinese drive cycles have similar values to one another, regardless of modal or transient. Japanese drive cycles, on the other hand, tend to have less abrupt deceleration. For average acceleration and deceleration comparisons, NEDC has the maximum value for both. For NEDC's transient replacement, WLTC, the average deceleration is less abrupt, which better corresponds to real-driving behaviours. The older modal drive cycles tend to have less aggressive acceleration and deceleration compared to newer transient drive cycles. This is crucial to what has been emphasised in previous parts of this review, where modal cycles are not a good representation of realistic driving, as the modal drive cycles change speed more consistently and linearly than transient.

2.8.4 Transient Drive Cycle Developmental Procedure Using the Micro-Trip Method

As stated previously, transient drive cycles are based on real-world conditions. Figure 2-17 outlines the most used transient drive cycle development procedure, using the micro-trips method. To accurately represent driving in the real world, the first step is to collect speed vs. time data with a physical car on real roads, with the aid of a GPS data logger.

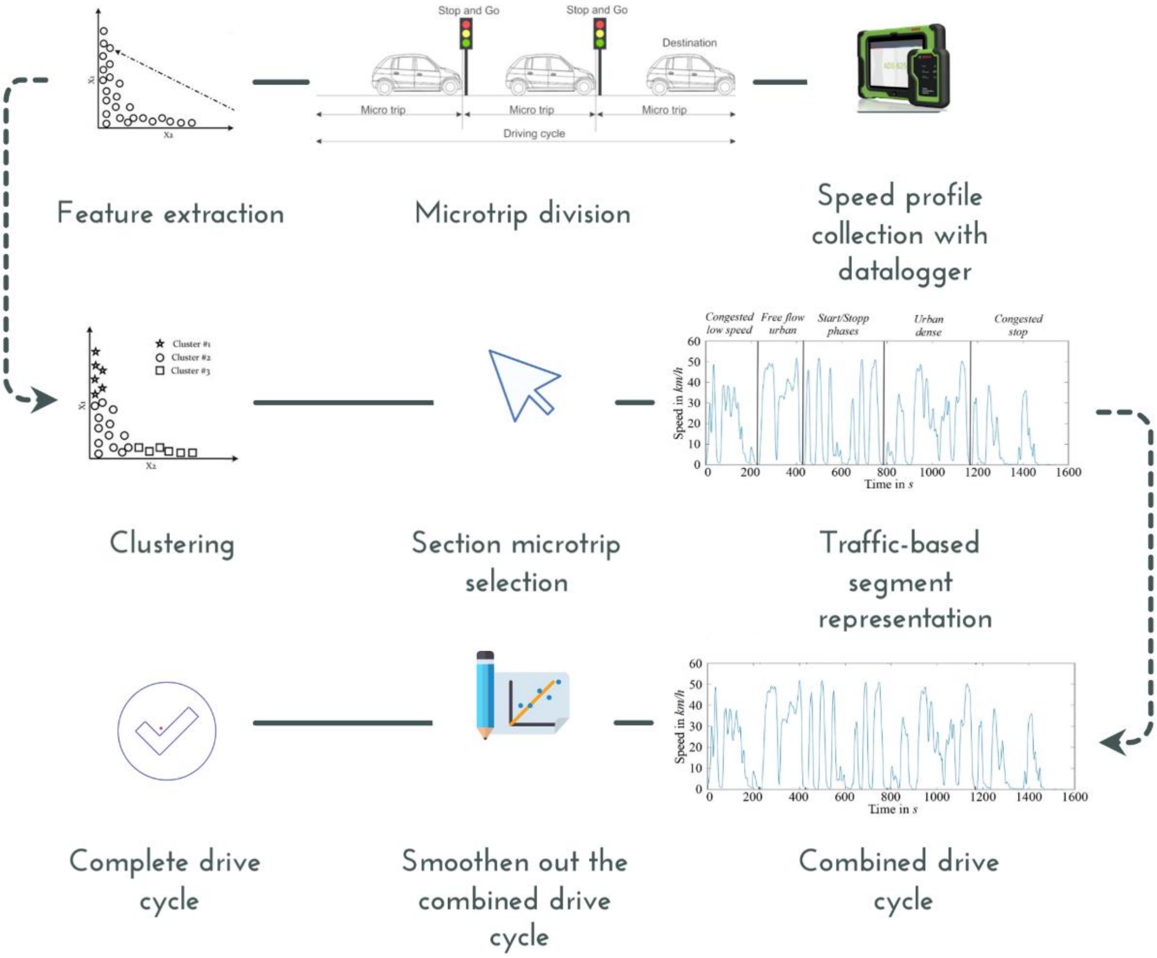

Figure 2-17: Transient drive cycle development procedure using micro-trip clustering technique.

The next stage is microtrip division. A micro-trip is defined as a discrete period between two points at which the vehicle is immobile or idling [121]. Microtrips are identified for all speed vs. time profiles collected, creating a series of micro-trips. Depending on the purpose of the drive cycle in development, certain features of each micro-trip (such as average speed or idle percentage) are extracted and plotted onto a two-dimensional scatter plot [121]. A general list of features and definitions can be found in Table *2-9*. Methods such as K-means clustering, Markov chain, and Monte Carlo can be used to sort the data and remove outliers, typically referred to as micro-trip clustering [121].

After removing the outliers, a set list of traffic conditions is pre-determined (congested urban, urban, extra-urban, and motorway traffic) and the planned duration of each segment can be set [121]. The list may vary depending on the purpose of the drive cycle. This forms the basis of the creation of 'representative micro-trips,' which means that the collected micro-trips are filtered even further, with several being chosen to represent the pre-determined traffic condition segments [121]. For example, one selection method involves choosing the micro-trips within the centre regions of the driving features 2-D scatter plot clusters and then piecing them together until each traffic segment is represented and the planned duration of each traffic segment is met [121]. This 'pieced-together' drive cycle forms the first iteration of the full-duration drive cycle. With filtering techniques, the drive cycle can be smoothed and made ready for implementation.

Table 2-9: List of examples of drive cycle features and definitions [58].

Drive Cycle Feature	Definition
Average speed	Sum of all speed data values divided by the number of data points (equal to the total duration if datalogging interval is 1 s)
Idle time percentage	Ratio of time stopped divided by total time (percentage)
Velocity variance	Sum of the speed at a given time minus the average velocity squared, divided the total number of data points $\sigma_v = \frac{1}{n}\sum_{i=1}^{n}(v_i - v_{avg})^2$
Energy	Sum of squared speed values

Maximum speed	Maximum speed value
Minimum speed	Minimum speed value
Difference between maximum speed and minimum speed	Minimum speed subtracted from maximum speed
Average acceleration or deceleration	Sum of all acceleration or deceleration values divided by the total number of data points
Acceleration variance	Sum of the acceleration values at a given time minus the average acceleration, squared, divided by the total number of data points $\sigma_a = \frac{1}{n}\sum_{i=1}^{n}(a_i - a_{avg})^2$
Average acceleration	Sum of all acceleration values divided by the number of data points
Average deceleration	Sum of all deceleration values divided by the number of data points
Percentage of cruising	Time travelling at a constant speed divided total time (percentage)
Maximum acceleration or deceleration	Maximum value of acceleration or deceleration
Minimum acceleration or deceleration	Minimum value of acceleration or deceleration
Total distance	Total distance travelled (can be obtained by integrating the speed vs. time graph)
Average square acceleration	Sum of acceleration squared divided by the number of data points
Relative acceleration	Sum of speed values multiplied by acceleration at a given time over the total distance

Relative deceleration	Sum of speed values multiplied by deceleration at a given time over the total distance
Percentage of time when absolute acceleration and deceleration > 1.5 m s^{-2}	Time during which the acceleration > 1.5 m s^{-2} divided by the total time (percentage)
Percentage of time when absolute velocity times acceleration is between 3 and 6 m^{2} s^{-3}	Time during which the absolute velocity is between 3 and 6 m^{2} s^{-3} divided by the total time (percentage)

2.8.5 Standardised Transient 'Drive Cycle' Testing Protocols for Electrochemical Device Testing

Drive cycles (when converted into power cycles) are required to size, design, and optimise powertrains based on electrochemical power sources (and hybrids thereof) including batteries, fuel cells, and supercapacitors. However, there is a lack of pre-converted protocols that can be used. Strictly, drive cycles show speed (km h^{-1}) vs. time (s) data; however, speed is not a relevant parameter when designing electrochemical power systems which deliver power from current, and voltage. Power cycles and current cycles are power vs. time and current vs. time data converted from speed vs. time data. The Fuel Cells and Hydrogen Joint Undertaking (FCH JU) has a version of the EUDC converted to current vs. time to allow fuel cells to be operated under a drive cycle via current control.[122] However, this is limited to the EUDC cycle, which is a modal cycle and is less representative of realistic driving scenarios, compared to transient cycles. There is a lack of publicly available material covering the generation and use of transient power cycles for electrochemical devices. However, there is a commonly used procedure to convert drive cycles to power cycles. This considers the opposing forces of a vehicle, namely aerodynamic drag, rolling resistance, gradient resistance, and gradient force. If a drive cycle can be converted to a power cycle, bench testing with drive cycles can be achieved if there is a cycler that supports arbitrary power control. Voltage or current control can also be achieved by estimating the current or voltage demand at each time point and varying the other parameters to generate a power cycle.

2.8.6 Using Power Cycles as a Sizing Tool for Electric and Hybrid Vehicles of Different Architectures

Currently, most commercially available hybrid vehicles involve hybridising an ICE with a battery pack. However, much research has also gone into electrochemical hybrid vehicles, namely the hybridisation of batteries, fuel cells, and/or supercapacitors. When a power cycle is pre-determined from a theoretical drive cycle, this power cycle can be used for the initial propulsion source sizing of vehicles. Single power source vehicles are usually oversized to account for various power losses during a vehicle's propulsion (transmission losses, aerodynamic drag, and motor losses). However, the source sizing becomes more complicated for hybrid vehicles, as there is more than one energy and power source to size and each power unit may experience a vastly different power demand profile from that demanded by the overall vehicle power requirement. More complications can also be traced to the hybrid architecture and energy management strategy used. Hybrid architecture can be divided into three main categories: series (range extender), parallel, and series-parallel [123], [124].

For pure BEVs, the sizing chosen for the battery pack should account for both the power and range requirements, in that order. The battery pack needs to be able to fulfil the maximum power requirement of a chosen drive cycle. The number of cells shall then be iterated to increase in a chosen increment until the required range of the vehicle is fulfilled. This initial sizing can be executed in a software-in-the-loop simulation software or program. Both the power and range requirement should factor in the battery degradation at the end-of-life, as it is likely that the performance of the battery has decreased, particularly in terms of maximum power drop and capacity fade. The battery cells can either be sized to operate at a maximum power or a suitable nominal depending on the design goals of the vehicle. Operating the cells at maximum power benefits in decreasing the overall weight of the vehicle; however, battery degradation is more severe. On the contrary, operating the cells at nominal power may increase battery life, but drastically increases the weight of the vehicle.

2.8.7 Drive Cycles and Duty Cycles for Different Propulsion Systems—Differences, Complications, and Accuracy

Most road vehicles can be divided into three major types of propulsions, internal combustion engine (ICE) propulsion, which commonly requires fuels such as petrol or diesel; electrochemical propulsion, which utilises batteries, fuel cells, and supercapacitors; and hybrid propulsion, which can be any combination of the above. These different propulsion systems differ in the way that they produce power, and thus different sizing strategies of energy sources should be considered when using duty cycles as a required power and energy estimation tool. For ICE vehicles (ICEVs), certain power outputs can only be reached with certain angular velocities, typically measured in revolutions per minute (RPM), and the fuel economy differs when running an engine at different rates.[125] ICEV manufacturers typically use engine power and fuel economy vs. engine speed graphs to describe this (Figure 2-18(a)). For this engine, maximum power can be reached when the engine speed is around 5000 rpm. ICEVs tend to gradually build up in power and torque as the engine revolutions per minute (RPM) increases and eventually drop down gradually. This gradual build-up and drop-down behaviour varies depending on the gears and the gear ratios designed by the manufacturer.

For vehicles equipped with electric motors, such as EVs and FCEVs, there is instant torque at 0 rpm, which aids in acceleration from a standstill. Figure 2-18(b) shows the power and torque delivery of a typical electrochemical vehicle (EV or FCEV). For short acceleration, instant torque produced by the EV is the main contributor to faster acceleration. However, 0 to 60 mph does not tell the entire story about the acceleration capabilities (and power demand) of electric motors. As an electric motor's angular velocity (rpm) increases, back electromotive force (EMF) also increases, which reduces the voltage the motor can deliver, and the instant torque characteristics of an EV or FCEV start to diminish. The region after around 2500 rpm in Figure 2-18(b) shows the effect of back EMF on torque. In addition, power tends to increase almost linearly as rpm increases in an electric vehicle and stabilise after a certain RPM, after around 2500 rpm in the case of Figure 2-18(b).

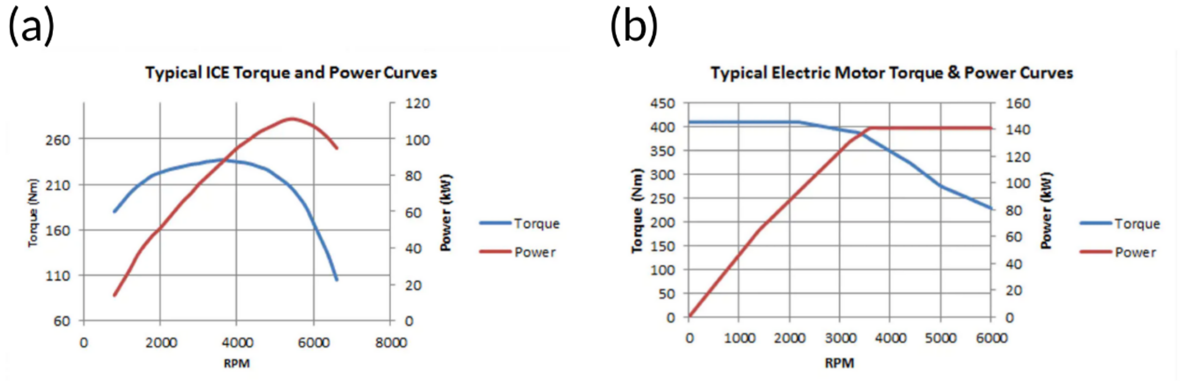

Figure 2-18: Comparison of power and torque delivery characteristics of ICEVs and EVs. (a) Power and torque vs. engine speed graph for a typical ICEV [86]. (b) Power and torque vs. RPM graph for a typical EV or FCEV [86].

Because of the difference in power delivery patterns of different propulsion sources, manufacturers need to take this into account when using conventional duty cycles as in their sizing calculations; or a propulsion-specific drive cycle needs to be used for that sizing to acquire accurate performance evaluation, optimisation, and range estimation. Jeong *et al*. simulated electric vehicle driving based on conventional drive cycles and found the performance evaluation inadequate; the conventional drive cycle performance was evaluated against an electric drive cycle data logged in Gwacheong, Korea [88]. The higher acceleration behaviour of electric motors was not represented in such drive cycles.

Meddour *et al*. optimised battery sizing and electric motor cost and losses in MATLAB and ANSYS for an electric vehicle based on four conventional drive cycles: WLTP, FTP-75, Artemis 150, and Artemis Urban [126]. It was found in the more urban drive cycles, there are more minor motor losses due to the low torque demands. Referring to the above discussion of how electric vehicles may produce higher torque, especially from a standstill to acceleration, the motor loss estimation would be inaccurate if an electric-only drive cycle is to be used.

Zhao *et al*. developed an electric cycle in Xi'an, China named XA-EV-UDC and discovered that when using conventional international drive cycles such as FTP-72, FTP-75, JC08, 10-15 Mode, NEDC, and ECE-15 for range estimation and energy consumption, the relative errors can be as high as 38% and 21%, respectively [127].

Koossalapeerom *et al*. developed two motorcycle drive cycles using both a CV and electric motorcycle using the same route in Khon Kaen City, Thailand and compared parameters such as velocity, acceleration, and energy consumption between the two drive cycles. It was seen that the electric motorcycle produced a drive cycle with less time spent during acceleration and deceleration. In addition, the energy consumption of the electric drive cycle can be eight times lower than the CV motorcycle [128]. Figure 2-19 shows the comparison between the electric and gasoline drive cycle, it can also be seen, qualitatively, that the gasoline vehicle averaged higher in terms of maximum speed. Furthermore, the acceleration profile is different between the two vehicles.

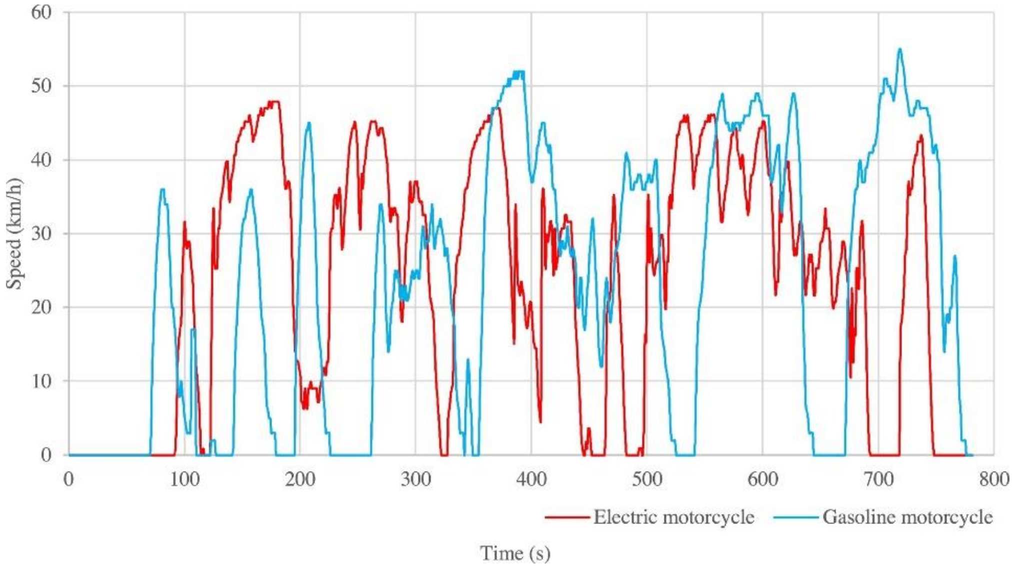

Figure 2-19: Comparison between electric and CV motorcycle drive cycles in Khon Kaen City, Thailand (Koossalapeerom et al. [89]).

Borgia *et al*. conducted a similar study based on three commercially-available LDVs with different powertrains: namely electric (2020 Renault Zoe), ICE-battery hybrid (2016 Toyota Yaris), and CV (2018 Fiat Panda), using a 17.8 km long route in Rome, Italy, and found similar results. Drive cycles were collected and constructed based on the three vehicles during both intermediate and harsh driving scenarios. The microtrip clustering technique was used to formulate the drive cycles. The cycles were named SEVCI and SEVCH drive cycles, with 'I' representing intermediate, and ‘H’ representing harsh. It was also discovered that the time spent during acceleration and deceleration is less frequent that of CVs, resulting in a less average acceleration overall [129]. It is suggested that regenerative braking in EVs can contribute to this, as this phenomenon provides more constant braking or deceleration behaviour compared to purely using frictional brakes [129]. In addition, it is suggested that the instant torque behaviour of electric motors assists in faster acceleration times, which brings a vehicle to constant cruising quicker, resulting in lesser acceleration times. A drive cycle comparison of the three vehicles can be found in Figure 2-20, all vehicles were tested both in terms of intermediate and harsh driving. An interesting finding from the formulated drive cycles is that, when using the SEVCI drive cycle for range estimation of the Renault Zoe, the result is similar to that of WLTP’s, suggesting that conventional drive cycles may provide accurate range estimation or EVs. It was later debunked in the paper that this is a ‘coincidence [129].’ It is suggested that the shorter highway driving duration of WLTP balances out the lesser acceleration times of the SEVCI drive cycle. The authors suggested that an EV drive cycle should be used when developing electric vehicles instead of conventional worldwide cycles. A summary of the aforementioned comparisons and findings by these authors can be found in Table 2-10.

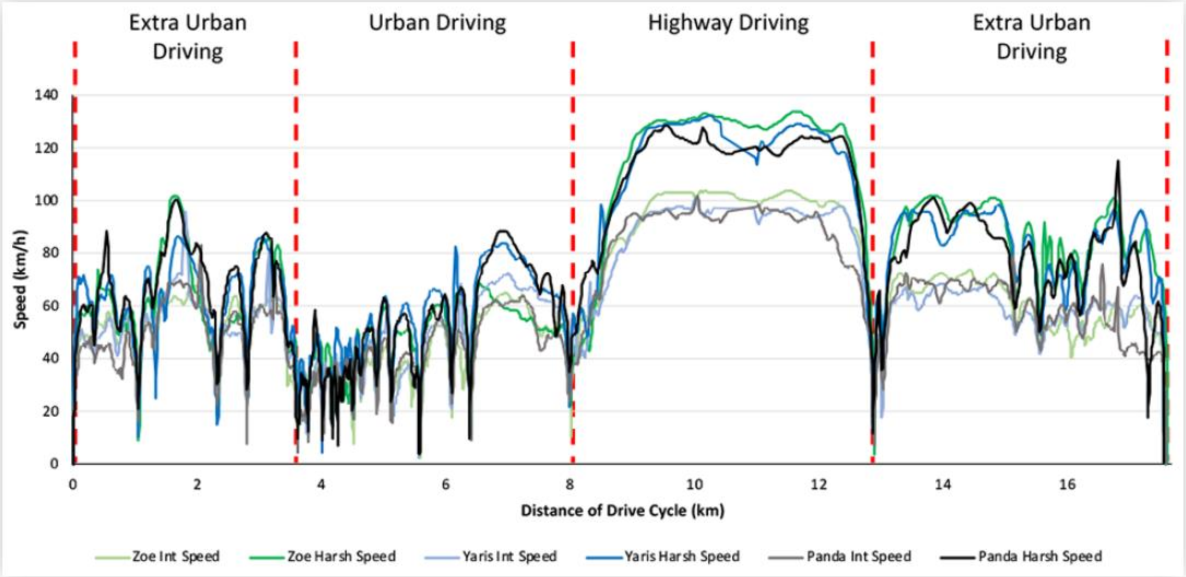

Figure 2-20: Comparison of EV, hybrid, and CV LDV drive cycles during intermediate and harsh driving (Bogia et al.) [90].

Table 2-10: Comparison of previous work on electric drive cycles and conventional drive cycles. Papers which use conventional CV drive to test electric vehicles are also included.

Author	**Parameters Compared**	**Drive Cycles Used**	**Conclusions or Takeaway**
Jeong *et al*. [54]	Performance evaluation, acceleration	Non-legislated Gwacheong, Korea drive cycle	Higher acceleration of electric motors not accurately represented in conventional drive cycles
Meddour *et al*. [87]	Battery sizing, electric motor cost, electric motor loss	WLTP, FTP-75, Artemis 150, and Artemis Urban	Torque demands vary drastically between drive cycles, choosing an accurate drive cycle is important
Zhao *et al*. [88]	Range estimation, energy consumption	XA-EV-UDC, FTP-72, FTP-75, JC08, 10–15 Mode, NEDC, and ECE-15	Using conventional drive cycles for range estimation and energy consumption can produce a relative error as high as 38.14% and 21.17%, respectively
Koossalapeerom *et al*. [89]	Time spent during acceleration and deceleration, time spent cruising, speed, energy consumption, EV vs. CV	Non-legislated EV and CV motorcycle drive cycle in Khon Kaen City, Thailand	The EV drive cycle has less time spent during acceleration and deceleration, suggesting higher cruising times. Energy consumption of EV drive cycle can be as high as eight times lower than that of CV drive cycle
Borgia *et al*. [90]	Acceleration, deceleration, range estimation, intermediate vs. harsh driving, overall drive cycle attributes, EV vs. hybrid vs. CV	SEVCI, SEVCH, WLTP, NEDC	Acceleration and deceleration times are less for the EV when compared to CV, regenerative braking and electric motor characteristics are the main cause.

Another complication of using power cycles for sizing purposes is the lack of consideration of power or fuel used when the vehicle is stopped (for ICE vehicles, idling). As the conversion of the drive cycle to the power cycle relies on the speed at a given time, the idling power is always considered zero, which is not realistic. With ICEVs, the engine may still operate during idling, in electrochemical hybrid vehicles, the battery or fuel cell may still be using power. Some vehicles have start-stop technology to prevent this, but there is always some power needed for the vehicle control system and the auxiliary systems, for example, radio systems, infotainment screens, climate control systems, and alternators. Efficiency and parasitic losses that would vary depending on the powertrain setup are not considered. For example, if an electrochemical propulsive vehicle is required to operate at high speeds for an extended period, there would be a higher requirement for cooling for the batteries and fuel cells, which is not accounted for in the power curve. Parasitic loads in a vehicle can be divided into two categories: rigid and flexible. Rigid loads mean that the load required is ‘set’ and does not allow room for more or less power consumption without affecting the proper operation of the vehicle’s powertrain [130]. Most components that are utilised to keep a PEMFC stack healthy require rigid loads; these can include cooling pumps, recirculating pumps, blowers, and vacuum pumps. Some motor components such as a motor lube pump also require rigid loads [130]. Flexible loads, on the other hand, can allow for a change in power consumption without compromising the safety and powertrain capabilities of a vehicle [130]. These types of parasitic loads can include lights, windshield wipers, windows, and battery-charging systems [130]. Manufacturers tend to ‘oversize’ the energy and power systems to account for fuel or energy used during idle, caused by parasitic loads.

3 Experimental Methodology

3.1 Experimental Methodology Chapter Introduction

The Experimental Methodology section focuses on the techniques, protocols, and parameters used for the laboratory experiments of this thesis. This section focuses purely on laboratory experiments; the formulation of the MATLAB HybeMass model is discussed in the Results and Discussion section instead of this one.

This section starts with an overview of the project's workflow and then dives into the bench-top testing of the fuel cell and battery counterparts in detail, including conditions used for conducting X-ray CT on the cylindrical batteries.

The section also includes explanations of the data interpretation techniques, calculations, and equations used on the electrochemical and X-ray CT data to characterise and quantify the amount of degradation that occurred during endurance testing of the two electrochemical devices. The electrochemical techniques used to characterise PEMFCs include polarisation and power curves, cyclic voltammetry, linear sweep voltammetry, and EIS. The electrochemical techniques used to characterise LiBs include capacity fade and EIS. For certain scenarios, X-Ray CT techniques were also conducted on LiBs as an add-on.

3.2 Overview of Project Workflow

This thesis aims to develop design tools and experimental systems for the advancement of fuel cell-battery hybrid-powered vehicles. The tools and techniques developed are focused on the comprehensive assessment, characterisation, and validation of hybridisation aimed at enhancing the durability and minimising the weight of FCHEVs. Figure 3-1 outlines the overarching depiction of the procedural framework followed throughout this PhD project. Both PEMFCs and LiBs were subjected to rigorous testing under conditions mirroring real-world driving scenarios. To replicate authentic electrochemical device testing in a vehicular context, drive cycles were utilised. These drive cycles were converted into power cycles, delineating the requisite power profiles versus time for the specific electrochemical hybrid vehicles under investigation—namely, Light Duty Vehicles (LDVs), class 8 heavy goods vehicles (HGVs), and buses.

The power requirements which were obtained were pivotal in determining the optimal sizing of the energy systems encompassing fuel cells and batteries for the respective electrochemical hybrid vehicles. The sizing of these components was tailored on a case-by-case basis scenario, contingent upon the distinct design objectives and functional purposes of each vehicle type. The division of power cycles between two primary electrochemical sources, namely Proton Exchange Membrane Fuel Cell (PEMFC) stacks and Lithium-ion Battery (LiB) packs, was executed using a percentage-split energy management strategy. The two steps mentioned above, boxed in dashed lines in Figure 3-1, required a MATLAB Simulink model built by the researcher called HybeMass. The MATLAB programme included electrochemical sources at either pack-level or stack-level, specifically calibrated to provide the propulsive force requisite for an actual road vehicle. The programme also provided power system weight estimations for the vehicle in question, which allowed the user to compare the weight implications between different hybridisation degrees and operating powers.

Furthermore, an innovative feature was integrated into the HybeMass program—a 'power source weight to overall vehicle weight feedback loop.' This forward-looking mechanism systematically factored in the additional weight implications stemming from the integration of PEMFCs and LiBs into the vehicle structure, which can make the vehicle sizing process more efficient. By identifying a dynamic equilibrium point, this feature enabled the vehicle to sustain propulsion even in the presence of these supplementary power systems along with their associated parasitic components’ weight. Traditionally, vehicle sizing procedures adopted by designers and documented in scientific literature involved predetermined vehicle weight values. Yet, these initial estimations often necessitated later-stage adjustments within the automotive development V-cycle, particularly if the cumulative weight of the incorporated power systems surpassed the vehicle's propulsion capability. The feedback loop circumvents this iterative approach, thereby enhancing the efficiency of the overall automotive system design process. This programme is equipped with a vehicle and power systems calculator to quantify and optimise the analysis of hybridisation for weight.

This Experimental Methodology section will outline the characterisation techniques used to analyse the PEMFC and LiB. The techniques were required for the ‘bench testing on different cyclers’ stage (final stage) of the overall project methodology overview outlined in Figure 3-1. The characterisation of degradation phenomena was underpinned by a suite of in-situ techniques, notably encompassing polarisation curves, cyclic voltammetry (CV), hydrogen crossover linear sweep voltammetry (LSV), capacity fade plots, and electrochemical impedance spectroscopy (EIS). Complementary ex-situ methodologies, such as X-ray computed tomography (CT), further bolstered the qualification of degradation effects. The aim of this final stage is to identify and characterise the severity of degradation of the PEMFCs and LiBs under various drive cycles or vehicle scenarios, simulating a hybrid vehicle in operation.

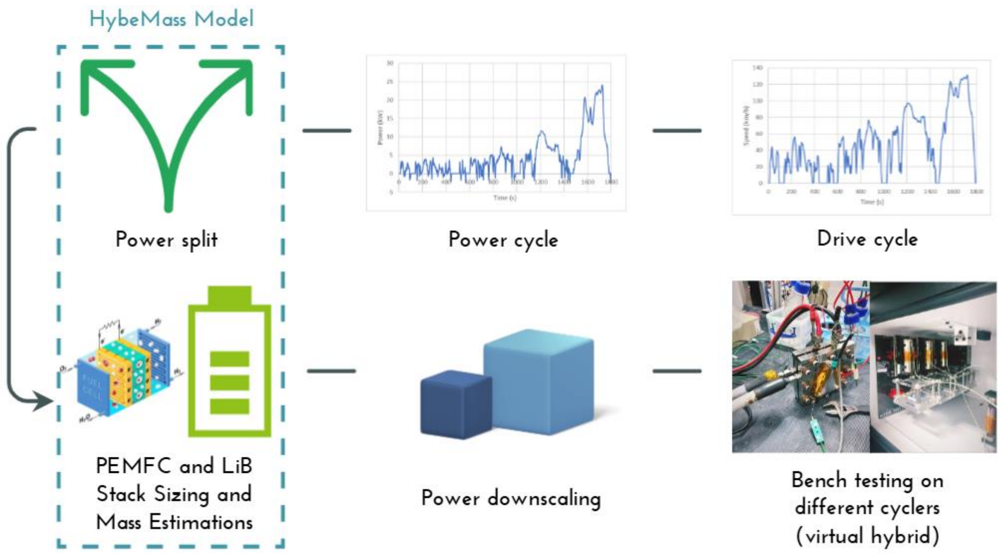

Figure 3-1: Project methodology overview. At first, a drive cycle in velocity vs. time was chosen to represent the vehicle type in question and can then be converted to a power cycle in power vs. time, this is the required duty cycle for the vehicle. Then, the duty cycle is split between the fuel cell and the battery. The fuel cell and battery were sized to account for the required divided power demand; this process also determines the mass of the PEMFC, battery, and their parasitics and auxiliary components. The aforementioned two steps comprise the self-developed HybeMass MATLAB model, which will be further discussed in Chapter 1 of this thesis. The mass estimations of different vehicle types are discussed in Chapter 3 of the thesis. The duty cycle division is then downscaled to a cell level for degradation testing on a bench and cell level, both electrochemical results and imaging analysis were conducted for this step, further discussed in Chapter 2 of the thesis.

3.3 Fuel Cell Testing

3.3.1 Cell Preparation, Specifications, and Operating Conditions

The Scribner 850e was used to test a 25 cm^2 active area PEMFC under various drive cycles, which can control a fuel cell under constant current, voltage or power. Depending on the Hybridisation for X test in mind, the number of iterations for the drive cycle control differs. WLTP Class 3, World Harmonised Vehicle Cycle (WHVC), and Orange County Bus Cycle (OC BUS) drive cycles were used to represent passenger car, HGV, and bus driving, respectively. As shown in Figure 3-2, the PEMFC used for testing consists of a polytetrafluoroethylene-based (PTFE) membrane, a carbon gas diffusion layer (GDL), a microporous layer (MPL) a platinum-carbon (Pt/C) catalyst, flow field plates (multi-serpentine style) and stainless-steel endplates. A list of specifications used for this project is provided in Table 3-1. A PTFE-based membrane is usually referred to by its commercial names, such as Nafion or Gore-Select; the type used in the current study was Gore-Select. The author has chosen this brand of membrane as it is widely used in the automotive sector, such as in the Toyota Mirai FCHEV. Commercial carbon GDLs, MPLs and Pt/C catalysts were used; the combination of GDL, MPL and Pt/C catalysts can be called a gas diffusion electrode (GDE). The GDE used in this project was from the South African manufacturer HyPlat (0.4 mg_{Pt} cm^{-2}). The Commercial GDE is used instead of in-house manufacturing to provide repeatability and accurate performance comparison for a systematic and integration-type project. By using commercial GDEs the variability in manufacture was minimised. Serpentine flow field plates and stainless steel end plates are supplied by Scribner Associates.

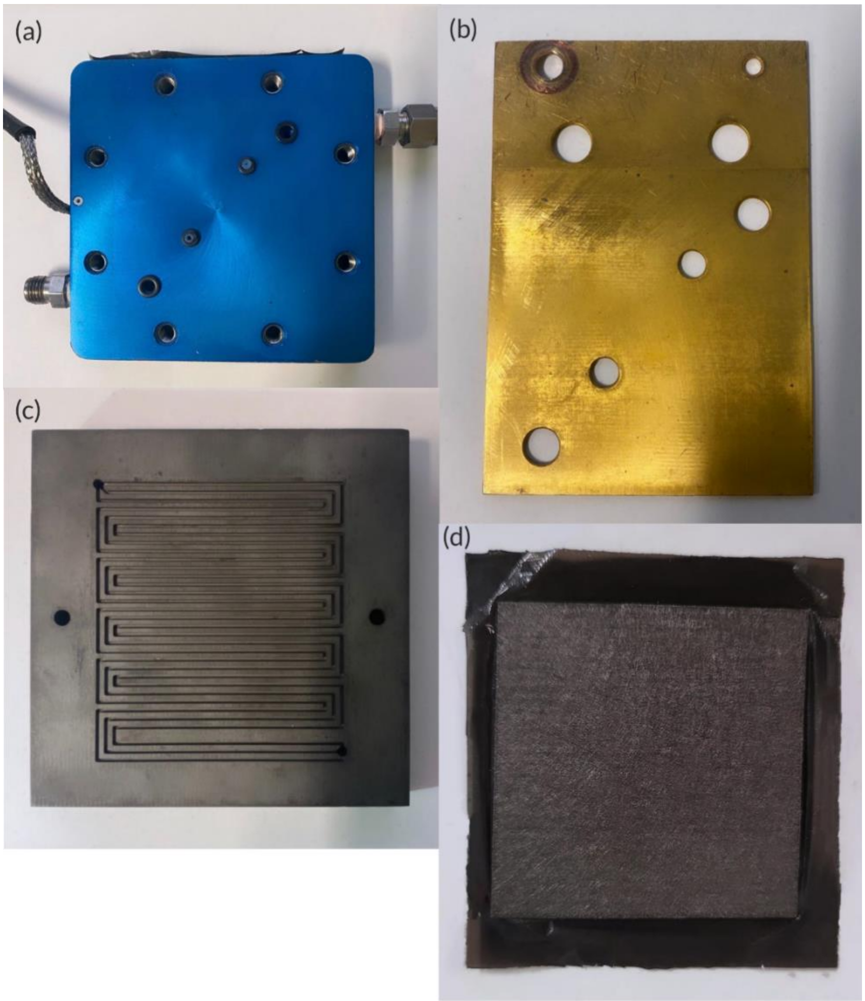

Figure 3-2: Overview of PEMFC assembly. Components may be subject to minor changes depending on the test station used and the experiment conducted. (a) Endplate. (b) Current collector. (c) Multi-serpentine flow field plate. (d) MEA

Table 3-1: Component specifications for fuel cell assembly.

Component	Specification or Manufacturer
PTFE membrane	Gore-Select
GDE	HyPlat (Pt/C catalyst Pt loading: 0.4 mg/cm2Pt)
Flow field plate	Scribner
Stainless-steel BIP	Scribner

Together, the GDL, Pt/C catalyst and PTFE membrane form the membrane electrode assembly (MEA) of the fuel cell. The membrane electrode assembly is assembled in-lab by ‘sandwiching’ the PTFE membrane between two HyPlat GDEs. A single HyPlat GDE has two sides, one consisting of the GDL and the other of the Pt/C catalyst. The two GDEs are oriented in such a way that the Pt/C sides face each other, with the PTFE membrane in between. A photograph of the layout is shown in Figure 3-2(d). The MEA assembly was then hot-pressed with a temperature of 150°C on both the anode and cathode side, with a clamp force of 1,700 lbs, or 7,560 N, and 3 min. Then, the fuel cell was assembled in the order shown in Figure 3-2. The bolts used to hold together the fuel assembly were tightened with a final torque of 4 Nm.

The operating conditions of the PEMFC adhered to the EU Reference Automotive Conditions suggested by FCH. These conditions are listed in Table 3-2. The dew point temperatures (DPT) for the anode and cathode were set at 64 and 53 °C, respectively, paired with a cell temperature of 80 °C, which allowed a relative humidity (RH) of 50% for the anode and 30% for the cathode [131]. Prior to any experiments, the fuel cell was conditioned by first heating the PEMFC to the desired operating temperature (80 °C) and holding it at that temperature for 30 minutes. Then, the cell was operated at a constant current of 5 A until the voltage stabilised. Later, polarisation curves from OCV to 0.3 V and 0.3 V back to OCV were collected until the curves were stable.

Table 3-2: Scribner PEMFC operating parameters, following the FCH EU Reference Automotive Conditions [122].

Parameter	Unit	Value
Cell temperature	°C	80
Anode gas inlet temperature	°C	85
Anode gas inlet dew point temperature (DPT)	°C	64
Anode gas inlet absolute pressure	kPa	250
Anode stoichiometry	-	1.3
Cathode gas inlet temperature	°C	85
Cathode gas inlet dew point temperature (DPT)	°C	53
Cathode gas inlet absolute pressure	kPa	230
Cathode stoichiometry	-	1.5

3.3.2 Drive Cycle Endurance Testing for PEMFCs

The dynamic load cycling endurance test was used to simulate one year (equivalent to 15,400 km [132]) of LDV FCHEV driving or 100 drive cycles of HGV and bus FCHEV driving. The total distances of drive cycles were calculated by integrating the speed vs. time curves. The drive cycle was then looped for a number of required repetitions to meet the annual LDV driving distance of 15,400 km [132], or 100 cycles for HGV and bus [3].

The Scribner 850e system is capable of running a cell under a dynamic load, with the help of its arbitrary control feature. The feature can control a PEMFC via three modes: constant current, constant voltage, or constant power. More than one control mode was chosen for comparing the power responsiveness of the PEMFC when tested under a drive cycle. Due to factors such as gas lag, it was presumed that the actual power produced by the PEMFC differs depending on the type of control mode used. Each control mode has its advantages and disadvantages and can allow a different insight into PEMFC analysis. A comparison of different output power is provided in the Results and Discussion section.

The procedures for dynamic load testing took inspiration from FCH's dynamic load cycling endurance test protocols. The FCH protocol is created for FCEVs (non-hybrids) and utilises the NEDC drive cycle. However, the NEDC cycle is now considered outdated and less representative of realistic driving representation when compared to the WLTP Class 3 and newer transient drive cycles [133]. Some changes and updates were made for a more accurate and in-depth analysis, including the inclusion of the newer transient drive cycles featuring a wide range of vehicle purposes (LDV, HGV, and bus) and a more accurate depiction of an electrochemical hybrid vehicle. The PEMFC was first set according to the EU Reference

Automotive conditions listed in Table 3-2. Then, the new MEA was conditioned using the steps described previously, in the ‘Cell Preparation, Specifications’ section. After conditioning was complete, beginning-of-life (BoL) data were collected; these data included polarisation curves, CV, LSV and EIS. Next, the cell was subjected to arbitrary current or power control, following the drive cycle of choice, for a number of required repetitions. After every 50 to 100 cycles (case-dependent) of this arbitrary control, the arbitrary control was paused briefly to enable the collection of the same curves (polarisation curve, CV, LSV and EIS) that were collected for the BoL data, forming an incremental set of electrochemistry data from BoL to EoT which can be compiled for degradation analysis. For CV and LSV tests, the cathode side is purged with nitrogen gas prior to running the experiment. The frequencies and conditions of these electrochemistry data collection are outlined in Table 3-3.

Table 3-3: Endurance testing data collection frequency and conditions.

Technique	Frequency	Conditions
Polarisation curve	BoL, every 50 or 100 drive cycles, EoT	OCV to 0.3 V to OCV; 30 s pt^{-1}; 0.025 V pt^{-1}
CV	BoL, every 50 or 100 drive cycles, EoT	0.06 V to 1 V to 0.06 V; 20 mV/s; 0.1 s pt^{-1}
LSV	BoL, every 50 or 100 drive cycles, EoT	0.06 V to 0.6 V; 5 mV s^{-1}; 0.1 pt s^{-1}
EIS	BoL, every 50 or 100 drive cycles, EoT	Perturbation alternating current is set to 10% of the direct current; 10000 to 0.1 Hz

3.3.3 Degradation Characterisation of PEMFCs

3.3.3.1 Polarisation Curve

The polarisation curve displays the voltage vs. density loading. An explanation of the different regions of a polarisation curve can be found in Table 3-4. At low current densities, the cell potential decreases as a result of activation polarisation [8]. During this stage, the catalyst activation barrier must be overcome for products to become reactants [8]. At moderate current densities, Ohmic or charge transport losses contribute to drops in cell potential [8]. This is caused by the resistance of the polymer electrolyte membrane to ions and the resistance of imperfect electrodes [8]. At high current densities, concentration or mass transport polarisation causes a further decrease in cell potential. The difference in this decrease is that it no longer has a linear relationship with current density [8]. This voltage loss is caused by mass transport and is due to changes in the concentration of the reactants at the surface of the electrodes as hydrogen and oxygen are consumed [8].

Table 3-4: Classification of different regions of a polarisation curve [8]. The voltage loss of each region is caused by a different mechanism.

Region	Cause of voltage loss
Activation	Overpotential
Ohmic	Charge transport
Concentration	Mass transport

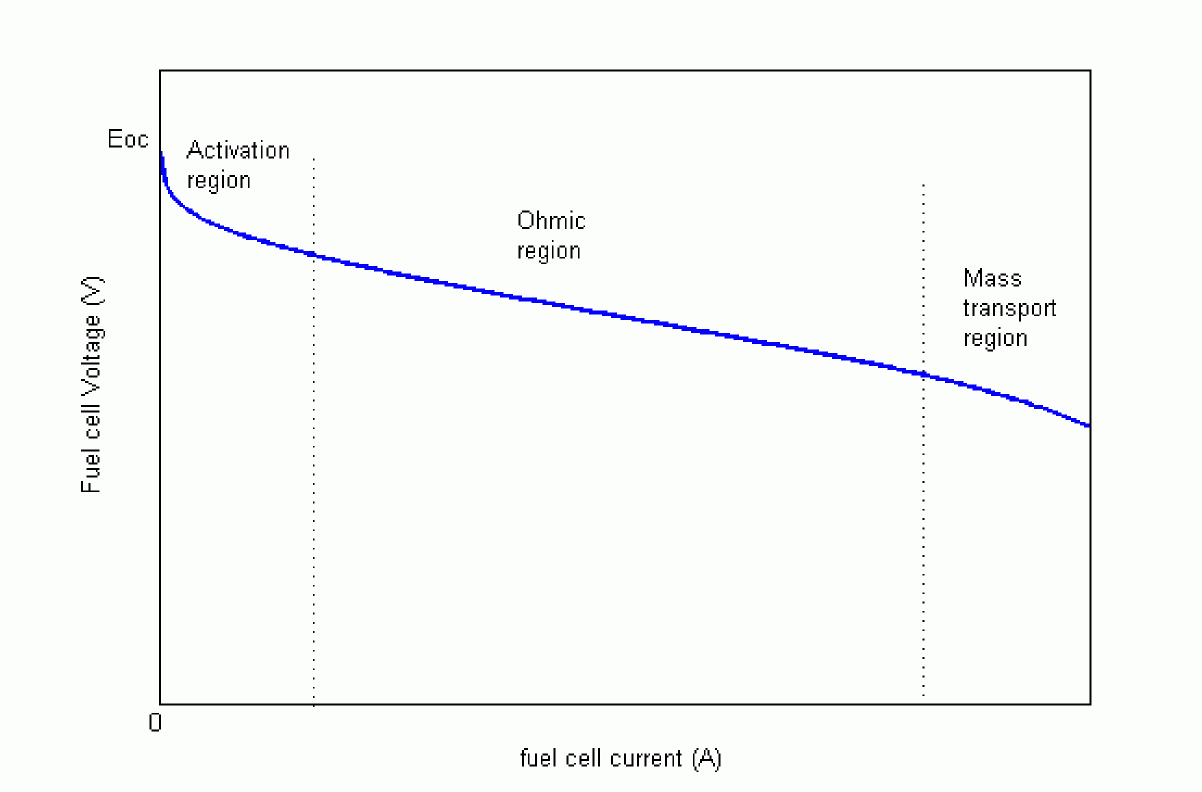

Figure 3-3: Example fuel cell polarisation curve showing all regions of voltage drop. Each region represents a different mechanism of voltage drop [134].

Considering all of the voltage losses of the polarisation curve, the total fuel cell potential can be calculated as [8]:

$$\mathrm{E} = \mathrm{E_r} - \mathrm{E_{act}} - \mathrm{E_{ohm}} - \mathrm{E_{mass}} \tag{3-1}$$

where $\mathrm{E_r}$ is the reversible potential, $\mathrm{E_{act}}$ is the activation loss, $\mathrm{E_{ohm}}$ is the Ohmic loss, and $\mathrm{E_{mass}}$ is the mass transfer loss.

The activation loss can be calculated using the following equation [8]:

$$E_{act} = \frac{RT}{\alpha_t nF} \ln \frac{i}{i_0}$$

(3-2)

where α_t is the charge transfer coefficient, n is the numver of electrons transferred in the reaction, F is the Faraday constant, and i is the current density [8].

The Ohmic losses can be calculated using the following equations [8]:

$$E_{ohm} = iR_i$$

(3-3)

where R_i is the internal resistance.

The mass transport losses can be calculated using the following equation [8]:

$$E_{mass} = \frac{RT}{\eta_e F} \ln \frac{i_L}{i_L - i}$$

(3-4)

where η_e is the number of electrons being transferred, and i_L is the limiting current density.

The total fuel cell potential calculation shown in Equation (3-1) can then be modified to:

$$E = E_r - \frac{RT}{\alpha_t F} \ln \frac{i}{i_0} - iR_i - \frac{RT}{\eta_e F} \ln \frac{i_L}{i_L - i}$$

(3-5)

Aside from voltage vs. current density in a polarisation curve, this project also heavily used the power vs. current density curve. This curve was especially useful for verifying if the PEMFC are still able to cope with maximum power demands. In addition, a series of power vs. current density curves can be plotted to visualise the drop in power between different endurance cycles; these curves are usually presented on the same curves as the voltage vs. current density curves, which will be shown in the Results and Discussion section. On rare occasions, power vs. voltage curves were also used as visual checks to see how the voltage corresponding to maximum power has shifted throughout endurance testing.

3.3.3.2 Cyclic Voltammetry (CV) and Electrochemical Surface Area (ECSA)

One of the main causes of PEMFC degradation caused by dynamic loads is the degradation of the Pt/C catalyst, particularly in the loss of ECSA [43]. The ECSA decay rate can be represented as a function of the remaining surface area of the Pt catalyst [43]. Figure 3-4 is an example of collected CV curves with regions of interest labelled. CV diagrams are shown in current (A), or current density (A cm^{-2}) vs. voltage (V). ECSA estimation is calculated by integrating the curve of either the hydrogen atom desorption or adsorption region, as these two regions are proportional to the number of hydrogen molecules reactive with the Pt catalyst [135]. In this project, the adsorption region was always integrated instead of the desorption region to keep the data analysis consistent. The following equation was used to estimate ECSA [135]:

$$\mathrm{ECSA} = \frac{\mathrm{Q_{Pt}}}{\mathrm{210L}}$$

(3-6)

where L is the mass of platinum per unit area (mg cm^{-2}), which was 0.4 mg cm^{-2} for HyPlat, $\mathrm{Q_{Pt}}$ is the charge area of hydrogen adsorption or desorption and 210 is the charge required to reduce a monolayer of protons on platinum in the unit of μC cm^{-2}.

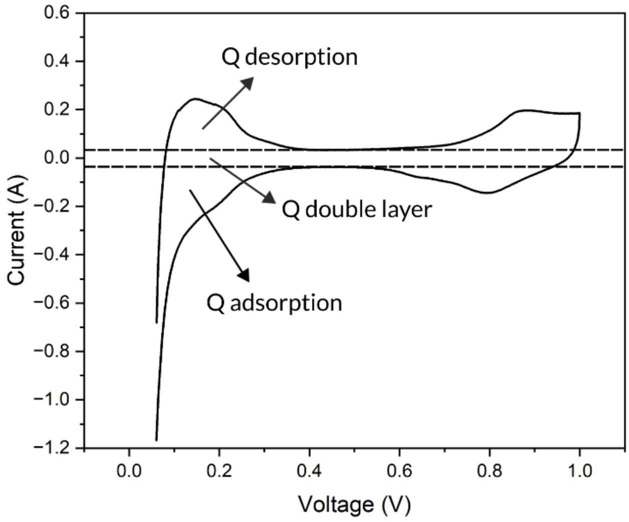

Figure 3-4: Regions of interest for calculating ECSA from CV curves.

ECSA estimations, however, can only capture degradation mechanisms within the activation and charge transfer regions, as it is mainly an estimation of catalyst availability. However, the researcher still regarded it as one of the most important characterisation techniques in this project as it provides valid numerical comparisons between all endurance testing scenarios.

3.3.3.3 LSV

Linear sweep voltammetry (LSV) is used to identify short-circuiting and fuel crossover [136]. These curves are collected every 50 to 100 cycles during endurance testing for diagnosis of the two aforementioned characteristics. The technique is performed with hydrogen on the anode and nitrogen (or another type of suitable inert gas) on the cathode [136]. Figure 3-5 shows two example curves of LSV, with one curve representing a pristine cell, and one curve representing a degraded cell with an internal short. LSV plots tend to show current density (mA cm^{-2}) vs. voltage (V). The region of interest to diagnose degradation is when the curve reaches an equilibrium, which can be easily identified after the voltage of 0.25 V in the pristine cells' curves shown in Figure 3-5. It can be seen that the degraded cell does not reach a complete equilibrium but shows an upwards gradient, instead. This upward gradient is a sign of internal shorting, indicating that the cell has a finite resistance [136]. With the slope of the voltage vs. current plot, the resistance can be estimated. Another degradation mechanism to identify is fuel crossover [136]. According to Department of Energy (DOE) standards, if the equilibrium part of the LSV exceeds a current density of 20 mA cm^{-2}, the cell is considered to be chemically unstable, and fuel crossover is suggested [137]. Hydrogen crossover flux can be calculated using the following equation [136]:

$$J_{crossover,H_2}=\frac{i_{lim}}{nF} \tag{3-7}$$

where i_{lim} is the limiting current density, n is the number of electrons, and F is the Faraday constant.

When a cell experiences fuel crossover, performance decreases and degradation occur. The performance decrease is mainly caused by the decrease in fuel efficiency due to the lack of reactants [136]. Degradation mechanisms may include membrane thinning or breakage and pinhole formation; most of this is caused by heat generation [136].

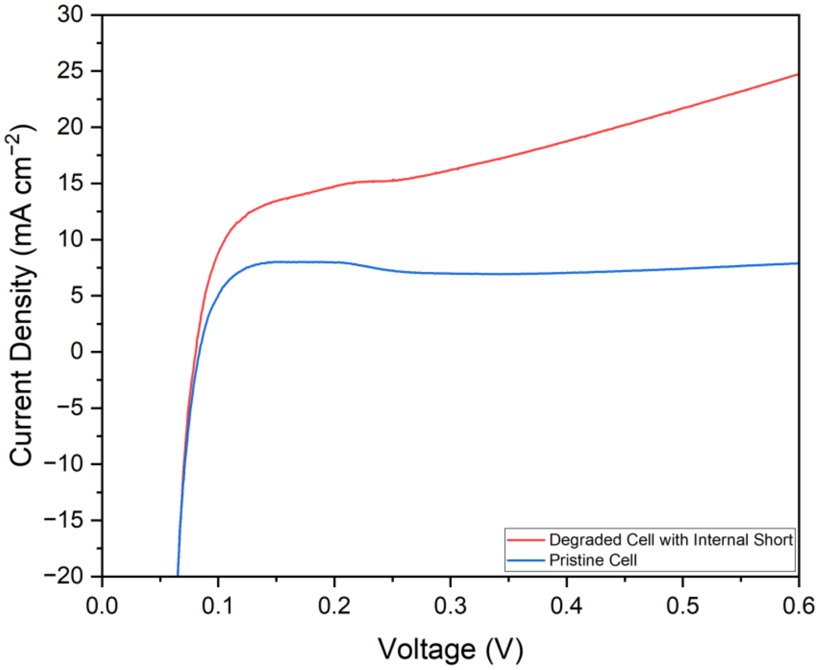

Figure 3-5: Example of two LSVs, showing a pristine cell and degraded cell. The upward gradient of the curve of the degraded cell represents an internal short [136].

3.3.3.4 EIS

EIS is a non-destructive diagnostic technique that applies an AC potential or current to a fuel cell and measures the cell current using a potentiostat or galvanostat [41]. The aim is to perturb the equilibrium state of the cell. There are three electrodes involved in EIS collection, which are summarised in Table 3-5.

Table 3-5: List of required electrodes for a potentiostat and their purposes.

Electrode	Purpose
Working electrode	Voltage control and current measurement
Reference electrode	Measures the working electrode's voltage
Counter electrode	Completes the circuit

In a galvanostat, the system takes the signal block as an input, which generates a constant current, ramps and sine waves [138]. The signal is then fed into a control amplifier that compares and matches the cell current with the desired current [138]. The three electrodes are connected in series; the counter electrode is connected with the control amplifier to complete the circuit [138], the reference electrode measures the working electrode's voltage and the working electrode measures current and controls it accordingly [138]. The electrometer acts as the feedback signal of the circuit and measures the voltage difference between the reference and working electrodes [138]. The I/E converter is a resistor that works in conjunction with the working electrode to obtain cell current by measuring the voltage drop across the resistor [138].

Depending on the experiment, EIS collection is carried out at different stages and timestamps, in either 50 (annual LDV experiments) or 100 drive cycle (HGV and bus experiments) intervals; but it is always collected for beginning-of-test and end-of-test conditions. GEIS collections were held at 100, 300, and 800 mA cm^{-2} current densities, and 0.5 and 0.65 V voltages. The AC amplitude used was 10% of DC.

After data collection, Nyquist plots were fitted into an equivalent circuit model using RelaxIS software. The equivalent circuit model used is shown in Figure 3-6. From this model, the Ohmic (R_{Ω}), anode charge transfer (Ran), cathode charge transfer (R_{ca}), and mass transfer (R_{ca}) resistance can be interpolated. A combination of constant phase elements (CPE) and capacitors was used. CPE is considered to be in between a resistor and a capacitor, which is arguably more representative and popularised for a PEMFC's charge transfer region [139]. In addition, because CPEs have an extra degree of freedom than capacitors, the error of the fit is usually less [139]. One of the benefits of this model is that it differentiates the anode and cathode charge transfer resistance separately while keeping a low fitting error.

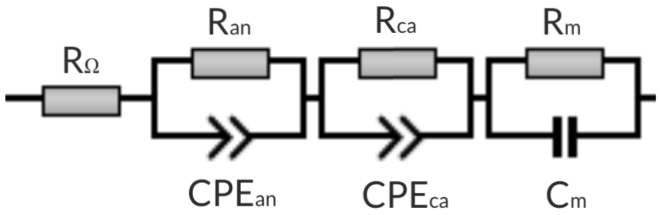

Figure 3-6: Equivalent circuit model used to fit PEMFC EIS data. With this model, the Ohmic (R_{Ω}), anode charge transfer (R_{an}), cathode charge transfer (R_{ca}), and mass transfer (R_{ca}) resistance can be interpolated. This model is adapted from Kang et al.[140].

3.4 Battery Cycling for Hybridisation for X Analysis

3.4.1 Cell Specifications

A commercial LG INR21700 M50 cell was chosen for use in Hybridisation for X tests. The specifications of the cell are outlined in Table 3-6.

Table 3-6: LG INR21700 M50 parameters [110].

Parameter	Specification
PE chemistry	NMC 811

NE chemistry	Graphite-SiO$_x$
Size	21700
Capacity (Ah)	5
Nominal Energy (Wh)	18.2
Minimum Energy (Wh)	16.6
Nominal Voltage (V)	3.63
Maximum Charge Voltage (V)	4.2
Maximum Charge C-Rate at 25 °C	0.7C
Maximum Continuous Charge Power (W)	12
Maximum Continuous Discharge Power at 25 °C and 1C (W)	20
Shipped SOC (%)	30
Mass (kg)	0.068

The aim was to have the battery cover the remaining power requirements that are not accounted for by the fuel cell. The requirement from the sized battery pack was scaled down to that of a single LG 21700 cell. The cell had a capacity of 5 Ah and a nominal voltage of 3.63 V [141], which was important for sizing an electrochemical hybrid vehicle when paired with a maximum current value. The maximum and cut-off voltage values of 4.2 V and 2.5 V [141], respectively, were important for setting the safety limits of charge and discharge cycles on the Maccor battery cycler.

The maximum charge C-rate was useful for determining the quickest charging times upon completion of a discharge-dominant drive cycle, to recover the SOC of the battery. The maximum charge current can be calculated as:

$$\mathrm{I}_{\mathrm{charge}}^{\mathrm{max}} = \mathrm{C\ rate}_{\mathrm{charge}}^{\mathrm{max}} \times \mathrm{capacity} \tag{3-8}$$

which, for this cell, has a value of:

$$\mathrm{I}_{\mathrm{charge}}^{\mathrm{max}} = 0.7\ \mathrm{C} \times 5\ \mathrm{Ah} = 3.5\ \mathrm{A} \tag{3-9}$$

The maximum discharge C-rate can be used to set the discharge current limits of the drive cycle profile. The maximum discharge current can be defined as:

$$\mathrm{I}_{\mathrm{discharge}}^{\mathrm{max}} = \mathrm{C\ rate}_{\mathrm{discharge}}^{\mathrm{max}} \times \mathrm{capacity} \tag{3-10}$$

which, in this case, has a value:

$$\mathrm{I}_{\mathrm{discharge}}^{\mathrm{max}} = 1.5\ \mathrm{C} \times 5\ \mathrm{Ah} = 7.5\ \mathrm{A} \tag{3-11}$$

3.4.2 Drive Cycle Endurance Cycling for Batteries

The Biologic 800 series cycler was chosen to cycle the M50 LiBs. The goal of this project is to use the battery cycler for application-based testing, specifically cycling cells under drive cycles using the 'Urban Profile' feature. Table 3-7 shows the procedures of drive cycle bench testing for the M50 LiBs. The cell is first discharged at a slow constant current C-rate of C/20. This first step is to prepare the commercial cell for further analysis with a full slow discharge, as the nominal shipping SOC of the M50 is around 30% [110].

In step 2, the cell is constant-current charged at 0.7C. To replicate the realism of hybrid electric vehicle (HEV) charging, the cells are charged to a 50% SOC instead of the standard CC-CV charging protocol for battery cycling [142], [143]. A typical EV, such as a Nissan Leaf, charges at C-rates of 0.11C, 0.11C and 0.79C for AC home charging, AC fast charging and DC rapid charging, respectively. Step 2 mirrors the DC rapid charging scenario, by employing a similar C-rate. This parallels the work of other authors, such as the study of a modelling representation of a lithium-ion battery for real-time degradation control under the US06 and LA92 drive cycle, by Zhao *et al*. In their study, the cells were charged back using CC-CV charging at a C-rate of 1C CC after each drive cycle completion [144].

After the cell is charged, it undergoes a drive cycle discharge of the corresponding protocol. A drive cycle discharge differs from the standard CC discharge in the sense that C-rate is varied during the discharge process, typically in terms of every second. The drive cycles contain both charge and discharge time steps while being discharge dominant; charging time steps suggest the capabilities for regenerative braking. But for the sake of naming convention, this step would be called drive cycle discharge here-on-after.

Usually, one drive cycle isn't enough to fully discharge the M50 cell to its cut-off voltage of 2.5 V; but rather multiple repetitions of drive cycle discharge would be needed. This is where step 4 comes into place, looping step 3 (drive cycle discharge step) a number of times until the voltage reaches its discharge cut-off limit. To determine the number of loops needed, test drive cycle discharge runs were usually conducted on a pristine M50 cell. After determining the number of loops needed, the 'test-run' cell was discarded and a new cell would be connected for drive cycle endurance testing. After multiple drive cycle discharges, the cell needed to be recharged to 50% SOC. Step 5 is a loop step that brings the procedure back to step 2; essentially, steps 4 and 5 are nested loops. With this setup, it is assumed that the driver of the virtual FCHEV only charges car if the battery pack is near depletion. In experimental terms, relevant rest steps are needed between these steps for safety and to prevent unwanted cell damage; these steps not shown in Table 3-7.

Table 3-7: LiB drive cycle testing procedures.

Step	Control
1	CC discharge at C/20
2	CC charge at 0.7C
3	Urban Profile
4	Repeat loop of Step 3
5	Repeat loop of Step 2

The loop counts of step 4 and 5 can be adjusted for the endurance analysis. In the LDV's case, the drive cycle count was set to 662 cycles, to simulate one year of WLTP Class 3b driving while keeping the estimated yearly distance consistent to the value of 15,400 km proposed by FCH fuel cell testing protocols. By keeping the distance constant for the fuel cell and the battery, a scaled-down virtual hybrid vehicle can be tested using the appropriate cyclers for different electrochemical devices. As for HGV and bus scenarios, the cycle count is kept to 100 as per the reasons mentioned in the Drive Cycle Endurance Testing for PEMFCs section.

3.4.3 Degradation Characterisation of LiBs

3.4.3.1 SoH

State-of-Health (SoH) vs. cycle or time graphs is a commonly used degradation analysis tool for dynamic load cycling. SoH is not something that can be measured straight from a battery cycler, as the term is defined by three parameters: namely capacity, internal resistance, and self-discharge [12][145]. The third parameter of SoH, self-discharge, is not applicable to drive cycle tests, as it is a parameter related to calendar ageing [12][145].

Capacity fade can be analysed with a capacity vs. time or cycle graph. Typically, the charge capacity at the end of a CC-CV step is of interest. Because of the lack of CC-CV charging steps in the drive cycle endurance testing procedure, diagnostic cycles were conducted at the EoT. The diagnostic cycle procedure used is shown in Table 3-8. In Step 1, the cell is discharged at a moderately slow C-rate of C/10, to prepare the cell for a full charge. Steps 2 and 3 charges the cell using CC-CV protocol. The same CC C-rate as the drive cycle endurance procedure was used. After reaching 4.2 V during CC, the cell was CV charged at 4.2 V until the current reaches the cut-off current limit of C/20 or 0.25 A [141]. The aforementioned 3 steps were crucial in determining the capacity of the cell. Capacity could then be compared between BoL and EoT.

Table 3-8: Diagnostic cycle procedures used to determine capacity fade and EIS. Diagnostic cycles are performed at BoL and EoT (662 drive cycles for LDVs, 100 cycles for HGVs and buses).

Step	Control
1	CC discharge at C/10
2	CC charge at 0.7C
3	CV charge at 4.2V
4	EIS

Internal resistance is a combination of Ohmic, charge transfer, and diffusional resistance [146]. These parameters can be interpolating via EIS fitting. The diagnostic cycle shown in Table 3-8 also includes a fourth step, which collects a potentiostatic EIS at an amplitude of 0.01 V from 10,000 to 0.01 Hz. The equivalent circuit model used to fit the EIS Nyquist plot is shown in Figure *3-7*, adapted from Iurilli et al.[41]. With the model, Ohmic (R_Ω) and mid-frequency (R_{mid}) resistance, and low frequency Warburg (W_{low}) impedance can be interpolated. Together, they make up the definition of internal resistance. R_Ω is in the high-frequency region of above 1000 Hz. Both R_{mid} and W_{low} can represent charge transfer resistance. The mid-frequency region of R_{mid} is between 1000 Hz and 0.1 Hz. W_{low} shows diffusional resistance. W_{low} is located in the low-frequency region of under 0.1 Hz. The actual equivalent circuit model presented by Iurilli et al. uses two parallel CPEs and Rs (RPs) connect in series instead of one. However, Iurilli et al.'s model is more suitable for Nyquist plots with two semicircles instead of one. Because of the NMC-811 chemistry of M50 cells, only one semicircle is observed [41], so the author has removed one RP. The author has observed that the fit error was over a reasonable limit when two RPs were used.

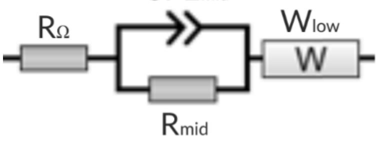

Figure 3-7: EIS equivalent circuit model for LiBs. RΩ represents the Ohmic resistance, Rmid represents the resistance at the mid-frequency region, and Wlow is the Warburg element representing the low-frequency region.

3.4.3.2 X-Ray Computed Tomography (CT)

After the M50 cells have been cycles for either a year or 100 drive cycles, non-destructive X-ray computed tomography (CT) were conducted on them using the Nikon XTH 225 CT with a 0.5 mm copper filter and a tungsten target. The M50 cells were probed with beam energy, current, and power of 200 kV, 162 µA, and 32.4 W, respectively. A total of 2028 projections were collected with an exposure time of 1s. A voxel size of 38.5 µm could be achieved with this setup. The aforementioned parameters and conditions are summarised in Table 3-9.

Table 3-9: X-ray conditions used for scanning M50 21700 LiB cells.

Parameter	Condition
Beam energy (kV)	200
Beam current (µA)	162
Power (W)	32.4
Number of projections	2028
Voxel size (µm)	38.5

After scanning, the projections were reconstructed using Nikon CT Pro 3D software, as well as applying beam-hardening adjustments. Different slices of interests were compiled after reconstructing. Any damages and changes to the cell such as rotation and delamination were further analysed in Avizo 2019.4 software. Figure 3-8 shows annotations on an example slice on how changes in rotations were calculated. For rotation, the angle between the outer-most endpoint of the jellyroll, labelled Pr (point of interest for rotation), to origin of the axis in white, labelled C (centre of slice), was measured for both the BoL and EoT cell. The difference in degrees between the BoL and EoT measurement is the angle of rotation of the cell.

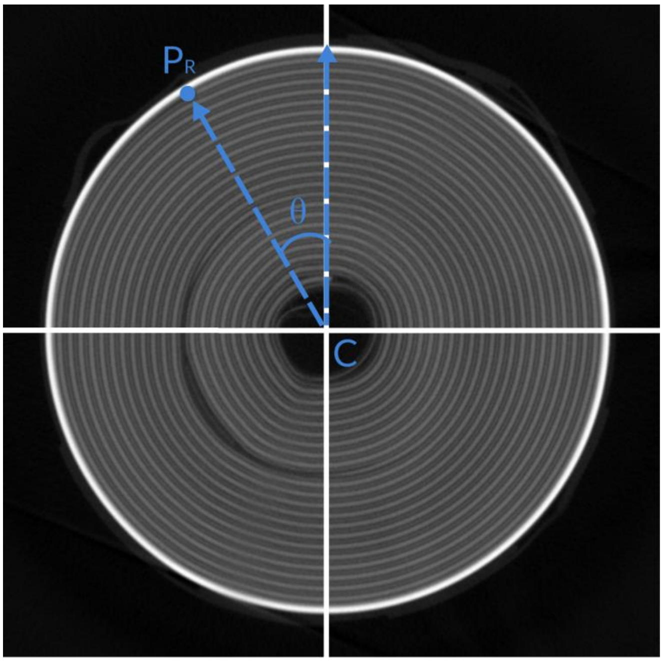

Figure 3-8: X-ray CT slice rotation measurement methodology.

Delamination usually occurred around the innermost jelly roll region. For delamination, the distance from the point of delamination, labelled Pd (point of interest for delamination), to the centre point of the slice (C) was measured. The notation is that: the lesser the distance Pd is to C, the more severe the delamination. The delta distance was calculated between BoL and EoT.

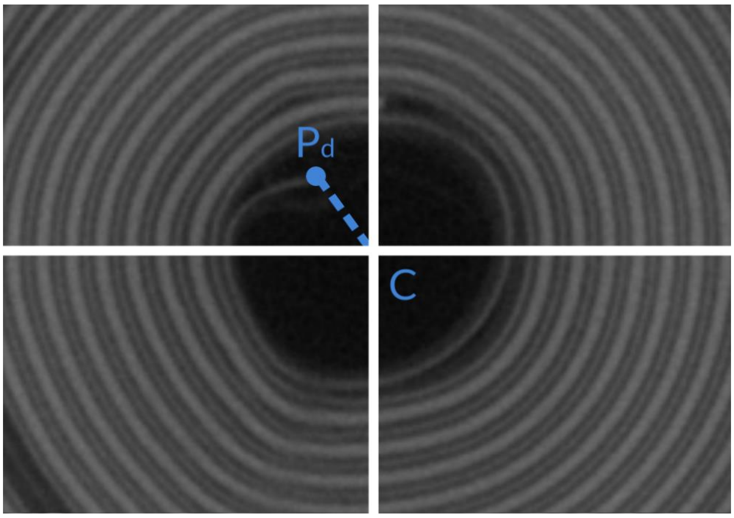

Figure 3-9: X-ray CT slice delamination measurement methodology.

4 Results and Discussion

4.1 Results and Discussion Chapter Introduction

The results and discussion start with the HybeMass MATLAB model development aspect of the project as the first chapter. The focus is then transitioned towards the drive cycle endurance bench testing results of the project for the second chapter, using degradation characterisation techniques to analyse the results. Lastly, the third chapter talks about the different mass implications of different hybrid ratios, fully testing the HybeMass model and the effectiveness of the system weight feedback loop. The drive cycle endurance testing chapter focuses on 0.8 HD scenarios.

The PEMFC counterpart degradation bench testing results are characterised using polarisation curves, CV for ECSA estimation, LSV, and EIS; and the Li-ion battery counterpart is characterised using capacity fade, EIS, and X-ray CT.

To present this work, PEMFC and LiB characterisations are divided into different sections. Then, the subsections are first divided by vehicle purpose (LDV, HGV, and bus), then by the characterisation technique used. This division of sections allows easy visualisation of performance and degradation comparisons between vehicles of the same scenario but with different powertrain configurations.

4.2 HybeMass MATLAB Model Development

4.2.1 Drive Cycle to Power Cycle Conversion

To convert a drive cycle to a power cycle, the concepts of force balance and vehicle dynamics are to be used. From a simplified perspective, there are four opposing forces a vehicle needs to overcome to move. These are the aerodynamic drag, rolling resistance, gradient resistance, and inertial force [61], which are illustrated in Figure 4-1. Once the magnitude of these forces is known, the power required at the wheels can be calculated using Equation (*4-1*):

$$\mathrm{P} = \mathrm{F}_{\mathrm{tot}}\mathrm{v}$$

(4-1)

where P is the required power, F_{tot} is the total opposing force, and v is the velocity at a given point in time.

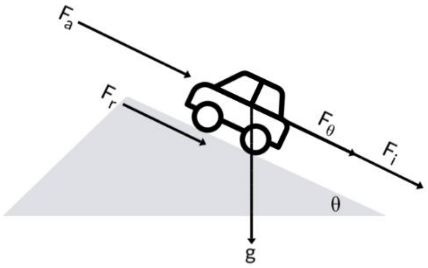

Figure 4-1: Notation and schematics of the drive cycle to power cycle conversion. F_a, F_r, F_θ, *and* F_i *are aerodynamic drag, rolling resistance, gradient resistance, and inertial force, respectively.*

Aerodynamic drag can be calculated as follows:

$$F_a = \frac{1}{2}\rho c_d A v^2$$

(4-2)

where ρ is the air density, c_d is the air drag coefficient, and A is the vehicle's frontal area. The vehicle's velocity at a point in time can be obtained from the chosen driving cycle.

The rolling resistance force can be calculated as follows:

$$F_r = mgc_{rr}\cos(\theta)$$

(4-3)

where m is the mass of the vehicle, g is gravitational acceleration, c_{rr} is the rolling resistance coefficient, and θ is the road gradient.

The gradient resistance force can be calculated as follows:

$$F_\theta = mg\sin(\theta)$$

(4-4)

The inertial force can be calculated as:

$$F_i = ma$$

(4-5)

where a is the vehicle's acceleration.

Vehicle acceleration values can be obtained by differentiating the speed vs. time graph of a drive cycle.

The total opposing forces can be calculated as follows:

$$F_{tot} = F_a + F_r + F_\theta + F_i \tag{4-6}$$

and the total power required can be computed from:

$$P_{req} = F_{tot} v \tag{4-7}$$

In a drive cycle, the above calculations for P_{req} are computed after each second to compile an overall power cycle by plotting the required power with respect to time. Any negative region of the power cycle is a potential for regenerative braking, though the 'negative required power' can never be recovered in full, as losses always occur during regen.

4.3 Downscaling Stack Level Power Cycles to Cell-Level

Using the HybeMass model, the required stack-level power profiles could be extracted for both the PEMFC stack and battery pack counterparts, in the units of kW. These profiles needed to be downscaled to a cell level to be tested on an electrochemical bench scale, in the units of W. The profiles are extracted from MATLAB to a spreadsheet, and the maximum stack or pack operational power of both the PEMFC stack and battery pack was determined using Excel functions. With this computed, a list of ratios relative to the maximum operational power (r) can be compiled for the stack power of every timestamp (in seconds) of drive cycle. The cell power of either the PEMFC or LiB cell at each time stamp (P_i) can then be calculated using the following equation:

$$P_i = P_{cell\_op} \times r_i \tag{4-8}$$

Where P_i is the required cell power at i timestamp of the drive cycle, P_{cell_op} is the cell operating power, and r_i is the ratio of the required stack power at i timestamp to the maximum required stack power. The calculated P_i's can be compiled into designated file formats to export into the Scribner fuel cell testing station or Biologic 800 series battery cycler for drive cycle endurance testing. Due to the time constraints of this project, only 0.8 HD configurations, a common HD similar to that of a first-generation Toyota Mirai, were downscaled and further tested using drive cycle endurance bench testing.

4.4 Purpose and Application of the HybeMass Model

A MATLAB model, HybeMass, is developed; this model examines both the hybridisation degree and cell operating power, identifying the requirements for PEMFC and LiB cell numbers, and overall power system and gross vehicle mass (GVM). Typically, automotive engineering follows the V-model concept, which begins with full vehicle conception and moves to module and component design and simulation, and finally component and full vehicle testing. In this work, the introduction of a feedback loop in the proposed the HybeMass MATLAB model to improve the efficiency of the V-model process for module and component design and simulation, specifically eliminating the need for a priori understanding of the vehicle's power demand. Identifying the optimal HD to minimise the vehicle's mass which can be used as a key design factor to extend the range. A diagram of the V-model was shown in Figure 1-1 [147], which is a standardised method of vehicle development used by automotive manufacturers; the boxes with the dashed lines show the steps where the HybeMass mode may be capable of shortening or removing some of the steps in the vehicle design and testing process. The left side of the 'V' typically involves simulation and software use, while the right side of the 'V' typically involves physical implementation and testing. Engineers and the research and development (R&D) team typically need to step back to the left side of the 'V' during physical testing and implementation stages if something wasn't designed or engineered adequately; improper vehicle sizing may cause a step backward during these design stages. It is far more time and cost-efficient to ensure the sizing issues are addressed in the software and simulation changes (left V); the HybeMass software aims to remove sizing issues before reaching the physical testing and implementation stages. Although not highlighted in Figure 1-1, problems with sizing may still occur during the system verification stage. This stage is the second-last stage before a vehicle is subject to mass manufacturing, identifying sizing issues at this late stage may induce major developmental setbacks. It is crucial to address the sizing complication early.

Transient drive cycles are used to estimate the power demands of vehicles of different scenarios to determine the appropriateness of the suggested system for light-duty vehicles (LDV), Class 8 heavy goods vehicles (HGVs), and bus applications. To ensure accuracy parasitic component masses, auxiliary power draw, and efficiency losses are also considered in the relevant systems within the model. By developing our HybeMass model we hope to enable the extension of these studies by enabling developers to explore the impact of the sizing of and HD of FCHEV's (fuel cell hybrid electric vehicles) on energy management. By providing this additional design consideration, our model will enable the optimisation of the system for the range and use case of vehicles, minimising the opportunities for overdesign in net-zero vehicles. The model is capable of supporting both parallel and FCREx vehicles.

4.5 Power Systems Sizing and Weight Estimations - HybeMass Model

A power source sizing and mass estimation model was developed from the ground-up in MATLAB Simulink, referred to hereafter as the HybeMass model. The model developed is composed of five subsystems: a power cycle convertor, parasitic losses and efficiency adjustments, cell count calculator, system mass feedback loop, and PEMFC diode and LiB overcharge protection. A flow diagram of the aforementioned subsystems is shown in *Figure 4-2*. The MATLAB program developed here 'self-updates' the newly added PEMFC and battery cell mass upon the pre-existing vehicle chassis mass to find the optimum number of cells needed to minimise the mass of the vehicle. The full formulation of the model is described in depth below.

The cell count calculator subsystem calculates the number of PEMFC and LiB cells required to support the vehicle, as well as calculating the PEMFC stack and LiB pack mass. In addition, the new gross vehicle mass (GVM) with power systems can be calculated. The power cycle convertor subsystem utilises vehicle design and powertrain development equations which will be outlined in further subsections (Power Cycle Convertor Subsystem) to convert a drive cycle to a power cycle. This converted power cycle only factors in tractive power and the mass of parasitic components, excluding the power draw by parasitic and auxiliary components. These losses and efficiency losses in the powertrain are obtained in the next subsystem. Finally, the PEMFC diode and LiB overcharge protection subsystem, can be used to obtain separate power division profiles for the PEMFC stack and LiB pack. This subsystem extends beyond a simple arbitrary division of power with the model ensuring the PEMFC stack does not observe a negative voltage and the LiB pack is not overcharged within this system.

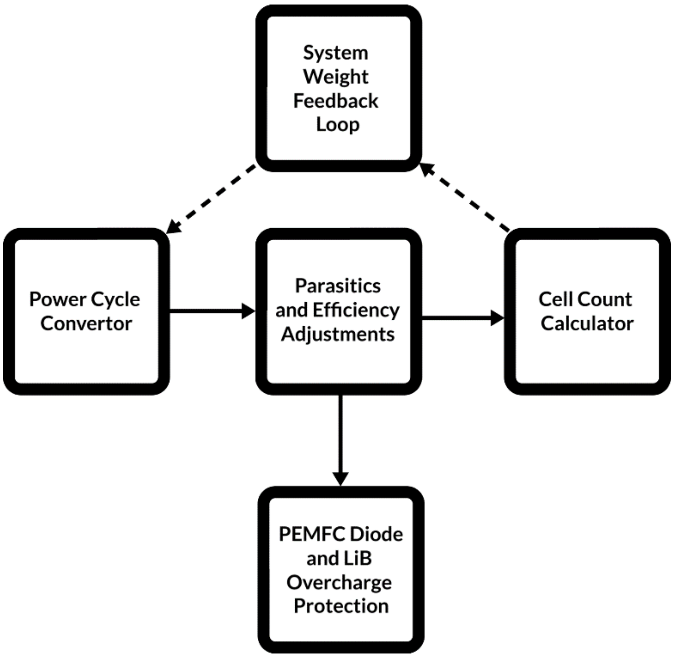

Figure 4-2: HybeMass model, general overview of subsystems.

A simplified Energy Management System (EMS), percentage split, was used for the model. This approach assumes a linear division of required power between the PEMFC stack and LiB pack. For example, the PEMFC stack may account for 80% of the required power at a given second while the LiB pack accounts for the rest 20%, suggesting a 0.8 HD. As the proposed study focuses on the mass and HD of systems, the EMS is kept simple to allow consistency and accuracy. There are more dedicated EMSs for PEMFC-battery hybrid vehicles in literature, such as equivalent consumption minimisation strategy (ECMS), fuzzy logic control (FLC), and rate limited power (RLP) control [148]. Dedicated EMS may prolong PEMFC or LiB durability; however, they may skew the HD. This is a particular challenge for approaches including RLP, which rarely use the PEMFC stack at peak efficiency [148]. The percentage split approach deployed in this work ensures that the system is performing at the HD intended.

4.5.1 Power Cycle Converter Subsystem

The Power Cycle Converter Subsystem revolves around the drive cycle power estimation technique outlined in the Drive Cycle to Power Cycle Conversion subsection. Three types of vehicles were modelled using the HybeMass model: an LDV, Class 8 HGV (GVM > 15,000 kg), and a bus. The parameters used for the LDV, HGV, and bus scenarios are presented in Table 4-1 with each vehicle scenario requiring specific inputs. Where possible, parameters from the fewest number of manufacturers possible have been chosen. Given the aim of the model to minimise the cell count, only the chassis and vehicle dynamic parameters were needed to be obtained from manufacturer specification sheets. The parameters were selected as close to the 2015 Nissan Leaf (chassis and vehicle dynamics parameters) and 2017 Toyota Mirai (hydrogen tank size and mass of hydrogen) for LDVs, and the Tesla Semi (chassis and vehicle dynamics parameters) for HGVs. The bus parameters were selected based on parameters estimated by Yang et. al. [149], with the engine mass subtracted to provide input for the chassis mass. The stored hydrogen mass for the HGV and bus is taken from previous commercially available vehicles of the same scenario, namely the Toyota Mirai and Hyundai Xcient Class 8 HGV or from previous literature analysing the same type of vehicle, for example, the bus's hydrogen mass (mH_2) of 11 kg [150]. Where commercial data was available, i.e. for LDVs, the hydrogen tank's mass (m_{tank}) was obtained from manufacturers' data sheets. The mass of hydrogen tanks for HGVs and buses is rarely published in data sheets as very few commercially available models exist. In this case, the gravimetric capacity (wt %) targets outlined by the Department of Energy (DOE) were used to calculate the tank's mass from the hydrogen mass. The DOE estimates a target of 5.5 wt% for automotive-grade hydrogen storage for 2025 [151]. Therefore, when calculated using the estimated hydrogen requirement of 35 kg and 11 kg for the HGV and bus, respectively, the mass of each tank was found to be 636 kg and 200 kg, respectively. Due to the early stage of deployment of FCHEVs, it is difficult to incorporate specifics regarding the hydrogen tank, especially in how much the weight of the tank would change between different hybrid degrees. For future work, a ratio between the different hybrid degrees could be implemented for the tank weight estimation. When running the model, a MATLAB setup file is to be executed before running the Simulink model to initialise the aforementioned parameters.

Table 4-1: Vehicle mass and dynamic parameters for LDV, HGV, and bus scenarios [149], [150], [151], [152], [153], [154], [155], [156], [157], [158].

Parameters	Vehicle Type	Description	Value
C_d	LDV	Drag coefficient	0.28
A	LDV	Frontal area (m^2)	2.27
GVM	LDV	Gross vehicle mass (kg)	1780
m_{tank}	LDV	Mass of Hydrogen tank (kg)	87.5
m_{H2}	LDV	Mass of Hydrogen contained (kg)	5
m_{batt}	LDV	Mass of battery in commercial vehicle (kg)	151
C_d	HGV	Drag coefficient	0.36
A	HGV	Frontal area (m^2)	9

GVM	HGV	Gross vehicle mass (kg)	37195
m_{tank}	HGV	Mass of Hydrogen tank (kg)	636
m_{H2}	HGV	Mass of Hydrogen contained (kg)	35
m_{batt}	HGV	Mass of battery in commercial vehicle (kg)	2293
Cd	Bus	Drag coefficient	0.65
A	Bus	Frontal area (m^2)	7.78
GVM	Bus	Gross vehicle mass (kg)	17600
m_{tank}	Bus	Mass of Hydrogen tank (kg)	200
m_{H2}	Bus	Mass of Hydrogen contained (kg)	11
m_{engine}	Bus	Mass of engine in commercial vehicle (kg)	1093

Automotive-grade commercial PEMFCs and LiBs were chosen to propel the vehicle in the MATLAB model. A commercial PEMFC stack from a 2017 Toyota Mirai was used to characterise the fuel cell in the model. The primary design parameter used in the sizing model was the maximum power of a cell, which, while not provided by the manufacturer's datasheets can be estimated from the maximum power of the stack and number of cells which form the stack (128 kW and 370 cells respectively) suggesting the maximum cell power is 346 W or 1.46 W cm^{-2} (237 cm^{-2} active area) [153], [154].

For the LiB proportion of the powertrain, the LG M50 cylindrical 21700s were chosen. The specifications of the cell were outlined in Table 3-6 in the previous sections. A maximum continuous discharge power of 20 W (1C discharge) was estimated by the authors from cycling and characterising the cell via a Maccor battery cycler, and a maximum charging power of 12 W was estimated based on the manufacturer's specification sheets [141].

Cell operating power is another degree of freedom that can drastically affect the mass of an FCHEV. The Toyota Mirai and LG M50 cells can either run at maximum power or a nominal power to fulfil the power requirements of the vehicle. Here, we defined a nominal operating power to be half of the maximum power of the cells, which results in 173 W and 10 W for the Toyota Mirai PEMFC and M50, respectively. The maximum power of both the fuel cell stack and battery pack are unlikely to be used due to the accelerated degradation associated with this decision, however in this scenario the pack mass will be minimised. When running at a nominal power, the stack and pack mass naturally increases, however, there is a corresponding improvement in system durability. The selection of the operating condition is a decision driven by a range of factors including cost, mass, and lifetime, so to assess a range of considerations, four conditions were explored: maximum PEMFC power, maximum battery power (MPML), maximum PEMFC power, nominal battery power (MPNL), nominal PEMFC power, maximum battery power (NPML), and nominal PEMFC power, nominal battery power (NPNL) as outlined in Table 4-2. In the MPML scenario for LDVs, the power required to support the vehicle is around 62 kW. In the NPML for LDVs, the total required power to support the vehicle is 66 kW. It is assumed that the PEMFC paired with the LiB can only support 66 kW due to the PEMFC operating at nominal power, but in realistic vehicle engineering scenarios, the PEMFC can still have the 'potential' to produce more power or operate at its maximum power. If the PEMFCs were to operate at maximum power in the NPML configuration, the maximum vehicle output power would equate to 119 kW, which is similar to that of a second-generation Toyota Mirai, which produces 128 kW of power from the fuel cell stack [153].

Table 4-2: Operational terminology and maximum power output of PEMFC and LiB cells.

Operation Terminology	PEMFC Maximum Power (W)	LiB Maximum Power (W)
MPML	20	20
MPNL	20	10
NPML	10	20
NPNL	10	10

To accurately reflect the power estimation in each scenario it is important to consider parasitic losses and auxiliary power draw of vehicles, including the wider fuel cell balance-of-plant (BoP) and battery pack components, infotainment, and climate control systems. The PEMFC and LiB BoP and parasitic components are estimated using a gravimetric cell-to-pack ratio (GCTP) approach. The GCTP is a ratio commonly used by the battery and BEV industry to account for the extra mass the parasitic components may add. The GCTP ratio factors in components such as battery management systems (BMS), thermal management systems (TMS), metal cases, cabling, and beams [18]. Different manufacturers have different estimates for GCTP, a GCTP of 0.64 is used for this analysis, which is the estimate for a 2017 Tesla Model 3 [18]. While the GCTP is a well-defined and understood parameter in BEV's the equivalent, gravimetric cell to stack ratio (GCTS), for fuel cell systems have not widely been reported yet. Here, this was estimated from data available from a Toyota Mirai. It has been reported that a single cell in the Mirai has a mass of 102 g [159] with the full fuel cell system weighing 52 kg, with respect to specification sheets published by Toyota [68]. From this we can estimate an approximate GCTS for the Toyota Mirai system of 0.65. This does not include the mass of the hydrogen tank for fuel supply as this is incorporated at later stages of the model.

Table 4-14 shows the schematics of the power cycle converter subsystem of the HybeMass model. $\mathrm{F_a}$, $\mathrm{F_r}$, and $\mathrm{F_i}$ are calculated separately using Equations (1) to (3). The forces are each multiplied by the instantaneous velocity to determine the power required. The power values are then totalled to obtain the required power curve. The subsystem's computed results were then provided to the parasitics and efficiency adjustments subsystem, discussed in more detail in the Parasitics and Efficiency Adjustments subsection.

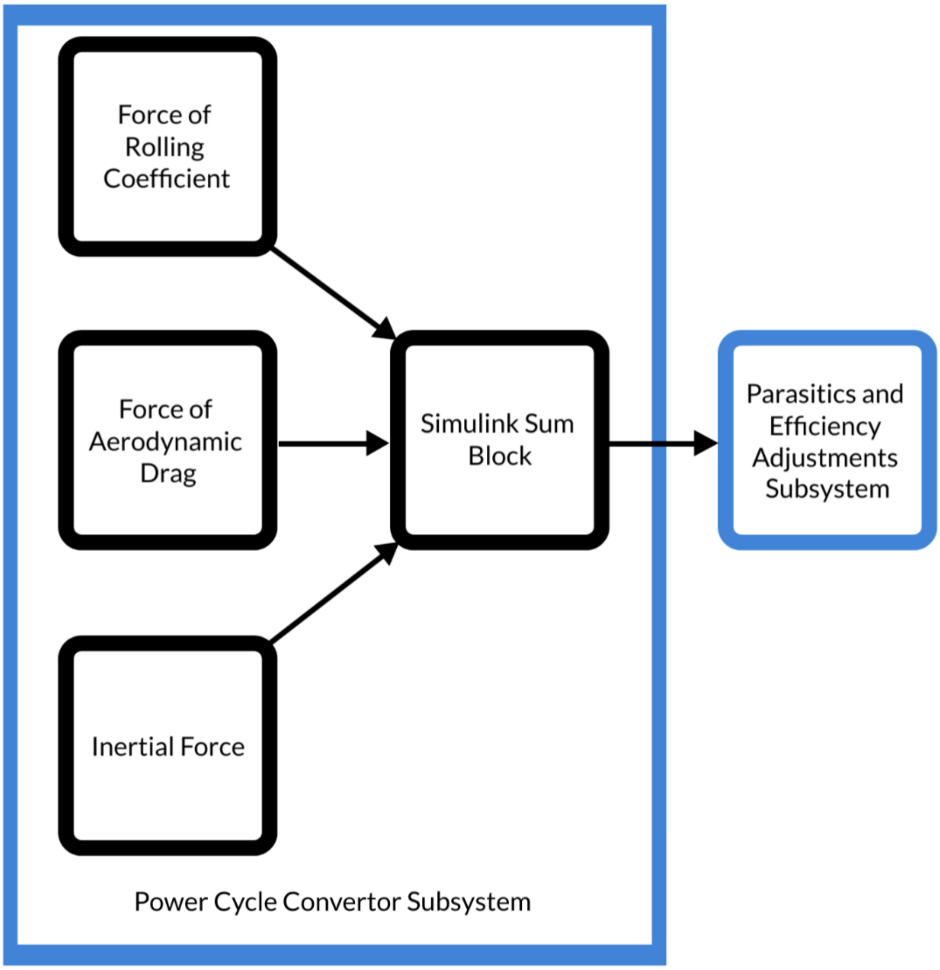

Figure 4-3: Model overview of power cycle convertor subsystem. This subsystem converts a drive cycle to a power cycle to determine the maximum required power of the proposed vehicle.

4.5.2 System Mass Feedback Loop

The system mass feedback loop which has been developed for this model enables the optimal hybridised configuration for the vehicle, minimising the mass of the final system. Firstly, the required power can be defined as purely tractive power. The analysis can be further in depth as per simulation and design requirements. The tractive power required should equal to the total power the PEMFC stack and LiB pack can produce. A stack and pack is defined as the product of the power of a single PEMFC or LiB multiplied by the total number of PEMFC and LiB cells in the system, this equation is shown in Equation (6) below.

$$\mathrm{P_{PEMFC} \times N_{PEMFC} + P_{LiB_{cell}} \times N_{LiB_{cell}} = P_{req}}$$

(4-9)

where $\mathrm{P_{PEMFC}}$ and $\mathrm{P_{LiB_{cell}}}$ are the power output of a single PEMFC or LiB cell, respectively, this power can be rated at nominal or maximum (or in between). $\mathrm{N_{PEMFC}}$ and $\mathrm{N_{LiB_{cell}}}$ is the number of PEMFCs and LiB cells, respectively. $\mathrm{P_{req}}$ is the required power.

If only accounting for tractive power ($\mathrm{P_{tractive}}$), the tractive power can be calculated using the power estimation method described in Drive Cycle to Power Cycle Conversion subsection. The overall equation is shown in Equation (4-10).

$$\mathrm{P_{tractive} = F_{tot} \times v = (F_a + F_r + F_i) \times v = (\frac{1}{2}\rho c_d A v^2 + mgc_{rr}\cos(\theta) + ma) \times v}$$

(4-10)

The singular PEMFC and LiB cells can operate at nominal or maximum power, as explained in the Power Cycle Converter System subsection. The mass of the vehicle can be broken down into the mass of the vehicle's body (no power source components), $\mathrm{m_{v_{body}}}$, and the mass of the power sources, in this case, the PEMFC stack and LiB pack, the mass of the stack and pack can be calculated as the number of cells ($\mathrm{N_{PEMFC}}$, $\mathrm{N_{LiB_{cell}}}$) multiplied by a singular cell mass ($\mathrm{m_{PEMFC}}$, $\mathrm{m_{LiB_{cell}}}$). $\mathrm{N_{PEMFC}}$ and $\mathrm{N_{LiB_{cell}}}$ are the parameters to be solved by these equations. The full equation is shown in Equation (4-11), which acts as the basis of the system mass feedback loop equation.

$$\begin{aligned}&\mathrm{P_{PEMFC} \times N_{PEMFC} + P_{LiB_{cell}} \times N_{LiB_{cell}}}\\ &= \frac{1}{2}\mathrm{\rho c_d A v_{P_{max}}^3 + \left(m_{v\_body} + N_{PEMFC} m_{PEMFC} + N_{LiB_{cell}} m_{LiB_{cell}}\right) g c_{rr} v_{P_{max}}}\\ &+ \mathrm{\left(m_{v_{body}} + N_{PEMFC} m_{PEMFC} + N_{LiB_{cell}} m_{LiB_{cell}}\right) a_{P_{max}} v_{P_{max}}}\end{aligned}$$

(4-11)

Where $\mathrm{a_{P_{max}}}$ and $\mathrm{v_{P_{max}}}$ is the acceleration and speed at the maximum required power time step, respectively.

4.5.3 Parasitics and Efficiency Adjustments

The aforementioned equations in the System Mass Feedback Loop subsection only account for the tractive power of the vehicle and do not consider additional, parasitic mass introduced by the PEMFC and LiB systems. As discussed previously, additional components including cables, control and thermal management systems and housing/endplates are needed for the PEMFC stack and LiB pack to function properly, as mentioned previously, GCTP and GCTS values are used to estimate the additional mass of the parasitic components. For a more detailed analysis, the system mass feedback equations should account for the extra power required from the parasitic mass ($\mathrm{P_{m_{parasitics}}}$), shown in Equation (4-12).

$$\mathrm{P_{PEMFC} \times N_{PEMFC} + P_{LiB_{cell}} \times N_{LiB_{cell}} = P_{tractive} + P_{m_{parasitics}}} \tag{4-12}$$

By adding GCTP ratios to Equation (4-11), a new source power equating to required power equation is shown in Equation (4-13). In this equation, $\mathrm{P_{req}}$ is now added with the parasitics mass, accounted for by GCTP and GCTS ratios. The GCTS and GCTP ratios are accounted for separately in $\mathrm{m_{PEMFC}}$ and $\mathrm{m_{LiB_{cell}}}$ fields. For simplicity, the terms ‘$\mathrm{\frac{N_{PEMFC}m_{PEMFC}}{GCTS_{PEMFC}}}$’ and ‘$\mathrm{\frac{N_{LiB_{cell}}m_{LiB_{cell}}}{GCTP_{LiB}}}$’ will be called $\mathrm{m_{stack}}$ and $\mathrm{m_{pack}}$ in further mentioned equations, respectively.

$$\begin{aligned} &\mathrm{P_{PEMFC} \times N_{PEMFC} + P_{LiB_{cell}} \times N_{LiB_{cell}}} \\ &= \frac{1}{2}\mathrm{\rho c_d A v_{P_{max}}^3} + \left(\mathrm{m_{v_{body}}} + \frac{\mathrm{N_{PEMFC}m_{PEMFC}}}{\mathrm{GCTS_{PEMFC}}} + \frac{\mathrm{N_{LiB_{cell}}m_{LiB_{cell}}}}{\mathrm{GCTP_{LiB}}}\right)\mathrm{g c_{rr} v_{P_{max}}} \\ &+ \left(\mathrm{m_{v\_body}} + \frac{\mathrm{N_{PEMFC}m_{PEMFC}}}{\mathrm{GCTS_{PEMFC}}} + \frac{\mathrm{N_{LiB_{cell}}m_{LiB_{cell}}}}{\mathrm{GCTP_{LiB}}}\right)\mathrm{a_{P_{max}} v_{P_{max}}} \end{aligned} \tag{4-13}$$

In a parallel powertrain configuration, the PEMFC stack or LiB pack’s total power should equal to the required power allocated by the HD. The HD suggests to the ratio split of the PEMFC stack or battery pack. Since HD is defined as the power of the PEMFC to the total power, the ratio split of the LiB pack can be defined as $1 - \mathrm{HD}$. The two separate equations for the PEMFC and LiB are shown in Equations (4-14) and (4-15).

$$\begin{aligned} &P_{PEMFC} \times N_{PEMFC} \\ &= \left[\frac{1}{2}\rho c_d A v_{P_{max}}^3 + \left(m_{v_{body}} + m_{stack} + m_{pack}\right) g c_{rr} v_{P_{max}} \right. \\ &\left. + \left(m_{v_{body}} + m_{stack} + m_{pack}\right) a_{P_{max}} v_{P_{max}}\right] \times HD \end{aligned}$$

(4-14)

$$\begin{aligned} &P_{LiB\_cell} \times N_{LiB\_cell} \\ &= \left[\frac{1}{2}\rho c_d A v_{P_{max}}^3 + \left(m_{v_{body}} + m_{stack} + m_{pack}\right) g c_{rr} v_{P_{max}} \right. \\ &\left. + \left(m_{v_{body}} + m_{stack} + m_{pack}\right) a_{P_{max}} v_{P_{max}}\right] \times (1 - HD) \end{aligned}$$

(4-15)

The realistic application of the equation can be improved further by factoring accessory load values (P_{acc}) and efficiency losses such as DC/DC convertor loss. The new equation for P_{req} is shown in Equation (4-16).

$$P_{PEMFC} \times N_{PEMFC} + P_{LiB_{cell}} \times N_{LiB_{cell}} = P_{tractive} + P_{m_{parasitics}} + P_{acc}$$

(4-16)

Equation (14) shows the equation used to factor in parasitics and accessory load and efficiency losses [43].

$$P_{req} = \frac{\frac{P_{tractive}}{\eta_{inv}} + P_{acc}}{\eta_{dc}}$$

(4-17)

Where η_{inv} and η_{dc} are the efficiency factors for the inverter and DC/DC converter, respectively. P_{acc} is the parasitics and accessory load power draw. In the case of the LDV, the maximum parasitic and accessory load power draw is 12.9 kW, with the breakdown of these loads shown in Table 4-3. This analysis considers the worst-case scenario of the power draw. In reality, an FCHEV LDV uses a fraction of this at any given time with an estimated average of 5 kW used in LDV applications for the parasitic and accessory loads [160]. This data is not widely available for bus and HGV scenarios, therefore in this model, the estimated power loading has been scaled to 12.5 and 20 kW, respectively, based on the mass of the vehicles. These efficiency and accessory load values make up the bulk of the parasitic and efficiency loss subsystem. The subsystem also contains a regenerative braking factor of 0.8 to adjust for charging losses [152].

Table 4-3: Breakdown and estimate of parasitic and auxiliary power draw for an FCHEV LDV, values adapted from Lawrence et al. [161]. For loads with varying power demands, the highest possible power demand is considered.

Component	Power (W)
Exterior lights	175
Headlights	125
Interior lights	64
Windshield wipers	64
Power windows	180
AC compressor	4000
Cabin heater	3000
Cooling fans	400
Cabin blower	250
Cooling pumps	180
Rear defog	150
12 V battery charging	120
PEMFC cooling pump	600
PEMFC recirculating pumps	400
Motor lube pumps	120
PEMFC blower	2000
Power steering	800
Vacuum pumps	200
Controllers, relays, and contractors	100

The total required power ($\mathrm{P_{req}}$) is now updated with parasitics and accessory power draw and efficiency factors, as shown in Equation (15).

$$P_{\mathrm{PEMFC}} \times N_{\mathrm{PEMFC}} + P_{\mathrm{LiB_{cell}}} \times N_{\mathrm{LiB_{cell}}} = P_{\mathrm{req}} = \frac{\dfrac{P_{\mathrm{tractive}} + P_{m_{\mathrm{parasitics}}}}{\eta_{\mathrm{inv}}} + P_{\mathrm{acc}}}{\eta_{\mathrm{dc}}}$$

(4-18)

The final equations to obtain N_{PEMFC} and $N_{\mathrm{LiB_{cell}}}$ was updated with tractive power, power caused by the additional mass of the parasitics (BoP and battery system components), power of parasitics and auxiliary power draw, and efficiency loss factors. Equations (4-19), (4-20), and (4-21) show the updated and final versions of the goal seek equation. Equation (4-19) represents the overall power system power output, while Equations (4-20) and (4-21) represent the PEMFC stack and LiB pack power output, respectively.

$$P_{\mathrm{PEMFC}} \times N_{\mathrm{PEMFC}} + P_{\mathrm{LiB_{cell}}} \times N_{\mathrm{LiB_{cell}}} \\ = \frac{\dfrac{\frac{1}{2}\rho c_d A v_{P_{\max}}^3 + \left(m_{v_{\mathrm{body}}} + m_{\mathrm{stack}} + m_{\mathrm{pack}}\right) g c_{rr} v_{P_{\max}} + \left(m_{v_{\mathrm{body}}} + m_{\mathrm{stack}} + m_{\mathrm{pack}}\right) a_{P_{\max}} v_{P_{\max}}}{\eta_{\mathrm{inv}}} + P_{\mathrm{acc}}}{\eta_{\mathrm{dc}}}$$

(4-19)

$$P_{\mathrm{PEMFC}} \times N_{\mathrm{PEMFC}} \\ = \frac{\dfrac{\left[\frac{1}{2}\rho c_d A v_{P_{\max}}^3 + \left(m_{v_{\mathrm{body}}} + m_{\mathrm{stack}} + m_{\mathrm{pack}}\right) g c_{rr} v_{P_{\max}} + \left(m_{v_{\mathrm{body}}} + m_{\mathrm{stack}} + m_{\mathrm{pack}}\right) a_{P_{\max}} v_{P_{\max}}\right]}{\eta_{\mathrm{inv}}} + P_{\mathrm{acc}}}{\eta_{\mathrm{dc}}} \\ \times \mathrm{HD}$$

(4-20)

$$P_{\mathrm{LiB\_cell}} \times N_{\mathrm{LiB\_cell}} \\ = \frac{\dfrac{\left[\frac{1}{2}\rho c_d A v_{P_{\max}}^3 + \left(m_{v_{\mathrm{body}}} + m_{\mathrm{stack}} + m_{\mathrm{pack}}\right) g c_{rr} v_{P_{\max}} + \left(m_{v_{\mathrm{body}}} + m_{\mathrm{stack}} + m_{\mathrm{pack}}\right) a_{P_{\max}} v_{P_{\max}}\right]}{\eta_{\mathrm{inv}}} + P_{\mathrm{acc}}}{\eta_{\mathrm{dc}}} \\ \times (1 - \mathrm{HD})$$

(4-21)

The above equations satisfy for a parallel hybrid powertrain scenario involving hybrid degree. The equations can be modified to fit the purpose of a fuel cell range extender (FCREx) electric vehicle. In this type of vehicle powertrain, the fuel cell only accounts for the average power and stays constant; this average power can be calculated using the equation below:

$$P_{\mathrm{PEMFC}} \times N_{\mathrm{PEMFC}} = \frac{1}{t_{dc}} \sum_{i=1}^{t_{dc}} P_i$$

(4-22)

Where t_{dc} is the duration of the drive cycle in seconds, and P_i is the power required at a specific second of the drive cycle. The new equations to represent the PEMFC stack and LiB pack accounted power are shown in Equations (*4-23*) and (*4-24*), respectively. The LiB pack accounts for the remainder of the total required power (P_{req}) not accounted for by the PEMFC stack.

$$P_{PEMFC} \times N_{PEMFC} = \frac{1}{t_{dc}} \sum_{i=1}^{t_{dc}} \frac{\frac{\left[\frac{1}{2}\rho c_d A v_i^3 + \left(m_{v_{body}} + m_{stack} + m_{pack}\right) g c_{rr} v_i + \left(m_{v_{body}} + m_{stack} + m_{pack}\right) a_{P_{max}} v_i\right]}{\eta_{inv}} + P_{acc}}{\eta_{dc}} \tag{4-23}$$

Where v_i is the speed at a given second of the drive cycle.

$$P_{LiB_{cell}} \times N_{LiB_{cell}} = \frac{\frac{\left[\frac{1}{2}\rho c_d A v_{P_{max}}^3 + \left(m_{v_{body}} + m_{stack} + m_{pack}\right) g c_{rr} v_{P_{max}} + \left(m_{v_{body}} + m_{stack} + m_{pack}\right) a_{P_{max}} v_{P_{max}}\right]}{\eta_{inv}} + P_{acc}}{\eta_{dc}} - \frac{1}{t_{dc}} \sum_{i=1}^{t_{dc}} \frac{\frac{\left[\frac{1}{2}\rho c_d A v_i^3 + \left(m_{v_{body}} + m_{stack} + m_{pack}\right) g c_{rr} v_i + \left(m_{v_{body}} + m_{stack} + m_{pack}\right) a_{P_{max}} v_i\right]}{\eta_{inv}} + P_{acc}}{\eta_{dc}} \tag{4-24}$$

4.5.4 Cell Count Calculator and its Synergy with Other Subsystems

The cell count subsystem is the constant update and display of the cell count calculated. *Figure 4-4* shows the detailed connections and layout of the system mass feedback loop and cell count calculator subsystem, as well as its synergy with the power cycle converter subsystem and parasitics and efficiency adjustments subsystem. Two MATLAB function blocks are used to input Equations 17 and 18. The solver functions are connected to these two equations to obtain a result for N_{PEMFC} and $N_{LiB_{cell}}$. The N_{PEMFC} and $N_{LiB_{cell}}$ values are constantly re-uploaded into the system mass feedback loop for recalculation of the power requirements and newly updated cell count. Every time N_{PEMFC} and $N_{LiB_{cell}}$ values update, the power requirements are directly affected due to the change in power systems mass, allowing a new power cycle to be obtained in the power cycle converter subsystem. The parasitics and efficiency subsystem applies factors to the new power cycle, and the max power considering GCTS and GCTP factors, parasitics power draw, and efficiency losses are used to size the re-occurring PEMFC and LiB cell count (N_{PEMFC} and $N_{LiB_{cell}}$), This constant is updated constantly with the new maximum required power from a 'To Workspace' block found in the power cycle converter subsystem. Forming a loop of newly calculated required power accounting for the additional mass of the newly added PEMFC and LiB cells, realising the system mass feedback loop feature. After $\mathrm{N_{PEMFC}}$ and $\mathrm{N_{LiB_{cell}}}$ are obtained, the mass of the PEMFC stack and battery stack can be obtained by multiplying the result by the destined singular cell mass; a GCTS or GCTP factor is then applied to account for parasitics mass. For the PEMFC stack counterpart, a pre-determined hydrogen tank mass can be added to the overall BoP and the overall power systems mass.

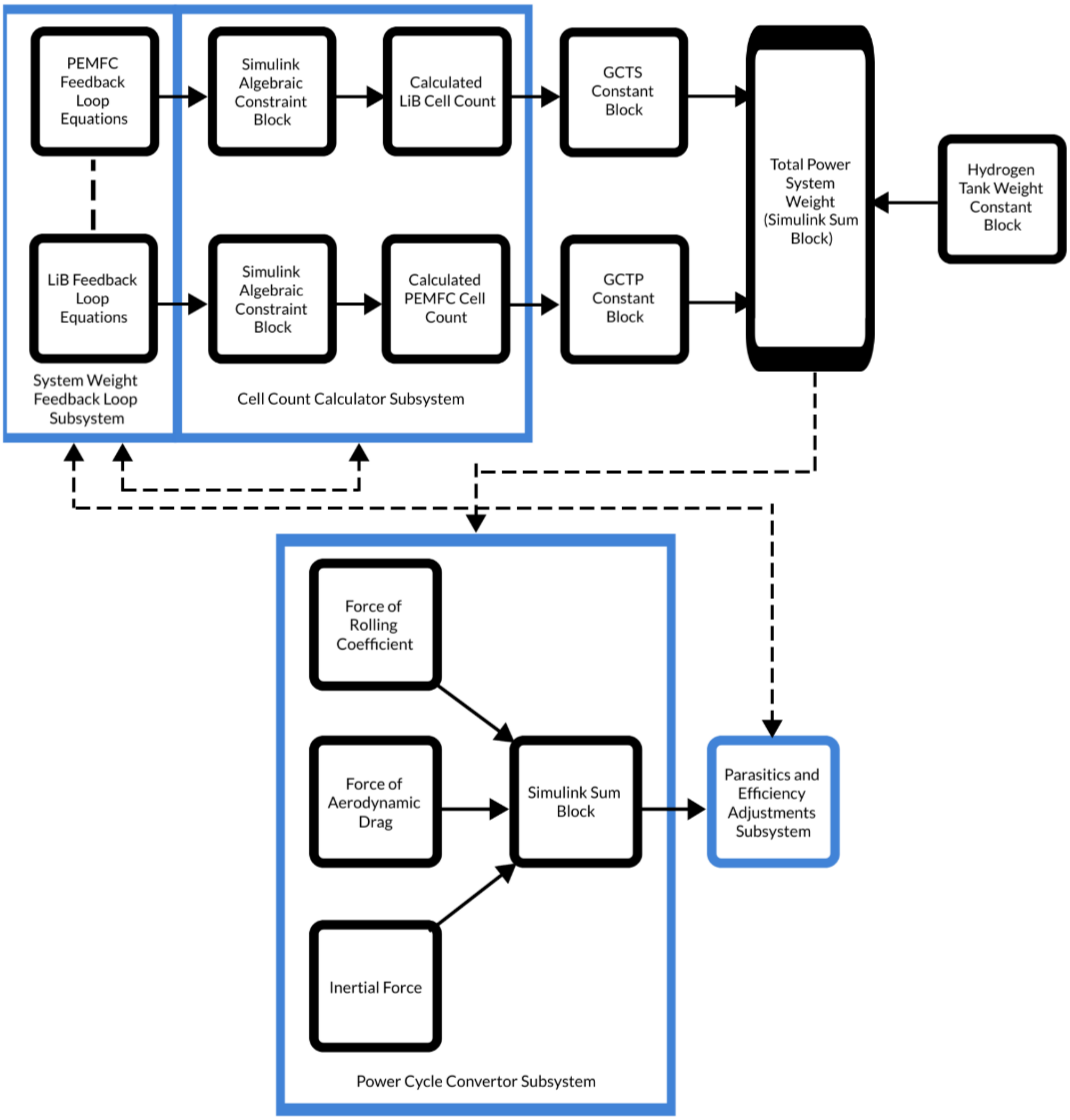

Figure 4-4: Detailed block layout of system mass feedback loop subsystem.

4.5.5 PEMFC Diode and LiB Overcharge Protection Subsystem

The diodes and overcharge protection subsystem are useful for exporting separate power cycles for the PEMFC stack and LiB pack. The exported power cycles can be used for further analysis such as bench or hardware-in-the-loop drive cycle testing. However, even with the pre-determined percentage split or EMS, there are some modifications that has to be applied to the power cycle to prevent charging the PEMFC stack or overcharging the LiB pack. The PEMFC stack power profile should never have a required power less than 0 W, while the LiB pack should not have a regen more than $\mathrm{N_{LiB\_cell}}$ multiplied by the maximum charge power a M50 cell can take. Due to the power-based approach of the MATLAB modelling process, no state-of-charge estimations and state-of-charge-related regenerative braking limits were implemented into the model. Switches are implemented within the model to act as diodes and overcharge protection to prevent these safety issues. This subsystem is useful for exporting power profiles for the PEMFC stack and LiB pack so that these devices can be used for physical testing such as facilitating hardware-in-the-loop bench testing based on drive cycles.

4.6 Putting it All Together – Case Study of Creating PEMFC Testing and Battery Cycling Cell Duty Profiles for an HGV Powertrain

Together with the aforementioned HybeMass model capabilities and the power cycle downscaling technique, examples of extracted cell duty profiles are shown using the HGV scenario as a reference. At first, required vehicular power profiles with PEMFC stack and LiB pack power divisions are obtained from the HybeMass model, shown in Figure 4-5. This figure shows both the parallel powertrain, shown in Figure (a), using a 0.8 HD split and the FCREx powertrain, shown in Figure (b). In the parallel example (a), a visible 0.8 HD split between the PEMFC stack and LiB pack power can be spotted.

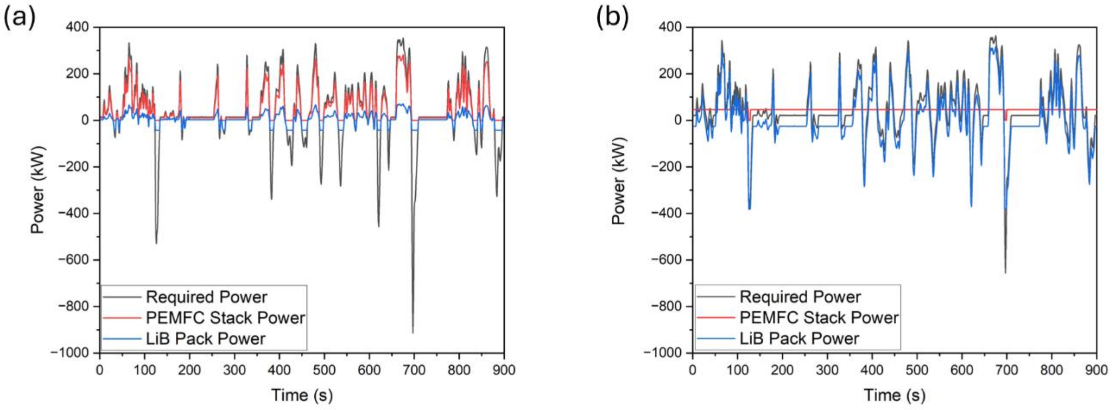

Figure 4-5: Vehicular power profiles for the HGV powertrain, which shows the required power, PEMFC stack power, and LiB pack power. Both the parallel and FCREx powertrain configurations are shown. (a) Parallel architecture. (b) FCREx architecture.

These profiles are useful for visualising how the theoretical vehicle in mind is operating in terms of power in kilowatts but do not provide a reference for bench-testing individual cells in terms of Watts. However, by following the procedures outlined previously, individual cell power profiles can then be obtained, for both the PEMFC and LiB cells, an example using MPML configuration shown in Figure 4-6. It should be noted the many parts of the PEMFC and LiB cell power in Figure (a) overlap, appearing that only LiB Cell Power (red) is displayed. In the parallel profile at the cell level, the 0.8 HD split can no longer be visually identified, as the vehicular profile was normalised into individual cells operating at a maximum cell operating power. By combining hundreds and thousands of these cells into a PEMFC stack or battery pack, the full vehicular profile can then be accounted for in a theoretical full-sized hybrid vehicle. A limitation of this experimental method is that it is assumed that all cells in this theoretical PEMFC stack or LiB pack would 'behave' in a similar way in terms of degradation. A second limitation is that it was not considered whether the cells were in series or parallel layouts. In this subsection, the researcher wants to emphasise the key differences between a vehicular profile and a cell profile, and that hybrid degrees can only be visualised at a stack or pack level, as well as showing a 'case study' of working out the individual cell profile.

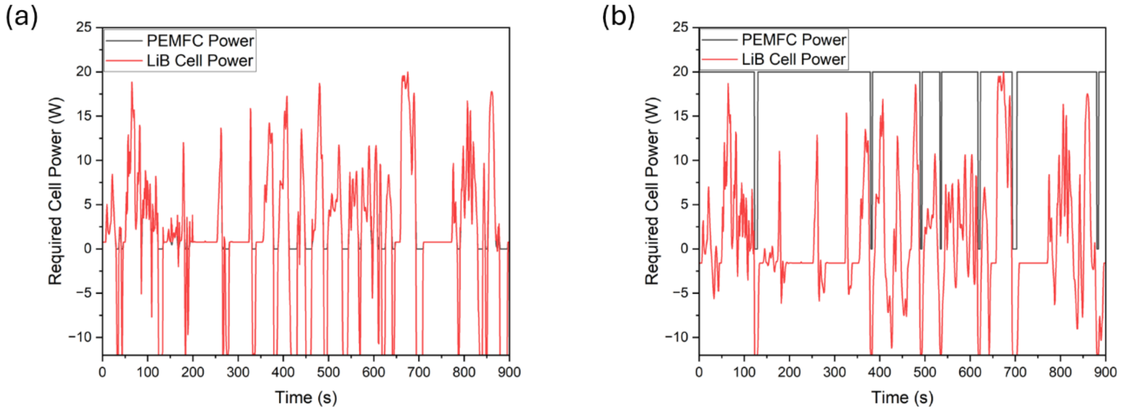

Figure 4-6: Example cell power profiles for the HGV powertrain (MPML configuration), which shows both the PEMFC and LiB operating at a cell-level. (a) Parallel architecture. (b) FCREx architecture.

4.7 PEMFC and LiB Drive Cycle Endurance Testing for Parallel Architecture

This section discusses the results of drive cycle endurance testing done on purely parallel architecture scenarios; FCREx powertrains will be located in the next section, instead. PEMFC degradation is discussed first, then LiB degradation. PEMFC degradation includes analysis such as polarisation and power curves, CV and ECSA, LSV, and EIS. LiB degradation includes analysis such as capacity fade, EIS, and X-ray CT.

4.7.1 Parallel LDV

For the LDV powertrain results, the MPML, MPNL, NPML, and NPNL scenarios will discussed in conjunction with each other. The PEMFC results will be discussed first, which then comes the LiB results. Figure 4-7 shows the PEMFC power cycle profiles at cell level for the different cell operating scenarios tested, while Figure 4-8 shows the corresponding LiB power profiles. In these two figures, negative power suggests that power is drawn from the source (e.g. a discharge state for LiBs), and positive power suggests that the power source is being charged. PEMFCs would never experience a positive power due to the inability to 'charge PEMFCs.'

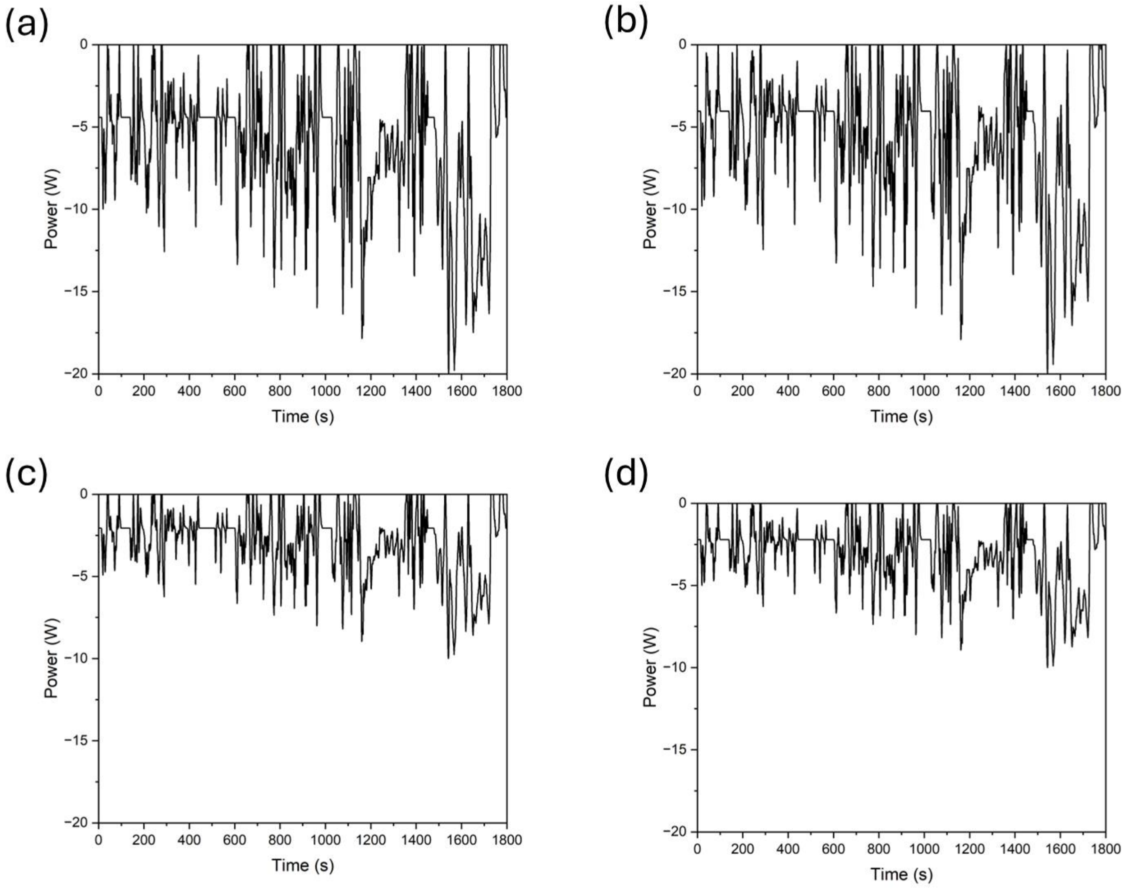

Figure 4-7: PEMFC power cycle profiles of different cell operating power scenarios for parallel LDVs. (a) MPML (b) MPNL (c) NPML (d) NPNL

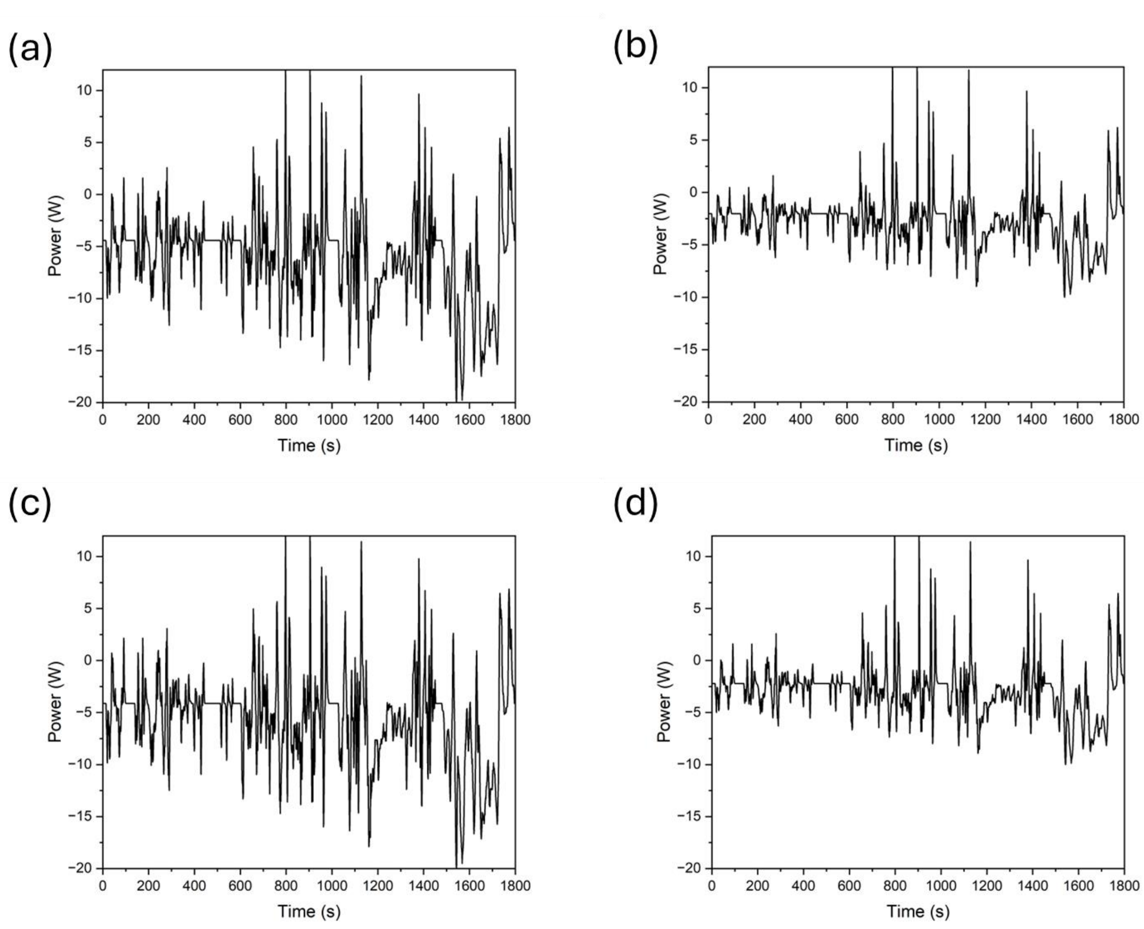

Figure 4-8: LiB power cycle profiles of different cell operating power scenarios for parallel LDVs. (a) MPML (b) MPNL (c) NPML (d) NPNL

4.7.1.1 PEMFC - Polarisation Curves

To ensure the quality of the MEAs manufactured in-lab, a BoL polarisation and power curve is usually collected before the start of any drive cycle endurance testing. The main three criteria focused on were that OCV was more than 0.9 V, the current density at 0.3 V was more than 1750 mA cm^{-2}, and maximum power could reach more than 20 W. If these criteria weren't met, the MEA was discarded. Because each MEA is hand-made, the performance may vary; it is important to focus on the delta polarisation performance decrease between the different configurations rather than the absolute.

Figure 4-9 contains double Y-axis graphs that show the polarisation and power curve comparisons between different operating configurations at 0.8 HD. For the MPML configuration, shown in Figure 3-9(a), at 600 mA cm^{-2}, the voltage decreased from an initial value of 0.77 V to 0.77 V, 0.75 V, 0,75 V and 0.7 V, after 200, 400, 600 and 662 WLTP Class 3 cycles, respectively, with a total power decrease of 13% after 662 cycles. At 1,200 mA cm^{-2}, the voltage decreased from an initial value of 0.70 V to 0.67 V, 0.65 V, 0.65 V and 0.55 V, after 200, 400, 600 and 662 cycles, respectively, with a power decrease of 20% after 662 cycles. For the MPNL configuration, shown in Figure 3-9(b), at 600 mA cm^{-2}, the voltage decreased from an initial value of 0.75 V to 0.72 V, 0.7 V, 0.67 V and 0.62 V, after 200, 400, 600 and 662 WLTP Class 3 cycles, respectively, with a total power decrease of 18% after 662 cycles. At 1,200 mA cm^{-2}, the voltage decreased from an initial value of 0.67 V to 0.6 V, 0.57 V, 0.55 V and 0.4 V, after 200, 400, 600 and 662 cycles, respectively, with a power decrease of 37% after 662 cycles. It can be seen that at EoT, 0.4V at 1200 mA cm^{-2} is already in the mass transfer region, which is considered a non-desirable operational region for PEMFCs. For the NPML configuration, shown in Figure 3-9(c), at 600 mA cm^{-2}, the voltage decreased from an initial value of 0.77 V to 0.75 V, 0.75 V, 0.75 V and 0.75 V, after 200, 400, 600 and 662 WLTP Class 3 cycles, respectively, with a total power decrease of 12% after 662 cycles. At 1,200 mA cm^{-2}, the voltage decreased from an initial value of 0.7 V to 0.65 V, 0.65 V, 0.62 V and 0.62 V, after 200, 400, 600 and 662 cycles, respectively, with a power decrease of 3% after 662 cycles. For the NPNL configuration, shown in Figure 3-9(d), at 600 mA cm^{-2}, the voltage decreased from an initial value of 0.75 V to 0.72 V, 0.66 V, 0.65 V and 0.65 V, after 200, 400, 600 and 662 WLTP Class 3 cycles, respectively, with a total power decrease of 15% after 662 cycles. At 1,200 mA cm^{-2}, the voltage decreased from an initial value of 0.65 V to 0.57 V, 0.43 V, 0.43 V and 0.45 V, after 200, 400, 600 and 662 cycles, respectively, with a power decrease of 28% after 662 cycles. The voltage drops at 600 and 1200 mA cm^{-2} for all configurations are shown in Figure 4-10. It is evident that the PEMFC experienced the most polarisation curve degradation between the first 200 cycles. Between 400 and EoT, the performance decreased at a slower rate. For certain scenarios, such as MPNL and NPNL, the region where the PEMFC reaches its maximum power transfers from the Ohmic region to the concentration region near EoT, which is considered a non-desirable region for PEMFCS to operate at.

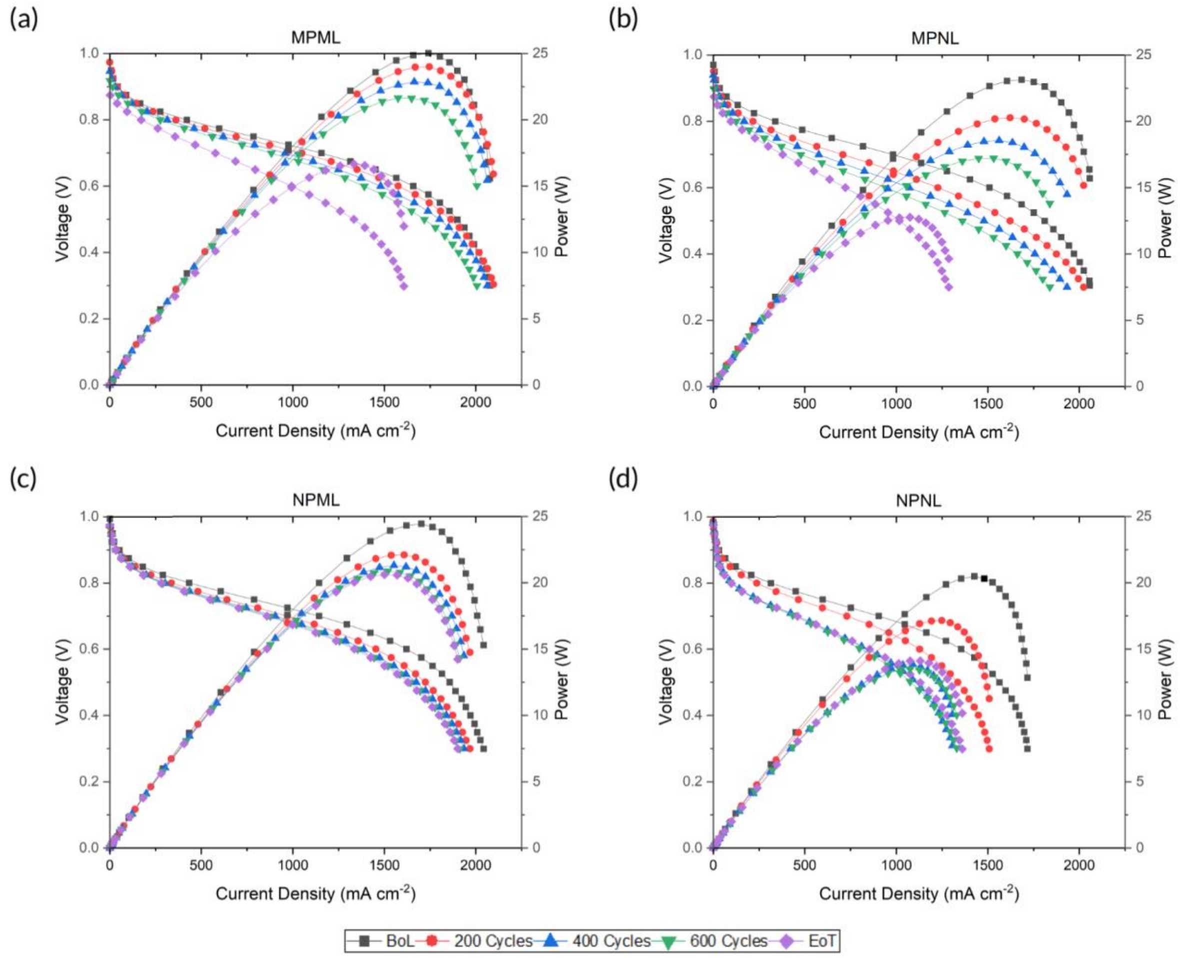

Figure 4-9: Polarisation and power curve comparison between different operating power configurations at a 0.8 HD.

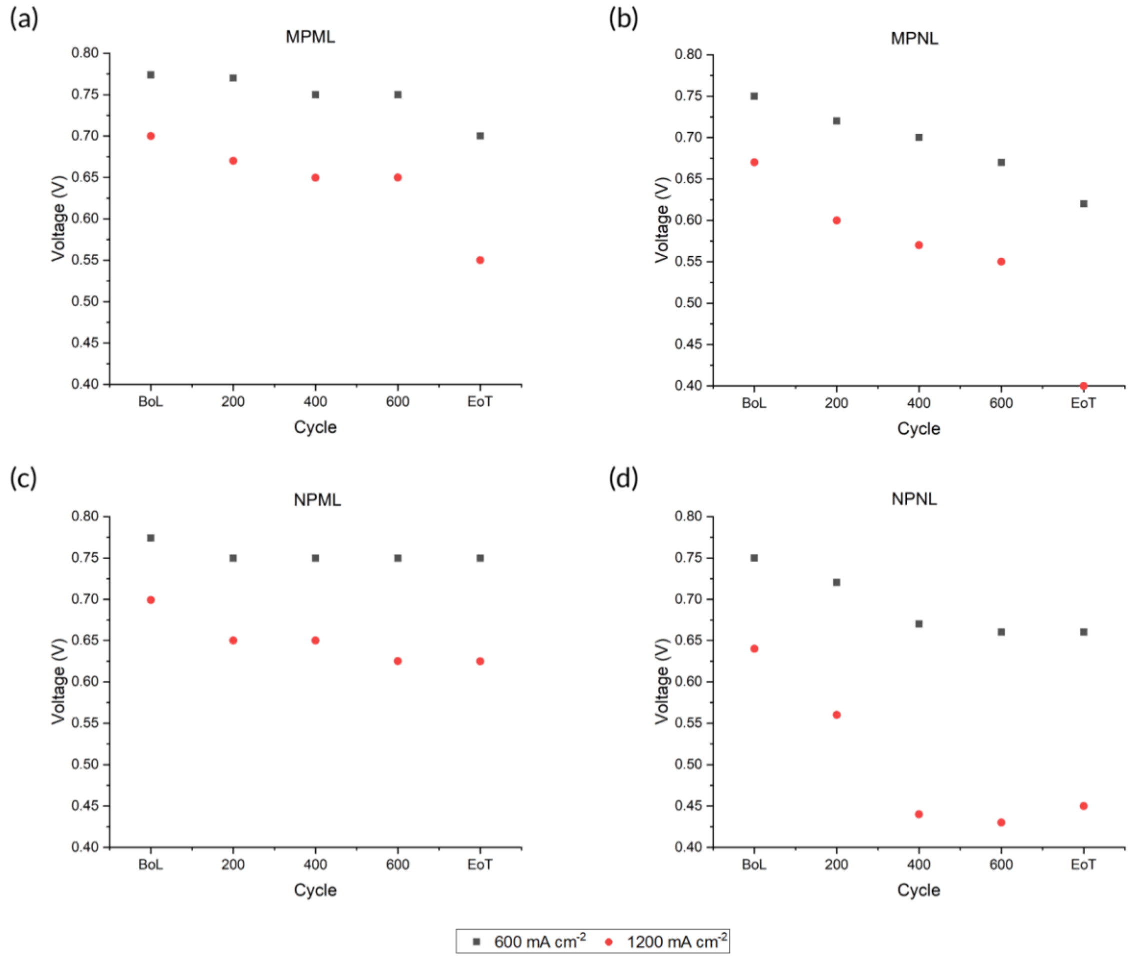

Figure 4-10: Voltage comparisons at 600 and 1200 mA cm^{-2} current densities between different operating power scenarios.

Table 4-4 outlines the voltage change in terms of percentage between BoL to EoT. In terms of voltage changes at 600 mA cm^{-2}, no drastic changes occurred between the operations of the PEMFC at a maximum or nominal condition. This suggested that more dynamic transient loadings do not cause more severe voltage drops than less dynamic transient loadings at the beginning of the charge transfer region. The maximum voltage drop for maximum operating power occurred between 600 cycles to EoT during the MPNL configuration. This is interesting because, in the nominal operating scenarios, the highest voltage drop at 600 mA cm^{-2} occurred between 200 to 400 cycles. One would expect that more dynamic transient loadings would cause more degradation earlier than less dynamic transient loadings. However, this could relate to the robustness of the MEAs made in-house. More testing and validation would be required to see if this becomes a recurring scenario.

Performance at 1200 mA cm^{-2} is important to analysis as it is typically near the end of the charge transfer region and close to the region that produces the maximum power. It can be seen that with maximum operating power setups, the voltage dropped more drastically when compared to the NPML configuration, especially between 600 cycles to EoT. However, an interesting observation was that voltage decreased by 25% for the NPNL scenario between 200 cycles to 400 cycles, which seemed quite dramatically for merely a nominal operating performance. It can suggest that the magnitude of transientness does not directly correspond to the rate of voltage drop. But then, the NPML scenario would contradict the aforementioned statement as it has less voltage drop compared to the other scenarios during both 600 and 1200 mA cm^{-2} current densities. More testing and validation are needed whether the magnitude of transientness affects the rate of voltage drop. The author has provided the tools and techniques for future analysis.

Table 4-4: Voltage percentage change between different cycles at 600 and 1200 mA cm^{-2} current densities for all operating power conditions.

Operating power	Δ Cycle	Δ Voltage at 600 mA cm^{-2} (%)	Δ Voltage at 1200 mA cm^{-2} (%)
MPML	BoL to 200	−1.3	−4.2
	200 to 400	−1.3	−3.0
	400 to 600	−1.3	0
	600 to EoT	0	−15
MPNL	BoL to 200	−4.0	−11
	200 to 400	−2.8	−5.0
	400 to 600	−4.3	−3.5
	600 to EoT	−7.5	−27
NPML	BoL to 200	−2.6	−7.1
	200 to 400	0	0
	400 to 600	0	−4.6
	600 to EoT	0	0
NPNL	BoL to 200	−4.0	−12
	200 to 400	−8.3	−25
	400 to 600	−1.5	0
	600 to EoT	0	4.7

Aside from quantifying voltage changes in a polarisation curve, power curves are also just as important in judging the performance and validity of different operating scenarios. Figure 4-11 shows the maximum power changes between the different cycles and operating power scenarios in a graphical format. For both configurations with a maximum PEMFC operating power (MPML and MPNL), the most significant power drop occurred between 600 cycles and EoT (662 cycles). It can be seen for both maximum PEMFC operating power scenarios, the maximum power dropped below 20 W at EoT, which is not feasible to cope with the maximum power demands of the theoretical vehicle. A trend is seen throughout the testing of other vehicle scenarios (HGV and bus), too. The researcher has decided to omit the MPNL scenario for future bench testing due to this reason; however, the MPML scenarios were still tested due to the potential of having the least mass compared to other operating powers. Having the least mass may be useful for a motorsport-based scenario, where having a lighter vehicle may be more important than prolonging the lifetime of the power components. The MPNL, however, is still included in mass and simulation analysis.

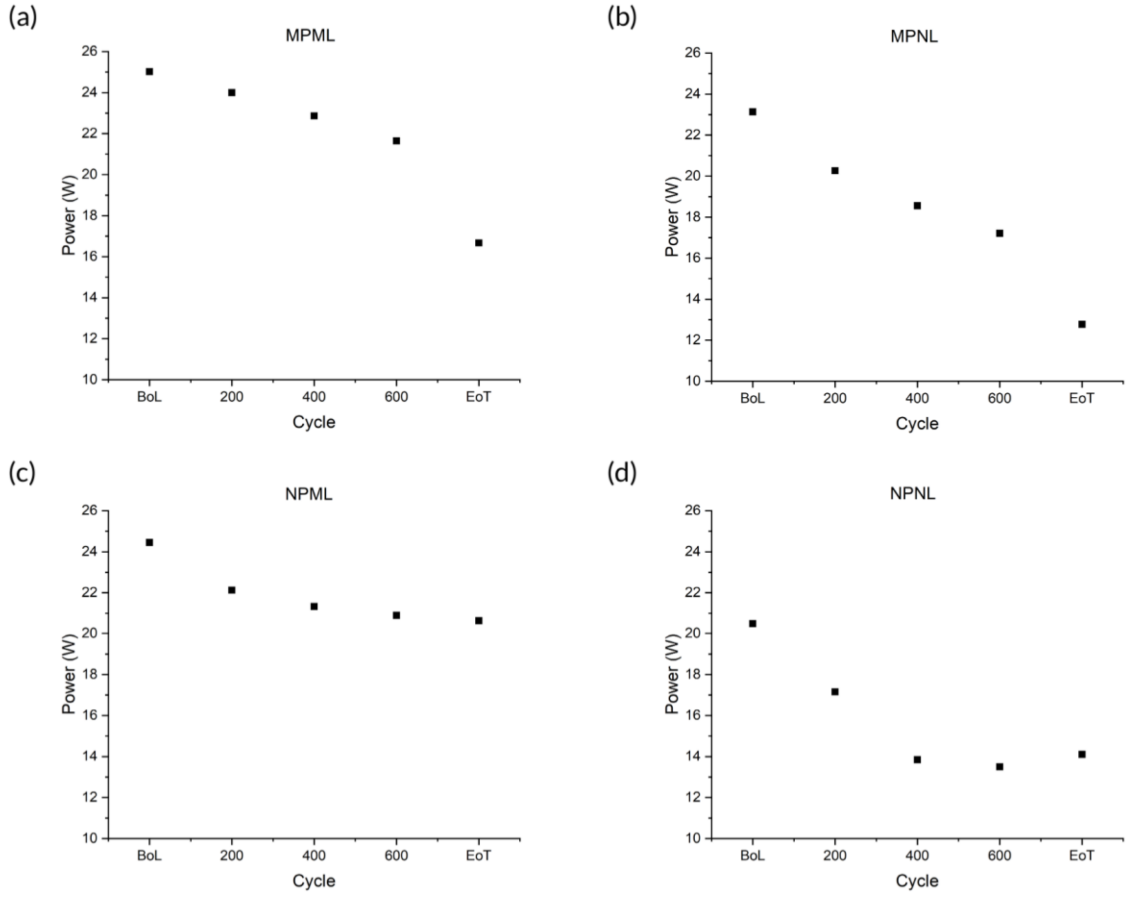

Figure 4-11: Changes in maximum power between different cycles and operating scenarios.

4.7.1.2 PEMFC - CV and ECSA

While polarisation and power curves give a general insight into the performance drops caused by degradation, CV and ECSA estimation can be used to quantify the degradation analysis for a deeper comparison between the different cell operating scenarios, especially within the activation and Ohmic regions. Figure 4-12 shows CV graph comparisons between BoL to EoT in 200-cycle increments for all cell operating scenarios; these graphs act as a visual comparison between the scenarios, ECSA drop will be discussed in later paragraphs. It can be seen visually from the hydrogen adsorption and desorption regions that the MP scenarios had the most significant aerial decrease between BoL and EoT. Out of which, the MPML scenario had the most significant initial ECSA decrease from BoL to 200 cycles.

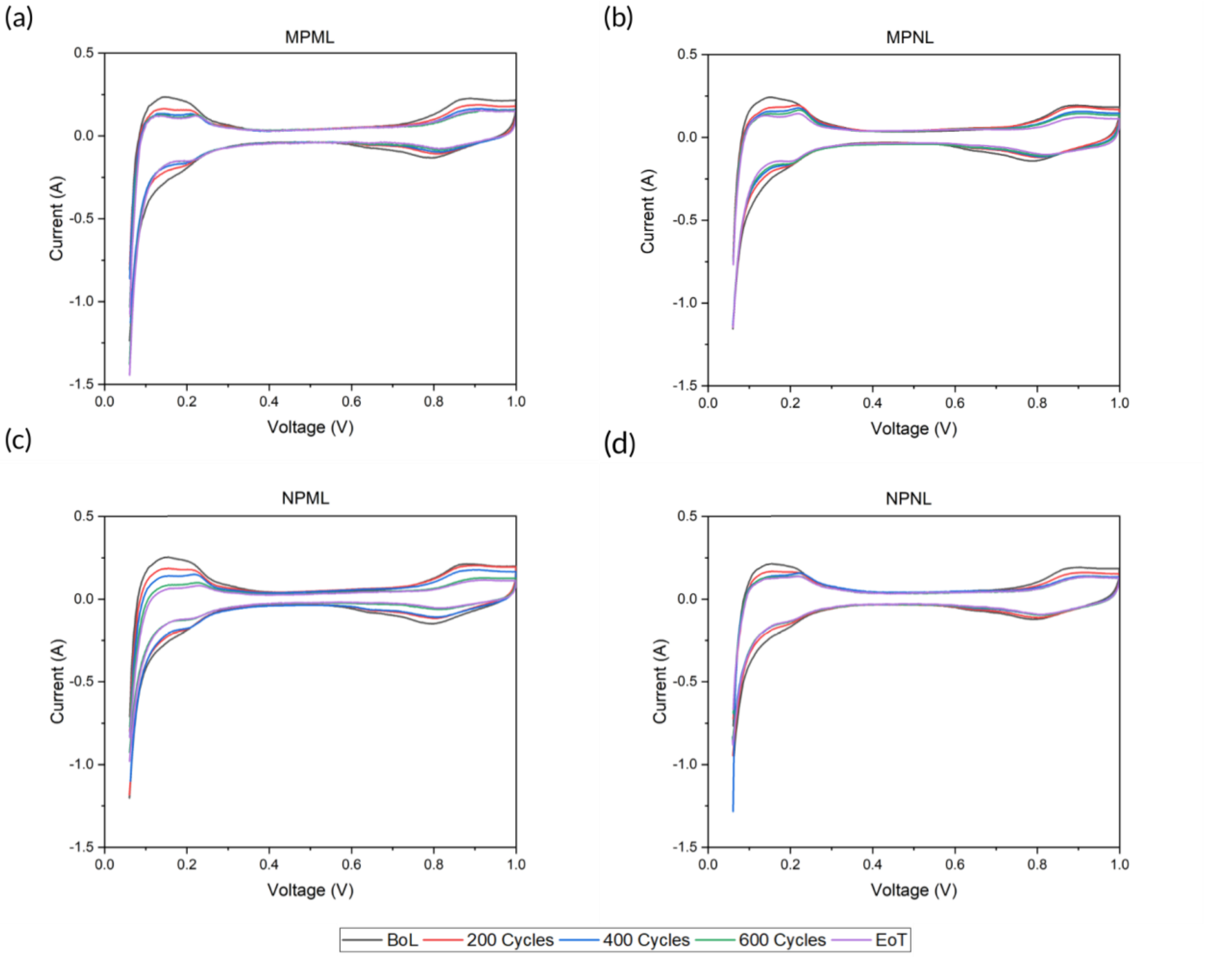

Figure 4-12: CV comparison between different cell operating power scenarios. The graphs were plotted between BoL to EoT in 200 cycle increments. (a) MPML (b) MPNL (c) NPML (d) NPNL

Figure 4-13 and Table 4-5 outline the ECSA changes in 200-cycle increments between BoL to EoT in visual and numerical format, respectively. The total ECSA decrease in terms of percentage is also presented in Table 4-5. NPNL had the lowest overall ECSA decrease between BoL to EoT, while MPML, MPNL, and NPML all had a ca. 35% decrease. This suggests that in drive cycle testing using the WLTP Class 3 cycle, running the PEMFC at its maximum operating power does not contribute directly to higher ECSA loss. The ECSA loss can come from other factors such as the high transientness of the drive cycle. As seen visually in CV graphs and mentioned previously, MPML had the most initial ECSA decrease of 22% from BoL to 200 cycles. The NPNL scenario had its highest ECSA decrease of 25% from 400 to 600 cycles;

this is also the highest 200-increment increase between all LDV cell operating power scenarios. In Figure 4-13(b), the MPNL scenario had the most linear and patterned ECSA decrease. An interesting observation is a 2% increase in ECSA from 600 cycles to EoT in the NPML scenario, suggesting a recovery of performance; however, more testing and validation is needed to prove this as ECSA computation is more of an estimation than an accurate calculation, the 2% can be regarded as an observational error.

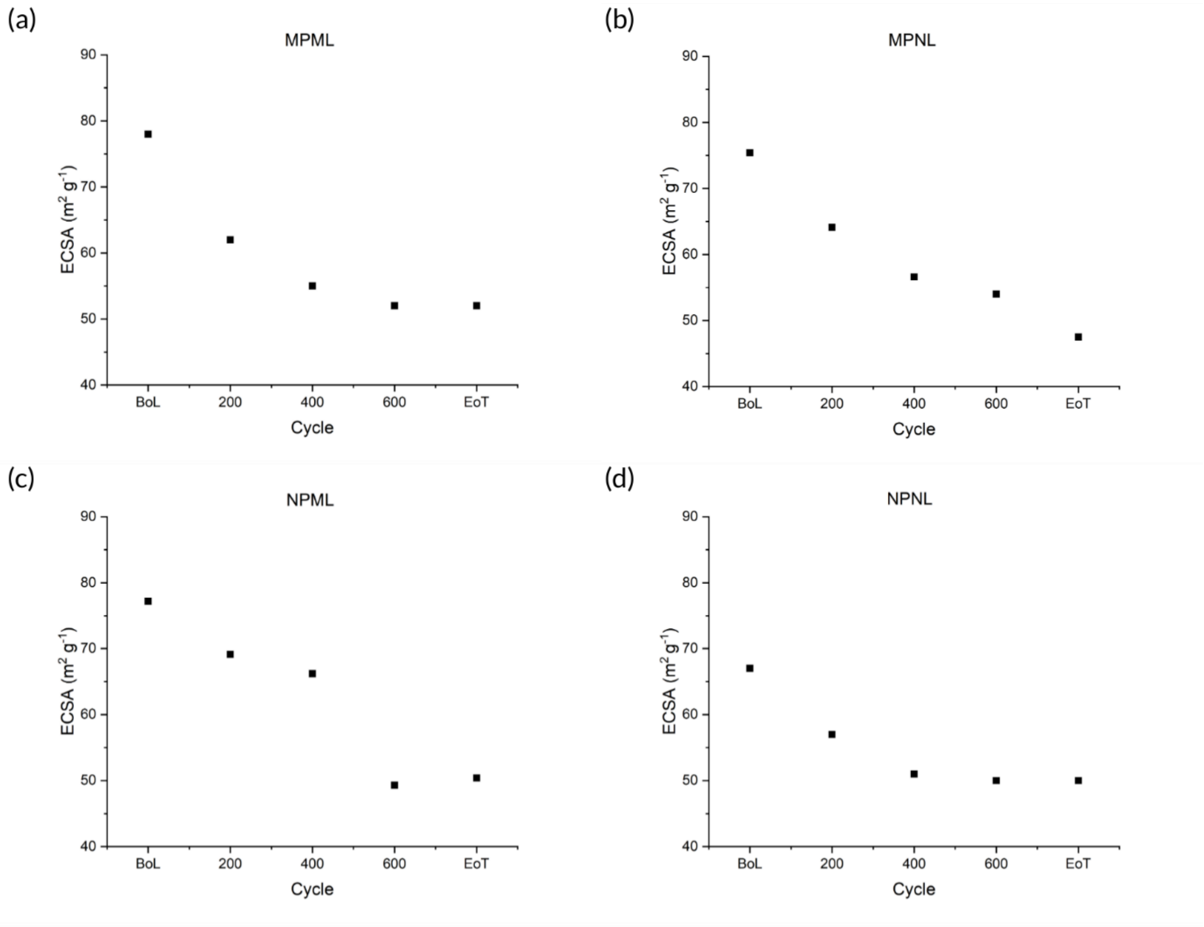

Figure 4-13: ECSA decrease for all cell operating power scenarios from BoL to EoT in 200 cycle increments. (a) MPML (b) MPNL (c) NPML (d) NPNL

Table 4-5: Table of ECSA decrease in terms of percentage for all LDV operating power scenarios in 200 cycle intervals and one role depicting the total ECSA change between BoL and EoT. Positive suggests an increase in ECSA (degradation reversed) while negative suggests a decrease in ECSA (degradation occurred).

Operating power	Δ Cycle	Δ ECSA (%)
MPML	BoL to 200	−22
	200 to 400	−11
	400 to 600	−7
	600 to EoT	0
	BoL to EoT	−35
MPNL	BoL to 200	−13
	200 to 400	−12
	400 to 600	−3.5
	600 to EoT	−11
	BoL to EoT	−35
NPML	BoL to 200	−10
	200 to 400	−4.3
	400 to 600	−25
	600 to EoT	+2.0
	BoL to EoT	−35
NPNL	BoL to 200	−14
	200 to 400	−11
	400 to 600	−2.0
	600 to EoT	0
	BoL to EoT	−25

4.7.1.3 PEMFC - LSV

According to DOE standards, if the equilibrium part of the LSV curve exceeds a current density of 20 mA cm^{-2}, the cell is considered to be chemically unstable [137]. In a 25 cm^{2} cell, this value suggests a maximum H_2 crossover rate of 2.59×10^{-6} mol s^{-1}. Figure 4-14 shows the LSV comparisons between different cell operating power scenarios for an LDV parallel FCHEV. All scenarios are under DOE limits aside from MPML, which had a current density of 52 mA cm^{-2} at EoT, more than 2.5 times the DOE limit. Table 4-6 shows a breakdown and calculated values of the hydrogen crossover rate in mol s^{-1} of all cell operating scenarios in 200-cycle increments. During 600 cycles and EoT for the MPML scenario, the hydrogen crossover rate exceeded DOE’s limit of 2.59×10^{-6} mol s^{-1}. All other scenarios were chemically stable throughout.

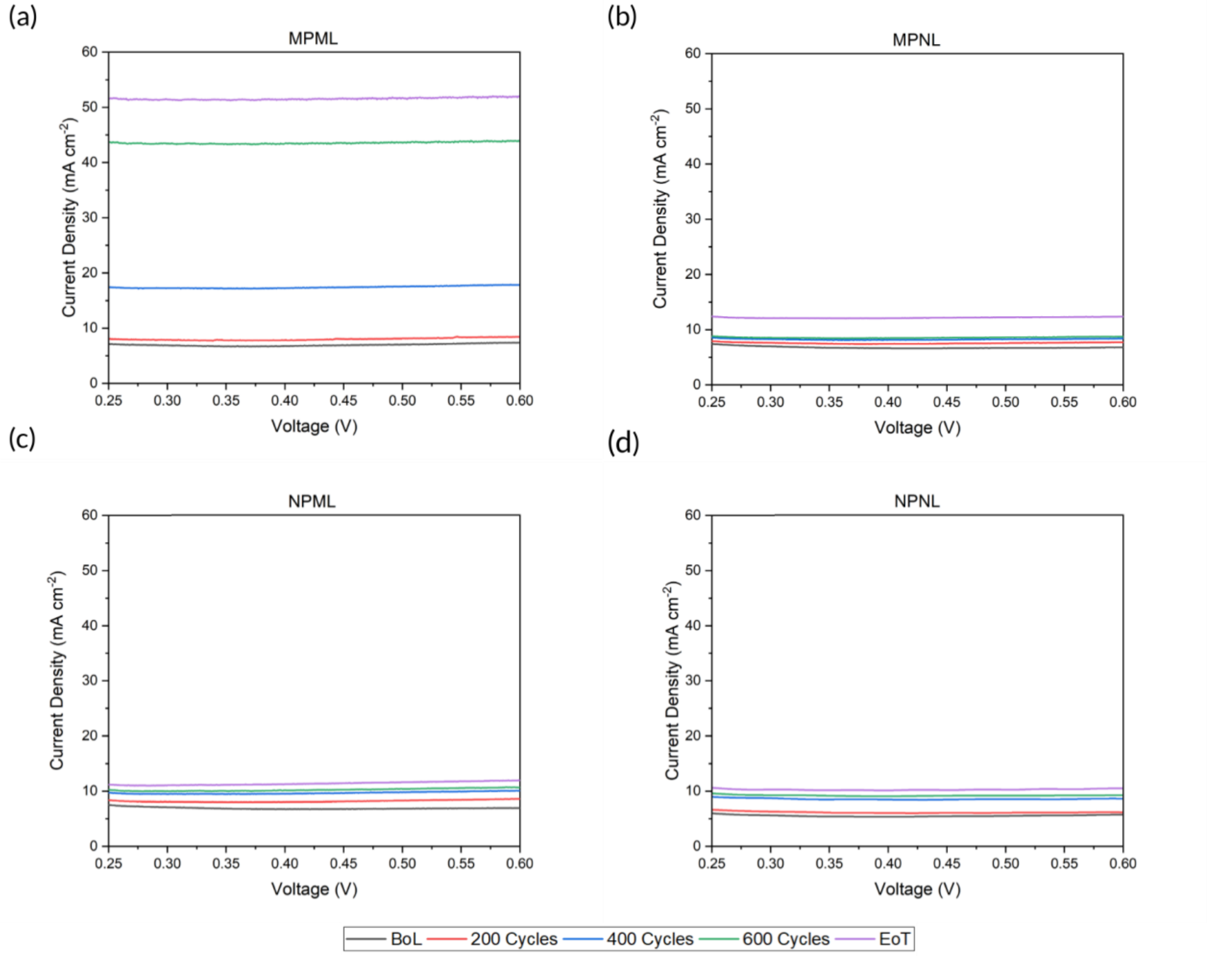

Figure 4-14: LSV curve comparisons between different operating power scenarios. The LSVs are plotted from the start of the equilibrium. If this equilibrium exceeds 20 mA cm^{-2}, the cell is considered as chemically unstable according to DOE standards [137]. (a) MPML (b) MPNL (c) NPML (d) NPNL

Table 4-6: H_2 crossover rate of all cell operating power scenarios in 200-cycle increments.

Operating power	Cycle	H_2 crossover rate (mol s^{-1})
MPML	BoL	9.57×10^{-7}
	200	1.04×10^{-6}
	400	2.33×10^{-6}
	600	5.70×10^{-6}
	EoT	6.74×10^{-6}
MPNL	BoL	8.81×10^{-7}
	200	9.98×10^{-7}
	400	1.09×10^{-6}
	600	1.13×10^{-6}
	EoT	1.61×10^{-6}
NPML	BoL	8.94×10^{-7}
	200	1.11×10^{-6}
	400	1.30×10^{-6}
	600	1.43×10^{-6}
	EoT	1.55×10^{-6}
NPNL	BoL	7.38×10^{-7}
	200	8.03×10^{-7}
	400	1.09×10^{-6}
	600	1.20×10^{-6}
	EoT	1.36×10^{-6}

4.7.1.4 PEMFC - EIS

EIS data were collected and plotted in 200-cycle increments for all cell operating power scenarios at 100, 300, and 800 mA cm^{-2} current densities, with the AC amplitude being 10% of the DC. Figure 4-15 shows the fitted and unfitted Nyquist plot comparisons for the MPML scenario in a visual format. Interestingly, the 100 mA cm^{-2} collection Nyquist plot showed a reduction in the size of the charge transfer semicircles between BoL and EoT, which shows that there is less resistance. The mass transfer arc is barely visible for a low current density such as 100 mA cm^{-2}; as this current primarily operates in the activation region. For the 300 mA cm^{-2} current density, the charge transfer semicircles increased slightly in size from BoL to 200 cycles; from 200 cycles onwards, the semicircles stayed relatively constant. It is difficult to identify the mass transport resistance changes by visualising the 300 mA cm^{-2} Nyquist plots, but this category of resistance can be extracted from the fitted Nyquist plots, along with estimates of Ohmic and charge transfer resistances. For the 800 mA cm^{-2} current density, the mass transfer arc was the most dominant form of increase, which increased from 200 to 400 cycles, and then a more significant increase was observed from 600 cycles to EoT. The Ohmic resistance stayed relatively consistent throughout all current densities and cycles.

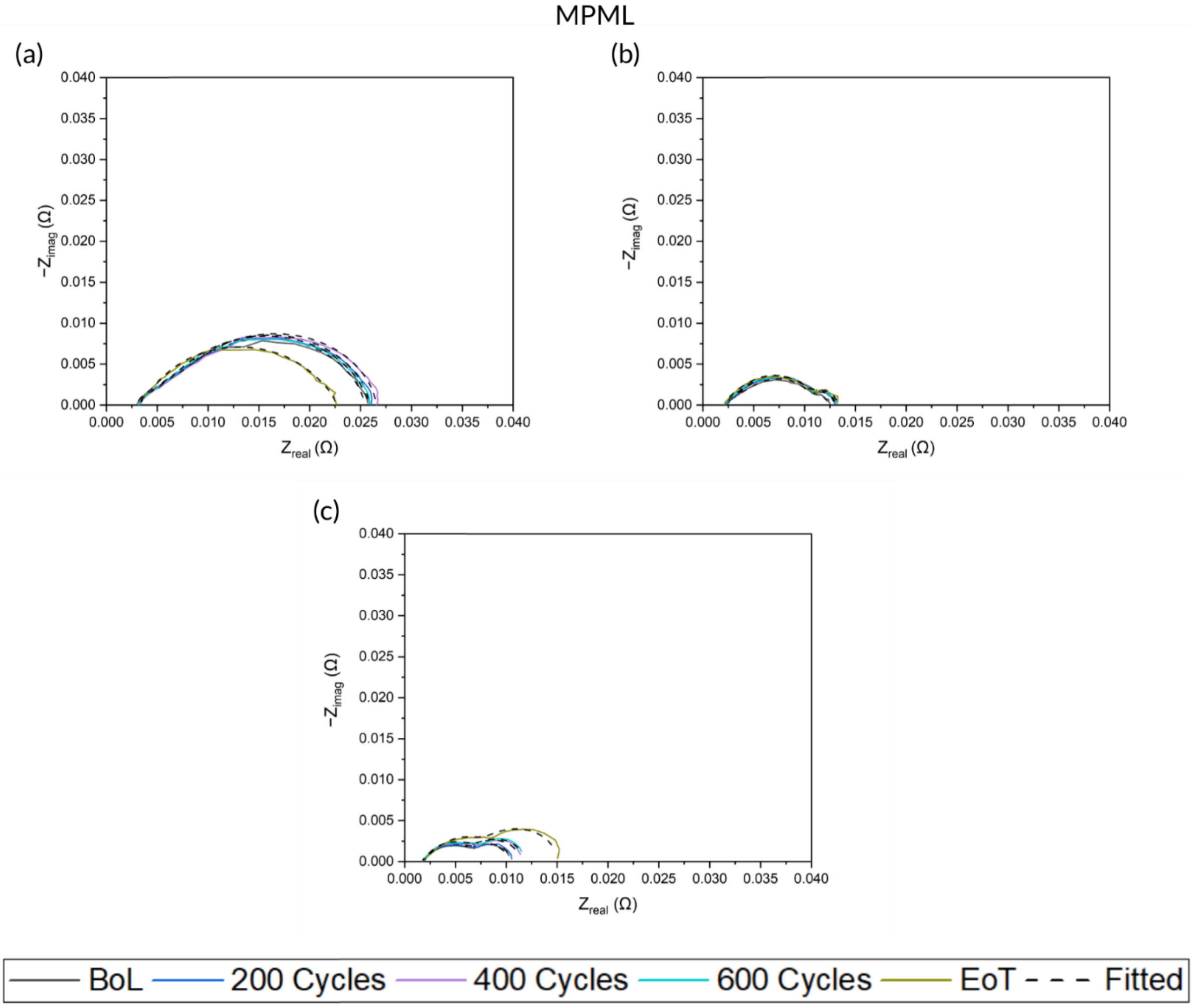

Figure 4-15: EIS Nyquist plot comparisons at 100, 300, and 800 mA cm^{-2} current density for the MPML scenario.

As mentioned in the previous paragraph, estimates of resistance values can be extrapolated from the fitted Nyquist plots, namely Ohmic (R_{Ω}), anode charge transfer (R_{an}), cathode charge transfer (R_{ca}), and mass transfer (R_m) resistances; these values for all current densities for the MPML scenario are shown in Table 4-7 to Table 4-10. As spotted visually and shown in Table 4-7, Ohmic resistance stays relatively constant for all current densities. Shown in Table 4-8 and Table 4-9, the charge transfer resistance is more dominant on the cathode side for the 100 mA cm^{-2} current density and stays this way until EoT. At 300 mA cm^{-2} current density, all the resistances stayed relatively constant from BoL to EoT; with the exception of slight increases of cathode charge transfer resistance. At 800 mA cm^{-2}, the anode charge transfer resistance had a major decrease from BoL to EoT; however, this was counteracted by the increase of cathode charge transfer resistance. In addition, there was also a drastic increase in mass transfer resistance from BoL to EoT.

Table 4-7: Ohmic resistance (R_Ω) changes for the MPML scenario for 100, 300, and 800 mA cm^{-2} current densities, shown in 200 cycle intervals.

Current density or voltage (mA cm^{-2} or V)	R_Ω BoL (mΩ cm^2)	R_Ω 200 cycles (mΩ cm^2)	R_Ω 400 cycles (mΩ cm^2)	R_Ω 600 cycles (mΩ cm^2)	R_Ω EoT (mΩ cm^2)
100 mA cm^{-2}	3.41	3.28	3.41	3.32	3.05
300 mA cm^{-2}	2.43	2.31	2.19	2.19	2.08
800 mA cm^{-2}	1.88	1.83	1.78	1.78	1.94

Table 4-8: Anode charge transfer resistance (R_{an}) changes for the MPML scenario for 100, 300, and 800 mA cm^{-2} current densities, shown in 200-cycle intervals.

Current density or voltage (mA cm^{-2} or V)	R_{an} BoL (mΩ cm^2)	R_{an} 200 cycles (mΩ cm^2)	R_{an} 400 cycles (mΩ cm^2)	R_{an} 600 cycles (mΩ cm^2)	R_{an} EoT (mΩ cm^2)
100 mA cm^{-2}	1.50	1.42	1.62	1.31	1.08
300 mA cm^{-2}	2.68	2.25	2.33	2.38	2.52
800 mA cm^{-2}	4.43	4.73	4.98	4.98	1.98

Table 4-9: Cathode charge transfer resistance (R_{ca}) changes for the MPML scenario for 100, 300, and 800 mA cm^{-2} current densities, shown in 200-cycle intervals.

Current density or voltage (mA cm^{-2} or V)	R_{ca} BoL (mΩ cm^2)	R_{ca} 200 cycles (mΩ cm^2)	R_{ca} 400 cycles (mΩ cm^2)	R_{ca} 600 cycles (mΩ cm^2)	R_{ca} EoT (mΩ cm^2)
100 mA cm^{-2}	18.6	19.0	19.3	19.7	17.8
300 mA cm^{-2}	1.90	2.25	2.53	2.52	2.78
800 mA cm^{-2}	3.50	3.58	4.63	4.63	7.15

Table 4-10: Mass transfer resistance (R_m) changes for the MPML scenario for 100, 300, and 800 mA cm^{-2} current densities, shown in 200 cycle intervals.

Current density or voltage (mA cm^{-2} or V)	R_m BoL (mΩ cm^2)	R_m 200 cycles (mΩ cm^2)	R_m 400 cycles (mΩ cm^2)	R_m 600 cycles (mΩ cm^2)	R_m EoT (mΩ cm^2)
100 mA cm^{-2}	1.95	2.22	2.22	1.43	0.64
300 mA cm^{-2}	5.32	6.12	5.96	5.92	5.87
800 mA cm^{-2}	0.39	0.30	0.38	0.38	3.95

Figure 4-16 shows the fitted and unfitted Nyquist plot comparisons for the MPNL scenario. Once again, the 100 mA cm^{-2} Nyquist plot showed a reduction of the size of the charge transfer semicircles between BoL and EoT, with a less significant change than that of MPML. For the 300 mA cm^{-2} current density, the charge transfer semicircles increased in size every 200 cycles from BoL to EoT, with the most visual increase from 600 cycles to EoT. The mass transfer arc increased from BoL to 200 cycles, then stayed more consistent from 400 to 600 cycles, with a more significant increase from 600 cycles to EoT. For the 800-mA cm^{-2} current density, the charge and mass transfer semicircles increased slightly from BoL to 200 cycles, stayed relatively consistent from 200 to 600 cycles, and then experienced a drastic increase from 600 cycles to EoT. The Ohmic resistance stayed relatively consistent throughout all current densities and cycles.

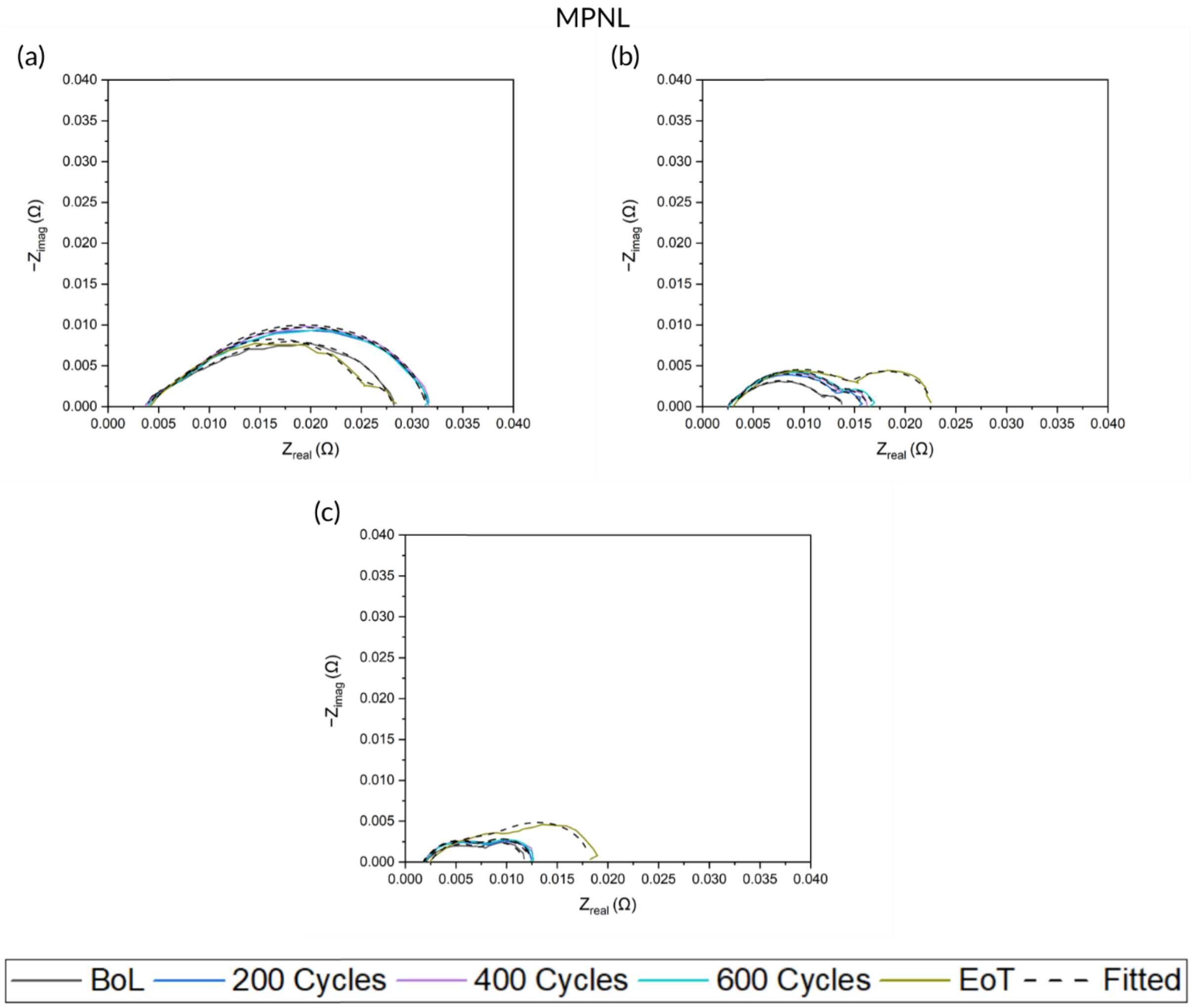

Figure 4-16: EIS Nyquist plot comparisons at 100, 300, and 800 mA cm^{-2} current density for the MPNL scenario.

Estimates of resistance values can be extrapolated from the fitted Nyquist plots; these values for all current densities for the MPNL scenario are shown in Table 4-11 to Table 4-14. Ohmic resistance was relatively constant for the 100 and 300 mA cm^{-2} current densities. At 800 mA cm^{-2} current density, the Ohmic resistance also stayed relatively constant throughout, except during 600 cycles to EoT, where it experienced a 27% increase. The charge transfer resistance is more dominant on the cathode side for the 100 mA cm^{-2} current density from BoL to 600 cycles, however, a drastic decrease was seen from 600 cycles to EoT, where an increase was seen on the anode side, instead. At 300 mA cm^{-2} current density, all the resistances stayed relatively constant from BoL to EoT; with the exception of increases in cathode charge transfer resistance from 600 cycles to EoT. At 800 mA cm^{-2}, both charge transfer and mass transfer resistance have seen increases from BoL to EoT; for mass transfer resistance, a decrease was spotted from BoL to 600 cycles first, and then an increase from 600 cycles to EoT.

Table 4-11: Ohmic resistance (R_{Ω}) changes for the MPNL scenario for 100, 300, and 800 mA cm^{-2} current densities, shown in 200-cycle intervals.

Current density or voltage (mA cm^{-2} or V)	R_{Ω} BoL (mΩ cm^2)	R_{Ω} 200 cycles (mΩ cm^2)	R_{Ω} 400 cycles (mΩ cm^2)	R_{Ω} 600 cycles (mΩ cm^2)	R_{Ω} EoT (mΩ cm^2)
100 mA cm^{-2}	4.04	3.89	3.92	4.21	4.26
300 mA cm^{-2}	2.75	2.58	2.57	2.71	3.16
800 mA cm^{-2}	2.02	1.90	1.81	1.90	2.42

Table 4-12: Anode charge transfer resistance (R_{an}) changes for the MPNL scenario for 100, 300, and 800 mA cm^{-2} current densities, shown in 200-cycle intervals.

Current density or voltage (mA cm^{-2} or V)	R_{an} BoL (mΩ cm^2)	R_{an} 200 cycles (mΩ cm^2)	R_{an} 400 cycles (mΩ cm^2)	R_{an} 600 cycles (mΩ cm^2)	R_{an} EoT (mΩ cm^2)
100 mA cm^{-2}	2.10	1.97	1.72	1.87	6.73
300 mA cm^{-2}	8.07	9.77	10.2	10.2	10.8
800 mA cm^{-2}	2.18	5.58	5.61	5.14	7.19

Table 4-13: Cathode charge transfer resistance (R_{ca}) changes for the MPNL scenario for 100, 300, and 800 mA cm^{-2} current densities, shown in 200-cycle intervals.

Current density or voltage (mA cm^{-2} or V)	R_{ca} BoL (mΩ cm^2)	R_{ca} 200 cycles (mΩ cm^2)	R_{ca} 400 cycles (mΩ cm^2)	R_{ca} 600 cycles (mΩ cm^2)	R_{ca} EoT (mΩ cm^2)
100 mA cm^{-2}	19.2	23.2	24.0	23.3	3.43
300 mA cm^{-2}	1.81	2.37	2.59	2.95	7.66
800 mA cm^{-2}	4.30	4.40	4	4.83	8.18

Table 4-14: Mass transfer resistance (R_m) changes for the MPNL scenario for 100, 300, and 800 mA cm^{-2} current densities, shown in 200 cycle intervals.

Current density or voltage (mA cm^{-2} or V)	R_m BoL (mΩ cm^2)	R_m 200 cycles (mΩ cm^2)	R_m 400 cycles (mΩ cm^2)	R_m 600 cycles (mΩ cm^2)	R_m EoT (mΩ cm^2)

100 mA cm^{-2}	2.81	2.35	2.05	2.11	13.6
300 mA cm^{-2}	1.11	0.92	0.90	0.96	0.99
800 mA cm^{-2}	3.11	0.39	0.40	0.53	7.67

Figure 4-17 shows the fitted and unfitted Nyquist plot comparisons for the NPML scenario. During the 100 mA cm^{-2} current densities, gradual increases in charge transfer resistance could be spotted from BoL to 600 cycles, with the maximum increase between 400 and 600 cycles, the resistance was relatively constant between 600 cycles and EoT. During the 300 and 800 mA cm^{-2} current densities, gradual increases of charge and mass transfer resistance could be spotted from BoL to 600 cycles, with the maximum increase between 400 and 600 cycles, the resistance was relatively constant between 600 cycles and EoT. In addition, in all current densities, an increase in Ohmic resistance could also be seen between 400 and 600 cycles. The interesting observation for this scenario is that the Ohmic and charge transfer resistances all increased similarly, no matter which current density the EIS was collected at.

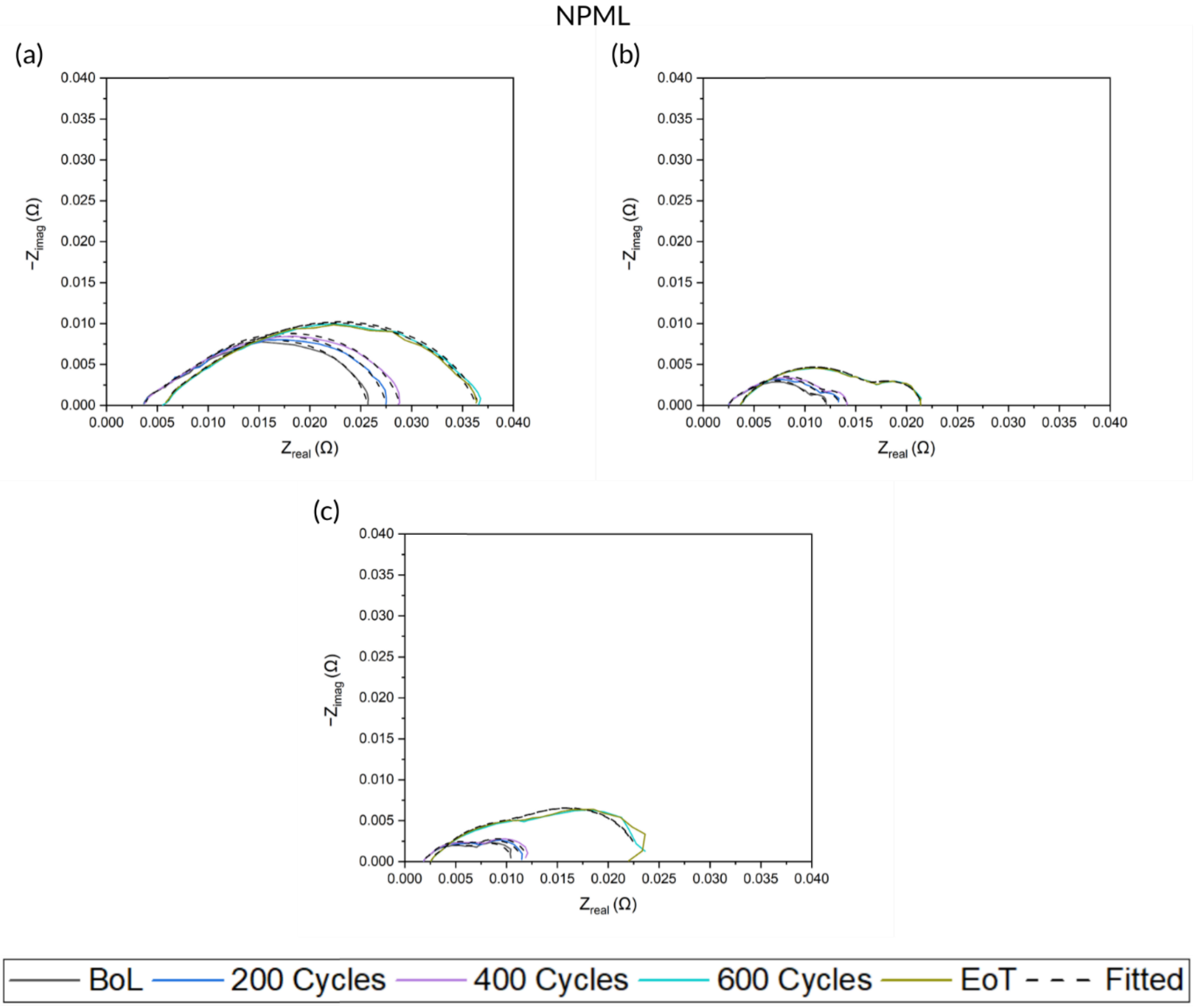

Figure 4-17: EIS Nyquist plot comparisons at 100, 300, and 800 mA cm^{-2} current density for the NPML scenario.

Estimates of resistance values can be extrapolated from the fitted Nyquist plots; these values for all current densities for the NPML scenario are shown in Table 4-15 to Table 4-18. Gradual increases in Ohmic resistance were spotted for all current densities. For charge transfer resistance, small increases were seen for both anode and cathode resistance for the 100 mA cm^{-2} scenario. A more drastic increase can be seen for the 300 and 800 mA cm^{-2} current densities, especially during 400 to 600 cycles. Mass transfer resistance stayed relatively constant and even experienced a decrease for the 300 mA cm^{-2} current density during 400 to 600 cycles to EoT.

Table 4-15: Ohmic resistance (R_Ω) changes for the NPML scenario for 100, 300, and 800 mA cm^{-2} current densities, shown in 200 cycle intervals.

Current density or voltage (mA cm^{-2} or V)	R_Ω BoL (mΩ cm^2)	R_Ω 200 cycles (mΩ cm^2)	R_Ω 400 cycles (mΩ cm^2)	R_Ω 600 cycles (mΩ cm^2)	R_Ω EoT (mΩ cm^2)
100 mA cm^{-2}	3.72	3.75	3.84	5.97	5.94
300 mA cm^{-2}	2.49	2.48	2.52	3.80	3.73
800 mA cm^{-2}	1.88	1.88	1.90	2.63	2.63

Table 4-16: Anode charge transfer resistance (R_{an}) changes for the NPML scenario for 100, 300, and 800 mA cm^{-2} current densities, shown in 200-cycle intervals.

Current density or voltage (mA cm^{-2} or V)	R_{an} BoL (mΩ cm^2)	R_{an} 200 cycles (mΩ cm^2)	R_{an} 400 cycles (mΩ cm^2)	R_{an} 600 cycles (mΩ cm^2)	R_{an} EoT (mΩ cm^2)
100 mA cm^{-2}	1.49	1.52	1.59	2.52	1.77
300 mA cm^{-2}	2.40	3.20	3.28	12.1	12.2
800 mA cm^{-2}	4.55	4.91	5.02	9.00	9.03

Table 4-17: Cathode charge transfer resistance (R_{ca}) changes for the NPML scenario for 100, 300, and 800 mA cm^{-2} current densities, shown in 200-cycle intervals.

Current density or voltage (mA cm^{-2} or V)	R_{ca} BoL (mΩ cm^2)	R_{ca} 200 cycles (mΩ cm^2)	R_{ca} 400 cycles (mΩ cm^2)	R_{ca} 600 cycles (mΩ cm^2)	R_{ca} EoT (mΩ cm^2)
100 mA cm^{-2}	18.1	19.8	21.2	26.1	26.6
300 mA cm^{-2}	2.00	2.34	2.62	4.49	4.47
800 mA cm^{-2}	3.73	4.24	4.66	10.5	10.5

Table 4-18: Mass transfer resistance (R_m) changes for the NPML scenario for 100, 300, and 800 mA cm^{-2} current densities, shown in 200 cycle intervals.

Current density or voltage (mA cm^{-2} or V)	R_m BoL (mΩ cm^2)	R_m 200 cycles (mΩ cm^2)	R_m 400 cycles (mΩ cm^2)	R_m 600 cycles (mΩ cm^2)	R_m EoT (mΩ cm^2)

100 mA cm^{-2}	2.37	2.50	2.23	2.02	2.05
300 mA cm^{-2}	5.18	5.34	5.67	1.02	0.95
800 mA cm^{-2}	0.40	0.44	0.48	0.77	0.83

Figure 4-18 shows the fitted and unfitted Nyquist plot comparisons for the NPNL scenario. The charge transfer resistances increased gradually for all current densities. The mass transfer resistances also increased gradually for 300 and 800 mA cm^{-2} current densities. For the 100 mA cm^{-2} collection, the charge transfer resistance increased the most from 600 to EoT. For the 300 and 800 mA cm^{-2} current density, the charge and mass transfer resistance increased the most from 200 to 400 cycles. Ohmic resistance also increased gradually for the 100 mA cm^{-2} collections; whereas the resistance stayed more consistent for 300 and 800 mA cm^{-2}.

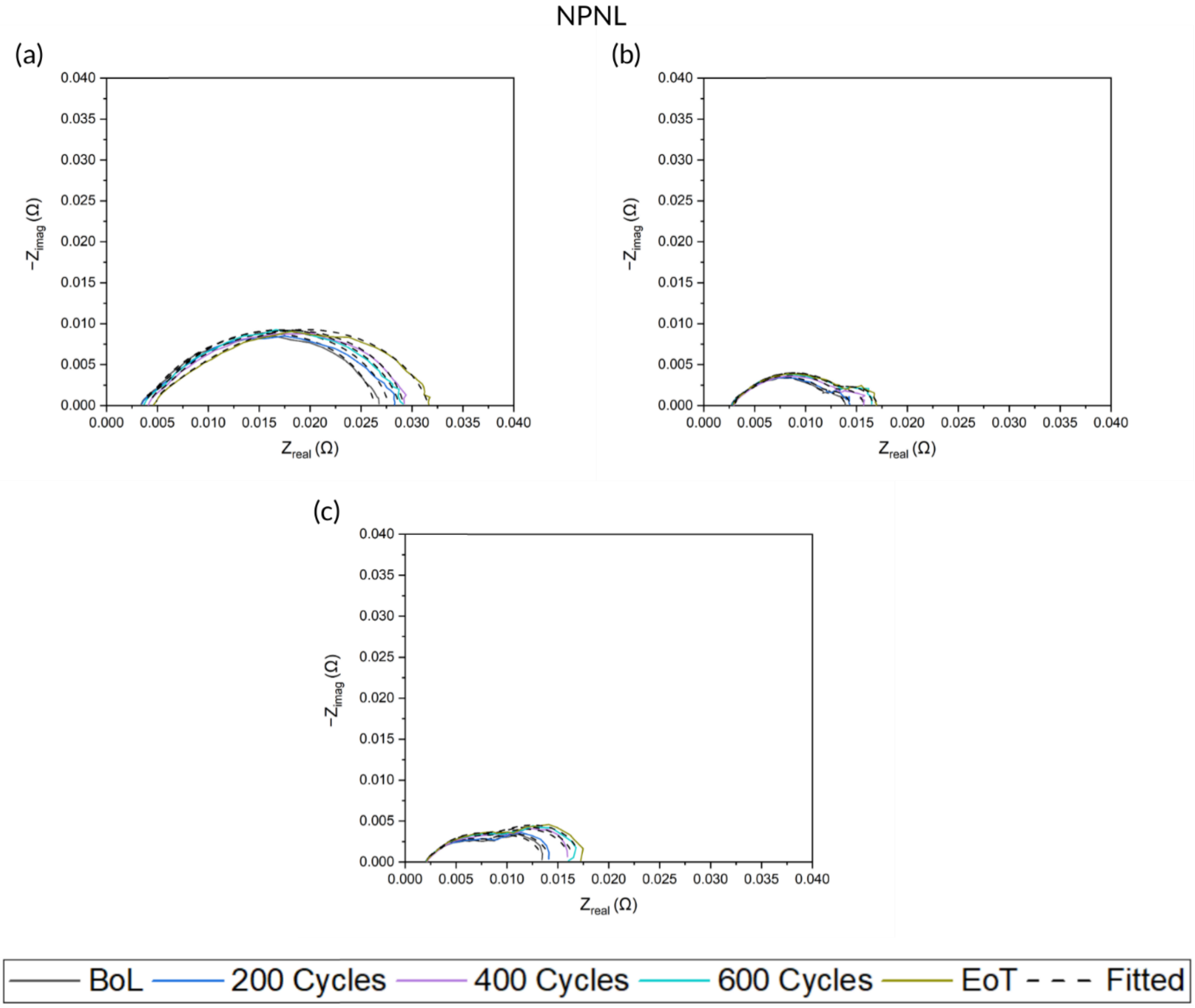

Figure 4-18: EIS Nyquist plot comparisons at 100, 300, and 800 mA cm^{-2} current density for the NPNL scenario.

Estimates of resistance values can be extrapolated from the fitted Nyquist plots; these values for all current densities for the NPML scenario are shown in Table 4-19 to Table 4-22. Gradual increases in Ohmic resistance were spotted for the 300 and 800 mA cm^{-2} current densities and stayed relatively consistent for the 800 mA cm^{-2} current density. An interesting occurrence is that the Ohmic resistance only has notable increases for NP scenarios rather than MP scenarios. The charge transfer resistances stayed relatively constant for the 100 mA cm^{-2} scenario. Both the anode and cathode charge transfer resistances increased gradually for the case of 300 and 800 mA cm^{-2}; with a more sudden increase in anode charge transfer resistance from 200 to 400 mA cm^{-2} during 800 mA cm^{-2}. Mass transfer resistance stayed relatively constant for the 100 and 300 mA cm^{-2} current densities. At 800 mA cm^{-2}, a decrease in mass transfer resistance was spotted from 200 to 400 cycles.

Table 4-19: Ohmic resistance (R_Ω) changes for the NPNL scenario for 100, 300, and 800 mA cm^{-2} current densities, shown in 200 cycle intervals.

Current density or voltage (mA cm^{-2} or V)	R_Ω BoL (mΩ cm^2)	R_Ω 200 cycles (mΩ cm^2)	R_Ω 400 cycles (mΩ cm^2)	R_Ω 600 cycles (mΩ cm^2)	R_Ω EoT (mΩ cm^2)
100 mA cm^{-2}	3.48	3.59	4.24	3.76	4.81
300 mA cm^{-2}	2.77	2.84	3.05	2.86	2.93
800 mA cm^{-2}	2.05	2.10	2.23	2.16	2.16

Table 4-20: Anode charge transfer resistance (R_{an}) changes for the NPNL scenario for 100, 300, and 800 mA cm^{-2} current densities, shown in 200-cycle intervals.

Current density or voltage (mA cm^{-2} or V)	R_{an} BoL (mΩ cm^2)	R_{an} 200 cycles (mΩ cm^2)	R_{an} 400 cycles (mΩ cm^2)	R_{an} 600 cycles (mΩ cm^2)	R_{an} EoT (mΩ cm^2)
100 mA cm^{-2}	1.26	1.30	1.70	0.80	1.64
300 mA cm^{-2}	8.02	8.42	8.73	9.71	10.1
800 mA cm^{-2}	2.25	2.53	6.58	6.92	6.92

Table 4-21: Cathode charge transfer resistance (R_{ca}) changes for the NPNL scenario for 100, 300, and 800 mA cm^{-2} current densities, shown in 200-cycle intervals.

Current density or voltage (mA cm^{-2} or V)	R_{ca} BoL (mΩ cm^2)	R_{ca} 200 cycles (mΩ cm^2)	R_{ca} 400 cycles (mΩ cm^2)	R_{ca} 600 cycles (mΩ cm^2)	R_{ca} EoT (mΩ cm^2)
100 mA cm^{-2}	19.7	21.7	20.3	22.8	23.3
300 mA cm^{-2}	2.08	2.17	2.67	3.19	3.17
800 mA cm^{-2}	5.70	6.02	6.56	7.45	7.45

Table 4-22: Mass transfer resistance (R_m) changes for the NPNL scenario for 100, 300, and 800 mA cm^{-2} current densities, shown in 200 cycle intervals.

Current density or voltage (mA cm^{-2} or V)	R_m BoL (mΩ cm^2)	Rm 200 cycles (mΩ cm^2)	R_m 400 cycles (mΩ cm^2)	R_m 600 cycles (mΩ cm^2)	R_m EoT (mΩ cm^2)
100 mA cm^{-2}	1.88	1.15	2.99	1.38	1.92
300 mA cm^{-2}	1.00	0.96	1.25	0.88	0.80
800 mA cm^{-2}	3.47	3.53	0.77	0.68	0.68

4.7.1.5 LiB – Charge Capacity

A list of capacity checks for all scenarios is shown in Table 4-23, including the capacity check of a pristine cell under the same diagnostic cycle conditions, being 4.88 Ah. The term 'capacity fade' mentioned in this section is based on the comparison to the measured pristine capacity of 4.88 Ah, instead of the theoretical 5 Ah obtained from LG Chem's INR21700 M50 specification sheets. This rule applies to all further analyses. Having the LiB running at nominal cell operating power did not necessarily suggest that the capacity fade would be less; in fact, the MPML scenario ended up having the least capacity fade. Interestingly, both the NL scenarios had the same capacity fade of 5.9%. The NPML had the most capacity fade of 13%.

Table 4-23: Capacity check of different cell operating scenarios (MPML, MPNL, NPML, NPNL). The capacity is checked after the CC-CV charging step of a standard diagnostic cycle at EoT.

Cell operating power	Capacity (Ah)
BoL	4.88
MPML	4.61
MPNL	4.59
NPML	4.24
NPNL	4.59

4.7.1.6 LiB - EIS

Nyquist plots of the collected EIS are shown in Figure 4-19; a comparison between BoL, MPML, MPNL, NPML, and NPNL conditions is shown. A pristine M50 cell was tested at BoL to act as reference data. As seen, running at the LiB at nominal operating power doesn't necessarily suggest that there would be less impedance. MPNL has the lowest overall impedance, but NPNL has as high of an overall impedance as the NL scenarios. NPML scenario had the most Ohmic resistance. It is difficult to examine the charge transfer resistance graphically; therefore, the extracted resistance data table is shown in Table 4-24, showing both Ohmic (R_{Ω}) and charge transfer (R_{ct}) resistance. It can be spotted that the MPML scenario had the most charge transfer resistance increases of 164%, NPNL is a close second, with an increase of 159%.

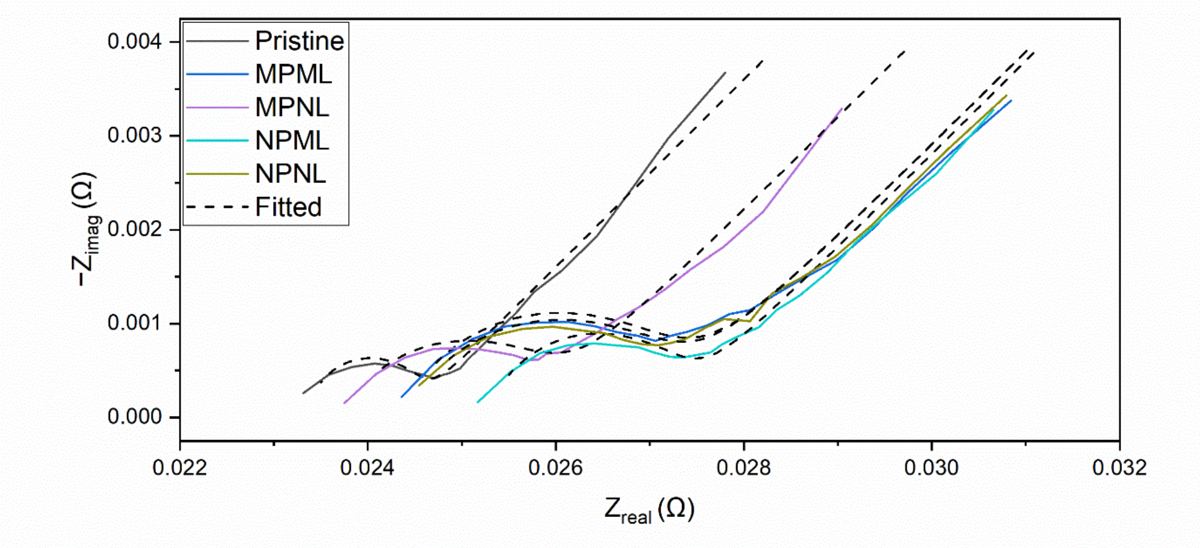

Figure 4-19: LiB M50 EIS Nyquist plot comparison between different operating scenarios (MPML, MPNL, NPML, and NPNL). The graph shows both fitted (dashed lines) and unfitted (solid lines) curves. Certain resistance values, such as Ohmic and charge transfer resistance, can be extracted from fitted curves. The EIS was collected at an amplitude of 10 mV in a frequency range of 10000 to 0.01 Hz.

Table 4-24: Extracted Ohmic (R_Ω) and charge transfer (R_{ct}) resistance values from fitting the EIS into an equivalent circuit shown in Figure 3-7.

Cell operating power	R_Ω (mΩ)	R_{ct} (mΩ)
BoL	23.3	1.06
MPML	24.3	2.80
MPNL	23.7	2.10
NPML	25.3	1.95
NPNL	24.4	2.75

4.7.1.7 LiB – X-Ray CT

Figure 4-20 shows comparisons of 2 slices of interest of X-Ray CT scans between BoL and EoT for the MPML cell operating power. The main degradation mechanisms spotted were delamination (top picture, Slice 1) and rotation (bottom picture, Slice 2). Delamination was the most significant at the innermost region of the jelly roll. Aside from delamination and rotation, slight deformation of the jelly roll was also spotted for both slices. Using the slice delamination measurement technique outlined in Figure 3-9, the innermost region of the jelly roll in Slice 1 experienced a 320 µm delamination shifting toward the centre point of the slice from BoL. Using the rotation measurement technique outlined in Figure 3-8, the jelly roll experienced a 6° rotation counterclockwise.

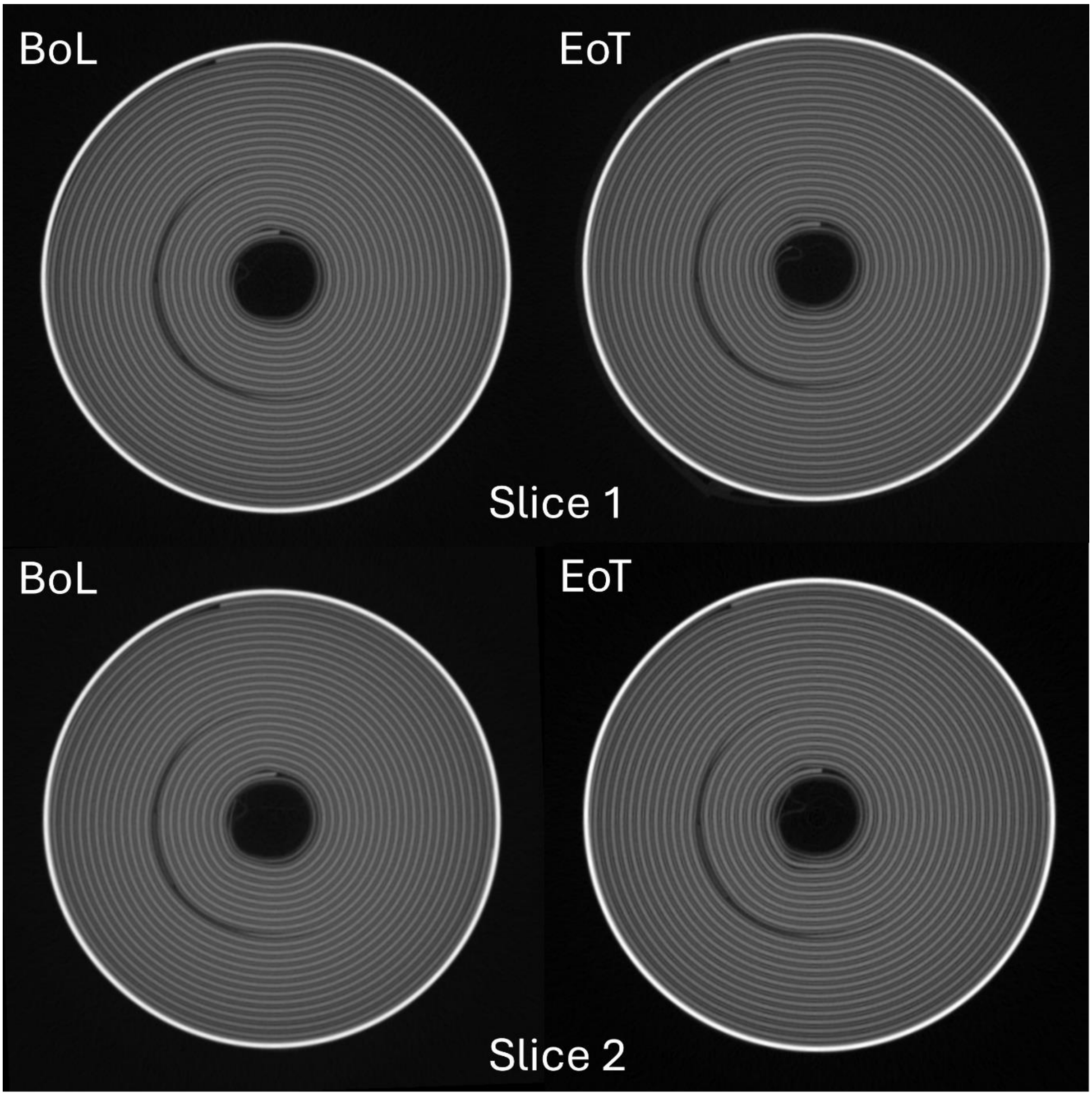

Figure 4-20: Comparison of X-Ray CT scans between BoL and EoT for the MPML cell operating power; two slices of interest are shown. Slice 1 encountered delamination while slice 2 encountered rotation.

4.7.2 Parallel HGV

Unlike the LDV section, the parallel HGV section's PEMFC data is broken down into different subsections covering the MPML, NPML, and NPNL cell operating power scenarios. The polarisation, CV, LSV, and EIS data can be found in each subsection. There is an extra subsection at the end explaining the advantages and disadvantages of each cell operating power scenario. For the LiB data, all cell operating power scenarios are discussed in conjunction with one another. Figure 4-21 shows the PEMFC power cycle profiles at the cell level for the different cell operating scenarios tested, while Figure 4-22 shows the corresponding LiB power profiles. In these two figures, negative power suggests that power is drawn from the source (e.g. a discharge state for LiBs), and positive power suggests that the power source is being charged.

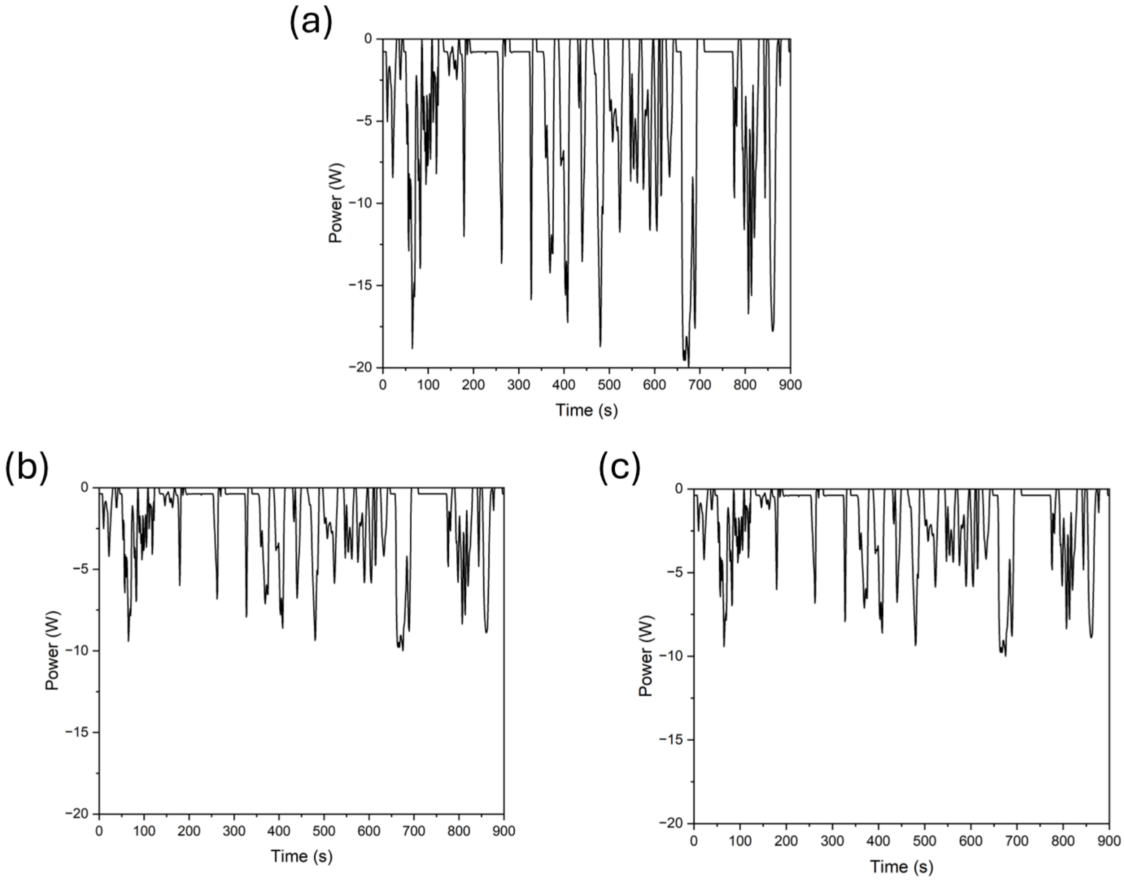

Figure 4-21: PEMFC power cycle profiles of different cell operating power scenarios for parallel HGVs. (a) MPML (b) NPML (c) NPNL

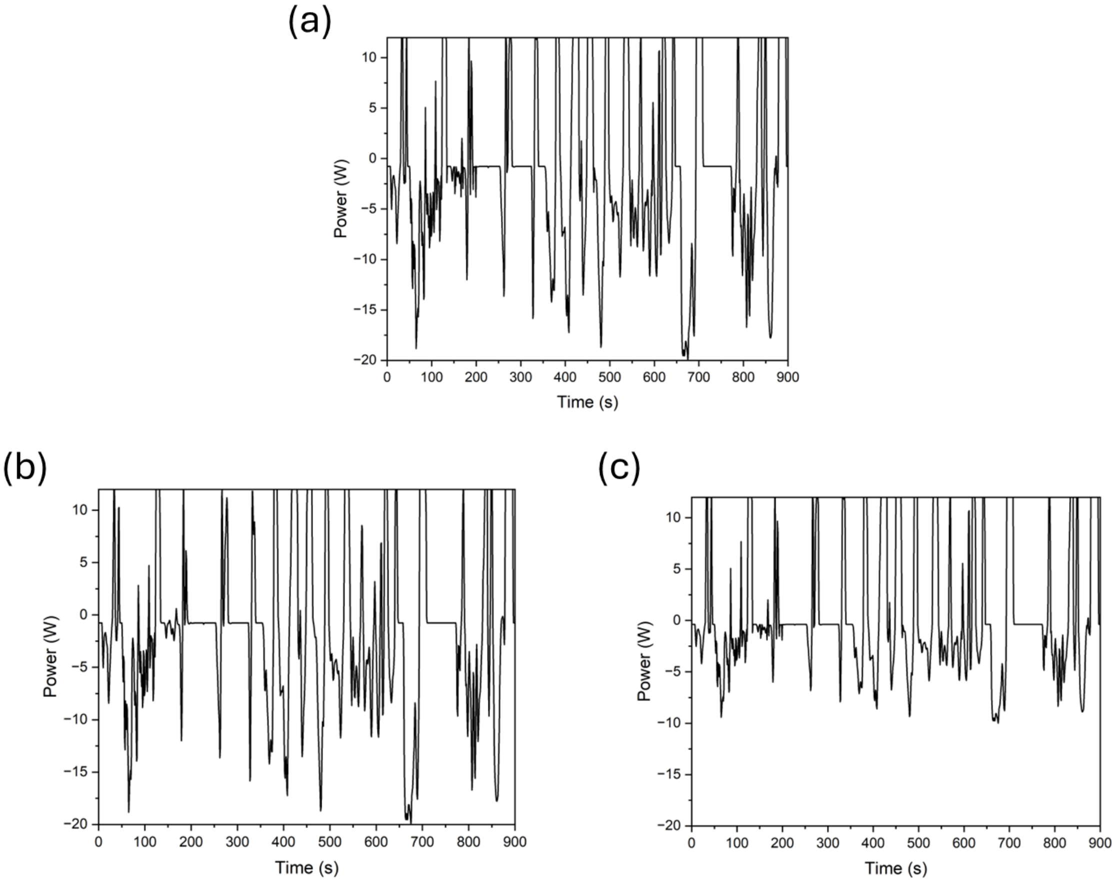

Figure 4-22: LiB power cycle profiles of different cell operating power scenarios for parallel HGVs. (a) MPML (b) NPML (c) NPNL

4.7.2.1 PEMFC Degradation Analysis

4.7.2.1.1 MPML

Figure 4-35 presents the electrochemical degradation analysis of the MPML cell operating power scenario for a parallel HGV. As shown in the polarisation and power curve in Figure 4-23a, at 600 mA cm^{-2}, the voltage decreased from 0.77 to 0.73 V between BoL and 100 drive cycles (EoT), with a degradation rate of 5.2% or 0.21% h^{-1}. At 1200 mA cm^{-2}, the voltage decreased from 0.68 to 0.65 V between BoL and EoT, a degradation rate of 4.4% or 0.18% h^{-1}. Kurtz et al. at the US National Renewable Energy Laboratory (NREL) and the Department of Energy (DOE) published similar data for automotive-use PEMFC voltage degradation rate at 1200 mA cm^{-2}; a value of 0.003% h^{-1} was suggested [162]. This rate is higher than that of NREL's standards for voltage degradation at 1200 mA cm^{-2} [162]. The maximum power dropped from 25 to 22 W, a 12% or 0.48% h^{-1} decrease. After 100 cycles, the PEMFC is still operating in the Ohmic region in order to reach maximum power, which is considered an ideal operational region for PEMFCs. In addition, the PEMFC reaches its maximum power at a lowered current density after 100 cycles.

As shown in the cyclic voltammetry plot in Figure 4-23b, the ECSA decreased from 71 to 52 $m^2\ g^{-1}$ between BoL and EoT, a 26% decrease. Figure 4-23c shows the LSV curve comparison between BoL and EoT. According to DOE standards, if the equilibrium part of the LSV exceeds a current density of 20 mA cm^{-2}, the cell is considered to be chemically unstable with severe hydrogen crossover [137], which is not the case for the EoT of this scenario. The hydrogen crossover rate increased from 7.9×10^{-7} to 8.16×10^{-7} mol s^{-1} between BoL and EoT, a 3.3% increase.

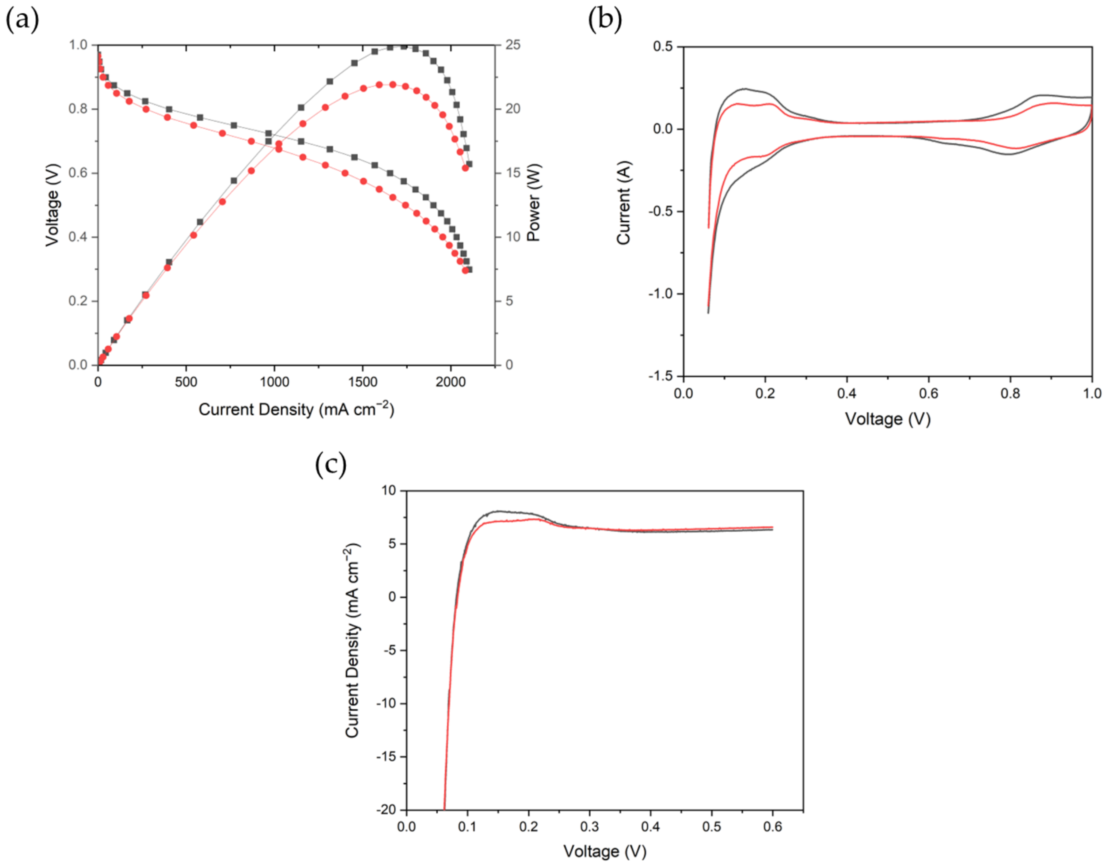

Figure 4-23: Electrochemical degradation analysis of the parallel HGV MPML cell operating power scenario, comparing BoL and EoT. (a) Polarisation and power curve. (b) Cyclic voltammetry (CV) for comparison and electrochemical surface area (ECSA) estimation; a 25.81% ECSA drop occurred. (c) Linear sweep voltammetry.

The power cycle of the EoT cycle (100 cycles) for the MPML HGV scenario was extracted and compared to the actual power demand, shown in Figure 4-24. It was seen from polarisation and power curves that the power demand has not dropped below the required maximum power demand of 20 W after 100 cycles. However, it can be seen that there are inconsistencies between the EoT power cycle output (red in the figure) and the power demand (black in the figure). This is likely due to factors such as gas lag or fuel starvation.

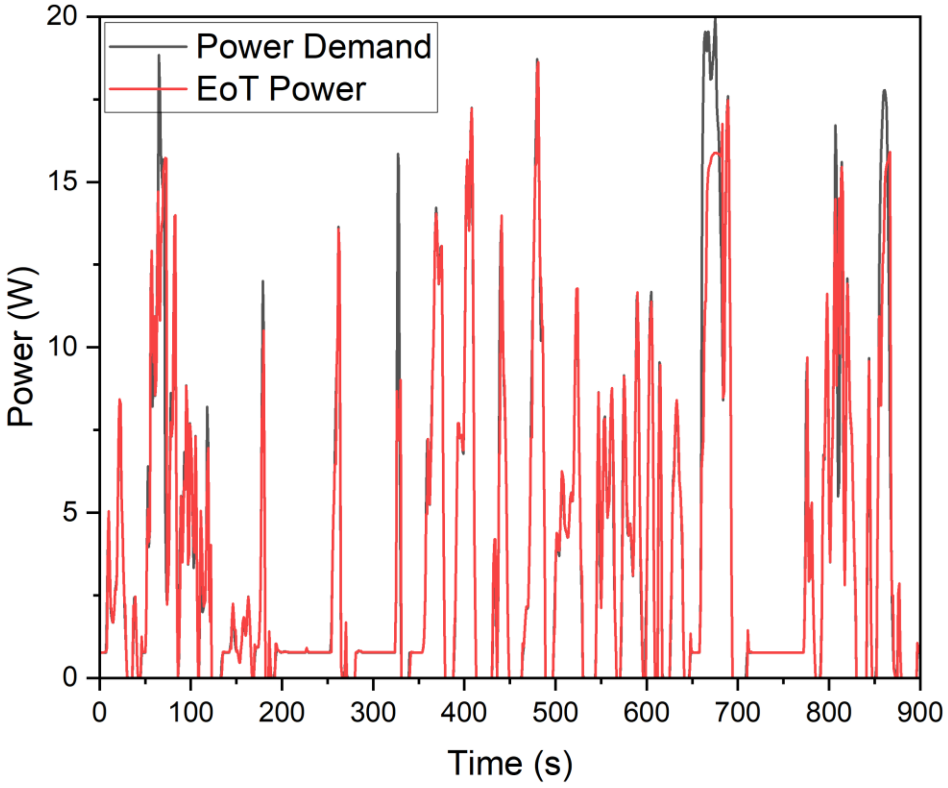

Figure 4-24: PEMFC power demand (from drive cycle) vs. EoT power cycle comparison for the MPML parallel HGV scenario.

Figure 4-25 shows Nyquist plots of EIS collected at different current densities (100, 300, 800, and 1200 mA cm^{-2}) and voltages (0.65 and 0.5 V) for the MPML parallel HGV under the WHVC drive cycle. Both the fitted and unfitted curves are plotted. For most current densities and voltages, the most significant change between BoL and EoT occurred at the low-frequency intercept with the real axis and the height of the semicircles. In some cases such as during the 0.65 and 0.5 V collections, this parameter decreased from BoL to EoT.

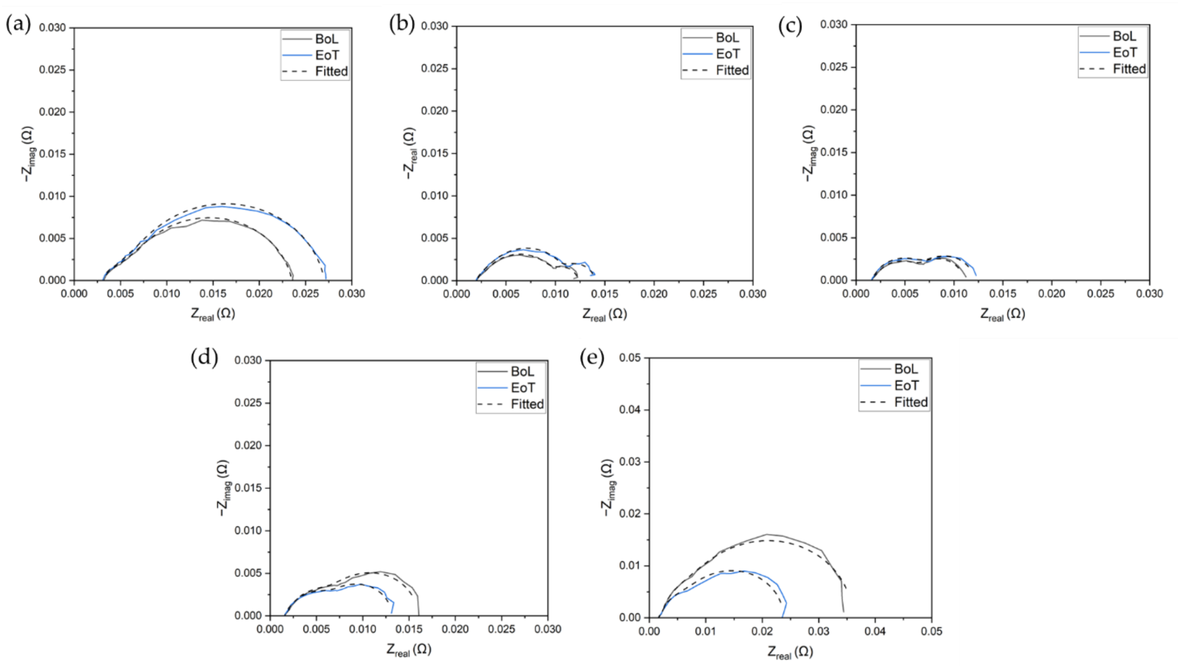

Figure 4-25: EIS Nyquist plots at different current densities and voltages for the MPML parallel HGV scenario under the WHVC drive cycle. (a) 100 mA cm^{-2}; (b) 300 mA cm^{-2}; (c) 800 mA cm^{-2}; (d) 0.65 V; (e) 0.5 V.

More information can be extracted by fitting the Nyquist plots with the equivalent circuit. After fitting, different resistance values such as Ohmic resistance (R_{Ω}), anode (R_{an}) and cathode charge transfer resistance (R_{ca}), and mass transport resistance (R_{m}) can be interpolated, as shown in Table 4-25. For all current densities, the changes in Ohmic resistance are negligible. At 100 mA cm^{-2} current density, the main form of resistance increase was the cathode charge transfer resistance. At 300 mA cm^{-2}, the main forms of resistance increase were the anode charge transfer and mass transfer resistance. Interestingly, the cathode charge transfer resistance experienced a decrease. At 800 mA cm^{-2} current density, resistances stayed relatively consistent, with the exception of a mass transfer resistance decrease. At 0.65 V, the main form of resistance increase was the mass transfer resistances; decreases occurred for both cathode and anode charge transfer resistance. At 0.5 V, the main form of resistance increase was the cathode charge transfer resistance. The mass transport resistance experienced a drastic decrease.

Table 4-25: Resistance values for the MPML parallel HGV scenario under the WHVC drive cycle, interpolated from EIS equivalent circuit fitting, including Ohmic resistance ($R_Ω$), anode (R_{an}) and cathode charge transfer resistance (R_{ca}), and mass transport resistance (R_m).

Current density or voltage (mA cm^{-2} or V)	$R_Ω$ BoL (mΩ cm^2)	$R_Ω$ EoT (mΩ cm^2)	R_{an} BoL (mΩ cm^2)	R_{an} EoT (mΩ cm^2)	R_{ca} BoL (mΩ cm^2)	R_{ca} EoT (mΩ cm^2)	R_m BoL (mΩ cm^2)	R_m EoT (mΩ cm^2)
100 mA cm^{-2}	82.5	79.2	32.6	33.4	436	523	36.3	39.5
300 mA cm^{-2}	52.6	49.3	17.4	57.6	175	80.1	60.8	161
800 mA cm^{-2}	42.0	40.1	113	133	108	120	9.19	5.44
0.65 V	41.5	38.8	120	42.4	225	160	10.8	85.7
0.5 V	42.9	41.8	18.1	15.7	133	422	704	113

4.7.2.1.2 NPML

Figure 4-26 presents the electrochemical degradation analysis of the NPML cell operating power scenario for a parallel HGV powertrain. As shown in the polarisation and power curve in Figure 4-26a, at 600 mA cm^{-2}, the voltage decreased from 0.77 to 0.75 V between BoL and 100 drive cycles (EoT), a decrease of 2.6% or 0.1% h^{-1}. At 1200 mA cm^{-2}, the voltage decreased from 0.67 to 0.65 V between BoL and EoT, a degradation rate of 3% or 0.12% h^{-1}. This rate is higher than that of NREL's standards for voltage degradation at 1200 mA cm^{-2} [162]. The maximum power dropped from 23 to 21 W, an 8.7% or 0.35% h^{-1} decrease. After 100 cycles, the PEMFC is still operating in the Ohmic region in order to reach maximum power, which is considered an ideal operational region for PEMFCS. The current density at which the PEMFC reaches maximum power is roughly the same at BoL and 100 cycles. However, since the voltage at maximum power decreased, the power produced also decreased.

As shown in the cyclic voltammetry plot in Figure 4-26b, the ECSA decreased from 54.5 to 50.5 m^2 g^{-1} between BoL and EoT, a 7.34% decrease. Figure 4-26c shows the LSV curve comparison between BoL and EoT. The cell is considered to be chemically stable according to DOE standards [137]. The hydrogen crossover rate increased from 1.07 × 10^{-6} to 1.1 × 10^{-6} mol s^{-1} between BoL and EoT, a 2.8% increase.

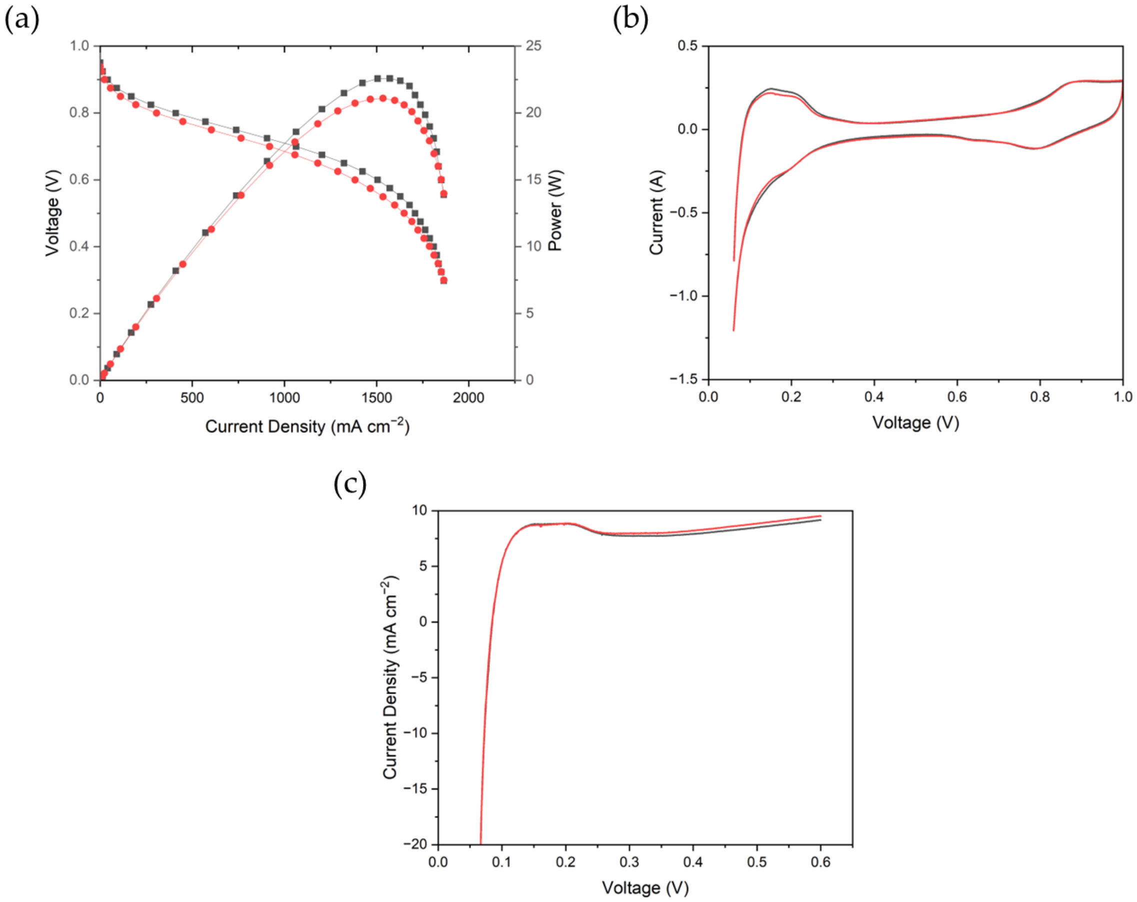

Figure 4-26: Electrochemical degradation analysis of the parallel HGV NPML cell operating power scenario, comparing BoL and EoT. (a) Polarisation and power curve. (b) Cyclic voltammetry (CV) for comparison and electrochemical surface area (ECSA) estimation; a 7.34% ECSA drop occurred. (c) Linear sweep voltammetry.

The EoT power cycle (100 cycles) for the NPML HGV scenario was extracted and compared to the power demand, shown in Figure 4-27. From previous polarisation curves outlining the NPML HGV scenario, it was seen that the PEMFC was still able to reach the required power of 10 W. There is a drastic improvement in the EoT power cycle when compared to the MPML scenario. Most times, the EoT power cycle was able to follow the power demand. There are minor inconsistencies in certain time stamps, as in the EoT power does not perfectly overlap with the power demand, but this was mostly caused by the dynamic load or power demands of this drive cycle, causing the PEMFC to experience gas lag and fuel starvation.

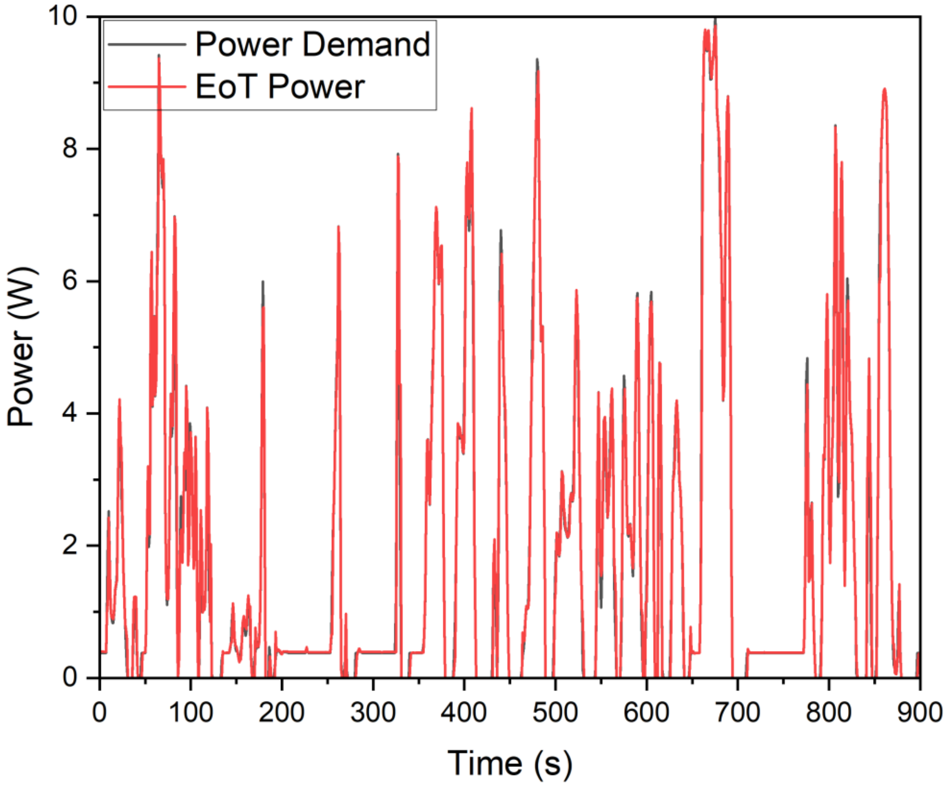

Figure 4-27: PEMFC power demand vs. EoT power cycle comparison for the NPML parallel HGV scenario.

Figure 4-28 shows Nyquist plots of EIS collected at different current densities (100, 300, 800, and 1200 mA cm^{-2}) and voltages (0.65 and 0.5 V) for the NPML parallel HGV under the WHVC drive cycle. Like the MPML cell operating power, the most significant change (both increase and decrease in semicircle size) between BoL and EoT occurred at the low-frequency intercept with the real axis and the height of the semicircles. Again, the EIS collection at 0.5 V had a significant decrease in resistance.

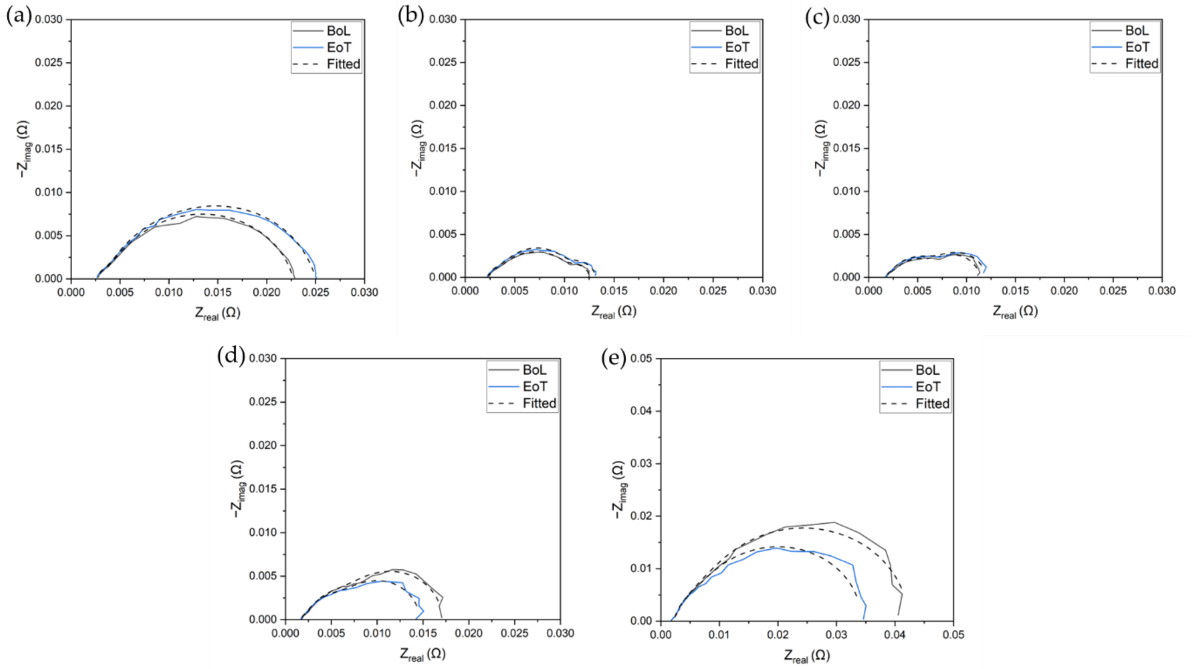

Figure 4-28: EIS Nyquist plots at different current densities and voltages for the NPML parallel HGV scenario under the WHVC drive cycle. (a) 100 mA cm^{-2}; (b) 300 mA cm^{-2}; (c) 800 mA cm^{-2}; (d) 0.65 V; (e) 0.5 V.

Table 4-26 shows the interpolated resistance values from fitting the EIS Nyquist plot into an equivalent circuit. For all current densities, the changes in Ohmic resistance are negligible. At 100 mA cm^{-2} current density, the main form of resistance increase was the cathode charge transfer resistance. In the NPML scenario, the most significant resistance increases happened at mass transport, especially for the EIS collection at 100 and 300 mA cm^{-2} current density. As mentioned previously, there was a drastic decrease in the low-frequency intercept with the real axis for the collection at 0.5 V, the interpolated resistance values show that most of this is caused by the decrease in cathode charge transfer resistance.

Table 4-26: Resistance values for the NPML parallel HGV scenario under the WHVC drive cycle, interpolated from EIS equivalent circuit fitting, including Ohmic resistance (R_{Ω}), anode (R_{an}) and cathode charge transfer resistance (R_{ca}), and mass transport resistance (R_m).

Current density or voltage (mA cm^{-2} or V)	R_{Ω} BoL (mΩ cm^2)	R_{Ω} EoT (mΩ cm^2)	R_{an} BoL (mΩ cm^2)	R_{an} EoT (mΩ cm^2)	R_{ca} BoL (mΩ cm^2)	R_{ca} EoT (mΩ cm^2)	R_m BoL (mΩ cm^2)	R_m EoT (mΩ cm^2)
100 mA cm^{-2}	69.4	66.4	23.7	21.7	457	383	16.8	153
300 mA cm^{-2}	60.3	55.5	178	54.8	48.9	72.8	25.0	145
800 mA cm^{-2}	46.1	43.8	117	128	105	115	13.7	10.2
0.65 V	44.8	42.8	127	124	240	186	15.5	11.6
0.5 V	45.7	44.5	148	123	844	673	17.3	15.9

4.7.2.1.3 NPNL

Figure 4-29 presents the electrochemical degradation analysis of the NPNL cell operating power scenario for a parallel HGV. As shown in the polarisation and power curve in Figure 4-29a, at 600 mA cm^{-2}, the voltage decreased from 0.76 to 0.73 V between BoL and EoT, a degradation rate of 4% or 0.16% h^{-1}. At 1200 mA cm^{-2}, the voltage decreased from 0.67 to 0.65 V between BoL and EoT, a degradation rate of 3% or 0.12% h^{-1}. This rate is higher than that of NREL's standards for voltage degradation at 1200 mA cm^{-2} [162]. The maximum power dropped from 22 to 20 W, a 9.1% or 0.36% h^{-1} decrease. The current density at which the PEMFC reaches maximum power is the same at BoL and EoT. However, since the voltage at maximum power decreased, the power produced also decreased.

As shown in the cyclic voltammetry plot in Figure 4-29b, the ECSA decreased from 88.3 to 74.3 m^{2} g^{-1} between BoL and EoT, a 16% decrease. Figure 4-29c shows the LSV curve comparison between BoL and EoT. The cell is considered to be chemically stable according to DOE standards [137]. The hydrogen crossover rate increased from 6.8 × 10^{-7} to 7.77 × 10^{-7} mol s^{-1} between BoL and EoT, a 14% increase.

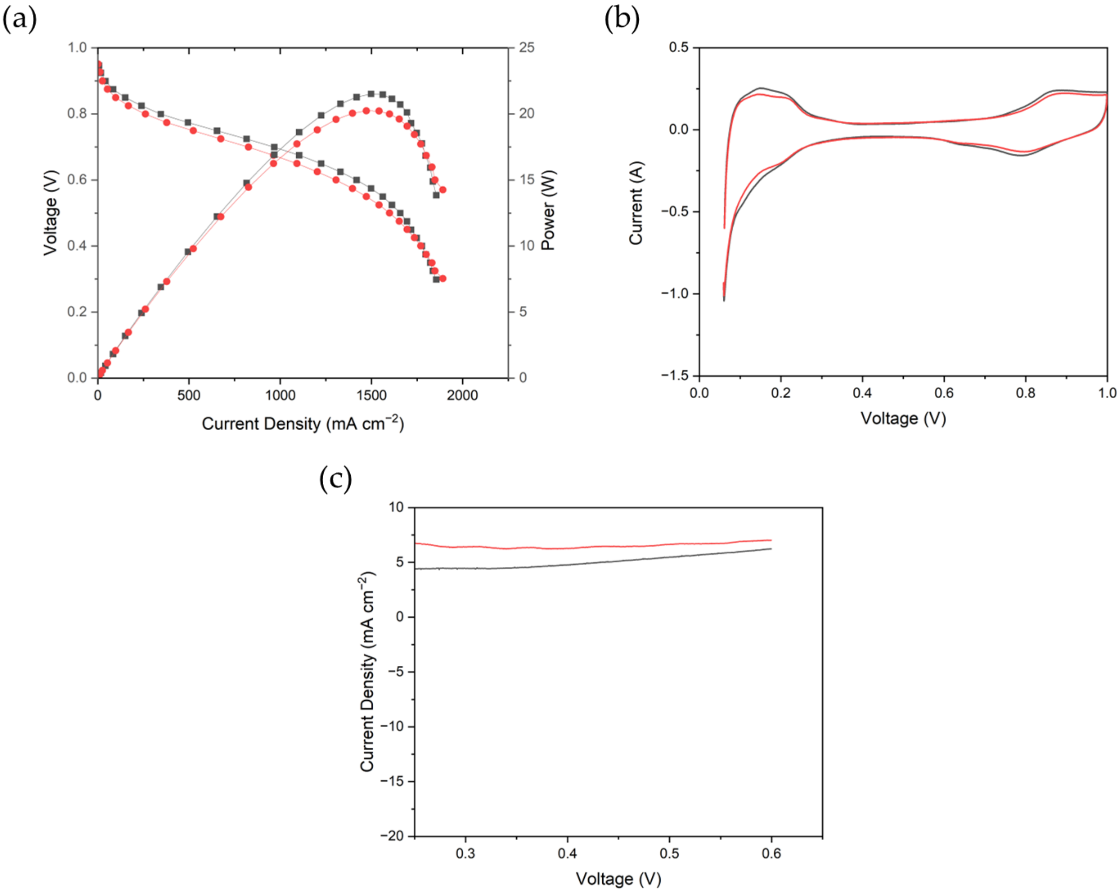

Figure 4-29: Electrochemical degradation analysis of the parallel HGV NPNL cell operating power scenario, comparing BoL and EoT. (a) Polarisation and power curve. (b) Cyclic

voltammetry (CV) for comparison and electrochemical surface area (ECSA) estimation; a 15.86% ECSA drop occurred. (c) Linear sweep voltammetry.

The power cycle at EoT for the NPNL HGV scenario was compared to the power demand, shown in Figure 4-30. The NPNL scenario has the most consistent power-follow out of all scenarios, with only minor inconsistencies caused by gas lag and fuel starvation. Seen in polarisation curves, it was seen that the PEMFC was still able to reach the required power of 10 W after 100 cycles. Overall, it was spotted that the consistency is higher between EoT power output and power demands for nominal PEMFC scenarios, as compared to maximum PEMFC scenarios.

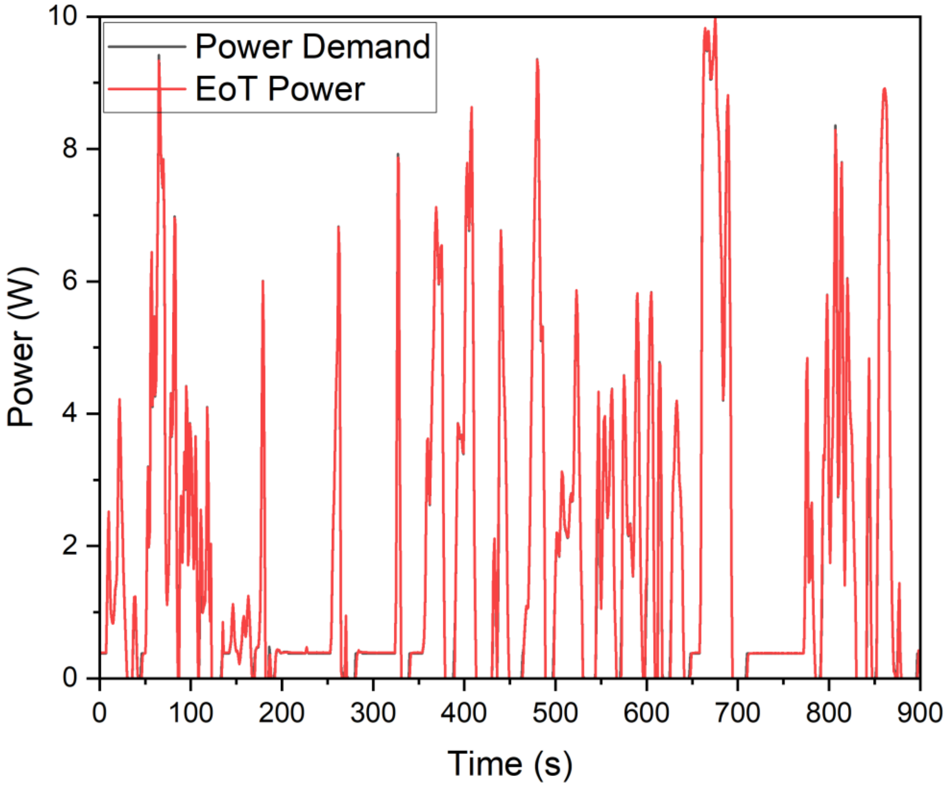

Figure 4-30: PEMFC power demand vs. EoT power cycle comparison for the NPNL parallel HGV scenario.

Figure 4-31 shows Nyquist plots of EIS collected at different current densities (100, 300, 800, and 1200 mA cm^{-2}) and voltages (0.65 and 0.5 V) for the NPNL parallel HGV under the WHVC drive cycle. In this scenario, there are changes in both low-frequency and high-frequency (Ohmic resistance) intercept with the real axis and the height of the semicircles. A decrease in Ohmic resistance occurred at the 800 mA cm^{-2} collection. The EIS collection at 0.5 V had a significant decrease in the low-frequency intercept with the real axis.

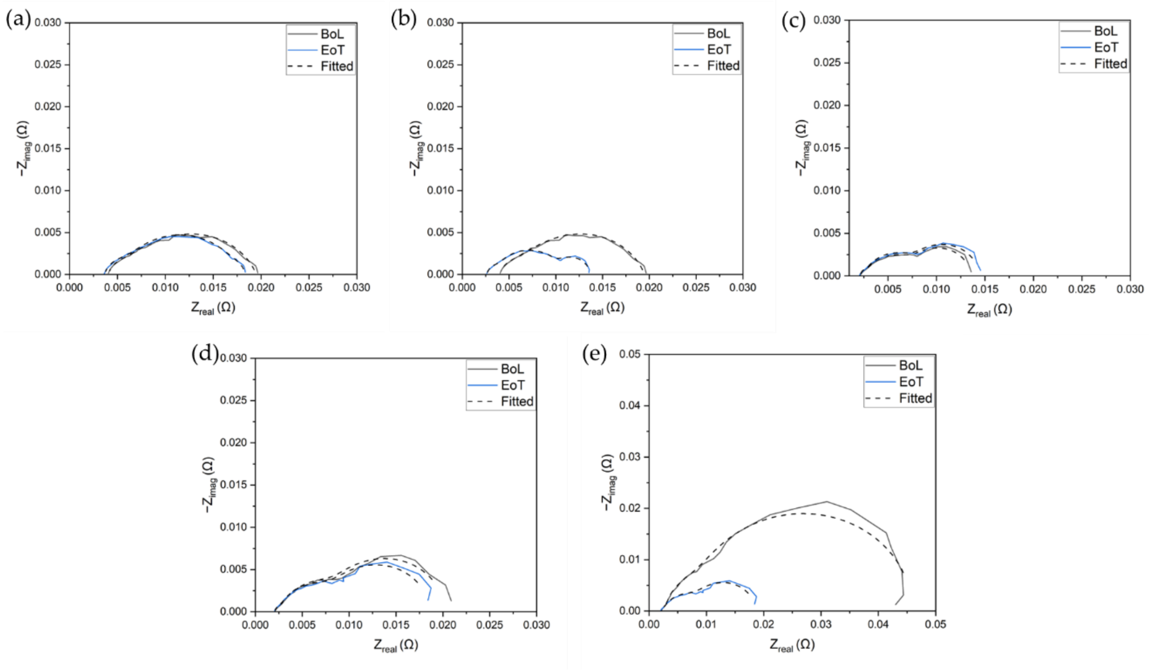

Figure 4-31: EIS Nyquist plots at different current densities and voltages for the NPNL parallel HGV scenario under the WHVC drive cycle. (a) 100 mA cm^{-2}; (b) 300 mA cm^{-2}; (c) 800 mA cm^{-2}; (d) 0.65 V; (e) 0.5 V.

Table 4-27 shows the interpolated resistance values from fitting the EIS Nyquist plot into an equivalent circuit. For the visible decrease of Ohmic resistance during the 300 mA cm^{-2} collection, a 4% decrease could be interpolated from the table. In this scenario, most charge transfer of the charge transfer resistances stayed relatively consistent, with only minor increases and decreases; except for the collection at 0.5 V, which a 73% decrease was spotted for the cathode charge transfer resistance. In terms of changes in resistances or impedance, this cell operating power scenario was the most optimal out of all three tested for the parallel WHVC powertrain.

Table 4-27: Resistance values for the NPNL parallel HGV scenario under the WHVC drive cycle, interpolated from EIS equivalent circuit fitting, including Ohmic resistance (R_{Ω}), anode (R_{an}) and cathode charge transfer resistance (R_{ca}), and mass transport resistance (R_m).

Current density or voltage (mA cm^{-2} or V)	R_{Ω} BoL (mΩ cm^2)	R_{Ω} EoT (mΩ cm^2)	R_{an} BoL (mΩ cm^2)	R_{an} EoT (mΩ cm^2)	R_{ca} BoL (mΩ cm^2)	R_{ca} EoT (mΩ cm^2)	R_m BoL (mΩ cm^2)	R_m EoT (mΩ cm^2)
100 mA cm^{-2}	102	91.7	23.8	58.0	327	282	34.0	25.9
300 mA cm^{-2}	69.2	66.3	72.7	166	78.5	82.3	108	25.9
800 mA cm^{-2}	54.6	52.9	122	123	142	164	17.0	18.1
0.65 V	54.2	51.9	146	147	286	249	17.2	14.3
0.5 V	54.1	51.9	154	147	918	249	19.8	14.3

4.7.2.1.4 MPML vs. NPML vs. NPNL in terms of PEMFC Degradation

Table 4-28 outlines the degradation between all scenarios, showcasing voltage decrease, maximum power decrease, and ECSA decrease. As expected, the MPML cell operating power scenario had the most voltage decrease from BoL to EoT at both 600 and 1200 mA cm^{-2} current density, a 5.2% (0.21% h^{-1}) and 4.4% (0.18% h^{-1}) decrease, respectively. The scenario also had the most maximum power decrease of 12% or 0.48% h^{-1}. The maximum power decreases of the other scenarios are similar, ranging from 8.7 to 9.1%. The maximum PEMFC (MP) scenario experienced more severe ECSA loss when compared to the nominal PEMFC (NP) scenarios, as high as triple the percentage decrease.

Table 4-28: Comparison of performance drops between all scenarios of the parallel HGV powertrain.

Operating Power	**Voltage decrease at 600 mA cm^{-2} (%)**	**Voltage decrease at 600 mA cm^{-2} (% h^{-1})**	**Voltage decrease at 1200 mA cm^{-2} (%)**	**Voltage decrease at 1200 mA cm^{-2} (% h^{-1})**	**Maximum power decrease (%)**	**Maximum power decrease (% h^{-1})**	**ECSA decrease (%)**
MPML	5.2	0.21	4.4	0.18	12	0.48	26
NPML	2.6	0.10	3.0	0.12	8.7	0.35	7.3
NPNL	4.0	0.16	3.0	0.12	9.1	0.36	16

4.7.2.2 LiB Degradation Analysis

4.7.2.2.1 Charge Capacity

A list of EoT capacity checks for all cell operating power scenarios for the parallel HGV powertrain under the WHVC drive cycle is shown in Table 4-29. Having the LiB running at nominal cell operating performance (NPNL) did not suggest that it will have less capacity fade; but in fact, it had more capacity fade than the MPML scenario. The MPML scenario had the least capacity fade of 0.6%. The NPML and NPML both had a capacity fade of 1.4%.

Table 4-29: Charge capacity checks for all cell operating power scenarios (MPML, NPML, and NPNL) for a parallel HGV under the WHVC drive cycle.

Cell operating power	Capacity (Ah)
BoL	4.88
MPML	4.85
NPML	4.81
NPNL	4.81

4.7.2.2.2 EIS

Nyquist plots of the collected EIS are shown in Figure 4-32; both fitted (dashed line) and unfitted (solid line) are shown. As seen, running at the LiB at nominal operating power doesn't necessarily suggest that there would be less impedance; but in fact, the most impedance. An extracted resistance data table is shown in Table 4-30, showing both Ohmic (R_Ω) and charge transfer (R_{ct}) resistance. Ohmic resistance had negligible change for all scenarios. The NPNL scenario had the most charge transfer resistance increase of 125% from BoL (pristine) to EoT. NPML scenario had the least resistance increase of 50%.

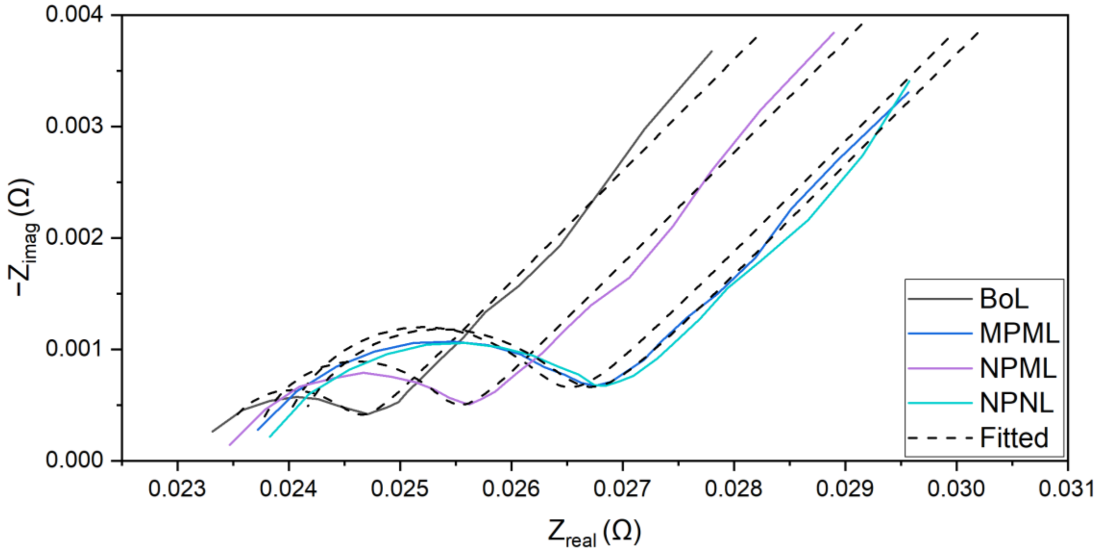

Figure 4-32: LiB M50 PEIS Nyquist plot comparison between different cell operating scenarios (MPML, NPML, and NPNL) for the parallel HGV powertrain under the WHVC drive cycle. The graph shows both fitted (dashed lines) and unfitted (solid lines) curves. Certain resistance values such as Ohmic and charge transfer resistance can be extracted from fitted curves. The EIS was collected at an amplitude of 10 mV within a frequency range of 10000 to 0.01 Hz.

Table 4-30: Extracted LiB Ohmic (R_Ω) and charge transfer (R_{ct}) resistance values for the parallel HGV scenario from fitting the EIS into an equivalent circuit.

Cell operating power	R_Ω (mΩ)	R_{ct} (mΩ)
BoL	23.3	1.06
MPML	23.9	2.27
NPML	23.6	1.59
NPNL	24.0	2.38

4.7.3 Parallel Bus – Millbrook Westminster London Bus Drive Cycle

The parallel bus section’s PEMFC data is broken down into different subsections covering the MPML, NPML, and NPNL cell operating power scenarios. The polarisation, CV, LSV, and EIS data can be found in each subsection. There is an extra subsection at the end explaining the advantages and disadvantages of each cell operating power scenario. For the LiB data, all cell operating power scenarios are discussed in conjunction with one another. Figure 4-33 shows the PEMFC power cycle profiles at the cell level for the different cell operating scenarios tested, while Figure 4-34 shows the corresponding LiB power profiles. In these two figures, negative power suggests that power is drawn from the source, and positive power suggests that the power source is being charged.

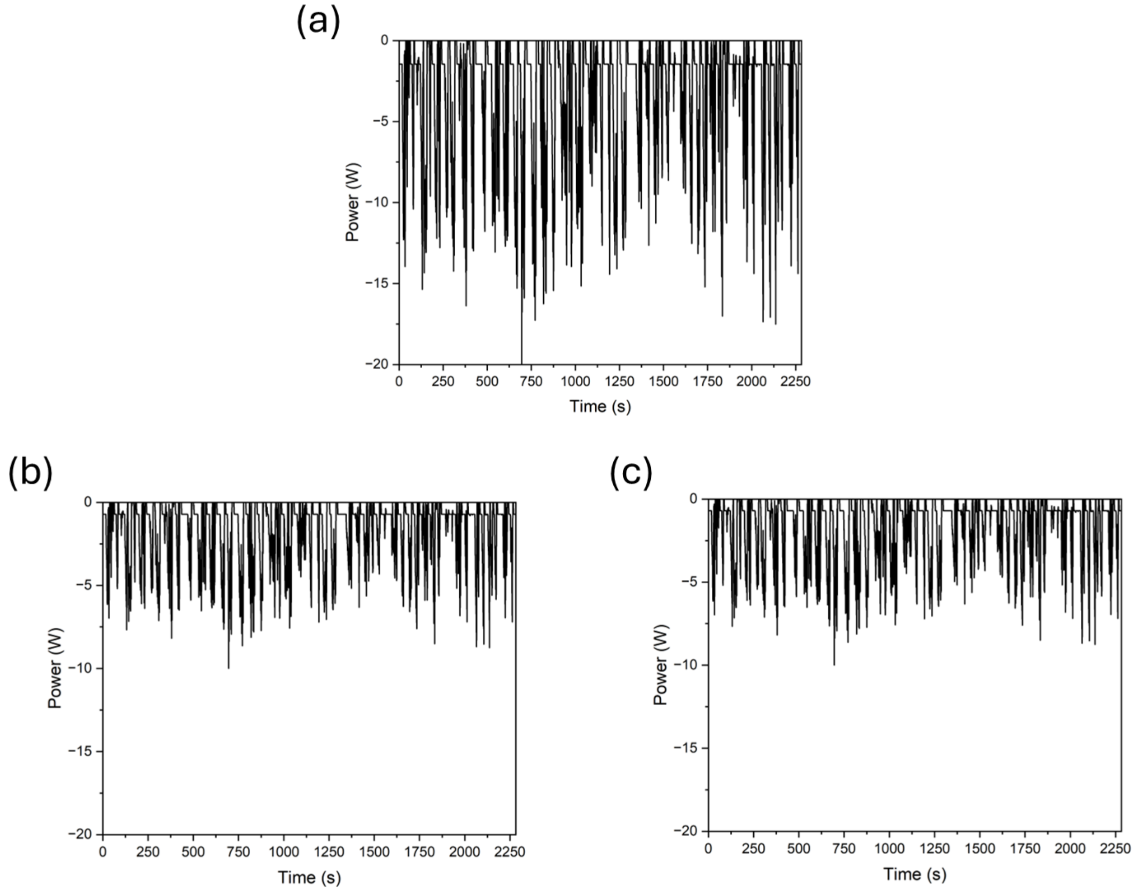

Figure 4-33: PEMFC power cycle profiles of different cell operating power scenarios for parallel buses. (a) MPML (b) NPML (c) NPNL

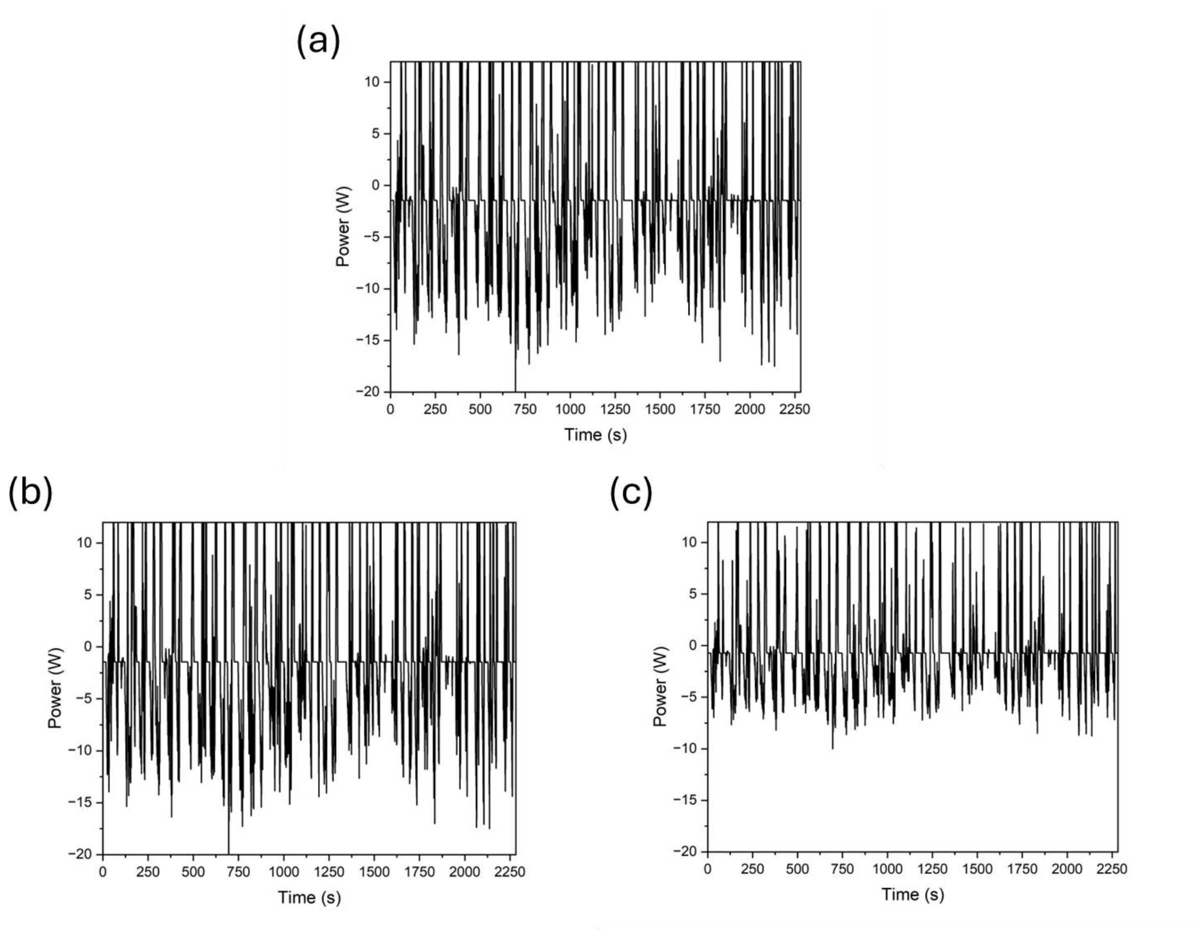

Figure 4-34: LiB power cycle profiles of different cell operating power scenarios for parallel buses. (a) MPML (b) NPML (c) NPNL

4.7.3.1 PEMFC Degradation Analysis

4.7.3.1.1 MPML

Figure 4-35 presents the electrochemical degradation analysis of the MPML cell operating power scenario. As shown in the polarisation and power curve in Figure 4-35a, at 600 mA cm^{-2}, the voltage decreased from 0.77 to 0.72 V between BoL and 100 drive cycles (EoT), with a degradation rate of 6.5% or 0.1% h^{-1}. At 1200 mA cm^{-2}, the voltage decreased from 0.67 to 0.60 V between BoL and EoT, a degradation rate of 11% or 0.17% h^{-1}. This rate is higher than that of NREL's standards for voltage degradation at 1200 mA cm^{-2} [162]. The maximum power dropped from 24 to 20 W, a 17% or 0.26% h^{-1} decrease. After 100 cycles, the PEMFC is still operating in the Ohmic region in order to reach maximum power, which is considered an ideal operational region for PEMFCs. However, the PEMFC reaches its maximum power at a lowered current density after 100 cycles.

As shown in the cyclic voltammetry plot in Figure 4-35b, the ECSA decreased from 73 to 50 m^2 g^{-1} between BoL and EoT, a 31% decrease. It can be seen that the CV curve has shown signs of minor electrical shorting at EoT, which can be identified further with LSV analysis.

Figure 4-35c shows the LSV curve comparison between BoL and EoT. According to DOE standards, if the equilibrium part of the LSV exceeds a current density of 20 mA cm^{-2}, the cell is considered to be chemically unstable with severe hydrogen crossover [137], which is not the case for the EoT of this scenario. However, the slight upward gradient of the equilibrium at EoT suggests signs of electrical shorting.

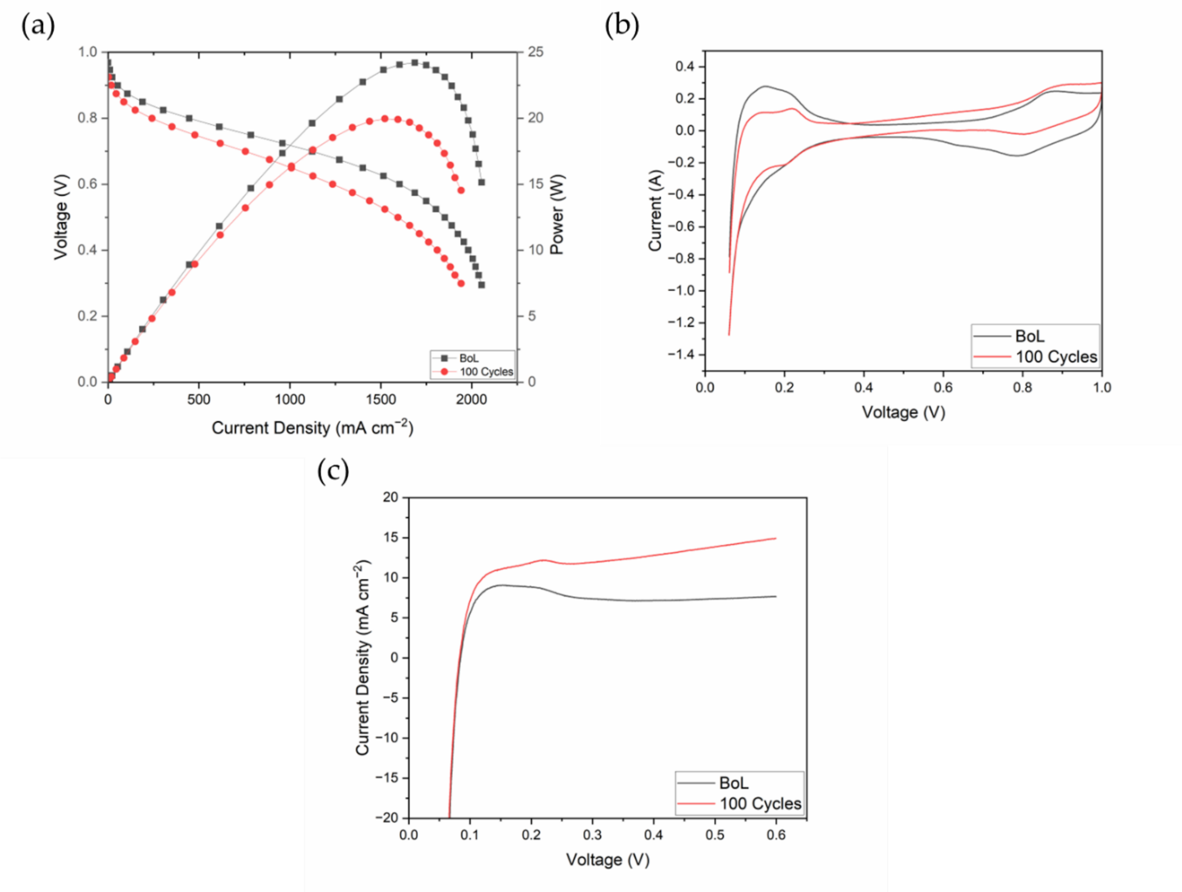

Figure 4-35: Electrochemical degradation analysis of the MPML scenario, comparing BoL and EoT. (a) Polarisation and power curve. (b) Cyclic voltammetry (CV) for comparison and electrochemical surface area (ECSA) estimation; a 31% ECSA drop occurred. (c) Linear sweep voltammetry.

The power cycle of the EoT cycle (100 cycles) for the MPML bus scenario was compared to the actual power demand, shown in Figure 4-36. It was seen from polarisation and power curves that the power demand has not dropped below the required power of 20 W after 100 cycles. However, inconsistencies between EoT power cycle and power demand were spotted due to gas lag or fuel starvation, which is a common occurrence for PEMFCs under high dynamic loads.

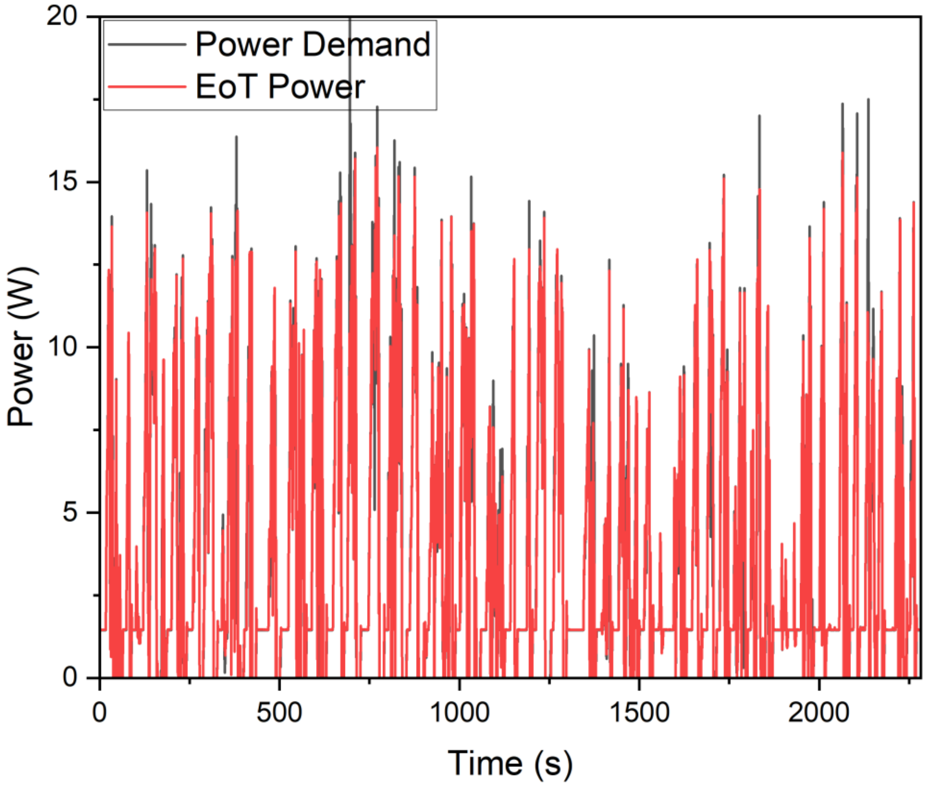

Figure 4-36: PEMFC power demand vs. EoT power cycle comparison for the MPML parallel bus scenario.

Figure 4-37 shows Nyquist plots of EIS collected at different current densities (100, 300, 800, and 1200 mA cm−2) and voltages (0.65 and 0.5 V) for the MPML parallel bus scenario under the Millbrook Westminster London Bus drive cycle. Both the fitted and unfitted curves are plotted. For most current densities and voltages, the most significant change between BoL and EoT occurred at the low-frequency intercept with the real axis and the height of the semicircles. The EIS collection at 0.5 V had the most significant increase in resistance.

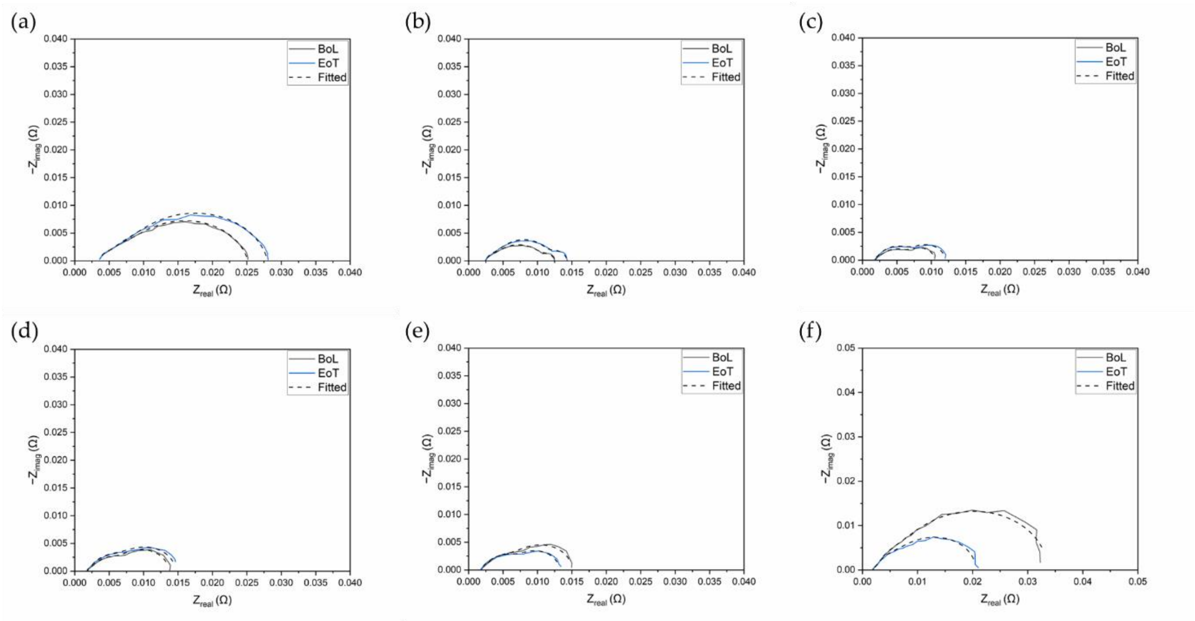

Figure 4-37: EIS Nyquist plots at different current densities and voltages for the MPML parallel bus scenario under the Millbrook Westminster London Bus drive cycle. (a) 100 mA cm^{-2}; (b) 300 mA cm^{-2}; (c) 800 mA cm^{-2}; (d) 1200 mA cm^{-2}; (e) 0.65 V; (f) 0.5 V.

More information can be extracted by fitting the Nyquist plots with the equivalent circuit. After fitting, different resistance values such as Ohmic resistance (R_{Ω}), anode (R_{an}) and cathode charge transfer resistance (R_{ca}), and mass transport resistance (R_m) can be interpolated, as shown in

Table 4-31. For all current densities, the changes in Ohmic resistance are negligible. In most current densities and voltages, the increase in cathode charge transfer resistance was the most dominant change between BoL to EoT, suggesting cathode degradation. Major mass transport increases were spotted between BoL and EoT at 300 mA cm^{-2} current density and 0.65 and 0.5 V voltages, which may suggest a reduced water content of the membrane [163]; interestingly, for the same current density and voltages, a decrease in charge transfer could also be spotted. For the case of the 300 mA cm^{-2} collection, charge transfer decreases occurred on the anode side, while for the case of the 0.65 and 0.5 V collection, charge transfer decreases occurred on both the anode and cathode sides.

Table 4-31: Resistance values for the MPML parallel bus scenario under the Millbrook Westminster London Bus drive cycle, interpolated from EIS equivalent circuit fitting, including Ohmic resistance (R_{Ω}), anode (R_{an}) and cathode charge transfer resistance (R_{ca}), and mass transport resistance (R_m).

Current density or voltage	R_{Ω} BoL (mΩ cm^2)	R_{Ω} EoT (mΩ cm^2)	R_{an} BoL (mΩ cm^2)	R_{an} EoT (mΩ cm^2)	R_{ca} BoL (mΩ cm^2)	R_{ca} EoT (mΩ cm^2)	R_m BoL (mΩ cm^2)	R_m EoT (mΩ cm^2)

(mA cm^{-2} or V)								
100 mA cm^{-2}	91.9	91.2	40.4	43.6	435	507	60.5	57.7
300 mA cm^{-2}	64.5	61.3	179	61.3	41.0	68.2	27.0	165
800 mA cm^{-2}	48.2	45.4	108	130	91.7	114	14.0	9.96
1200 mA cm^{-2}	47.2	45.3	107	130	169	178	16.6	11.3
0.65 V	46.9	44.8	113	47.4	198	148	16.9	88.5
0.5 V	48.3	46.6	157	16.3	616	123	16.9	329

4.7.3.1.2 NPML

The NPML scenario was assumed to be one of the most optimal setups for a parallel FCHEV bus scenario, where the PEMFC is not stressed to the maximum and the number of battery cells is kept to a minimum to reduce the weight of the heavier power system (battery pack). Figure 4-38 presents the electrochemical degradation analysis of the NPML cell operating power scenario. As shown in the polarisation and power curve in Figure 4-38a, at 600 mA cm^{-2}, the voltage decreased from 0.77 to 0.75 V between BoL and EoT, with a degradation rate of 2.6% or 0.041% h^{-1}. At 1200 mA cm^{-2}, the voltage decreased from 0.67 to 0.65 V between BoL and EoT, with a degradation rate of 3% or 0.047% h^{-1}, which was higher than the NREL results and 2020 DOE standards [162]. The maximum power dropped from 23 to 21 W, an 8.7% or 0.14% h^{-1} decrease. After 100 cycles, the PEMFC is still operating in the Ohmic region to achieve maximum power, which is considered an ideal operational region for PEMFCs. In addition, the PEMFC reaches its maximum power at a lowered current density after 100 cycles.

As shown in the CV graph in Figure 4-38b, the ECSA decreased from 79 to 73 m^2 g^{-1} between BoL and EoT, an 8.1% decrease. Figure 4-38c shows the LSV curve comparison between BoL and EoT. The cell is considered to be chemically stable at EoT according to DOE standards based on the LSV [137]. The hydrogen crossover rate increased from 1.03×10^{-6} to 1.21×10^{-6} mol s^{-1}, a 17% increase.

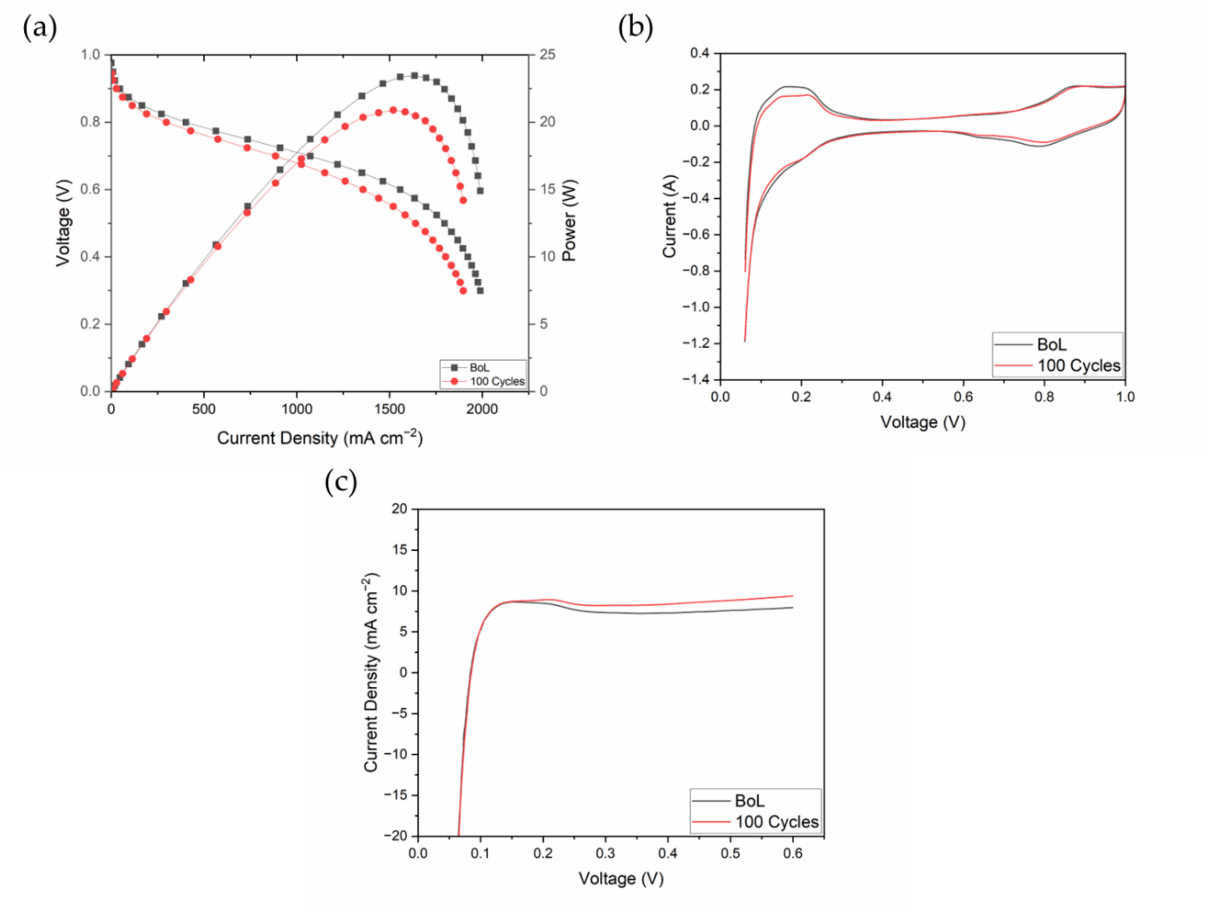

Figure 4-38: Electrochemical degradation analysis of the NPML scenario, comparing BoL and EoT. (a) Polarisation and power curve. (b) Cyclic voltammetry (CV) for comparison and electrochemical surface area (ECSA) estimation; an 8.09% ECSA drop occurred. (c) Linear sweep voltammetry.

The EoT power cycle (100 cycles) for the NPML bus scenario was extracted and compared to the power demand, shown in Figure 4-39. Typically, in a nominal PEMFC scenario, the PEMFC is still able to support the 10 W power demand after 100 cycles, which is also the case for the NPML scenario, as seen from polarisation curves. Most times, the EoT power cycle was able to follow the power demand. However, minor inconsistencies still occurred due to gas lag and fuel starvation.

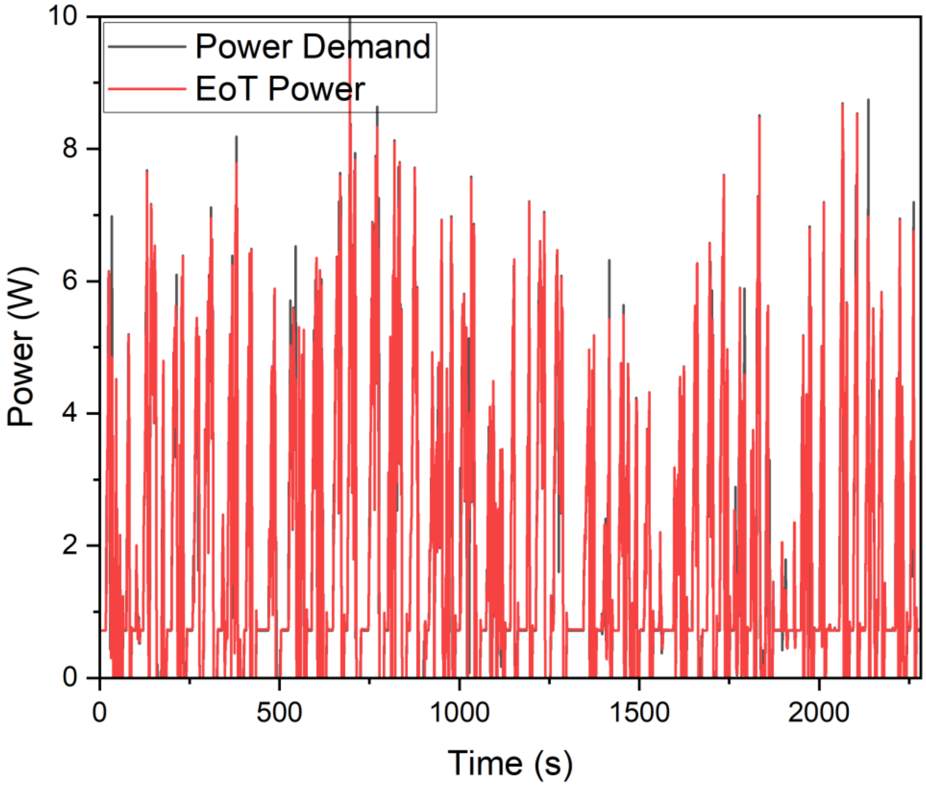

Figure 4-39: PEMFC power demand vs. EoT power cycle comparison for the NPML parallel bus scenario.

Figure 4-40 shows Nyquist plots of EIS collected at different current densities and voltages for the NPML scenario. For most current densities and voltages, the most visual change between BoL and EoT occurred at the low-frequency intercept with the real axis. This time, the height of the semicircles only had minor changes aside from the 1200 mA cm^{-2} and 0.5 V collections.

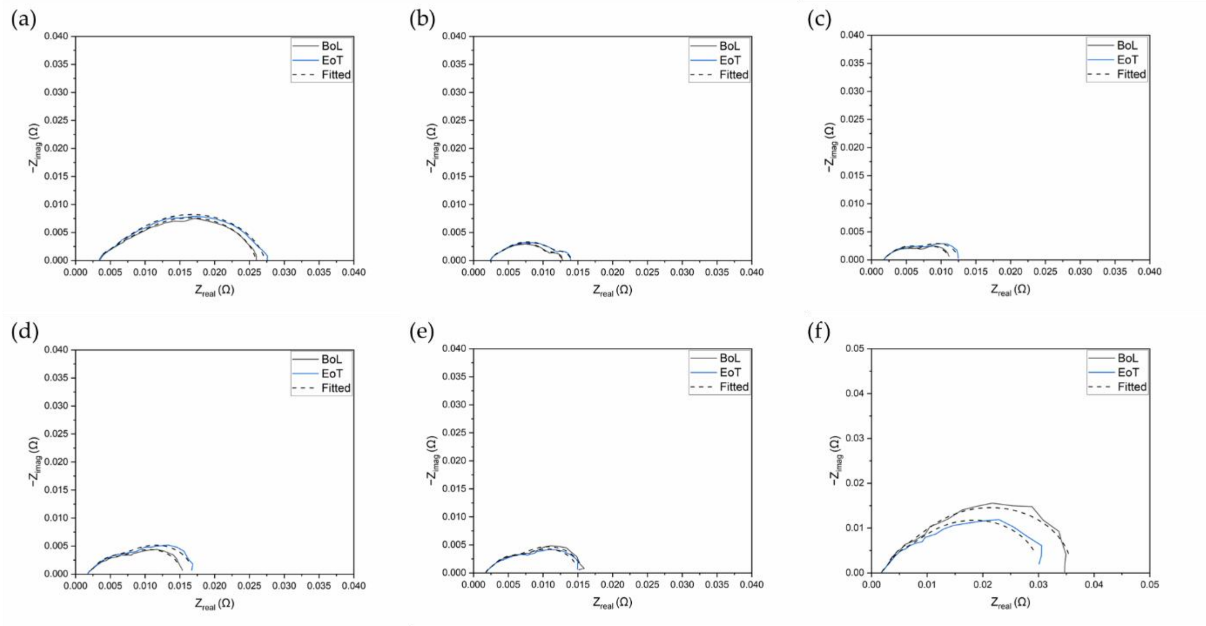

Figure 4-40: EIS Nyquist plots at different current densities and voltages for the NPML parallel bus scenario under the Millbrook Westminster London Bus drive cycle. (a) 100 mA cm^{-2}; (b) 300 mA cm^{-2}; (c) 800 mA cm^{-2}; (d) 1200 mA cm^{-2} (e) 0.65 V (f) 0.5 V

The resistance values for the NPML scenario were extracted and outlined in Table 4-32. Ohmic resistance changes are negligible for all current densities and voltages. Charge transfer resistance increases were the most significant during the 300 mA cm^{-2}, 0.65 V, and 0.5 V collections. Contradicting the MPML scenario, mass transfer resistance decreased while charge transfer resistance increased for these three current densities and voltages.

Table 4-32: Resistance values for the NPML parallel bus scenario under the Millbrook Westminster London Bus drive cycle, interpolated from EIS equivalent circuit fitting, including Ohmic resistance (R_{Ω}), anode (R_{an}) and cathode charge transfer resistance (R_{ca}), and mass transport resistance (R_{m}).

Current density or voltage (mA cm^{-2} or V)	**R_{Ω} BoL (mΩ cm^2)**	**R_{Ω} EoT (mΩ cm^2)**	**R_{an} BoL (mΩ cm^2)**	**R_{an} EoT (mΩ cm^2)**	**R_{ca} BoL (mΩ cm^2)**	**R_{ca} EoT (mΩ cm^2)**	**R_{m} BoL (mΩ cm^2)**	**R_{m} EoT (mΩ cm^2)**
100 mA cm^{-2}	90.5	87.3	45.3	38.5	449	510	64.3	45.8
300 mA cm^{-2}	60.6	63.4	75.7	212	57.5	49.9	123	24.6
800 mA cm^{-2}	45.9	46.6	119	132	99.8	118	12.5	12.7
1200 mA cm^{-2}	44.8	45.4	137	133	183	224	14.2	16.7
0.65 V	44.3	45.5	29.0	132	212	180	101	15.8
0.5 V	45.1	45.1	26.8	28.2	133	554	695	128

4.7.3.1.3 NPNL

The NPNL scenario is possible to maximise the durability of both the PEMFC and LiB while being the heaviest option. Figure 4-41 presents the electrochemical degradation analysis of the NPNL cell operating power scenario. As shown in the polarisation and power curve in Figure 4-41a, at 600 mA cm^{-2}, the voltage decreased from 0.75 to 0.72 V from BoL to EoT, a 4% or 0.06 %h^{-1} decrease. At 1200 mA cm^{-2}, the voltage decreased from 0.65 to 0.57 V between BoL and EoT, a degradation rate of 12% or 0.19% h^{-1}, much higher than NREL results and 2020 DOE standards [162]. This scenario currently has the highest voltage degradation rate at 1200 mA cm^{-2} out of all parallel bus cell operating power scenarios under the Millbrook Westminster London Bus drive cycle, even though the PEMFC counterpart is only running at nominal power. The maximum power dropped from 21 to 18 W, a 14% or 0.23% h^{-1} decrease. After 100 cycles, the PEMFC is still operating in the Ohmic region in order to reach maximum power, but is creeping close to the concentration region. The PEMFC reaches its maximum power at a significantly lowered current density after 100 cycles.

As shown in the CV graph in Figure 4-41b, the ECSA decreased from 80.1 to 68.5 m^2 g^{-1} between BoL and EoT, a 15% decrease. Figure 4-41c shows the LSV curve comparison between BoL and EoT. The cell is considered to be chemically stable at EoT according to DOE standards [137]. The hydrogen crossover rate increased from 7.58×10^{-7} to 8.46×10^{-7} mol s^{-1}, a 12% increase.

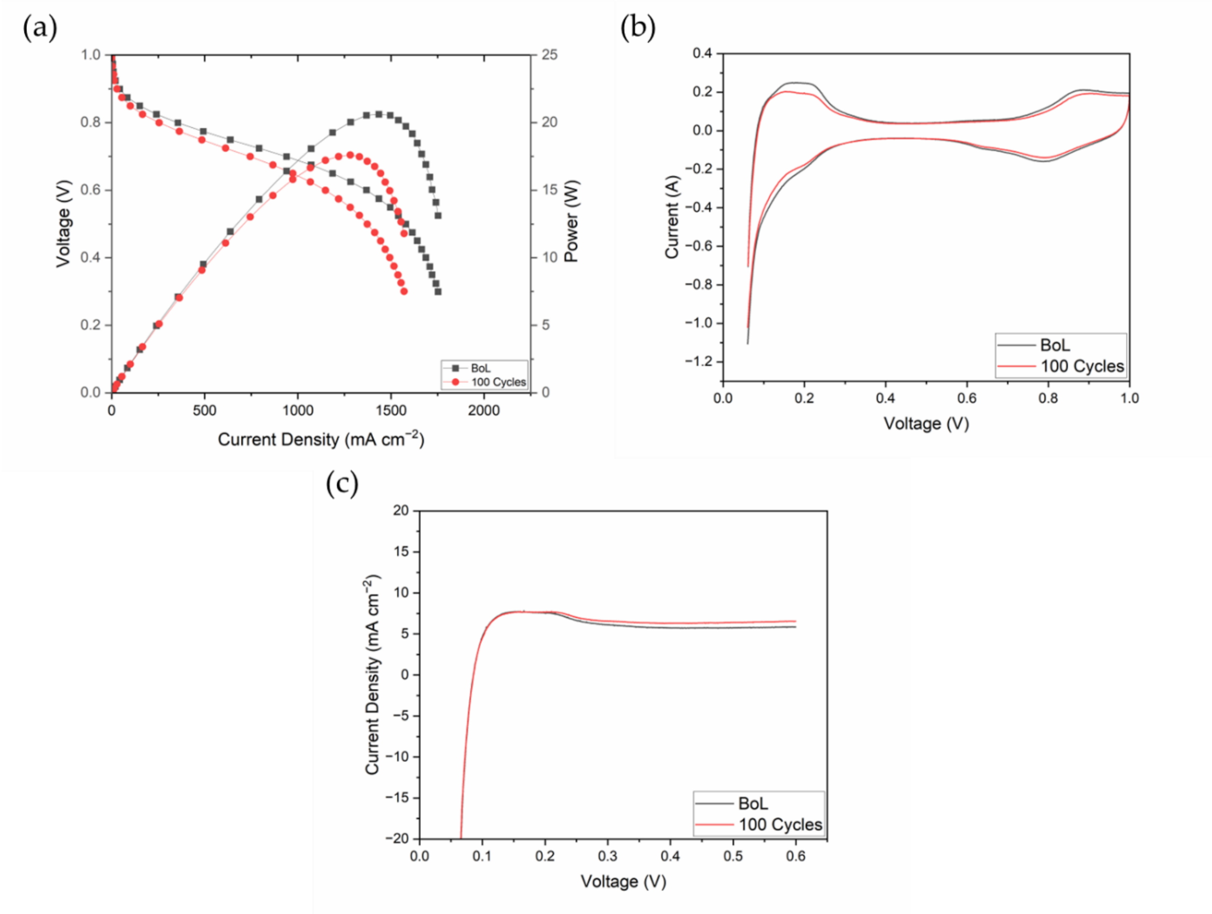

Figure 4-41: Electrochemical degradation analysis of the NPNL scenario, comparing BoL and EoT. (a) Polarisation and power curve. (b) Cyclic voltammetry (CV) for comparison and electrochemical surface area (ECSA) estimation; an 11.68% ECSA drop occurred. (c) Linear sweep voltammetry (LSV)

The EoT power cycle for the NPNL bus scenario was compared to the actual power demand, shown in Figure 4-42. As seen from polarisation curves, the PEMFC could still support the initial power demand of 10 W at EoT. At most timestamps, the EoT power cycle was able to follow the power demand. However, minor inconsistencies still occurred, which was to be expected as the Millbrook Westminster bus cycle is a highly dynamic drive cycle and can cause gas lag and fuel starvation.

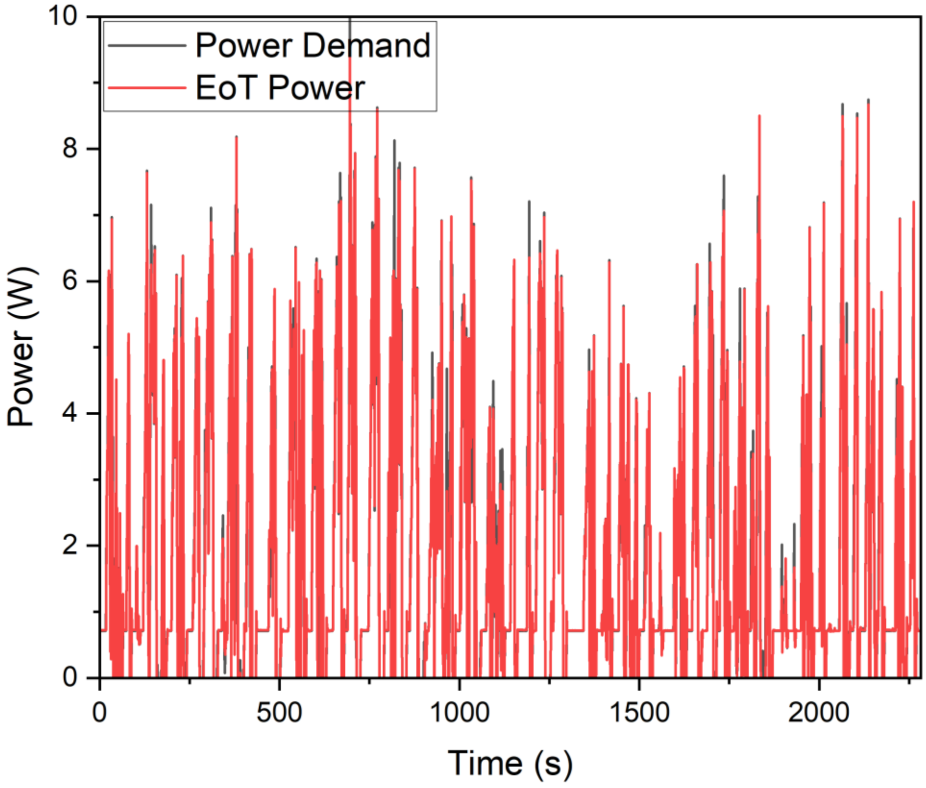

Figure 4-42: PEMFC power demand vs. EoT power cycle comparison for the NPNL parallel bus scenario.

Figure 4-43 shows Nyquist plots of both EIS collected at different current densities and voltages for the NPNL scenario. For all galvanostatic EIS collections, the most visual change between BoL and EoT occurred at the low-frequency intercept with the real axis.

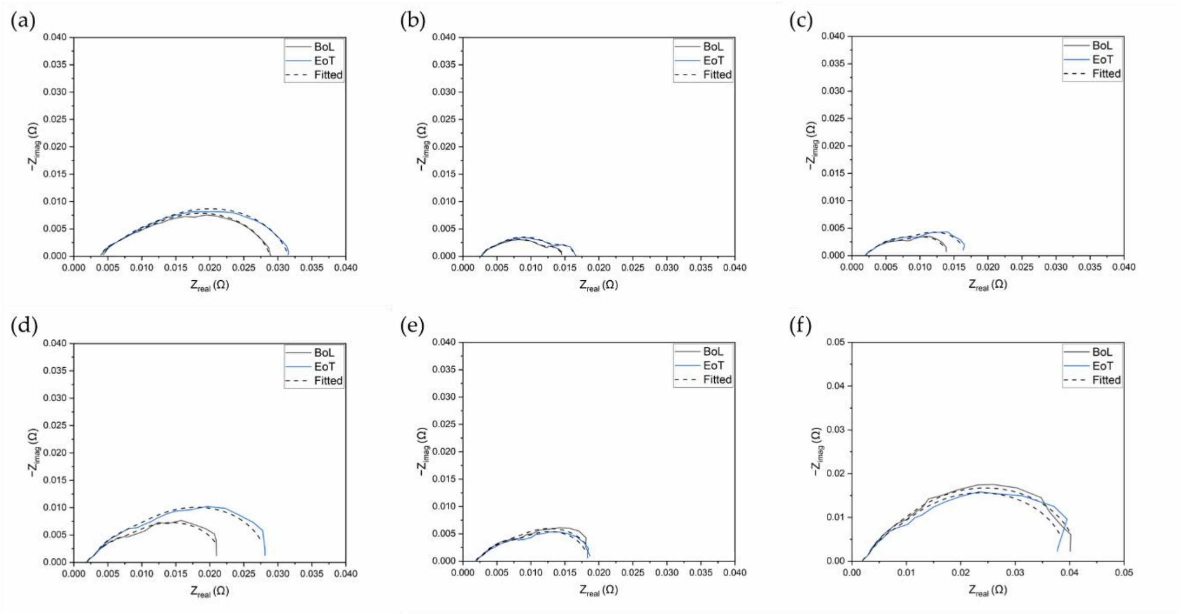

Figure 4-43: EIS Nyquist plots at different current densities and voltages for the NPNL parallel bus scenario under the Millbrook Westminster London Bus drive cycle. (a) 100 mA cm^{-2}; (b) 300 mA cm^{-2}; (c) 800 mA cm^{-2}; (d) 1200 mA cm^{-2} (e) 0.65 V (f) 0.5 V

The resistance values for the NPNL scenario were extracted and outlined in Table 4-33. Changes in Ohmic resistance are negligible for all current densities and voltages. The increases of charge and mass transfer resistances in this NPNL scenario are less significant than in other scenarios. For the 100 mA cm^{-2} collection, there was an increase in mass transfer resistance and a decrease in anode charge transfer resistance.

Table 4-33: Resistance values for the MPML parallel bus scenario under the Millbrook Westminster London Bus drive cycle, interpolated from EIS equivalent circuit fitting, including Ohmic resistance (R_{Ω}), anode (R_{an}) and cathode charge transfer resistance (R_{ca}), and mass transport resistance (R_m).

Current density or voltage (mA cm^{-2} or V)	R_{Ω} BoL (mΩ cm²)	R_{Ω} EoT (mΩ cm²)	R_{an} BoL (mΩ cm²)	R_{an} EoT (mΩ cm²)	R_{ca} BoL (mΩ cm²)	R_{ca} EoT (mΩ cm²)	R_m BoL (mΩ cm²)	R_m EoT (mΩ cm²)
100 mA cm^{-2}	103	112	96.7	56.3	470	538	50.5	83.2
300 mA cm^{-2}	69.4	72.8	203	232	59.4	72.7	32.6	33.0
800 mA cm^{-2}	50.4	53.3	152	181	131	165	14.6	16.8
1200 mA cm^{-2}	49.2	50.9	158	194	318	441	18.9	21.5
0.65 V	48.5	51.8	167	160	245	227	14.3	19.6
0.5 V	49.3	50.1	187	186	778	728	20.6	21.1

4.7.3.1.4 MPML vs. NPML vs. NPNL in terms of PEMFC Degradation

Table 4-34 outlines the degradation between all scenarios, showcasing voltage decrease, maximum power decrease, and ECSA decrease. The MPML scenario had the most voltage decrease at 600 mA cm^{-2}, with a decrease of 6.5% or 0.1% h^{-1}. However, it had a slightly lower voltage decrease at 1200 mA cm^{-2} than the NPNL scenario, 11% vs. 12%, respectively. Both the MPML and NPNL also had higher maximum power decreases of 17% and 14%, respectively, compared to the low 8.7% decrease of the NPML scenario. The maximum PEMFC (MP) scenario experienced more severe ECSA loss when compared to the nominal PEMFC (NP) scenarios, almost four times the percentage decrease of the NPML scenario. This was to be expected as the PEMFC was operating at double the power in the MP scenarios when compared to the NP scenarios.

Table 4-34: Comparison of performance drops between all scenarios of the parallel bus powertrain under the Millbrook Westminster London Bus drive cycle.

Operating Power	Voltage decrease at 600 mA cm^{-2} (%)	Voltage decrease at 600 mA cm^{-2} (% h^{-1})	Voltage decrease at 1200 mA cm^{-2} (%)	Voltage decrease at 1200 mA cm^{-2} (% h^{-1})	Maximum power decrease (%)	Maximum power decrease (% h^{-1})	ECSA decrease (%)
MPML	6.5	0.10	11	0.17	17	0.26	31
NPML	2.6	0.041	3.0	0.047	8.7	0.14	8.1
NPNL	4.0	0.060	12	0.19	14	0.23	15

4.7.3.2 LiB Degradation Analysis

4.7.3.2.1 Charge Capacity

A list of EoT capacity checks for all cell operating power scenarios for the parallel bus powertrain under the Millbrook London Westminster Bus drive cycle is shown in Table 4-35. These cells were subjected to 100 drive cycles of endurance testing. Interestingly, all cell operating power scenarios had similar capacity fades, ranging from 1 to 1.2 %, when compared to collected pristine cell's capacity of 4.88 Ah. Again, in this powertrain, having the battery running at a nominal operating power did not necessarily suggest that the capacity fade would be less.

Table 4-35: Capacity check for all cell operating power scenarios (MPML, NPML, and NPNL) for a parallel bus under the Millbrook London Westminster Bus drive cycle.

Cell operating power	Capacity (Ah)
BoL	4.88
MPML	4.83
NPML	4.82
NPNL	4.82

4.7.3.2.2 EIS

Nyquist plots of the collected EIS are shown in Figure 4-44; both fitted (dashed line) and unfitted (solid line) are shown. This time, running at the LiB at nominal operating power resulted in less overall impedance increase. Graphically, MPML and NPML cell operating power scenarios has a similar level of impedance increase from BoL. An extracted resistance data table is shown in Table 4-36, showing both Ohmic (R_{Ω}) and charge transfer (R_{ct}) resistance. It can be spotted that the NL scenarios had less charge transfer resistance increase than the ML scenarios. The maximum charge transfer resistance was spotted in the MPML scenario with an increase of 92% from BoL. Interestingly, the NPNL charge transfer resistance actually had a lesser value than BoL, though only slightly. The Ohmic resistances are relatively similar for all scenarios and only had minor increases.

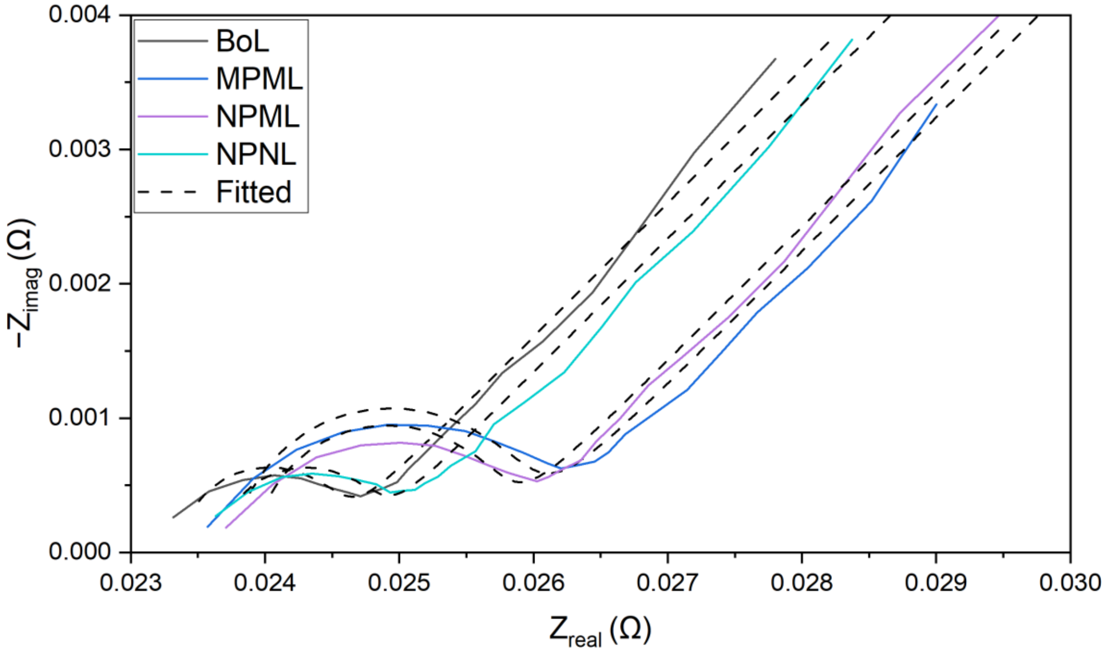

Figure 4-44: LiB M50 EIS Nyquist plot comparison between different cell operating scenarios (MPML, NPML, and NPNL) for the parallel bus powertrain under the Millbrook London Westminster Bus drive cycle. The graph shows both fitted (dashed lines) and unfitted (solid lines) curves. Certain resistance values such as Ohmic and charge transfer resistance can be extracted from fitted curves. The EIS was collected at an amplitude of 10 mV within a frequency range of 10000 to 0.01 Hz.

Table 4-36: Extracted Ohmic (R_{Ω}) and charge transfer (R_{ct}) resistance values from fitting the EIS into an equivalent circuit.

Cell operating power	R_{Ω} (mΩ)	R_{ct} (mΩ)
BoL	23.3	1.06
MPML	23.7	2.03
NPML	23.8	1.68

NPNL	23.6	1.04

4.8 PEMFC and LiB Drive Cycle Endurance Testing for Fuel Cell Range Extender (FCREx) Architecture

This section discusses the results of drive cycle endurance testing done on the FCREx powertrain architecture. PEMFC degradation is discussed first, then LiB degradation. PEMFC degradation includes polarisation and power curves, CV and ECSA, LSV, and EIS analysis. LiB degradation includes analysis such as capacity fade and EIS. Figure 4-45 shows the PEMFC power cycle profiles at the cell level for the different cell operating scenarios tested, while Figure 4-46 shows the corresponding LiB power profiles. In these two figures, negative power suggests that power is drawn from the source, and positive power suggests that the power source is being charged.

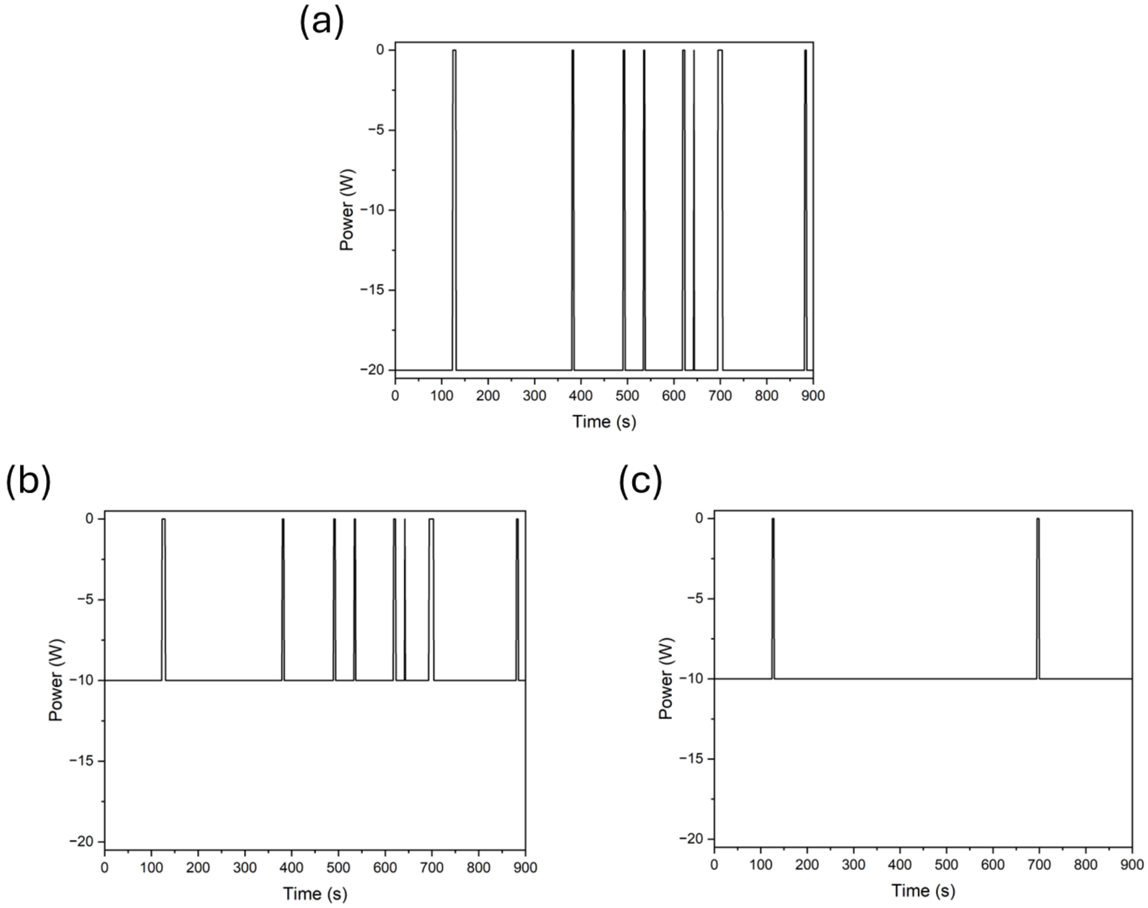

Figure 4-45: PEMFC power cycle profiles of different cell operating power scenarios for FCREx HGV. (a) MPML (b) NPML (c) NPNL

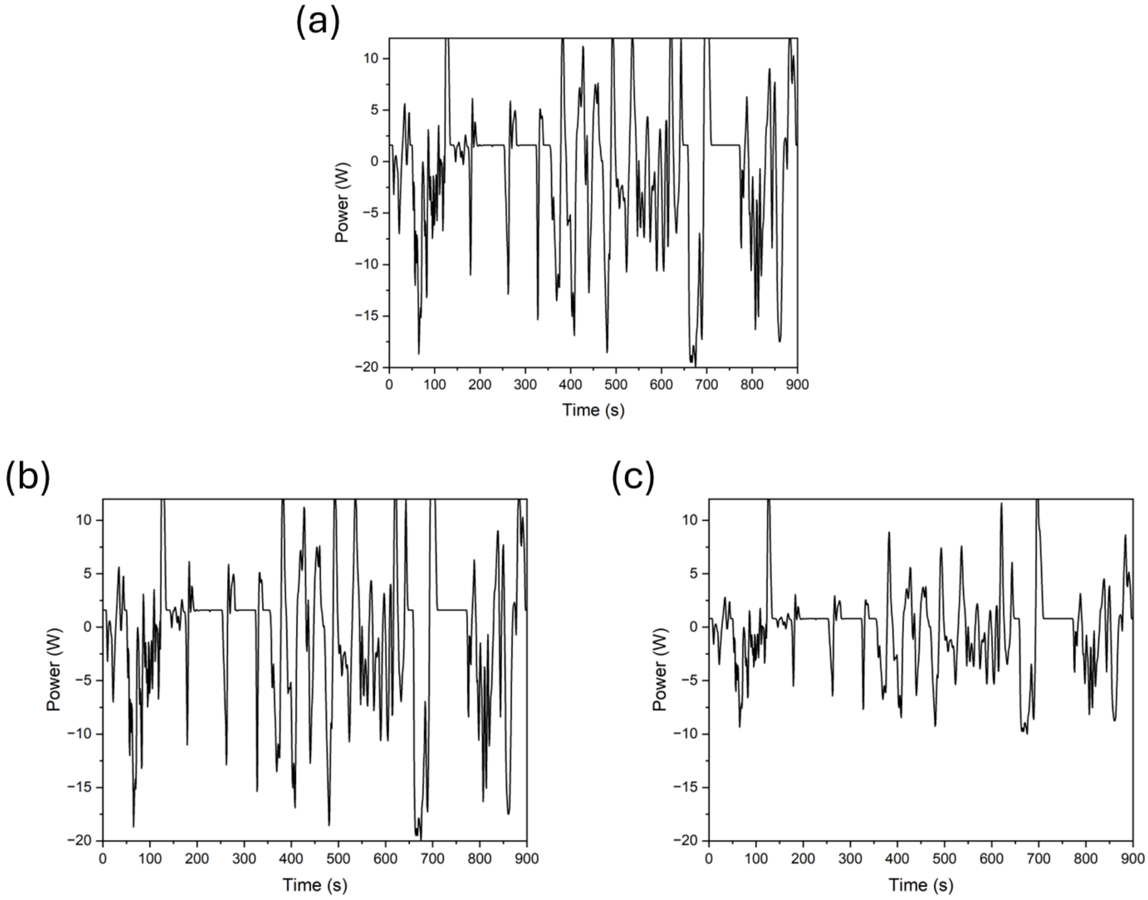

Figure 4-46: LiB power cycle profiles of different cell operating power scenarios for FCREx HGV. (a) MPML (b) NPML (c) NPNL

4.8.1 FCREx HGV

Similar to the parallel HGB and bus experimental data sections, the FCREx HGV section's PEMFC data is broken down into different subsections covering the MPML, NPML, and NPNL cell operating power scenarios. The polarisation, CV, LSV, and EIS data can be found in each subsection. There is an extra subsection at the end explaining the advantages and disadvantages of each cell operating power scenario. For the LiB data, all cell operating power scenarios are discussed in conjunction with one another.

4.8.1.1 PEMFC Degradation Analysis

A general electrochemical degradation overview is presented in three subsections featuring the different cell operating power scenarios: MPML, NPML, and NPNL. The last subsection provides a comparison between all scenarios, discussing the relative merits and demerits of the design choice for vehicles.

4.8.1.1.1 MPML

In theory, the MPML cell operating scenario has the capability of having the lightest power source configuration, allowing a reduced vehicle kerb, and gross vehicle mass (GVM); with the possible trade-off of more degradation to the power sources (each cell is stressed to the greatest extent). Figure 4-47 presents the electrochemical degradation analysis of the MPML cell operating power scenario. As shown in the polarisation and power curve in Figure 4-47(a), at 600 mA cm^{-2}, the voltage decreased from 0.73 to 0.72 V between BoL and 100 WHVC cycles (EoT), with a degradation rate of 1.4% or 0.055% h^{-1}. At 1200 mA cm^{-2}, the voltage decreased from 0.60 to 0.58 V between BoL and EoT, suggesting a degradation rate of 3.3% or 0.13% h^{-1}. By utilising the MPML configuration, the degradation rate at 1200 mA cm^{-2} was higher than NREL and DOE lab tests. The maximum power dropped from 20 to 17 W, a 15% or 0.6% h^{-1} decrease. This maximum power decrease suggests a major concern for this operating scenario, in that the PEMFC would no longer be capable of supporting required allocated power demands (20 W or 0.8 W cm^{-2} constant power) after the vehicle break-in period. In a real-life scenario looking to utilise a similar configuration to the MPML operating power, it is suggested that the PEMFCs are not stressed to the absolute maximum, but rather slightly below the maximum capable power, to account for this power decrease after the vehicle break-in period.

As shown in the cyclic voltammetry plot in Figure 4-47(b), the ECSA decreased from 64.2 to 56.7 m^2 g^{-1} between BoL and EoT, a 12% decrease. Figure 4-47(c) shows the LSV curve comparison between BoL and EoT. According to DOE standards, if the equilibrium part of the LSV exceeds a current density of 20 mA cm^{-2}, the cell is considered to be chemically unstable with severe hydrogen crossover [137], which is not the case for the EoT of this scenario. The hydrogen crossover rate changed from 1.17×10^{-6} to 1.36×10^{-6} mol s^{-1} from BoL to EoT, a 16% increase.

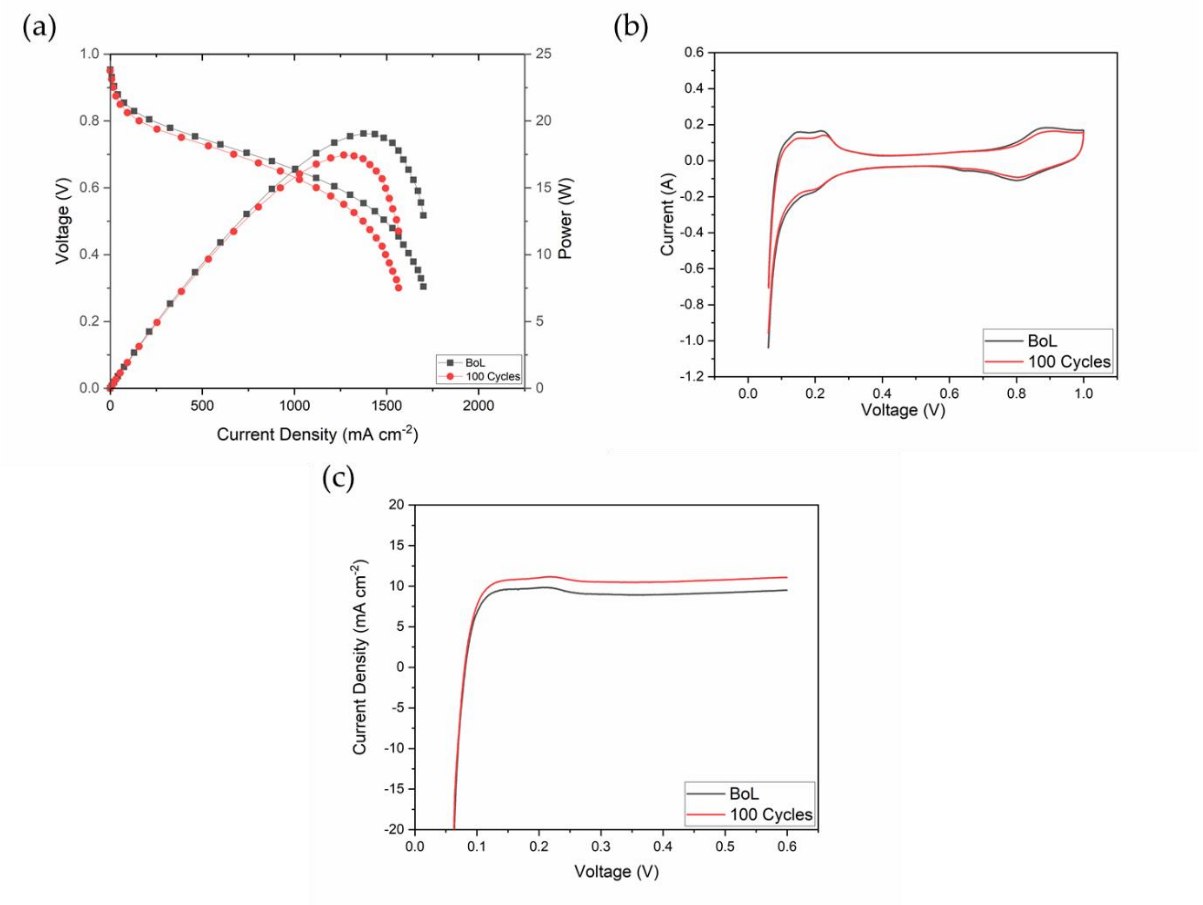

Figure 4-47: Electrochemical degradation analysis of MPML scenario, comparing between BoL and EoT. (a) Polarisation and power curve. (b) Cyclic voltammetry (CV) for comparison and electrochemical surface area (ECSA) estimation; an 11.68% ECSA drop occurred. (c) Linear sweep voltammetry (LSV).

Figure 4-48 shows Nyquist plots of both potentiostatic and galvanostatic EIS collected at different current densities (100, 300, 800, and 1200 mA cm^{-2}) and voltages (0.65 and 0.5 V) for the MPML scenario. Both the fitted and unfitted curves are plotted. For most current densities and voltages, the most significant change between BoL and EoT occurred at the low-frequency intercept with the real axis and the height of the semicircles. For the collection at 100 mA cm^{-2}, the largest changes occurred at the high-frequency intercept with the real axis and the height of the semicircles. The high-frequency intercept with the real axis infers the Ohmic resistance (R_{Ω}).

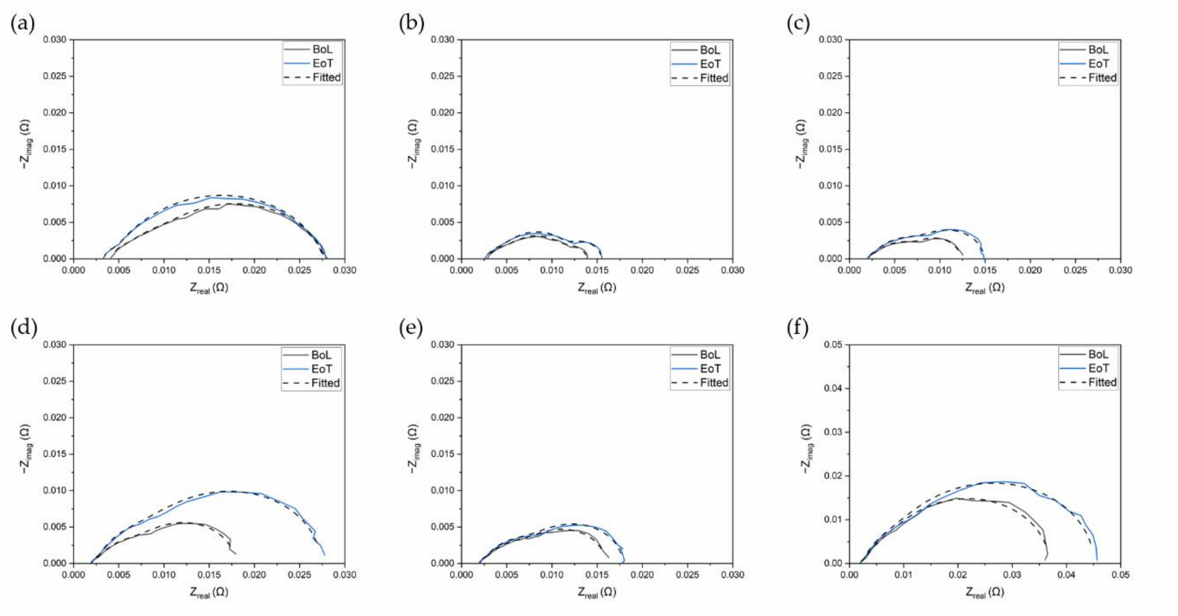

Figure 4-48: Galvanostatic and potentiostatic EIS Nyquist plots at different current densities and voltages for the MPML scenario. (a) 100 mA cm^{-2} (b) 300 mA cm^{-2} (c) 800 mA cm^{-2} (d) 1200 mA cm^{-2} (e) 0.65V (f) 0.5 V

More information can be extracted by fitting the Nyquist plots with the equivalent circuit outlined in Figure 3-6. After fitting, different resistance values such as Ohmic resistance (R_{Ω}), anode (R_{an}) and cathode charge transfer resistance (R_{ca}), and mass transport resistance (R_{m}) can be interpolated, as shown in Table 4-37. Aside from the collection at 100 mA cm^{-2}, which is within the Ohmic region, all other instances of Ohmic resistance are negligible. In most current densities and voltages, the increase in cathode charge transfer resistance was the most dominant change between BoL to EoT, suggesting cathode degradation. For 1200 mA cm^{-2}, both anode and cathode charge transfer resistance decreased; however, there has been an increase in mass transport resistance. This corresponds with the polarisation curve results shown in Figure 4-47(a), as the 1200 mA cm^{-2} current density is within the charge transfer region at BoL but has shifted to the mass transport region at EoT, a non-favourable operating region for PEMFCs. An increase in mass transport may suggest a reduced water content of the membrane [163].

Table 4-37: Resistance values for the MPML scenario interpolated from EIS equivalent circuit fitting, including Ohmic resistance (R_Ω), anode (R_{an}) and cathode charge transfer resistance (R_{ca}), and mass transport resistance (R_m).

Current density or voltage (mA cm^{-2} or V)	**R_Ω BoL (mΩ cm^2)**	**R_Ω EoT (mΩ cm^2)**	**R_{an} BoL (mΩ cm^2)**	**R_{an} EoT (mΩ cm^2)**	**R_{ca} BoL (mΩ cm^2)**	**R_{ca} EoT (mΩ cm^2)**	**R_m BoL (mΩ cm^2)**	**R_m EoT (mΩ cm^2)**
100 mA cm^{-2}	108	84.2	45.8	32.0	475	551	66.9	24.7
300 mA cm^{-2}	72.6	64.5	77.4	79.2	74.4	94.8	123	148
800 mA cm^{-2}	53.6	50.7	120	15.3	116	147	18.3	159
1200 mA cm^{-2}	51.4	49.1	137	19.2	241	176	17.9	440
0.65 V	51.5	49.6	136	14.6	195	152	16.5	229
0.5 V	51.7	49.0	156	206	693	855	19.4	16.8

4.8.1.1.2 NPML

The NPML scenario was assumed to be one of the most optimal setups for a range-extender FCHEV, where the PEMFC is not stressed to the maximum and the number of battery cells is kept to a minimum to reduce the weight of the heavier power system (battery pack). Figure 4-49 presents the electrochemical degradation analysis of the NPML cell operating power scenario. As shown in the polarisation and power curve in Figure 4-49(a), at 600 mA cm^{-2}, the voltage decreased from 0.76 to 0.75 V between BoL and EoT, a degradation rate of 1.3% or 0.053% h^{-1}. At 1200 mA cm^{-2}, the voltage decreased from 0.66 V to 0.65 V between BoL and EoT, a degradation rate of 1.5% or 0.061% h^{-1}, higher than NREL results and 2020 DOE standards [162]. The maximum power dropped from 24 to 23 W, a 4.2% or 0.17% h^{-1} decrease.

As shown in the CV graph in Figure 4-49(b), the ECSA decreased from 75.5 to 68.3 m^2 g^{-1} between BoL and EoT, a 9.5% decrease. Figure 4-49(c) shows the LSV curve comparison between BoL and EoT. The cell is considered to be chemically stable at EoT according to DOE standards based on the LSV. The hydrogen crossover rate increased from 8.16×10^{-7} to 9.59×10^{-7} mol s^{-1}, an 18% increase.

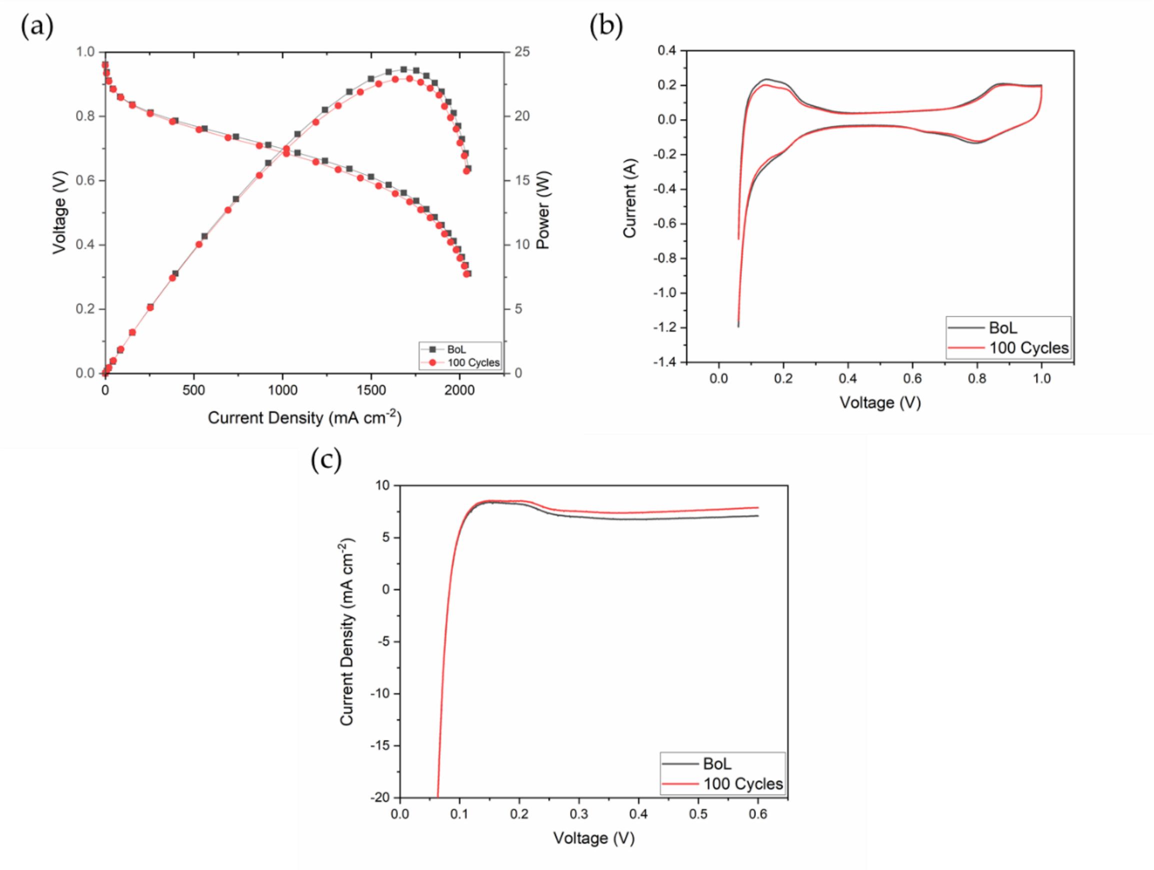

Figure 4-49: Electrochemical degradation analysis of NPML scenario. (a) Polarisation and power curve. (b) Cyclic voltammetry (CV) for comparison and electrochemical surface area (ECSA) estimation. (c) Linear sweep voltammetry (LSV).

Figure 4-50 shows Nyquist plots of both potentiostatic and galvonaostatic EIS collected at different current densities and voltages for the NPML scenario. For most current densities and voltages, the most visual change between BoL and EoT occurred at the low-frequency intercept with the real axis.

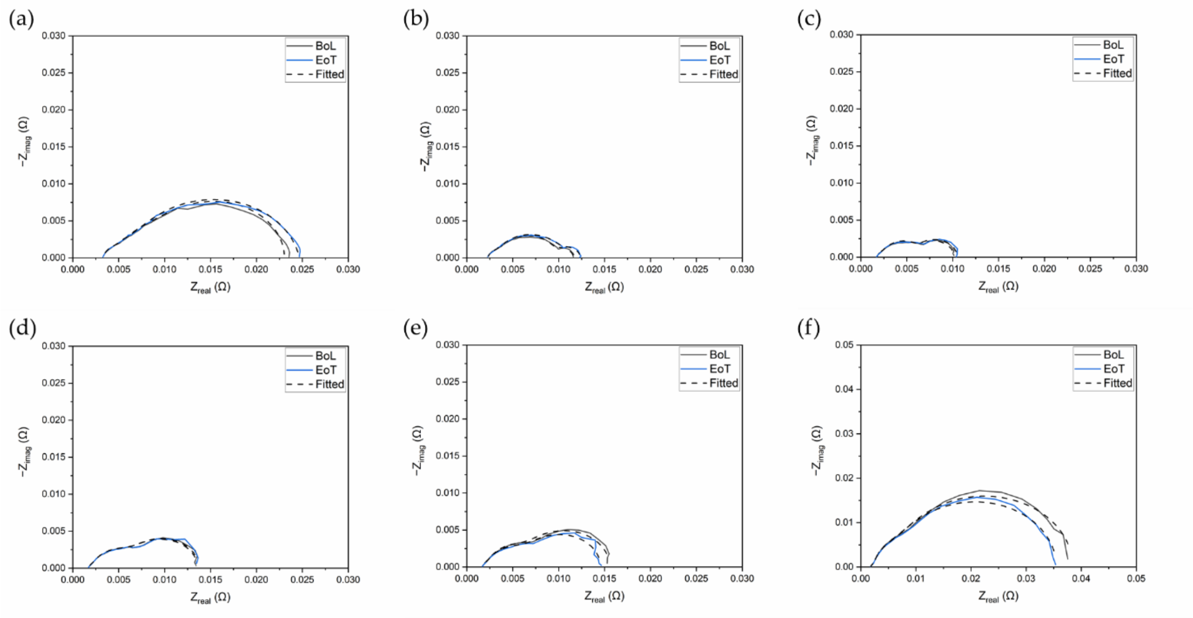

Figure 4-50: Galvanostatic and potentiostatic EIS Nyquist plots at different current densities and voltages for the NPML scenario. (a) 100 mA cm^{-2} (b) 300 mA cm^{-2} (c) 800 mA cm^{-2} (d) 1200 mA cm^{-2} (e) 0.65V (f) 0.5 V

The resistance values for the NPML scenario were extracted and outlined in Table 4-38. Mass transport resistance is negligible for all current densities and voltages. Anode and cathode charge transfer resistances were the main forms of impedance increase from BoL to EoT throughout most current densities and voltages. A severe mass transfer resistance was also spotted at 0.5 V, which can suggest a lowered water content of the cell [163].

Table 4-38: Resistance values for the NPML scenario interpolated from EIS equivalent circuit fitting, including Ohmic resistance (R_{Ω}), anode (R_{an}) and cathode charge transfer resistance (R_{ca}), and mass transport resistance (R_m).

Current density or voltage (mA cm^{-2} or V)	**R_{Ω} BoL (mΩ cm^2)**	**R_{Ω} EoT (mΩ cm^2)**	**R_{an} BoL (mΩ cm^2)**	**R_{an} EoT (mΩ cm^2)**	**R_{ca} BoL (mΩ cm^2)**	**R_{ca} EoT (mΩ cm^2)**	**R_m BoL (mΩ cm^2)**	**R_m EoT (mΩ cm^2)**
100 mA cm^{-2}	84.0	83.8	52.7	32.6	89.8	455	350	45.1
300 mA cm^{-2}	56.9	57.9	49.6	183	51.1	46.3	133	22.2
800 mA cm^{-2}	44.2	44.4	108	20.9	91.8	107	10.1	90.2
1200 mA cm^{-2}	43.5	43.8	120	113	168	176	8.80	10.7
0.65 V	42.3	43.8	26.2	116	224	193	96.8	10.9
0.5 V	45.1	45.4	18.1	15.2	769	121	129	705

4.8.1.1.3 NPNL

The NPNL scenario is a configuration that maximises the durability of both the PEMFC and LiB; it is also the heaviest option. Figure 4-51 presents the electrochemical degradation analysis of the NPNL cell operating power scenario. As shown in the polarisation and power curve in Figure 4-51(a), at 600 mA cm^{-2}, the voltage stayed at a consistent value of 0.77 V between BoL and EoT. At 1200 mA cm^{-2}, the voltage decreased from 0.69 V to 0.68 V between BoL and EoT, suggesting a degradation rate of 1.5% or 0.058% h^{-1}, higher than NREL results and 2020 DOE standards [162]. The maximum power dropped from 25 to 24 W, a 4% or 0.16% h^{-1} decrease.

As shown in the CV graph in Figure 4-51(b), the ECSA decreased from 74.4 to 68.4 m^2 g^{-1} between BoL and EoT, an 8.06% decrease. Figure 4-51(c) shows the LSV curve comparison between BoL and EoT. The cell is considered to be chemically stable at EoT according to DOE standards. The hydrogen crossover rate increased from 1.05 × 10^{-6} to 1.11 × 10^{-6} mol s^{-1}, an 5.7% increase.

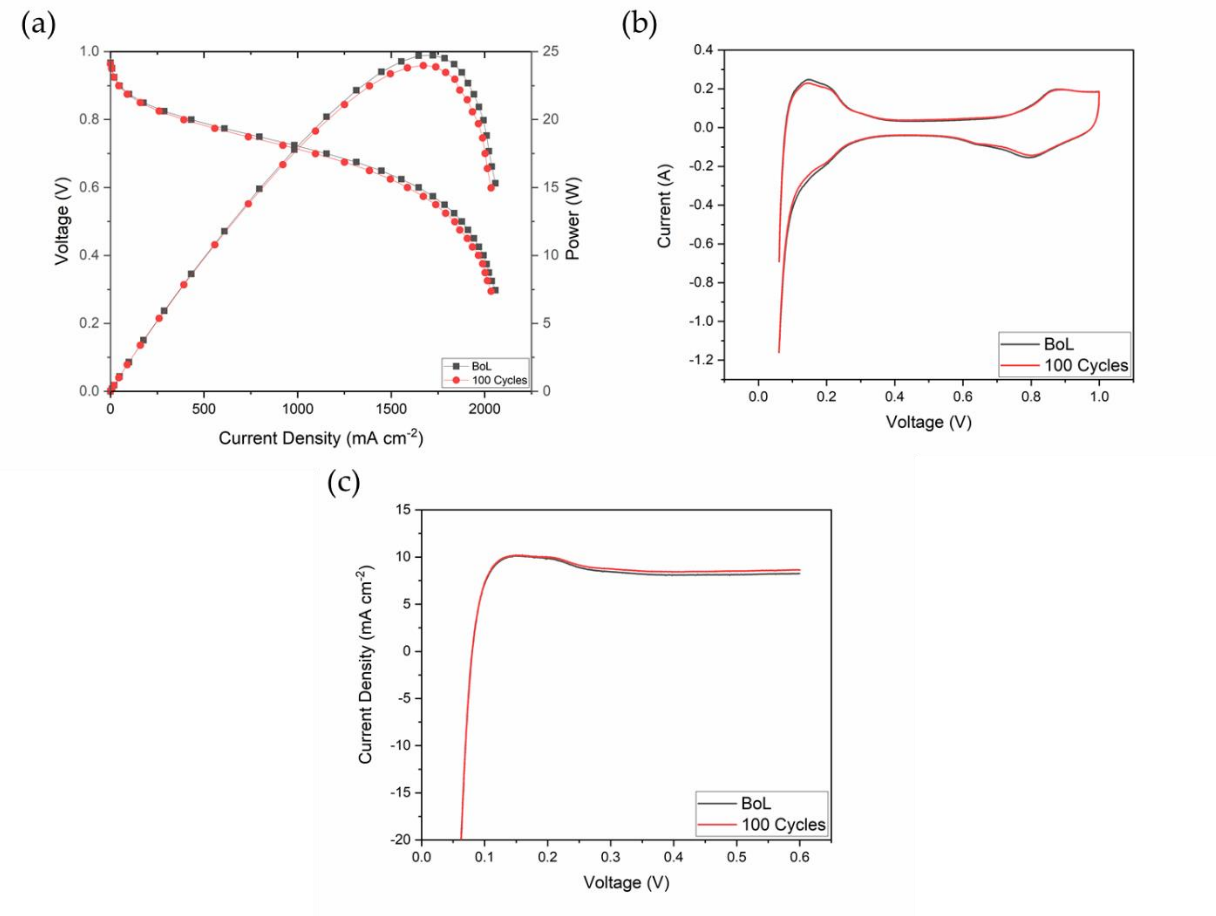

Figure 4-51: Electrochemical degradation analysis of NPNL scenario. (a) Polarisation and power curve. (b) Cyclic voltammetry (CV) for comparison and electrochemical surface area (ECSA) estimation. (c) Linear sweep voltammetry (LSV).

Figure 4-52 shows Nyquist plots of both potentiostatic and galvonaostatic EIS collected at different current densities and voltages for the NPNL scenario. For the galvanostatic EIS collections, the most visual change between BoL and EoT occurred at the low-frequency intercept with the real axis. For the potentiostatic EIS collections, the height of the semicircles increased.

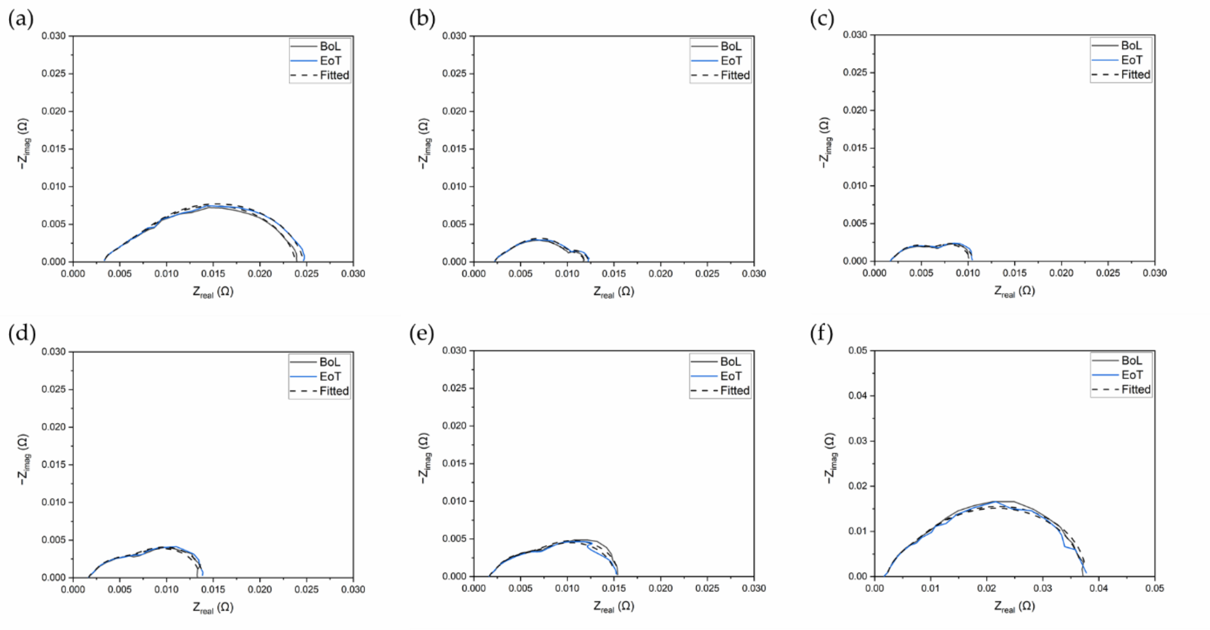

Figure 4-52: Galvanostatic and potentiostatic EIS Nyquist plots at different current densities and voltages for the NPNL scenario. (a) 100 mA cm^{-2} (b) 300 mA cm^{-2} (c) 800 mA cm^{-2} (d) 1200 mA cm^{-2} (e) 0.65V (f) 0.5 V

The resistance values for the NPNL scenario were extracted and outlined in Table 4-39. R_{Ω} is negligible for all current densities and voltages. Only minor resistances were spotted in this scenario, most of which involve the increase of R_m, especially at 300 mA cm^{-2}.

Table 4-39: Resistance values for the NPNL scenario interpolated from EIS equivalent circuit fitting, including Ohmic resistance (R_{Ω}), anode (R_{an}) and cathode charge transfer resistance (R_{ca}), and mass transport resistance (R_m).

Current density or voltage (mA cm^{-2} or V)	**R_{Ω} BoL (mΩ cm^2)**	**R_{Ω} EoT (mΩ cm^2)**	**R_{an} BoL (mΩ cm^2)**	**R_{an} EoT (mΩ cm^2)**	**R_{ca} BoL (mΩ cm^2)**	**R_{ca} EoT (mΩ cm^2)**	**R_m BoL (mΩ cm^2)**	**R_m EoT (mΩ cm^2)**
100 mA cm^{-2}	85.0	84.3	31.5	32.9	425	450	54.6	49.7
300 mA cm^{-2}	57.6	54.7	175	68.7	40.5	55.3	22.0	128
800 mA cm^{-2}	43.4	43.0	110	112	91.8	97.9	9.80	10.6
1200 mA cm^{-2}	42.5	42.1	125	123	163	173	8.90	9.40
0.65 V	42.5	41.7	124	141	209	187	12.0	8.20
0.5 V	43.9	43.8	153	166	732	703	14.2	12.4

4.8.1.1.4 MPML vs. NPML vs. NPNL in Terms of PEMFC Degradation

While the performance decreases align with general expectations in certain instances the magnitude of the degradation was comparatively large. Table 4-40 outlines the degradation between all scenarios, showcasing voltage decrease, maximum power decrease, and ECSA decrease. Voltage decrease was minimal between most scenarios, with some scenarios not experiencing any voltage decrease, such as at 600 mA cm^{-2} for NPNL. For the MPML scenario, however, a higher voltage drop (3.33%) was experienced at 1200 mA cm^{-2}. At this current density, the polarisation curve was at the end of the charge transfer region at EoT. When the curve migrates to the mass transport region, it is then considered a non-optimal region for PEMFCs to operate in. This also explains the high maximum power decrease for this scenario. PEMFCs typically reach their maximum power output near the end of the charge transfer region. In the EoT polarisation curve of the MPML scenario, the end of the charge transfer curve was reached at a lower current density and voltage than in other scenarios. The maximum power decreases in the other scenarios are similar, ranging from 4 to 4.2%.

The maximum PEMFC (MP) scenario experienced more severe ECSA loss when compared to the nominal PEMFC (NP) scenarios, as high as double the percentage decrease. Interestingly, the scenario that had the most voltage and maximum power decrease, MPML, did not have the most severe ECSA loss. ECSA estimations only capture catalyst accessibility and is only representative of the activation and charge transfer region. Two main types of degradation mechanisms measured by ECSA are particle coalescence and Ostwald ripening. Particle coalescence refers to smaller nanoparticles turning into larger ones, producing less surface area, making them more difficult to access [135]. Ostwald ripening refers to the dissolution and re-deposition of small nanoparticles onto larger ones to reach a more thermodynamically stable state [135][164]. The reduction of ECSA was not directly correlated to the maximum power decrease.

Table 4-40: Comparison of performance drops between all scenarios of the FCREx HGV powertrain.

Operating Power	**Voltage decrease at 600 mA cm^{-2} (%)**	**Voltage decrease at 600 mA cm^{-2} (% h^{-1})**	**Voltage decrease at 1200 mA cm^{-2} (%)**	**Voltage decrease at 1200 mA cm^{-2} (% h^{-1})**	**Maximum power decrease (%)**	**Maximum power decrease (% h^{-1})**	**ECSA decrease (%)**
MPML	1.4	0.055	3.3	0.13	15	0.60	11.7
NPML	1.3	0.053	1.5	0.061	4.2	0.17	9.54
NPNL	0	0	1.5	0.058	4.0	0.16	8.06

4.8.1.2 LiB Degradation Analysis

4.8.1.2.1 Charge Capacity

A list of EoT capacity checks for all cell operating power scenarios for the FCREx HGV powertrain is shown in Table 4-41. These cells were subjected to 100 drive cycles of endurance testing. Interestingly, two (MPML and NPNL) of the cell operating power scenarios had a minimal capacity fade of 0.2%. Again, in the FCREx HGV powertrain, having the battery running at a nominal operating power did not necessarily suggest that the capacity fade would be less. NPML had the most capacity fade of 1%.

Table 4-41: EoT capacity fade for different cell operating power scenarios for the FCREx HGV powertrain.

Cell operating power	Capacity (Ah)
BoL	4.88
MPML	4.87
NPML	4.83
NPNL	4.87

4.8.1.2.2 EIS

Nyquist plots of the collected EIS are shown in Figure 4-53; both fitted (dashed line) and unfitted (solid line) Nyquist plots are shown. As seen, running at the LiB at nominal operating power doesn’t necessarily suggest that there would be less impedance. Graphically, all four cell operating power scenarios have a similar level of impedance relative to each other. An extracted resistance data table is shown in Table 4-42, showing both Ohmic (R_Ω) and charge transfer (R_{ct}) resistance. It can be spotted that the NL scenarios had less charge transfer resistance increase than the ML scenarios. The maximum charge transfer resistance was spotted in the MPML scenario with an increase of 68% from BoL. The Ohmic resistances are relatively similar for all scenarios and only had minor increases.

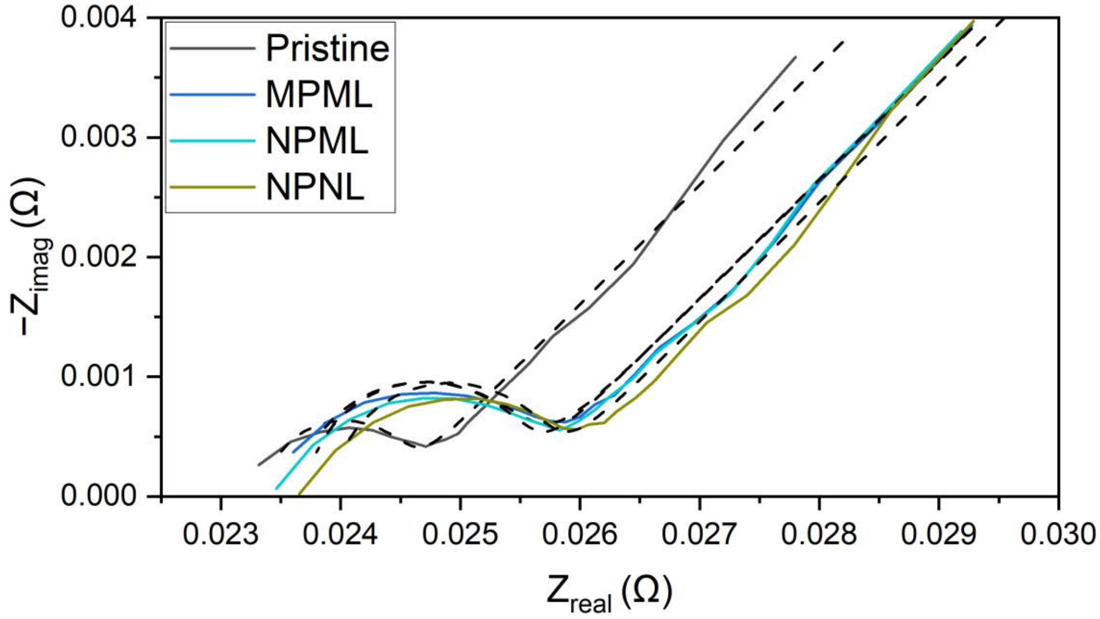

Figure 4-53: LiB M50 PEIS Nyquist plot comparison between different operating scenarios (MPML, NPML, and NPNL). The graph shows both fitted (dashed lines) and unfitted (solid lines) curves. Certain resistance values such as Ohmic and charge transfer resistance can be extracted from fitted curves. The EIS was collected at an amplitude of 10 mV within a frequency range of 10000 to 0.01 Hz.

Table 4-42: Extracted Ohmic (R_{Ω}) and charge transfer (R_{ct}) resistance values from fitting the EIS into an equivalent circuit.

Cell operating power	R_{Ω} (mΩ)	R_{ct} (mΩ)
BoL	23.3	1.06
MPML	23.6	1.78
NPML	23.7	1.67
NPNL	23.9	1.65

4.8.1.3 Degradation Cost Analysis Mini-Study for FCREx HGV

Combining the experimental data and MATLAB modelling results in this work, a mini-study could be conducted on the cost-effectiveness of running the PEMFC in terms of MPML, NPML, or NPNL. The PEMFC would eventually need to be replaced when it fails to support the power demands required, as maximum power drops were spotted during endurance testing. This poses a question of whether it would be cheaper to use fewer cells (e.g. MPML scenario) and replace the PEMFC stack more often or use more cells but replace the PEMFC stack less often. This study was conducted purely on the PEMFC counterpart rather than LiB, as the LiBs did not experience significant power drops during endurance testing.

To approach this question, a degradation cost per drive cycle was calculated, which refers to the amount of USD the PEMFC stack would have theoretically degraded during the duration of that one drive cycle, which, in this case, the WHVC drive cycle was used. Using the HybeMass model, the total required PEMFC stack power (including parasitics and auxiliary components) can be extracted in terms of kW. Referring to the APC roadmaps for PEMFCs mentioned in the Literature Review section in Table 2-1, the cost per kW ($/kW) for automotive grade PEMFC stacks is 112 $/kW. The total PEMFC stack cost for a given cell operating power scenario can be calculated as follows:

$$\mathrm{C_{stack}} = \mathrm{P_{stack}} \times \mathrm{C\ per\ kW} \tag{4-25}$$

Where C_{stack} is the total cost of the PEMFC stack for the intended cell operating power scenario, P_{stack} is the required stack power, and $C\ per\ kW$ is the cost per kW ($/kW) for automotive-grade PEMFCs according to APC roadmaps.

Using experimental data from PEMFC drive cycle endurance testing, the maximum power drop after 100 cycles of WHVC drive cycle could be extrapolated from the polarisation and power curves in terms of percentage drop. After obtaining the percentage drop after 100 cycles, the number of drive cycles that the PEMFC needs to endure to drop below its maximum required power threshold (10 W for nominal scenarios and 20 W for maximum scenarios at cell-level) can be calculated. After reaching this threshold, the PEMFC or the theoretical PEMFC stack is considered EoL will need to be replaced as it can no longer satisfy the power demands of the drive cycle. The degradation cost per drive cycle can then be calculated as:

$$\mathrm{C_{drive\ cycle}} = \frac{\mathrm{C_{stack}}}{\mathrm{N_{EoL}}} \tag{4-26}$$

Where $C_{drive\ cycle}$ is the degradation cost per drive cycle, C_{stack} is the cost of the stack, and N_{EoL} is the number of drive cycles the PEMFC can undergo until it reaches EoL (no longer able to support the required power). The unit obtained from this equation is $/dc, the amount of USD per drive cycle.

An assumption of this analysis is that the overall theoretical PEMFC stack would have even degradation rates throughout the individual cells. In other words, if one cell in the system can no longer fulfil the cell power demand (10 W or 20 W, depending on nominal or maximum operation), every other cell in the stack would encounter the same issue. Another assumption is that the PEMFC's power will drop by the same percentage amount after every 100 drive cycles tested after the initial one.

4.8.1.3.1 MPML PEMFC Degradation Cost Analysis for FCREx HGV

In the MPML scenario, the PEMFC is operating at a maximum cell operating power and is expected to degrade or drop below the required power threshold quickly. It was spotted that the cell tested has dropped below the required power threshold of 20 W (BoL: 20 W, EoT: 17 W) during the first 100 cycles tested, suggesting that the PEMFC would need to be replaced after the initial 100 cycles. Using Equation (4-26), it was calculated that the total overall PEMFC stack cost for this scenario is $5115. Given that the PEMFC needs to be replaced after the initial 100 cycles, the degradation cost per drive cycle ($C_{drive\ cycle}$) is $51.15/dc.

4.8.1.3.2 **NPML PEMFC Degradation Cost Analysis for FCREx HGV**

In the NPML scenario, the PEMFC is operating at a nominal cell operating power. After the initial 100 cycles, the PEMFC experienced a 4.2% maximum power drop, from 24 to 23 W. Using Equation (4-25), it was calculated that the overall PEMFC stack cost for this scenario is $10192, around double that of an MPML scenario. Assuming a 4.2% maximum power drop every 100 cycles, it is expected that the PEMFC will drop below the 10 W required power threshold after 1389 cycles. Using Equation (4-26), the PEMFC degradation cost per drive cycle for the NPML scenario is $7.34/dc. Even though the NPML stack costs almost double to make initially when compared to the MPML stack, the degradation per drive cycle is much less.

4.8.1.3.3 **NPNL PEMFC Degradation Cost Analysis for FCREx HGV**

Similar to the NPML, the PEMFC also operates at a nominal cell operating power in the NPNL scenario. Typically, for all NP scenarios, the PEMFC will degrade and drop below its required power threshold at a slower rate than MP scenarios. After the initial 100 cycles, the PEMFC experienced a 4% maximum power decrease, from 25 to 24 W. The overall PEMFC stack cost for the NPNL scenario is $10424. Assuming a 4% maximum power drop every 100 cycles, the PEMFC will drop below the 10 W required power threshold after 1500 drive cycles. This renders the PEMFC degradation cost per drive cycle for the NPNL scenario to be $6.95/dc. This scenario has the least PEMFC degradation cost per drive cycle out of all other scenarios. The NPML and NPNL scenarios cost much less to operate per drive cycle, but the MPML scenario has a lower initial PEMFC stack cost. The trade-off is between initial cost and maintenance or replacement cost.

4.8.2 FCREx Bus – Millbrook Westminster London Bus Drive Cycle

The FCREx bus section’s PEMFC data is broken down into different subsections covering the MPML, NPML, and NPNL cell operating power scenarios. The polarisation, CV, LSV, and EIS data can be found in each subsection. For the LiB data, all cell operating power scenarios are discussed in conjunction with one another. Figure 4-54 shows the PEMFC power cycle profiles at the cell level for the different cell operating scenarios tested, while Figure 4-55 shows the corresponding LiB power profiles. In these two figures, negative power suggests that power is discharged from the source, and positive power suggests that the power source is being charged.

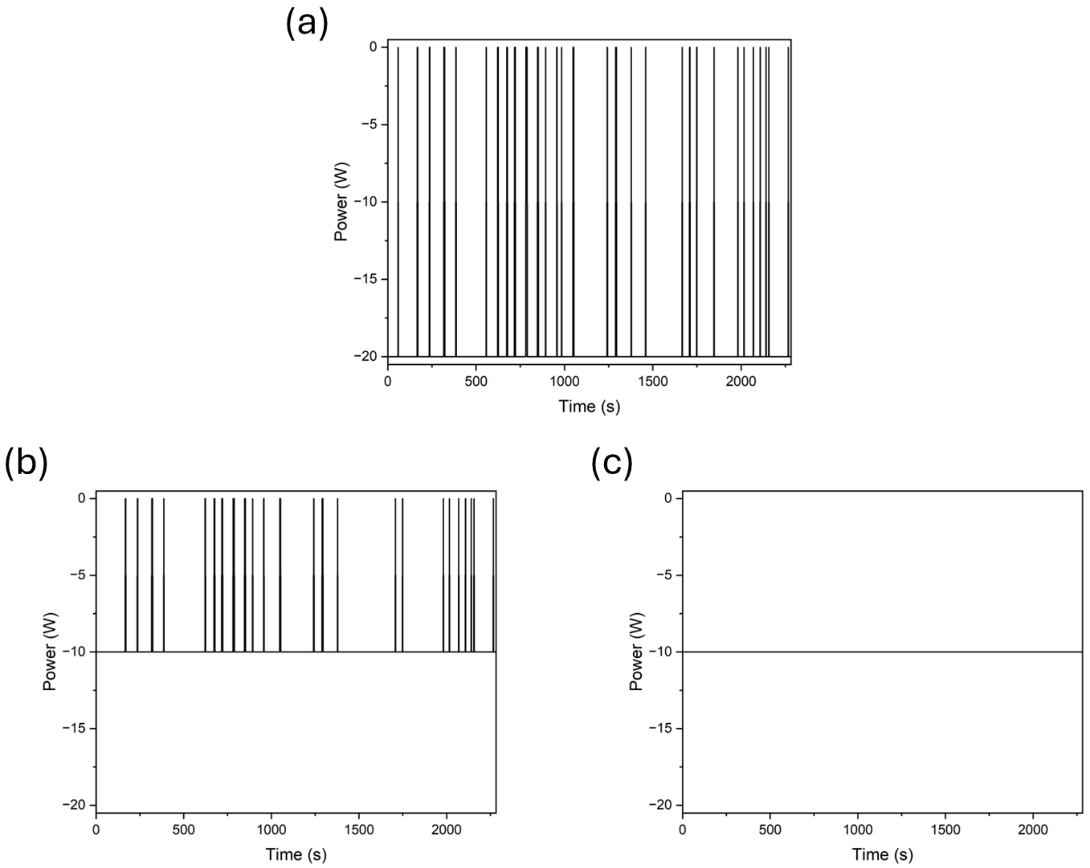

Figure 4-54: PEMFC power cycle profiles of different cell operating power scenarios for FCREx bus. (a) MPML (b) NPML (c) NPNL

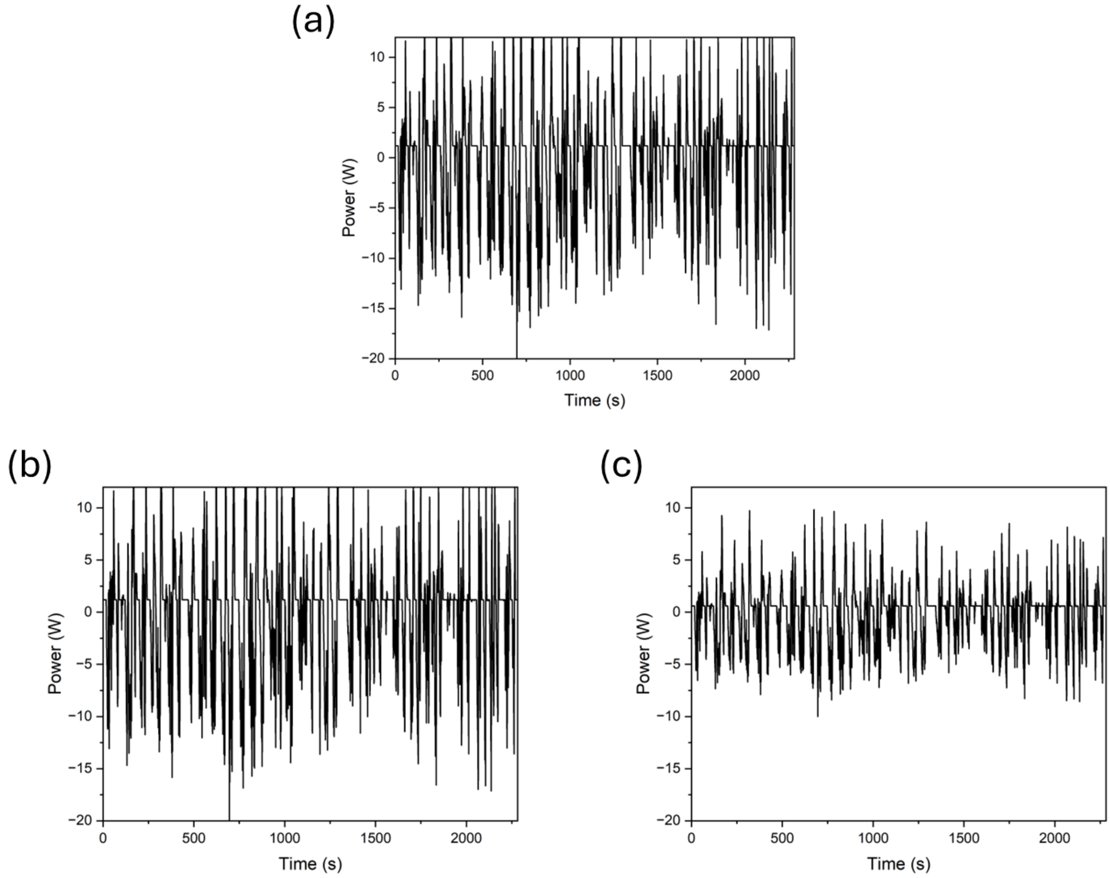

Figure 4-55: LiB power cycle profiles of different cell operating power scenarios for FCREx bus. (a) MPML (b) NPML (c) NPNL

4.8.2.1 PEMFC Degradation Analysis

4.8.2.1.1 MPML

Figure 4-56 presents the polarisation, CV, and LSV curves of the MPML cell operating power scenario for the FCREx bus powertrain under the Millbrook Westminster London Bus Drive Cycle. As shown in the polarisation and power curve in Figure 4-56a, at 600 mA cm^{-2}, the voltage decreased from 0.77 to 0.75 V between BoL and 100 drive cycles (EoT), suggesting a degradation rate of 2.6% or 0.041% h^{-1}. At 1200 mA cm^{-2}, the voltage decreased from 0.67 to 0.65 V between BoL and EoT, a degradation rate of 3% or 0.047% h^{-1}. By utilising the MPML configuration, the degradation rate at 1200 mA cm^{-2} was higher than NREL and DOE standards. The maximum power dropped from 24 to 21 W, a 13% or 0.2% h^{-1} decrease. Interestingly, unlike many of the other MPML scenarios for other vehicles, the EoT maximum power was still capable of producing power above 20 W, rendering its validity to continue operating in the MP configuration (20 W PEMFC requirement). More repeatable testing is required to further confirm this scenario's validity. After 100 cycles, the PEMFC produces its maximum power at a lower current density.

As shown in the cyclic voltammetry plot in Figure 4-56b, the ECSA decreased from 81.9 to 57.7 m^2 g^{-1} between BoL and EoT, a 30% decrease. Figure 4-56c shows the LSV curve comparison between BoL and EoT. According to DOE standards, if the equilibrium part of the LSV exceeds a current density of 20 mA cm^{-2}, the cell is considered to be chemically unstable with severe hydrogen crossover [137], which is not the case for the EoT of this scenario. The hydrogen crossover rate changed from 1.10 × 10^{-6} to 9.59 × 10^{-7} mol s^{-1} from BoL to EoT, a 13% decrease; the EoT had a slower hydrogen crossover rate than BoL.

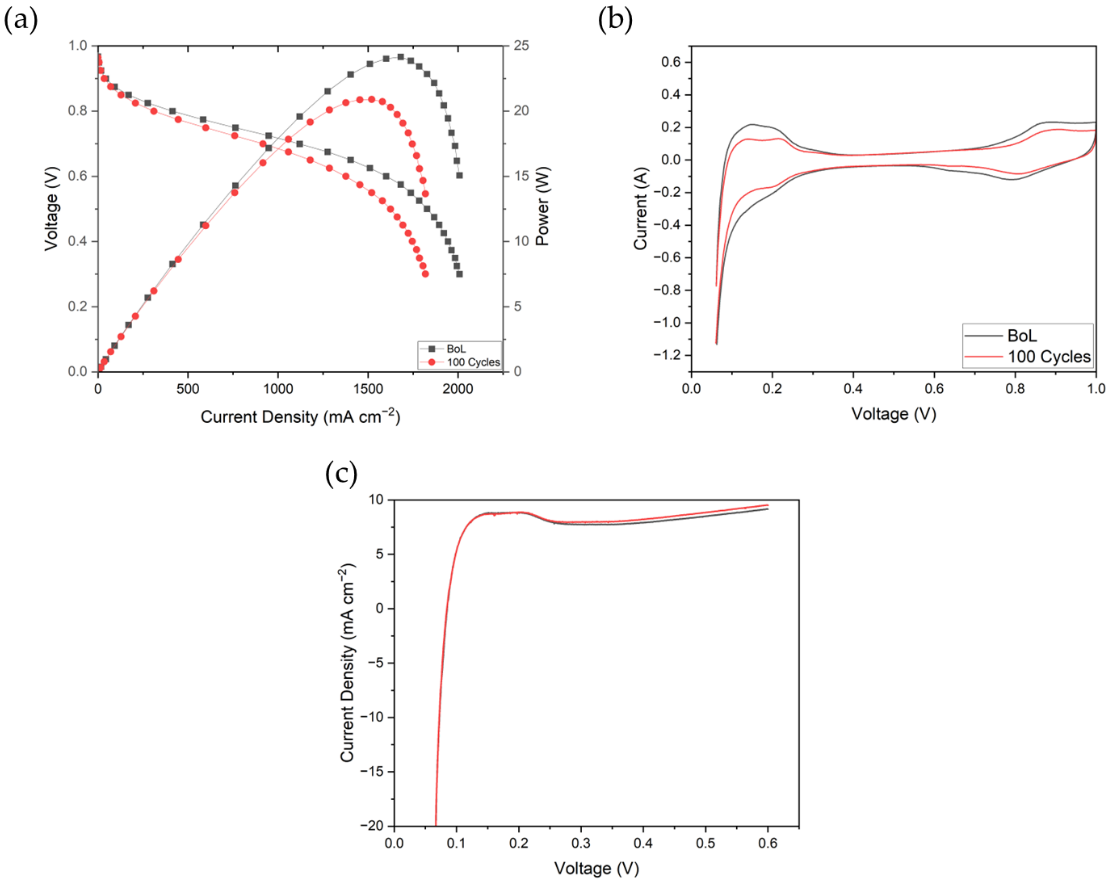

Figure 4-56: Electrochemical degradation analysis of MPML scenario. (a) Polarisation and power curve. (b) Cyclic voltammetry (CV) for comparison and electrochemical surface area (ECSA) estimation. (c) Linear sweep voltammetry (LSV).

Figure 4-57 shows Nyquist plots of EIS collected at different current densities and voltages for the MPML scenario. For most current densities and voltages, the most visual change between BoL and EoT occurred at the low-frequency intercept with the real axis. For current densities 100, 300, 800, and 1200 mA cm^{-2}, the size of the semicircles increased from BoL to EoT, suggesting an increase in either charge or mass transfer resistance. For collections at voltages 0.65 and 0.5 V, a decrease in the size of semicircles was seen instead from BoL to EoT.

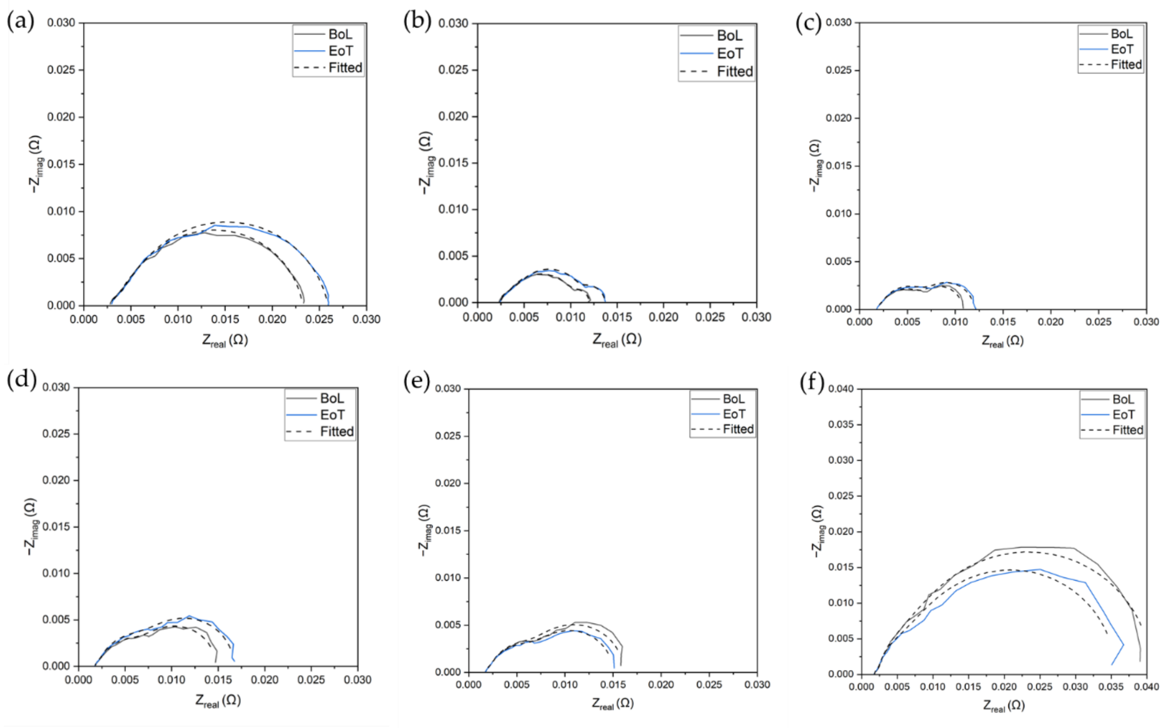

Figure 4-57: EIS Nyquist plots at different current densities and voltages for the MPML scenario. (a) 100 mA cm^{-2}; (b) 300 mA cm^{-2}; (c) 800 mA cm^{-2}; (d) 1200 mA cm^{-2}; (e) 0.65 V; (f) 0.5 V.

The resistance values for the MPML scenario were extracted and outlined in Table 4-43. Ohmic resistance changes are negligible for all current densities and voltages. There are a couple of interesting observations for the 300 mA cm^{-2} and 0.65 V collections. For the 300 mA cm^{-2}, there has been a drastic increase in mass transport resistance, but a drastic decrease in anode charge transfer resistance; cathode charge transfer resistance stayed relatively constant. For the 0.65 V collection, the opposite happened, a drastic decrease in mass transport resistance, but a drastic increase in anode charge transfer resistance; a slight increase in cathode charge transfer resistance was also spotted.

Table 4-43: Resistance values for the MPML FCREx bus scenario under the Millbrook Westminster London Bus drive cycle, interpolated from EIS equivalent circuit fitting, including Ohmic resistance (R_{Ω}), anode (R_{an}) and cathode charge transfer resistance (R_{ca}), and mass transport resistance (R_m).

Current density or voltage (mA cm^{-2} or V)	**R_{Ω} BoL (mΩ cm^2)**	**R_{Ω} EoT (mΩ cm^2)**	**R_{an} BoL (mΩ cm^2)**	**R_{an} EoT (mΩ cm^2)**	**R_{ca} BoL (mΩ cm^2)**	**R_{ca} EoT (mΩ cm^2)**	**R_m BoL (mΩ cm^2)**	**R_m EoT (mΩ cm^2)**
100 mA cm^{-2}	70.4	74.0	29.3	22.6	458	529	21.8	21.3
300 mA cm^{-2}	58.7	60.4	177	60.4	42.8	67.1	21.0	153
800 mA cm^{-2}	45.8	46.1	109	124	102	118	11.1	10.4

1200 mA cm⁻²	44.8	44.6	125	139	186	221	12.0	11.4
0.65 V	44.3	44.6	11.5	129	122	191	223	10.2
0.5 V	45.7	44.6	14.2	13.6	135	131	821	700

4.8.2.1.2 NPML

Figure 4-58 presents the polarisation, CV, and LSV curves of the NPML cell operating power scenario. As shown in the polarisation and power curve in Figure 4-58a, at 600 mA cm^{-2}, the voltage decreased from 0.77 to 0.75 V between BoL and 100 drive cycles, suggesting a degradation rate of 2.6% or 0.041% h^{-1}. At 1200 mA cm^{-2}, the voltage stayed at a consistent value of 0.67 V from BoL to EoT, which performed better than NREL and DOE standards. The maximum power dropped from 24 to 23 W, a 4.2% or 0.07% h^{-1} decrease. After 100 cycles, the PEMFC is still operating in the Ohmic region to reach maximum power, an optimal region for PEMFCs to operate at. The PEMFC reaches its maximum power at a slightly lowered current density after 100 cycles.

As shown in the cyclic voltammetry plot in Figure 4-58b, the ECSA decreased from 56.3 to 55.6 m^2 g^{-1} between BoL and EoT, a 1.2% decrease. Figure 4-58c shows the LSV curve comparison between BoL and EoT. At EoT, the equilibrium of the LSV was seen with a slight upward gradient, suggesting signs of minor electrical shorting. Because of this upward gradient, the hydrogen crossover rate was not calculated in this scenario due to the inability to find an accurate equilibrium current density value.

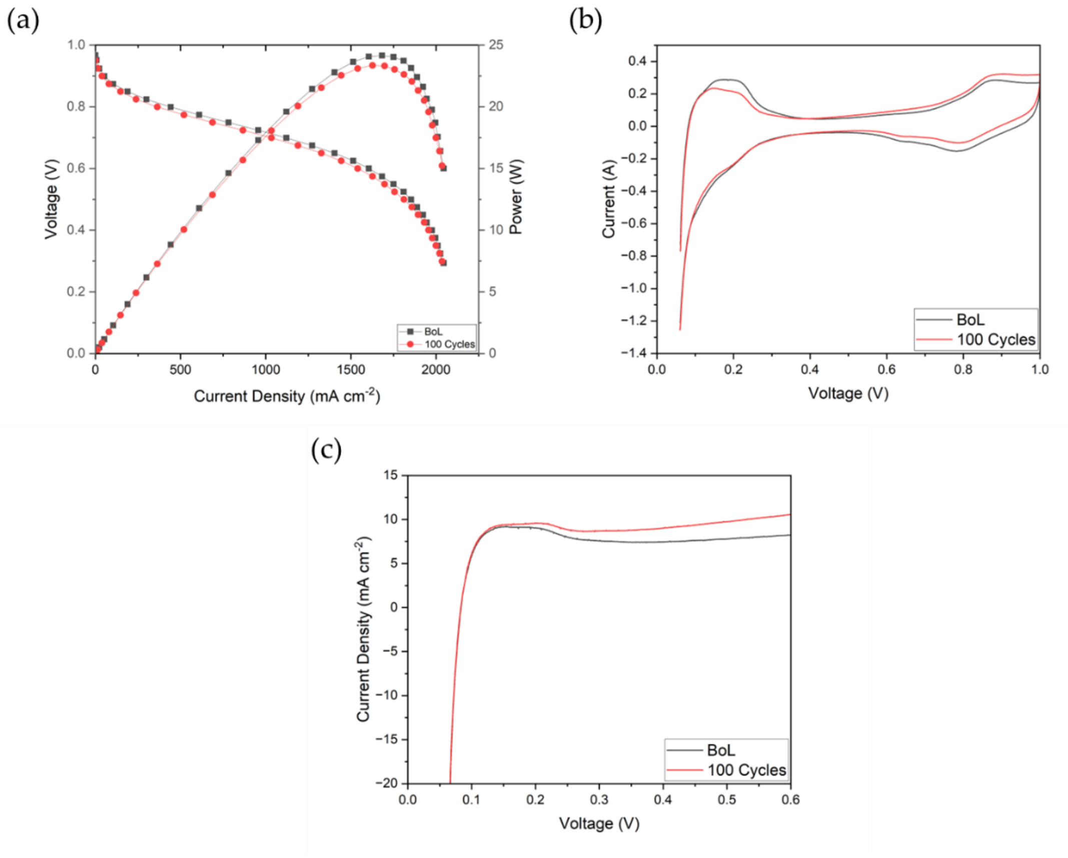

Figure 4-58: Electrochemical degradation analysis of NPML scenario. (a) Polarisation and power curve. (b) Cyclic voltammetry (CV) for comparison and electrochemical surface area (ECSA) estimation. (c) Linear sweep voltammetry (LSV).

Figure 4-59 shows Nyquist plots of EIS collected at different current densities and voltages for the NPML scenario. The changes in semicircle sizes and the low frequency intercepts with the real axis were very minor in this scenario, with three collections, 1200 mA cm^{-2}, 0.65 and 0.5 V, experiencing a decrease in the size of the semicircles from BoL to EoT.

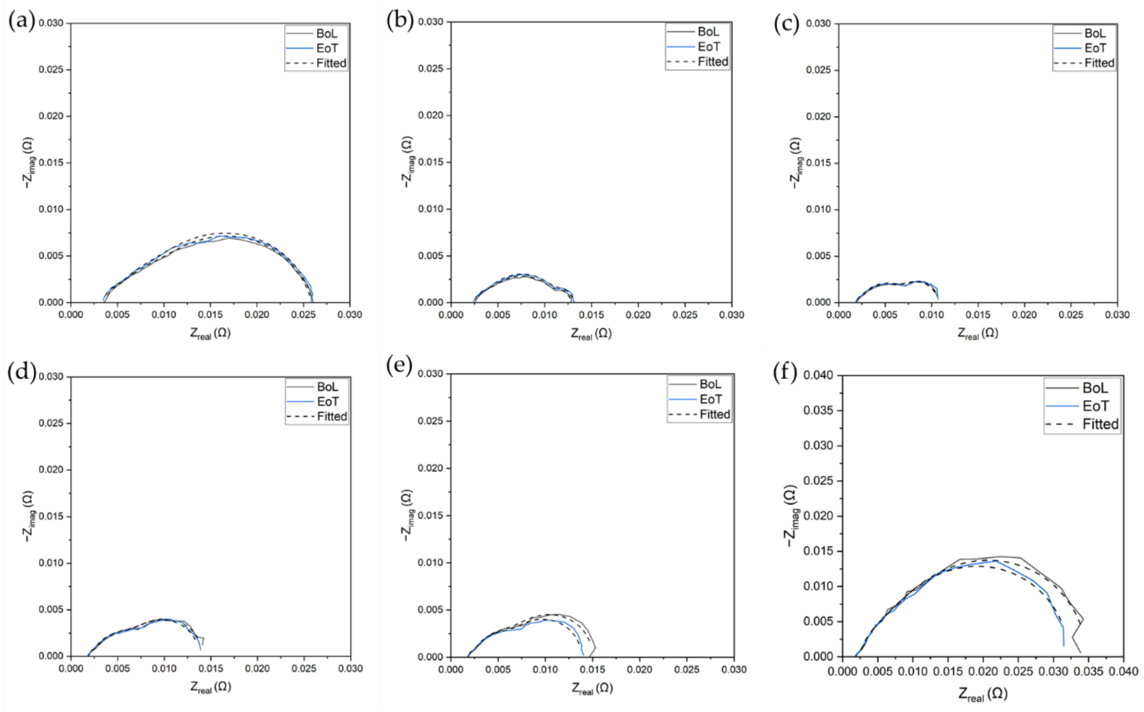

Figure 4-59: EIS Nyquist plots at different current densities and voltages for the NPML scenario. (a) 100 mA cm^{-2}; (b) 300 mA cm^{-2}; (c) 800 mA cm^{-2}; (d) 1200 mA cm^{-2}; (e) 0.65 V; (f) 0.5 V.

The resistance values for the NPML scenario were extracted and outlined in

Table 4-44. For most collections, Ohmic resistance changes are negligible for all current densities and voltages. A 6.6% decrease in Ohmic resistance was spotted for the 100 mA cm^{-2} collection. In addition, only minor charge and mass transfer resistance changes were spotted for most collections, excluding the 300 mA cm^{-2} collection. The most interesting resistance change occurred at the 300 mA cm^{-2} collection. At BoL, there was a high anode charge transfer resistance but a low cathode charge transfer resistance. This phenomenon reversed at EoT, where anode charge transfer resistance is low and cathode charge transfer resistance is high.

Table 4-44: Resistance values for the NPML FCREx bus scenario under the Millbrook Westminster London Bus drive cycle, interpolated from EIS equivalent circuit fitting, including Ohmic resistance (R_{Ω}*), anode (*R_{an}*) and cathode charge transfer resistance (*R_{ca}*), and mass transport resistance (*R_{m}*).*

Current density or voltage (mA cm^{-2} or V)	**R_{Ω} BoL (mΩ cm^{2})**	**R_{Ω} EoT (mΩ cm^{2})**	**R_{an} BoL (mΩ cm^{2})**	**R_{an} EoT (mΩ cm^{2})**	**R_{ca} BoL (mΩ cm^{2})**	**R_{ca} EoT (mΩ cm^{2})**	**R_{m} BoL (mΩ cm^{2})**	**R_{m} EoT (mΩ cm^{2})**
100 mA cm^{-2}	94.4	88.2	46.9	48.1	432	445	73.0	68.3
300 mA cm^{-2}	66.7	61.7	184	28.8	39.7	193	29.6	43.4
800 mA cm^{-2}	49.0	46.3	110	125	90.4	87.0	16.2	10.7
1200 mA cm^{-2}	47.5	45.5	116	118	171	167	18.2	13.8
0.65 V	47.1	45.7	114	107	196	175	17.5	16.3
0.5 V	48.1	46.8	175	134	625	605	17.9	17.5

4.8.2.1.3 NPNL

Two experiments and cells were conducted and tested for the NPNL scenario. Figure 4-60 displays the polarisation, CV, and LSV curves of the NPNL cell operating power scenario. These curves are colour-coded differently from previous iterations of these diagrams due to having two sets of fuel cell data, Experiments 1 and 2. As shown in the polarisation and power curve in Figure 4-60a, in Experiment 1, at 600 mA cm^{-2}, the voltage stayed at a constant value of 0.75 V between BoL and 100 drive cycles. In Experiment 2, the voltage decreased from 0.77 to 0.75 V at 600 mA cm^{-2}, a 2.6% or 0.041% h^{-1} decrease. At 1200 mA cm^{-2}, in Experiment 1, the voltage decreased from 0.68 to 0.66 V, a 2.9% or 0.046% h^{-1} decrease. In Experiment 2, the voltage at 1200 mA cm^{-2} decreased from 0.67 to 0.65 V, also a 2.9% or 0.046% h^{-1} decrease. The decrease in the 1200 mA cm^{-2} percentage per hour is higher than NREL standards for both Experiments 1 and 2. The maximum power dropped from 24 to 23 W for Experiment 1, a 4.2% or 0.07% h^{-1} decrease; a power decrease from 24 to 22 W was calculated for Experiment 2, an 8.3% or 0.13 % h^{-1} decrease. After 100 cycles for both experiments 1 and 2, the PEMFC is still operating in the Ohmic region to reach maximum power, an optimal region for PEMFCs to operate at. The PEMFC reaches its maximum power at a slightly lowered current density after 100 cycles for both experiments 1 and 2.

As shown in the cyclic voltammetry plot in Figure 4-60b, the BoL ECSAs in Experiment 1 and 2 are 58 and 81 m^{2} g^{-1}, respectively. The EoT ECSA of this scenario was not calculated due to signs of electrical shorting. This is also the reason why two cells were tested for this scenario, to confirm if the electrical shorting would be re-occurring. A more detailed view of the electrical shorting phenomenon can be identified in the LSV curves in Figure 4-60c. At BoL, the LSVs for both experiments were chemically stable and had no signs of electrical shorting, with a hydrogen crossover rate of 1.30×10^{-6} and 1.02×10^{-6} mol s^{-1} for Experiment 1 and 2, respectively. The EoT hydrogen crossover rate was not calculated due to the inability to find an equilibrium from the upward gradient.

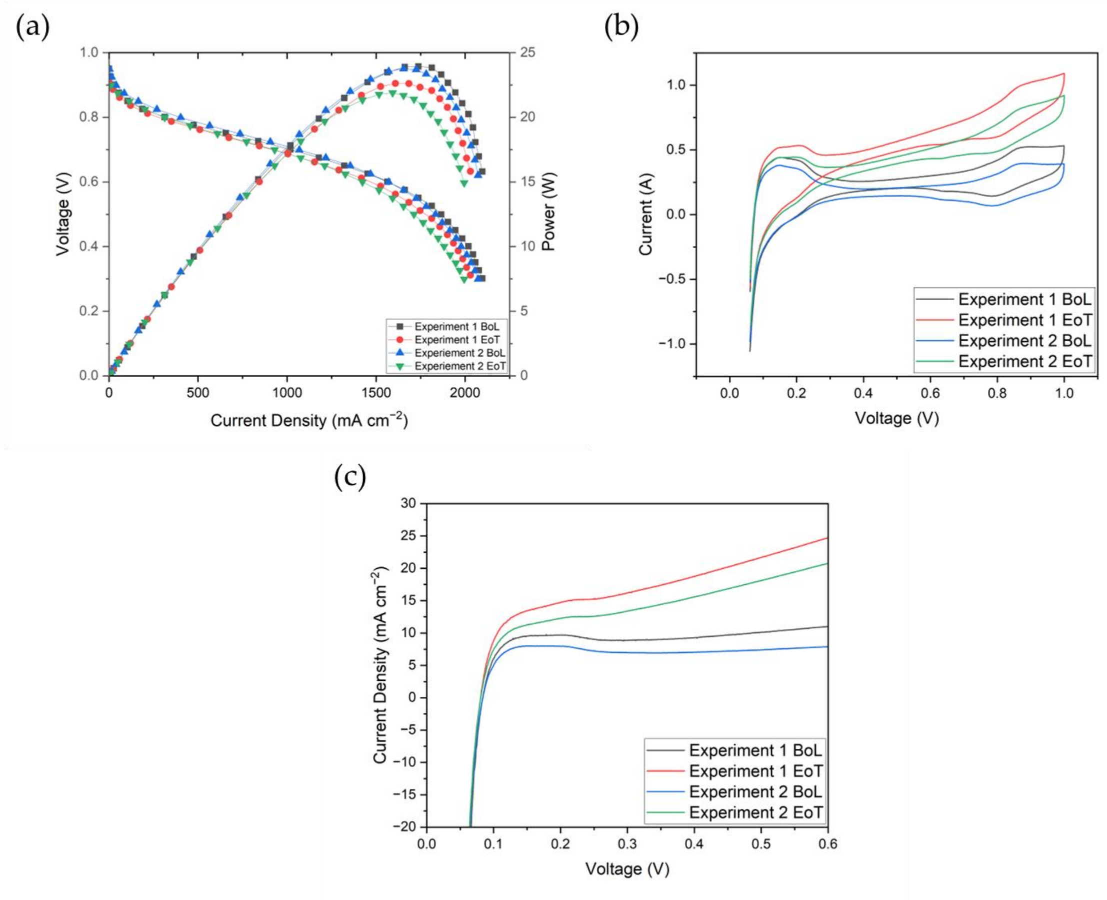

Figure 4-60: Electrochemical degradation analysis of NPNL scenario. (a) Polarisation and power curve. (b) Cyclic voltammetry (CV) for comparison and electrochemical surface area (ECSA) estimation. (c) Linear sweep voltammetry (LSV).

A trend that has been found for the FCREx scenarios is that having the PEMFC at a constant power throughout the entire drive cycle tends to increase the possibility of an electrical short in the LSVs. Figure 4-61 shows the required power profile for all cell operating power scenarios. For both the MPML and NPML scenarios, there are timestamps where the PEMFC's power had to reduce to 0 W to prevent the LiB from overcharging, these two scenarios did not have a LSV with electrical shorting. The NPNL scenario had a constant PEMFC power all along, without the need of 'shutting off' the PEMFC to prevent LiB overcharge which did cause an electrical short in the LSV. This behaviour was also spotted in other vehicle types and scenarios, more verification of this can be included in the future works of this study.

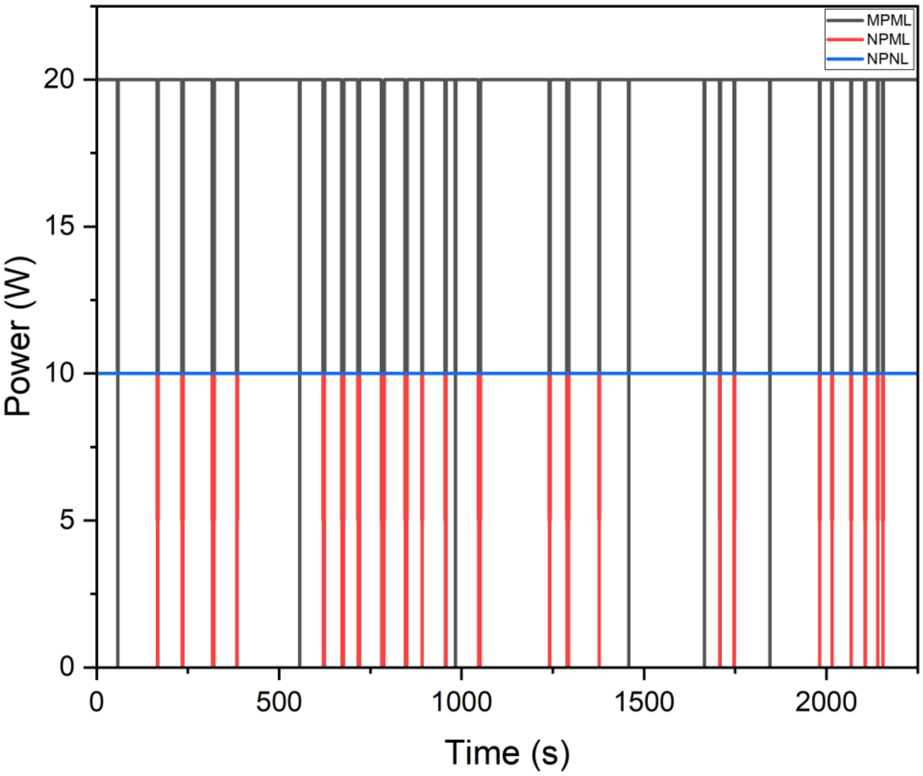

Figure 4-61: Comparison of required PEMFC power during the Millbrook Westminster London Bus drive cycle for different cell operating power scenarios, including MPML (black), NPML (red), and NPNL (blue).

Figure 4-62 shows Nyquist plots of EIS collected at different current densities and voltages for the NPNL scenario for both Experiment 1 and 2. During the 100 mA cm^{-2} collection for both experiments, the size of the semicircles and low-frequency intercept with the real axis decreased from BoL to EoT. At 300 mA cm^{-2}, the semicircles stayed similar in size from BoL to EoT for both experiments. During the 800 mA cm^{-2} collection, the semicircles and low-frequency intercept with the real axis increased for both experiments. For the 1200 mA cm^{-2} collection, the trend of the results differs for the two experiments. In Experiment 1, the size of the semicircles and low-frequency intercept with the real axis decreased from BoL to EoT. However, in Experiment 2, the opposite happened, showing an increase in semicircle size from BoL to EoT. For the collection at 0.65 V, all semicircles stayed relatively similar in size for both experiments. For the collection at 0.5 V, all semicircles and low-frequency intercepts with the real axis decreased from BoL to EoT for both experiments.

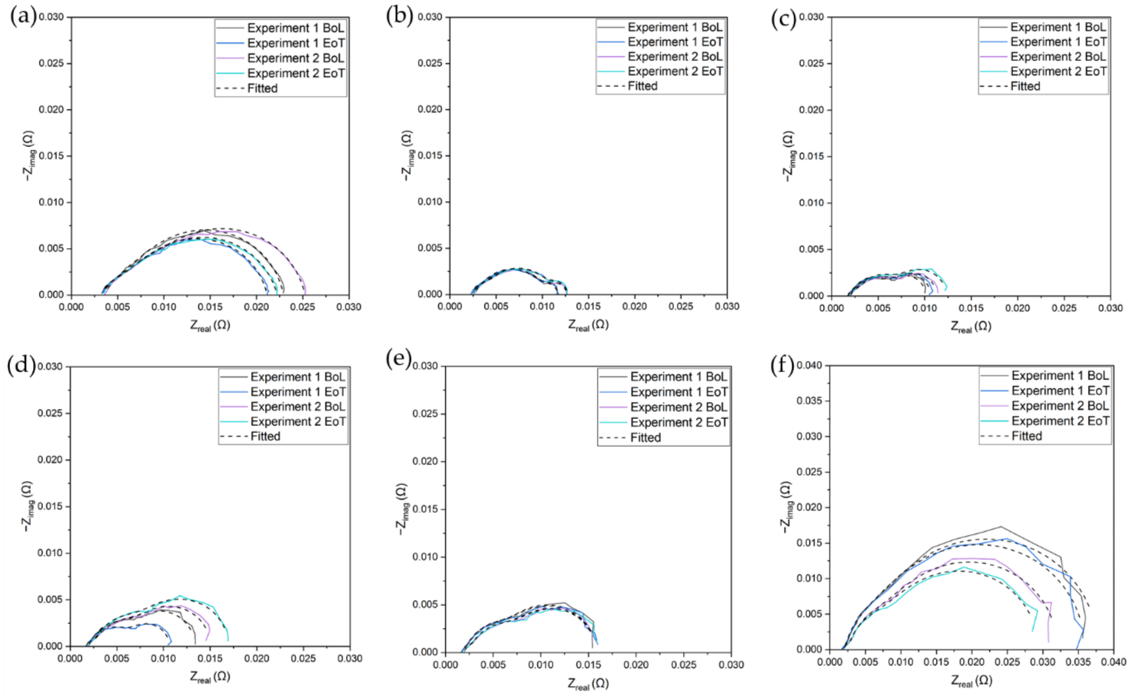

Figure 4-62: EIS Nyquist plots at different current densities and voltages for the NPNL scenario. (a) 100 mA cm^{-2}; (b) 300 mA cm^{-2}; (c) 800 mA cm^{-2}; (d) 1200 mA cm^{-2}; (e) 0.65 V; (f) 0.5 V.

The resistance values for the NPNL scenario for Experiments 1 and 2 were extracted and outlined in Table 4-45 and Table 4-46, respectively. For all collections, Ohmic resistance changes are negligible for all current densities and voltages. A 6.6% decrease in Ohmic resistance was spotted for the 100 mA cm^{-2} collection. In Experiment 1, the EIS collections at most current densities and voltages only had minor charge and mass transfer changes, aside from the 0.65 V collection. For the 0.65 V collection, there was a drastic increase in anode charge transfer resistance from BoL to EoT; however, there was also a drastic decrease in mass transport resistance. For Experiment 2, the collections at 300 and 800 mA cm^{-2} current density and 0.5 V only had minor charge and mass transfer changes. At 100 mA cm^{-2}, there was a 26%, 7.8%, and 35% decrease in anode charge transfer resistance, cathode charge transfer resistance, and mass transfer resistance, respectively. At 1200 mA cm^{-2}, there was a 10% and 20% increase in anode and cathode charge transfer resistance, respectively. Mass transport resistance stayed relatively constant.

Table 4-45: Experiment 1 resistance values for the NPNL FCREx bus scenario under the Millbrook Westminster London Bus drive cycle, interpolated from EIS equivalent circuit fitting, *including Ohmic resistance (R_Ω), anode (R_{an}) and cathode charge transfer resistance (R_{ca}), and mass transport resistance (R_m).*

Current density or voltage (mA cm^{-2} or V)	R_Ω BoL (mΩ cm^2)	R_Ω EoT (mΩ cm^2)	R_{an} BoL (mΩ cm^2)	R_{an} EoT (mΩ cm^2)	R_{ca} BoL (mΩ cm^2)	R_{ca} EoT (mΩ cm^2)	R_m BoL (mΩ cm^2)	R_m EoT (mΩ cm^2)
100 mA cm^{-2}	83.1	85.1	33.4	30.5	409	366	47.0	46.5
300 mA cm^{-2}	62.2	58.4	173	169	33.9	41.9	22.8	22.1
800 mA cm^{-2}	45.4	43.7	99.9	110	94.2	100	13.6	10.5
1200 mA cm^{-2}	43.8	43.7	116	110	162	100	11.7	10.5
0.65 V	42.5	42.2	28.0	130	226	208	97.2	11.1
0.5 V	44.9	43.2	150	149	733	691	14.8	13.4

Table 4-46: Experiment 2 resistance values for the NPNL FCREx bus scenario under the Millbrook Westminster London Bus drive cycle, interpolated from EIS equivalent circuit fitting, including Ohmic resistance (R_Ω), anode (R_{an}) and cathode charge transfer resistance (R_{ca}), and mass transport resistance (R_m).

Current density or voltage (mA cm^{-2} or V)	R_Ω BoL (mΩ cm^2)	R_Ω EoT (mΩ cm^2)	R_{an} BoL (mΩ cm^2)	R_{an} EoT (mΩ cm^2)	R_{ca} BoL (mΩ cm^2)	R_{ca} EoT (mΩ cm^2)	R_m BoL (mΩ cm^2)	R_m EoT (mΩ cm^2)
100 mA cm^{-2}	94.9	89.2	48.6	36.1	418	385	69.3	44.8
300 mA cm^{-2}	69.3	65.9	179	180	37.2	45.9	29.5	26.5
800 mA cm^{-2}	52.0	50.5	111	123	101	118	17.5	15.5
1200 mA cm^{-2}	50.4	49.4	125.3	138	182	218	18.0	17.7

0.65 V	50.0	49.3	126	136	199	195	18.4	16.3
0.5 V	49.8	49.4	25.8	148	146	516	579	20.3

4.8.2.1.4 MPML vs. NPML vs. NPNL in Terms of PEMFC Degradation

Table 4-47 outlines the degradation between all scenarios, showcasing voltage decrease, maximum power decrease, and ECSA decrease. Coincidentally, the MPML, NPML, and NPNL Experiment 2 scenarios all had a voltage decrease of 2.6% from BoL to EoT. NPNL Experiment 2, however, did not experience any voltage decrease at 600 mA cm^{-2}. At 1200 mA cm^{-2}, the NPML scenario had the most voltage drop of 4.2%. For MPML and NPNL, the drop is similar at 3%. In terms of voltage drops, running the PEMFC at nominal operating power did not suggest that the drop would be less. However, the maximum PEMFC operating power scenario (MPML) had more maximum power decrease than the nominal PEMFC operating power scenarios (NPML and NPNL). The maximum PEMFC (MP) scenario experienced the most ECSA loss. Again, ECSA couldn't be calculated for the NPNL scenarios due to the 'shorted' CV curves.

Table 4-47: Comparison of performance drops between all scenarios of the FCREx bus powertrain under the Millbrook Westminster London Bus drive cycle.

Operating Power	**Voltage decrease at 600 mA cm^{-2} (%)**	**Voltage decrease at 600 mA cm^{-2} (% h^{-1})**	**Voltage decrease at 1200 mA cm^{-2} (%)**	**Voltage decrease at 1200 mA cm^{-2} (% h^{-1})**	**Maximum power decrease (%)**	**Maximum power decrease (% h^{-1})**	**ECSA decrease (%)**
MPML	2.6	0.041	3.0	0.047	13	0.20	30
NPML	2.6	0.041	4.2	0.070	4.2	0.070	1.2
NPNL 1	0	0	2.9	0.046	4.2	0.070	N/A
NPNL 2	2.6	0.041	2.9	0.046	8.3	0.13	N/A

4.8.2.2 LiB Degradation Analysis

4.8.2.2.1 Charge Capacity

A list of EoT charge capacity checks for all cell operating power scenarios for the FCREx bus powertrain is shown in Table 4-48. The MPML cell operating power scenario had the most capacity fade of 1.4%, while the NPML scenario had the least capacity fade of 0.2%. In both of these two scenarios, the LiB was operating at maximum power; however, the rankings of the capacity fade were drastically different for these two. The NPNL scenario had a capacity fade of 1.2%.

Table 4-48: EoT capacity fade for different cell operating power scenarios for the FCREx bus powertrain.

Cell operating power	Capacity (Ah)
BoL	4.88
MPML	4.81
NPML	4.87
NPNL	4.82

4.8.2.2.2 EIS

Nyquist plots of the collected PEIS are shown in Figure 4-63; both fitted (dashed line) and unfitted (solid line) curves are shown. All EoT semicircles and diffusion tails ended up in a similar region. Running the LiB at nominal operating power doesn’t necessarily suggest that there would be less impedance. In fact, the scenario where the LiB is running at nominal operating power (NPNL) had the largest semicircle, graphically. An extracted resistance data table is shown in Table 4-49, showing Ohmic (R_{Ω}) and charge transfer (R_{ct}) resistance. The Ohmic resistances are relatively similar to each other. The NPNL had the most charge transfer resistance increases of 68%. The MPML and NPML scenarios had charge transfer increases of 56% and 43%, respectively.

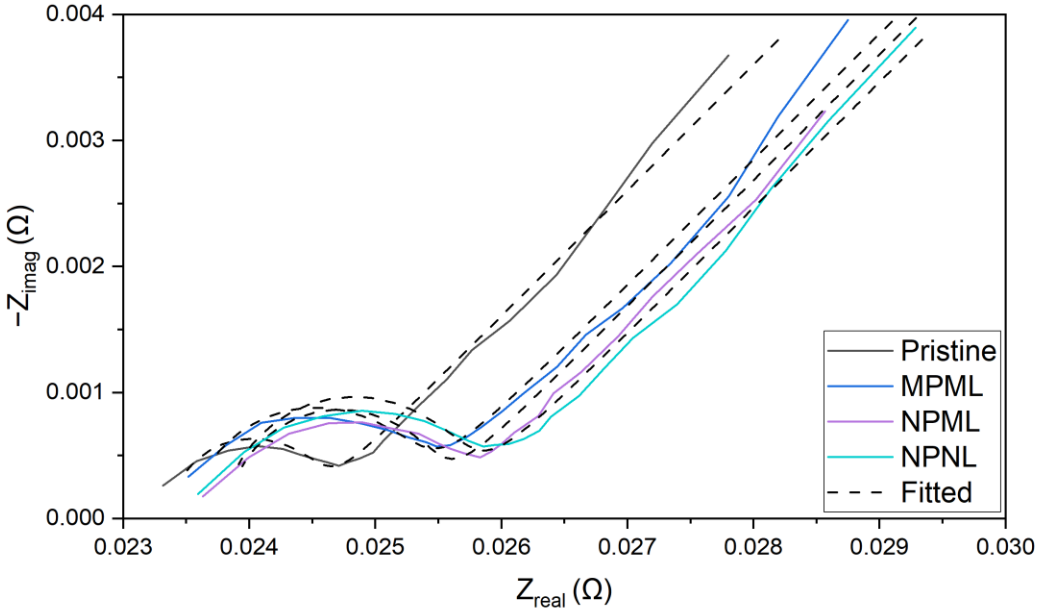

Figure 4-63: LiB M50 PEIS Nyquist plot comparison between different operating scenarios (MPML, NPML, and NPNL) for the FCREx bus powertrain. The graph shows both fitted (dashed lines) and unfitted (solid lines) curves. Certain resistance values such as Ohmic and charge transfer resistance can be extracted from fitted curves. The PEIS was collected at an amplitude of 10 mV within a frequency range of 10000 to 0.01 Hz.

Table 4-49: Extracted Ohmic (R_{Ω}) and charge transfer (R_{ct}) resistance values from fitting the EIS into an equivalent circuit.

Cell operating power	R_{Ω} (mΩ)	R_{ct} (mΩ)
BoL	23.3	1.06
MPML	23.5	1.65
NPML	23.8	1.52
NPNL	23.8	1.78

4.9 Observations of Degradation Performance between Parallel and FCREx Powertrains

In terms of degradation rate, a few benefits could be spotted in PEMFCs operating in a FCREx powertrain configuration than a parallel configuration. The first noticeable difference is the lessened maximum power decrease after 100 drive cycles for the HGV and bus scenarios, especially when the PEMFC is operating at nominal operating power. In the parallel HGV powertrain configuration, the maximum power decrease was 12%, 8.7%, and 9.,1% for the MPML, NPML, and NPML configurations, respectively; but for the FCREx HGV powertrain configuration, the maximum power decrease was 15%, 4.2%, and 4%, for the MPML, NPML, and NPML scenarios, respectively. The PEMFC had more maximum power decrease when operating in a maximum cell operating power scenario in the FCREx than the parallel powertrain. This shows us that running a PEMFC near maximum power constantly is worse than having a transient power demand PEMFC which hits near maximum power occasionally. However, because that the NP scenarios in the FCREx had less maximum power decrease than the parallel, it shows that PEMFCs are capable of operating at constant moderate power draw while receiving minimal degradation, rather than a more transient PEMFC that hits nominal power occasionally. The MP scenarios do show signs of ECSA improvements between the FCREx and the parallel powertrain scenario, such as in the HGV scenario; the MPML FCREx scenario only had an 11.7% ECSA decrease rather than 25.8% ECSA decrease in the parallel HGV scenario. This point needs to be further validated in future work as the comparison between FCREx and parallel bus scenarios only had minor improvements which are negligible.

The LiBs account for transient power demands in both parallel and FCREx scenarios; the comparison of LiB degradation performance between parallel and FCREx powertrain layouts is less significant due to this nature of operation. In addition, LiBs are known to handle transient power demands better than PEMFCs. The capacity fades and EIS analysis of LiBs did not experience a trend that the researcher can investigate further. In many cases, operating the LiBs at nominal cell operating power did not show an improvement over operating at maximum cell operating power.

4.10 Power System Mass Analysis using HybeMass Model

The results obtained from the model are presented below for three different vehicle scenarios, an LDV, Class 8 HGV, and a bus. The overall mass of the propulsion system is broken down into five different power system components, LiB component mass (shown in yellow), LiB mass (green), hydrogen tank mass (blue), PEMFC component mass (orange), and PEMFC mass (black). By exploring different HDs for these vehicles, it can be seen that the overall mass of the propulsion system reduces significantly as the extent of power delivered by the fuel cell increases. It is also clear that once a decision to hybridise a system is made the net mass change of the fuel cell system is relatively small when compared to the change in battery mass for all scenarios. It is clear from the results that operating a system with maximum PEM and LiB power (MPML) will provide the lowest system mass while the NPNL setup would most likely have the best durability. It is also evident that in some instances, a relatively low HD can increase the mass of the system, removing the most significant benefit assessed using this model. While the result suggest a HD of 1 is the lightest system, this solution has no LiBs included which is unlikely to be a satisfactory solution due to the accelerated degradation likely imposed on the PEMFC stack. In addition further BoP would be required to start the PEMFC's BoP. The PEMFC stack would be running at ambient conditions without a battery pack to power up BoP components such as heating cartridges, removing the ability to adjust for PEMFC operating parameters such as cell temperature and humidification. This may affect the performance of the stack. The LDV powertrain was omitted from the FCREx analysis as they are commonly set up as parallel powertrains in practice. The FCREx powertrain is more common amongst heavier vehicles such as HGVs and buses.

4.10.1 Parallel Powertrain

4.10.1.1 LDV

Figure 4-64 presents the mass distributions for an LDV FCHEV, FCEV, and BEV under different HDs and cell operating powers. It can be seen with a 0.2 HD for MPML and NPML, hybridisation increases the mass of the power system by 8% and 10%, respectively, when compared to a full BEV setup. The added system complexity of hybridisation combined with the extra mass makes these setups unfeasible. Aside from these HDs at these cell operating points, the trend is that higher HDs result in lower power systems mass for LDVs. Some future work that can be done to improve this analysis is to vary the hydrogen tank's weight depending on vehicle driving range requirements and HD.

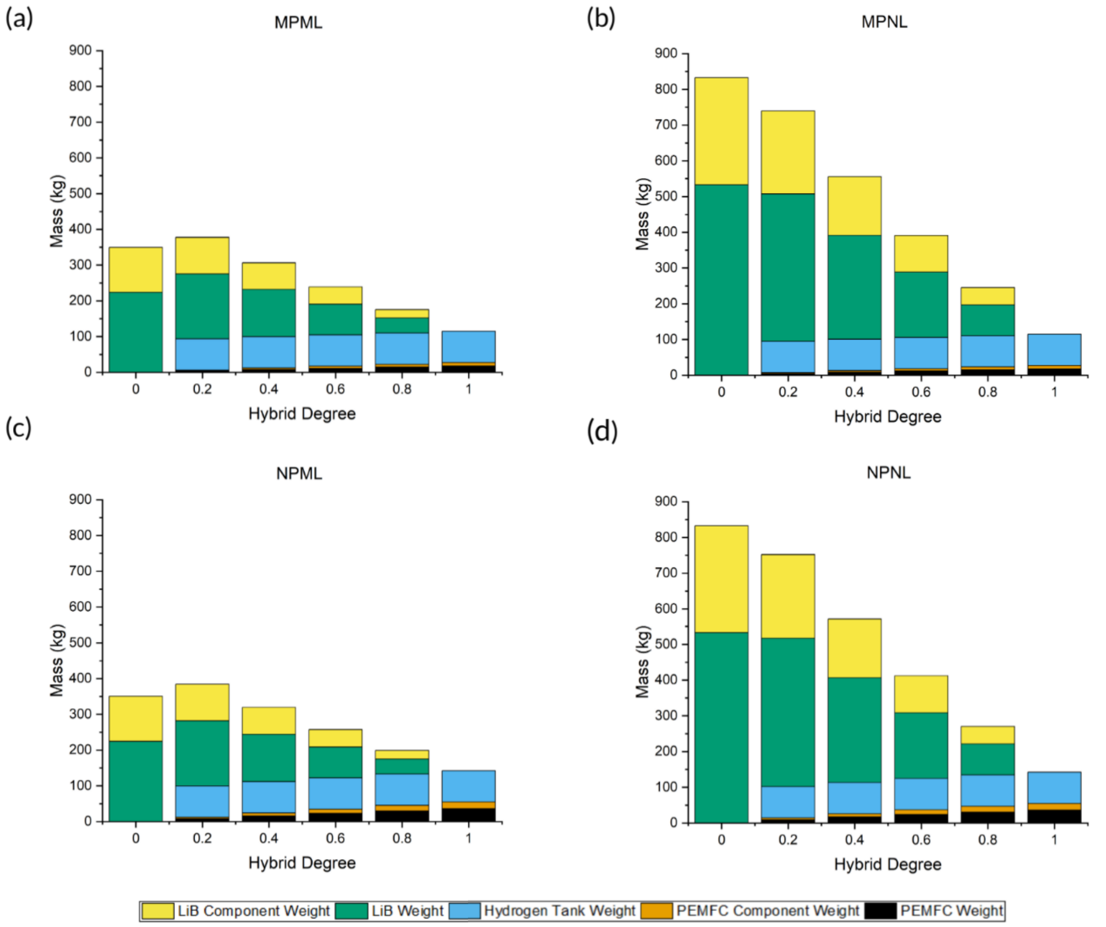

Figure 4-64: Power system mass distributions for an LDV FCHEV and FCEV scenario under different cell operating powers. (a) MPML (b) MPNL (c) NPML (d) NPNL

Table 4-50 shows the change in mass of the power systems with increasing HDs for the four scenarios examined. These results highlight potential mass reductions ranging from 43% to 71% for the 0.8 HD when compared to the full BEV. The 0.8 HD is a common degree for commercially available FCEVs, similar to that of a Toyota Mirai (0.71 HD) [5][6].

Table 4-50: Percentage power systems mass increase or reduction (%) of various HDs and cell operating power when compared to a full BEV in an LDV scenario. Positive nomenclature suggests an increase in mass while negative nomenclature suggests a decrease in mass.

Cell Operating Power	Hybridisation Degree				
	0.2	0.4	0.6	0.8	1.0
MPML	8	-12	-32	-50	-67
MPNL	-11	-33	-53	-71	-86
NPML	10	-9	-27	-43	-59
NPNL	-10	-31	-51	-68	-83

The NPML cell operating power is the best setup to prolong the durability of both the PEMFC and LiB, while maintaining a feasible power system mass. LiBs tend to have a higher dynamic response when compared to PEMFCs [165]. Having the PEMFC running at nominal powers would slow down its degradation rate and maximum power drop, as well as decreasing the transientness of the PEMFC power profile. Less transientness may prolong the lifetime of the PEMFC. A high level of transient operation accelerates the voltage decay of the PEMFC [44]. Gas lag and starvation are the main contributors causing the degradation of PEMFCs during dynamic loads, causing electrochemical surface area (ECSA) decrease [44]. LiB cells can cope with transient response better and experience less degradation when subjected to dynamic loads, allowing them to run at maximum operating power can bring mass-saving benefits. In a commercial scenario, the LiB cells may need to be oversized or to be operated at a near-maximum operating power instead of the absolute maximum to account for higher vehicle life expectancy. Even by running the PEMFCs at a nominal power at the popularised 0.8 HD, a 43% drop in mass is still expected when compared to a full BEV.

From Table 4-50, it can be seen the maximum propulsion system mass savings for the devices explored in this work when hybridising an LDV is 71% (0.8 HD MPNL). However, this scenario assumes a situation in which the fuel cell is operated at its maximum power with the LIB operating under nominal conditions. Operating a fuel cell at its maximum power will undoubtedly impact the durability, and by extension the lifetime cost of the propulsion system for the vehicle. It can be seen that a balance point shall be put into place when designing a FCHEV, obtaining both favourable mass reduction and vehicle life expectancy.

Overall, the results obtained from the model show vehicle mass reductions when hybridising, which increases the validity of hybridising for mass.

4.10.1.2 Class 8 HGV

Figure 4-65 presents the mass distributions for a heavy goods FCHEV, FCEV, or BEV under different HDs and cell operating powers. It can be seen with a 0.2 HD for MPML and NPML, hybridisation increases the power systems mass by 18% and 20%, respectively, when compared to a full BEV setup, which, if minimal system mass is the aim of hybridisation renders these solutions unfeasible. In addition to the 0.2 HD, a 3% increase in mass is also seen within the 0.4 HD when operating at NPML. Aside from the 0.2 and 0.4 HD, the trend is that higher HDs result in lower power systems mass for HGVs in a similar manner to the results seen previously.

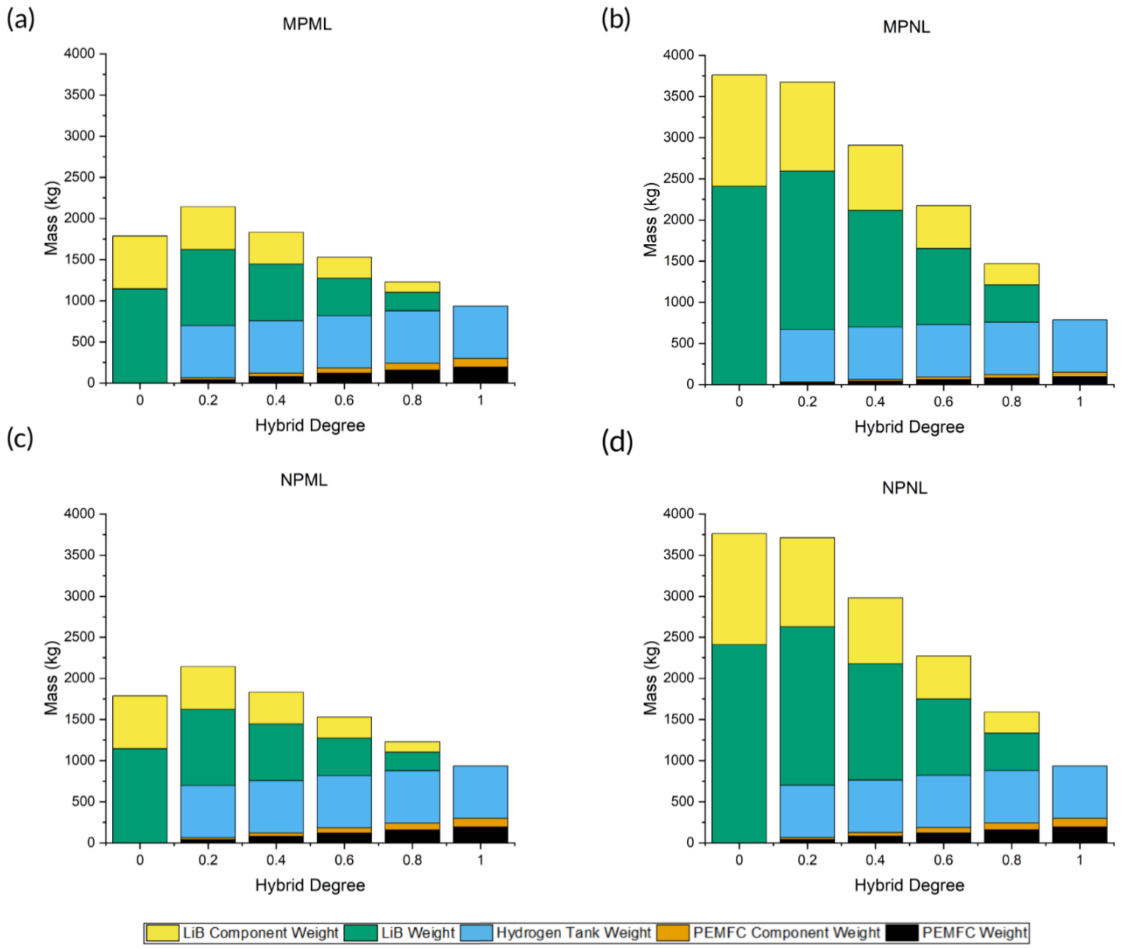

Figure 4-65: Power system mass distributions for a heavy-goods FCHEV and FCEV scenario under different cell operating powers. (a) MPML (b) MPNL (c) NPML (d) NPNL

Table 4-51 shows the increase or decrease of mass of the power systems of different HDs for the four scenarios explored in terms of percentage when compared to a full BEV. Mass reductions range from 38% to 61% for the 0.8 HD when compared to the full BEV, illustrating the benefit of hybridising to reduce the gross vehicle mass. The mass reductions for this common HD is not as significant as compared to the LDV scenario, but is still capable of reducing the mass by more than half (61% and 58% reduction) of that of a BEV. This would require cell operating power setups of MPNL and NPNL. As highlighted previously, MPNL scenario is unlikely to be optimal to maximise the lifetime of the system and therefore would likely be assessed in the broader context of vehicle operation. However, NPNL may be a viable option if a manufacturer is looking to prolong the life of power sources for as long as possible, with some sacrifices in increased weight. The total power systems mass of an NPNL 0.8 HD setup is 1592 kg; when comparing this to a commercial heavy-goods BEV's battery pack mass of 2293 kg [157], the mass is still less. The heaviest possible power systems option for the 0.8 HD would still be lighter than a heavy-goods BEV's battery pack.

Table 4-51: Percentage power systems mass increase or reduction (%) of various HDs and cell operating power when compared to a full BEV in an HGV scenario. Positive nomenclature suggests an increase in mass while negative nomenclature suggests a decrease in mass.

Cell Operating Power	Hybridisation Degree				
	0.2	0.4	0.6	0.8	1.0
MPML	18	−1	−20	−38	−56
MPNL	−2	−23	−42	−61	−79
NPML	20	3	−14	−31	−48
NPNL	−1	−21	−40	−58	−75

As for the optimal hybrid configuration of NPML, any HD over 0.6 would result in a power systems mass less than that of the full BEV counterpart and the estimated commercial LiB HGV's pack mass of 2293 kg [157].

4.10.1.3 Bus

Figure 4-66 presents the mass distributions for an FCHEV, FCEV, or BEV bus under different HDs and cell operating powers. Slightly different from the LDV and HGV scenarios, an increase in mass can only be seen with the NPML 0.2 HD configuration compared to a full BEV setup; all other configurations show improvements in mass reduction as the HD increases.

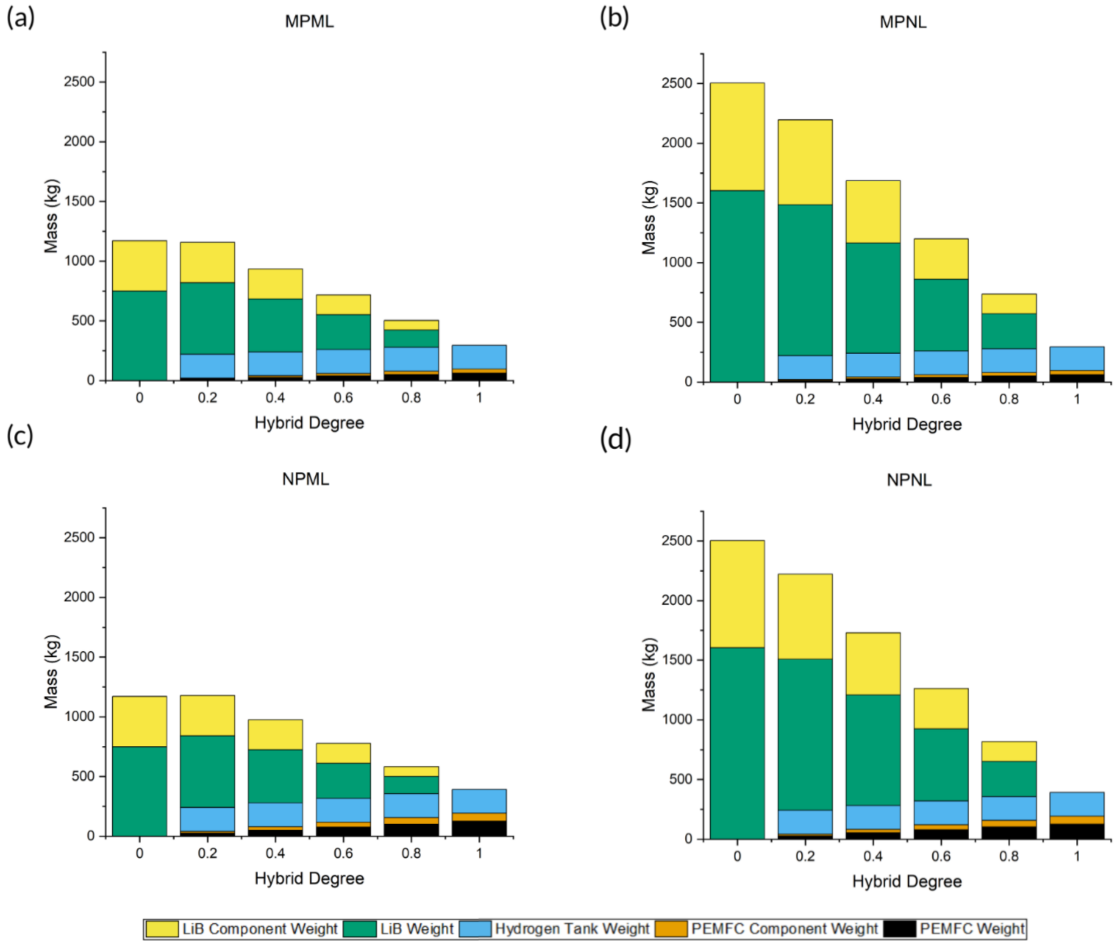

Figure 4-66: Power system mass distributions for a heavy-goods FCHEV and FCEV scenario under different cell operating powers. (a) MPML (b) MPNL (c) NPML (d) NPNL

Table 4-52 shows the increase or decrease of mass of the power systems of different HDs and cell operating power in terms of percentage when compared to a full BEV. Mass reductions range from 50% to 71% for the 0.8 HD when compared to the full BEV. The total power systems mass of a NPNL 0.8 HD setup is 583.4 kg; the mass is almost reduced by half when comparing this to a commercial ICEV bus's engine mass of 1093 kg [166], as outlined in previous chapters in Table 4-1. Even if adopting the NPNL cell operating power configuration for the 0.8 HD, the system mass would still be lighter than an ICEV bus's engine. Any HD over 0.6 would result in a power systems mass less than that of the full BEV counterpart and the estimated commercial LiB HGV's pack mass of 2293 kg [157].

Table 4-52: Percentage power systems mass increase or reduction (%) of various HDs and cell operating power when compared to a full BEV in a bus scenario. Positive nomenclature suggests an increase in mass while negative nomenclature suggests a decrease in mass.

Cell Operating Power	Hybridisation Degree				
	0.2	0.4	0.6	0.8	1.0
MPML	−1	−20	−39	−57	−75
MPNL	−12	−33	−52	−71	−88
NPML	1	−21	−34	−50	−66
NPNL	−11	−31	−50	−67	−84

4.10.2 FCREx Powertrain

4.10.2.1 FCREx HGV

Figure 4-67 presents the mass distributions for an FCREx HGV under different cell operating powers. As expected, when operating the LiB at nominal cell operating power, the total mass of the power system almost doubles. Because of the sizing strategy used for the FCREx scenarios, the mass of the PEMFC stack is very similar to each other across all cell operating scenarios. The PEMFC stack is only used to provide base driving and was sized to account for the average power; both tractive and parasitic power were accounted for during the average power calculation. The majority of masses of the power systems come from the LiB stacks and their components.

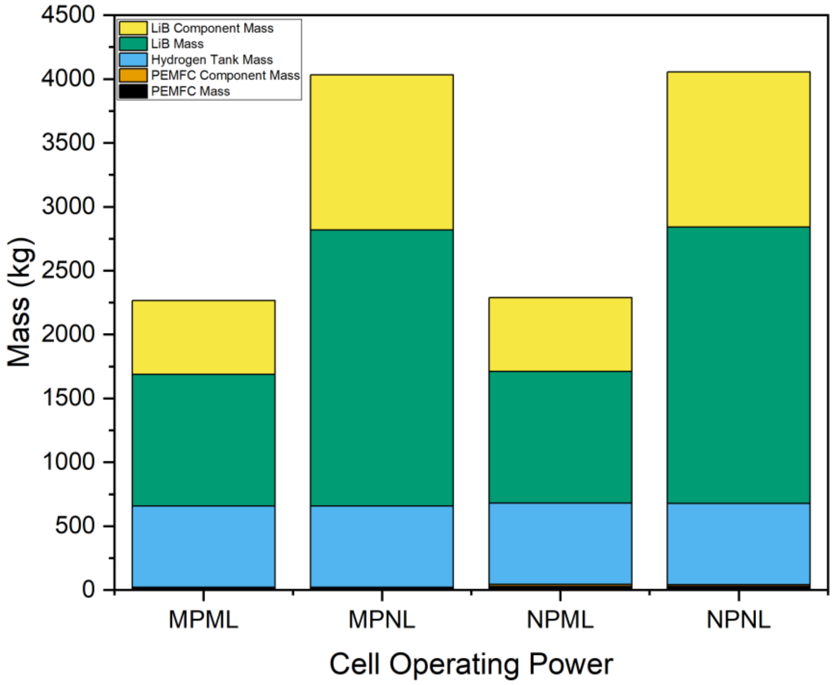

Figure 4-67: Power system mass distributions for an FCREx HGV under different cell operating powers, namely MPML, MPNL, NPML, and NPNL.

If comparing the same Class 8 HGV scenario between a parallel (Figure 4-65) and and FCREx (Figure 4-67) powertrain setup, the parallel setup can be more beneficial in terms of mass reduction for most parallel hybrid degrees. If comparing 0.2 or 0.4 hybrid degrees to the FCREx HGV setup, the mass is similar, it can be more viable to design an FCREx powertrain setup for potential stack and pack longevity and durability advantages.

4.10.2.2 FCREx Bus

Figure 4-68 presents the mass distributions for an FCREx bus under different cell operating powers. Similar to the FCREx HGV scenario, when operating the LiB at nominal cell operating power, the total mass of the power system almost doubles, mainly caused by the increased mass of the LiB stacks and their components. If comparing the same Class 8 bus scenario between a parallel (Figure 4-66) and and FCREx (Figure 4-68) powertrain setup, the parallel setup can be more beneficial in terms of mass reduction for the 0.6 and 0.8 hybrid degrees. As for the 0.2 or 0.4 parallel hybrid degrees to the FCREx bus setup, it is more viable to design an FCREx powertrain setup for potential stack and pack longevity and durability advantages as the total power system mass between the parallel and FCREx powertrain are similar.

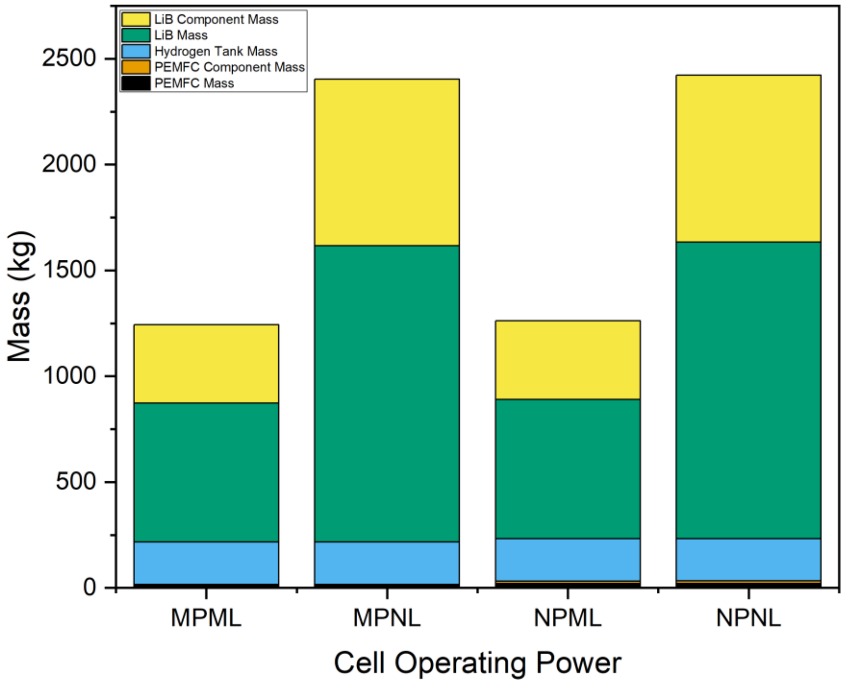

Figure 4-68: Power system mass distributions for an FCREx bus under different cell operating powers, namely MPML, MPNL, NPML, and NPNL.

5 Conclusions and Future Work

This modelling aspect of this research, featuring the self-built MATLAB model HybeMass, has thoroughly examined the HD and cell operating power, establishing the necessary parameters for PEMFC and LiB cell numbers, as well as the overall power system and GVM. The implementation of a novel system mass feedback loop has enabled the automatic adjustment of the required power demand based on the changing mass of the system. This adaptive approach identifies the optimal HD or sizing, crucial for minimising vehicle mass—a pivotal design factor contributing to extended range. The evaluation extended to transient drive cycles, allowing for the estimation of power demands in diverse scenarios for LDVs, Class 8 HGVs, and buses. To ensure precision, the model accounts for parasitic component masses, auxiliary power draw, and efficiency losses in the relevant systems.

For most parallel powertrain scenarios, an HD of 0.4 or more would result in a lesser power system mass when compared to a full BEV. MPML cell operating power configuration would typically provide the lightest power systems while having the lowest durability, especially for PEMFCs. Having LiBs operating at maximum cell operating power did not necessarily suggest that the degradation rate would be higher than at minimum. MPNL disregards the electrochemical benefits of PEMFCs and LiBs and is not a recommended setup. NPML utilises the advantageous electrochemical properties of both PEMFC and LiB and is considered a balance point for maintaining both feasible mass configuration and vehicle durability. NPNL is the ‘safest’ choice in terms of vehicle durability but results in the most mass. This would be a good setup if a manufacturer’s goal is to produce ‘longer-lasting’ vehicles, with an emphasis on longer-lasting PEMFCs. However, even with the NPNL hybridisation setup, the mass of the power systems for parallel powertrains is still less than that of BEVs.

The HybeMass model developed here is a useful tool to enable improve the efficiency of FCHEV component sizing for automotive manufacturers and researchers. The novel system weight feedback loop eliminates the need to estimate the vehicle's accurate GVM and power requirements a priori, instead calculating the number of PEMFC and LiB cells required alongside the total power requirements. The model has been demonstrated for different scenarios of automotive, namely LDV, HGV, and bus, across different HDs, operating powers, and vehicle architectures (parallel, series-parallel, and FCREx); allowing the user to identify viable configurations depending on the vehicle design goals and purpose. Further by introducing simple modifications to the input the model can be deployed across any vehicle class and type. The model acts as a quick visualisation, elimination and calculation step prior to hardware-in-the-loop testing or bench testing of individual PEMFC or battery cells and will support wider efforts to accelerate the electrification of transport in academia and industry.

For future work, a suitable ratio can be applied to adjust the hydrogen tank weight estimation between different hybrid degrees.

The experimental studies of this PhD research have provided insights into the extent of degradation of PEMFCs in FCHEVs, during the critical break-in period under a range of potential operating power scenarios. The integration of bench testing simulations, drive cycle analysis, and electrochemistry techniques has allowed for a comprehensive characterisation of PEMFC degradation. Different cell operating power scenarios were explored, including MPML, MPNL, NPML, and NPNL for LDVs, and MPML, NPML, and NPNL for HGVs and buses. For HGVs and buses, both the parallel and FCREx powertrain layouts were analysed.

Based on the results it can be seen that most powertrains operating in NP scenarios showed less PEMFC degradation than in MP scenarios, especially in terms of ECSA decrease. The same cannot be said for the comparison between NL and ML scenarios. When it comes to LiBs, the cell operating power did not influence the degradation rate.

For future work involving cell testing replicating HGVs, the PEMFC can be kept operating above a voltage of 0.7 V, to ensure the most optimal efficiency when powering vehicles of such type.

The cells for the HGV and bus scenarios were tested for a repetition of 100 drive cycles. This is a straightforward process for PEMFCs, as they do not need to be recharged. However, there is a point where this becomes a problem for LiBs, as they do need to be recharged. For example, a fully charged LG M50 may only undergo 40 drive cycles before it is at its lowest SOC, which would then need to be recharged. If this is the case, it would take two and a half charge cycles to fully achieve 100 drive cycles, which isn't a realistic recharge cycle count. So instead, the author has conducted 3 cycles which resulted in a total of 120 drive cycles, slightly over 100. Future work involving drive cycles and LiBs can focus on charge cycle count rather the actual number of drive cycles. But for this work, the drive cycle count was important to match the hybrid scenario of the systems; in other words, the LiBs need to undergo a similar amount of drive cycles as the PEMFCs to achieve a virtual hybridisation analysis.

As mentioned in the Results and Discussion section, there was a suggestion that the MPML of the FCREx powertrain may have advantages over the parallel powertrain in terms of slower ECSA loss. This poses the question of: is it more optimal to hold a PEMFC at peak power for a long period of time than a PEMFC being more transient and occasionally hitting peak power? For future work, more datasets can be collected using the protocols mentioned in this research to further examine this question.

From an electrochemical perspective, within the theoretical PEMFC stacks and LiB packs of this project, all cells are treated as homogeneous in terms of degradation. A further study can take this more into depth in terms of how the cells would behave if they were packaged in parallel vs. series. In addition, instead of a GCTP or GCTS ratio, one can factor in the parasitic components' weight by choosing models from manufacturers (such as commercial cooling systems) or designing or modelling one’s own parasitic components at a more detailed level. These two future work suggestions fall more into the mechanical and automotive engineering realm.

A more powertrain-based model can be created on the basis of the current HybeX model, featuring powertrain components such as motors and wheels. The choice of coaxial motors and wheel hub motors may affect the performance of a theoretical vehicle. Different component choices may also affect the mass of the vehicle. Future collaboration work can focus on expanding the HybeX model to more system-level and powertrain engineering work.

By combining the laboratory testing and MATLAB modelling aspects of this work, the degradation cost per drive cycle for different cell operating power scenarios could be calculated. In this thesis, only the FCREx HGV scenario was analysed. Additional powertrain layouts could also be considered for future work, following the same methodology.

Overall, the lab-based research underscores the complexity of PEMFC and LiB degradation in FCHEVs and the importance of a multi-faceted approach to understanding and mitigating degradation mechanisms. Future studies could explore ex-situ degradation analysis regarding the PEMFC, such as cross-sectional SEM. It has been noted that PEMFCs operating at a more constant power output during FCREx scenarios tend to result in a CV with electrical shorting after endurance bench testing, future work can be conducted to verify the cause and repeatability of this. In a bigger picture, since this PhD work puts more emphasis on the framework of testing methods for FCHEVs, more future work can benefit by utilising these methods and modelling work to provide more repeatability on drive cycle endurance testing for PEMFCs and LiBs, adding more insights revolving real-life condition automotive device testing by characterising them under multiple repeated tests. By advancing our understanding of PEMFC and LiB degradation and developing effective mitigation strategies, this research contributes to the ongoing advancement of fuel cell and battery technology in a vehicle-based scenario and accelerates the transition towards a cleaner, more sustainable transportation.

Bibliography

[1] N. Gray, S. McDonagh, R. O'Shea, B. Smyth, and J. D. Murphy, "Decarbonising ships, planes and trucks: An analysis of suitable low-carbon fuels for the maritime, aviation and haulage sectors," Feb. 23, 2021, *Elsevier Ltd*. doi: 10.1016/j.adapen.2021.100008.

[2] G. G. Nassif and S. C. A. de Almeida, "Impact of powertrain hybridization on the performance and costs of a fuel cell electric vehicle," *Int J Hydrogen Energy*, vol. 45, no. 41, pp. 21722–21737, Aug. 2020, doi: 10.1016/j.ijhydene.2020.05.138.

[3] B. G. Pollet, I. Staffell, and J. L. Shang, "Current status of hybrid, battery and fuel cell electric vehicles: From electrochemistry to market prospects," Dec. 01, 2012. doi: 10.1016/j.electacta.2012.03.172.

[4] J. Di Yang, J. Millichamp, T. Suter, P. R. Shearing, D. J. L. Brett, and J. B. Robinson, "A Review of Drive Cycles for Electrochemical Propulsion," *Energies (Basel)*, vol. 16, no. 18, p. 6552, Sep. 2023, doi: 10.3390/en16186552.

[5] N. Marx, D. Hissel, F. Gustin, L. Boulon, and K. Agbossou, "On the sizing and energy management of an hybrid multistack fuel cell – Battery system for automotive applications," *Int J Hydrogen Energy*, vol. 42, no. 2, pp. 1518–1526, Jan. 2017, doi: 10.1016/j.ijhydene.2016.06.111.

[6] S. C. A. de Almeida and R. Kruczan, "Effects of drivetrain hybridization on fuel economy, performance and costs of a fuel cell hybrid electric vehicle," *Int J Hydrogen Energy*, vol. 46, no. 79, pp. 39404–39414, Nov. 2021, doi: 10.1016/j.ijhydene.2021.09.144.

[7] Y. Preger and L. Torres-Castro, "DOE ESHB Chapter 3: Lithium-Ion Batteries." Accessed: Mar. 20, 2024. [Online]. Available: https://www.sandia.gov/app/uploads/sites/163/2021/09/ESHB-Ch3_Lithium-Batteries_Preger.pdf

[8] C. Spiegel, "PEM Fuel Cell Modeling and Simulation Using MATLAB ®," Elsevier, 2008, ch. 1, 2, pp. 1–124.

[9] R. Devanathan, N. Idupulapati, M. D. Baer, C. J. Mundy, and M. Dupuis, "Ab initio molecular dynamics simulation of proton hopping in a model polymer membrane," *Journal of Physical Chemistry B*, vol. 117, no. 51, pp. 16522–16529, Dec. 2013, doi: 10.1021/jp410229u.

[10] S. Lee *et al.*, "Self-assembled network polymer electrolyte membranes for application in fuel cells at 250 °C," *Nat Energy*, vol. 9, no. 7, pp. 849–861, Jul. 2024, doi: 10.1038/s41560-024-01536-4.

[11] K. Turcheniuk and D. Bondarev, "Ten years left to redesign lithium-ion batteries," *Nature Comment*, 2018, Accessed: Mar. 01, 2024. [Online]. Available: https://www.nature.com/articles/d41586-018-05752-3

[12] I. Buchmann, “Batteries in a portable world : a handbook on rechargeable batteries for non-engineers,” 4th ed., Richmond: Cadex Electronics Inc., 2016, ch. 9, pp. 414–478.

[13] N. Jones, “The new car batteries that could power the electric vehicle revolution,” *Nature News Feature*, Feb. 2024, doi: 10.1021/acscentsci.3c01478.

[14] J. Li *et al.*, “Toward Low-Cost, High-Energy Density, and High-Power Density Lithium-Ion Batteries,” Sep. 01, 2017, *Minerals, Metals and Materials Society*. doi: 10.1007/s11837-017-2404-9.

[15] T. Liu *et al.*, “Correlation between manganese dissolution and dynamic phase stability in spinel-based lithium-ion battery,” *Nat Commun*, vol. 10, no. 1, Dec. 2019, doi: 10.1038/s41467-019-12626-3.

[16] W. Li, E. M. Erickson, and A. Manthiram, “High-nickel layered oxide cathodes for lithium-based automotive batteries,” *Nat Energy*, vol. 5, no. 1, pp. 26–34, Jan. 2020, doi: 10.1038/s41560-019-0513-0.

[17] D. Hou *et al.*, “Effect of the grain arrangements on the thermal stability of polycrystalline nickel-rich lithium-based battery cathodes,” *Nat Commun*, vol. 13, no. 1, Dec. 2022, doi: 10.1038/s41467-022-30935-y.

[18] X. G. Yang, T. Liu, and C. Y. Wang, “Thermally modulated lithium iron phosphate batteries for mass-market electric vehicles,” *Nat Energy*, vol. 6, no. 2, pp. 176–185, Feb. 2021, doi: 10.1038/s41560-020-00757-7.

[19] D. Jugović and D. Uskoković, “A review of recent developments in the synthesis procedures of lithium iron phosphate powders,” May 15, 2009. doi: 10.1016/j.jpowsour.2009.01.074.

[20] K. Märker, P. J. Reeves, C. Xu, K. J. Griffith, and C. P. Grey, “Evolution of Structure and Lithium Dynamics in LiNi0.8Mn0.1Co0.1O2 (NMC811) Cathodes during Electrochemical Cycling,” *Chemistry of Materials*, vol. 31, no. 7, pp. 2545–2554, Apr. 2019, doi: 10.1021/acs.chemmater.9b00140.

[21] A. D. A. Bin Abu Sofian *et al.*, “Nickel-rich nickel–cobalt–manganese and nickel–cobalt–aluminum cathodes in lithium-ion batteries: Pathways for performance optimization,” Jan. 05, 2024, *Elsevier Ltd*. doi: 10.1016/j.jclepro.2023.140324.

[22] S. U. Muzayanha *et al.*, “A fast metals recovery method for the synthesis of lithium nickel cobalt aluminum oxide material from cathode waste,” *Metals (Basel)*, vol. 9, no. 5, May 2019, doi: 10.3390/met9050615.

[23] C. H. Chen, J. Liu, M. E. Stoll, G. Henriksen, D. R. Vissers, and K. Amine, “Aluminum-doped lithium nickel cobalt oxide electrodes for high-power lithium-ion batteries,” *J Power Sources*, vol. 128, no. 2, pp. 278–285, Apr. 2004, doi: 10.1016/j.jpowsour.2003.10.009.

[24] S. Vadivel, N. Phattharasupakun, J. Wutthiprom, S. Duangdangchote, and M. Sawangphruk, “High-performance li-ion batteries using nickel-rich lithium nickel cobalt aluminium oxide-nanocarbon core-shell cathode: In operando X-ray Diffraction,” *ACS Appl Mater Interfaces*, vol. 11, no. 34, pp. 30719–30727, Aug. 2019, doi: 10.1021/acsami.9b06553.

[25] S. Hwang and E. A. Stach, “Using in situ and operando methods to characterize phase changes in charged lithium nickel cobalt aluminum oxide cathode materials,” Jan. 06, 2020, *Institute of Physics Publishing*. doi: 10.1088/1361-6463/ab60ea.

[26] N. Omar *et al.*, “Assessment of Performance of Lithium Iron Phosphate Oxide, Nickel Manganese Cobalt Oxide and Nickel Cobalt Aluminum Oxide Based cells for Using in Plug-in Battery Electric Vehicle Applications,” *IEEE Conference on Vehicle Power and Propulsion (VPPC)*, 2011, doi: 10.1109/VPPC.2011.6043017.

[27] N. Jackson, R. Morgan, D. Brett, and N. Brandon, “Fuel Cell Roadmap 2020 Narrative Report,” 2021. Accessed: May. 07, 2025. [Online]. Available: https://www.apcuk.co.uk/wp-content/uploads/2021/09/https___www.apcuk_.co_.uk_app_uploads_2021_02_Exec-summary-Technology-Roadmap-Fuel-Cells-final.pdf

[28] A. Behera, “Fuel cells recycling,” in *Nanotechnology in Fuel Cells*, Elsevier, 2022, pp. 361–373. doi: 10.1016/B978-0-323-85727-7.00011-4.

[29] N. Jackson and D. Greenwood, “Electrical Energy Storage Roadmap 2020 Narrative Report,” 2021.

[30] J. G. . Hayes and G. A. . Goodarzi, “Electric powertrain : energy systems, power electronics & drives for hybrid, electric and fuel cell vehicles,” John Wiley & Sons Ltd, 2018, pp. 19–34.

[31] M. Younas, S. Shafique, A. Hafeez, F. Javed, and F. Rehman, “An Overview of Hydrogen Production: Current Status, Potential, and Challenges,” May 15, 2022, *Elsevier Ltd*. doi: 10.1016/j.fuel.2022.123317.

[32] *UK Hydrogen Strategy*. [Dandy Booksellers Ltd], 2021.

[33] V. Vallejo, Q. Nguyen, and A. P. Ravikumar, “Geospatial variation in carbon accounting of hydrogen production and implications for the US Inflation Reduction Act,” *Nat Energy*, vol. 9, no. 12, pp. 1571–1582, Oct. 2024, doi: 10.1038/s41560-024-01653-0.

[34] J. Huang, P. Balcombe, and Z. Feng, “Technical and economic analysis of different colours of producing hydrogen in China,” *Fuel*, vol. 337, Apr. 2023, doi: 10.1016/j.fuel.2022.127227.

[35] T. Technologies, “HYS2125 Tetronics Technologies Final Feasibility Report (Public) Tetronics Hydrogen Plasmolysis Production Feasibility Study Report Customer: BEIS Hydrogen Supply 2 Competition Document number: P1158-05-TD001 Revision number: R5_Public Version HYS2125 Tetronics Technologies Final Feasibility Report (Public).”

[36] K. Durkin *et al.*, “Hydrogen-Powered Vehicles: Comparing the Powertrain Efficiency and Sustainability of Fuel Cell versus Internal Combustion Engine Cars,” *Energies (Basel)*, vol. 17, no. 5, Mar. 2024, doi: 10.3390/en17051085.

[37] S. Pemberton, A. Nobajas, and R. Waller, “Rapid charging provision, multiplicity and battery electric vehicle (BEV) mobility in the UK,” *J Transp Geogr*, vol. 95, Jul. 2021, doi: 10.1016/j.jtrangeo.2021.103137.

[38] D. F. Syahbana and B. Trilaksono, “MPC and Filtering-Based Energy Management in Fuel Cell/ Battery/ Supercapacitor Hybrid Source,” 2019, doi: 10.1109/ICEEI47359.2019.8988849.

[39] “Hybrid Electric Vehicles.”

[40] *IECON 2013-39th Annual Conference of the IEEE Industrial Electronics Society : proceedings : Austria Center Vienna, Vienna, Austria, 10-14 November, 2013*. IEEE, 2013.

[41] P. Iurilli, C. Brivio, and V. Wood, “On the use of electrochemical impedance spectroscopy to characterize and model the aging phenomena of lithium-ion batteries: a critical review,” Sep. 01, 2021, *Elsevier B.V.* doi: 10.1016/j.jpowsour.2021.229860.

[42] B. G. Pollet, S. S. Kocha, and I. Staffell, “Current status of automotive fuel cells for sustainable transport,” Aug. 01, 2019, *Elsevier B.V.* doi: 10.1016/j.coelec.2019.04.021.

[43] Y. Wang, S. J. Moura, S. G. Advani, and A. K. Prasad, “Power management system for a fuel cell/battery hybrid vehicle incorporating fuel cell and battery degradation,” *Int J Hydrogen Energy*, vol. 44, no. 16, pp. 8479–8492, Mar. 2019, doi: 10.1016/j.ijhydene.2019.02.003.

[44] K. Meng, H. Zhou, B. Chen, and Z. Tu, “Dynamic current cycles effect on the degradation characteristic of a H2/O2 proton exchange membrane fuel cell,” *Energy*, vol. 224, Jun. 2021, doi: 10.1016/j.energy.2021.120168.

[45] M. Chandran, K. Palaniswamy, N. B. Karthik Babu, and O. Das, “A study of the influence of current ramp rate on the performance of polymer electrolyte membrane fuel cell,” *Sci Rep*, vol. 12, no. 1, Dec. 2022, doi: 10.1038/s41598-022-25037-0.

[46] R. Bisschop, O. Willstrand, F. Amon, and M. Rosengren, “Fire Safety of Lithium-Ion Batteries in Road Vehicles,” 2019, doi: 10.13140/RG.2.2.18738.15049.

[47] C. Hochgraf, “Electric Vehicles: Fuel Cells Introduction-Why Fuel Cells?,” *Encyclopedia of Electrochemical Power Sources*. pp. 236–248, 2009. doi: 10.1016/B978-044452745-5.00863-7.

[48] J. Francfort and K. Walkowicz, “Electrochemical Energy Storage Technical Team Roadmap,” *U.S. Drive*, no. June, p. 2, 2017.

[49] B. G. Pollet, I. Staffell, and J. L. Shang, “Current status of hybrid, battery and fuel cell electric vehicles: From electrochemistry to market prospects,” *Electrochim Acta*, vol. 84, pp. 235–249, 2012, doi: 10.1016/j.electacta.2012.03.172.

[50] C. Mi, M. A. Masrur, and D. W. Gao, *Hybrid Electric Vehicles: Principles and Applications with Practical Perspectives*, 1st ed. Chichester: Wiley, 2011. doi: 10.1002/9781119998914.

[51] P. Fisher, J. Jostins, S. Hilmansen, and K. Kendall, “Electronic integration of fuel cell and battery system in novel hybrid vehicle,” *J Power Sources*, vol. 220, pp. 114–121, 2012, doi: 10.1016/j.jpowsour.2012.07.071.

[52] K. Çağatay Bayindir, M. A. Gözüküçük, and A. Teke, “A comprehensive overview of hybrid electric vehicle: Powertrain configurations, powertrain control techniques and electronic control units,” *Energy Convers Manag*, vol. 52, no. 2, pp. 1305–1313, 2011, doi: 10.1016/j.enconman.2010.09.028.

[53] Y. Baik, R. Hensley, P. Hertzke, and S. Knupfer, “Making Electric Vehicles Profitable,” McKinsey & Company Automotive & Assembly. Accessed: May. 07, 2025. [Online]. Available: https://www.mckinsey.com/industries/automotive-and-assembly/our-insights/making-electric-vehicles-profitable

[54] A. Hermann, T. Chaudhuri, and P. Spagnol, “Bipolar plates for PEM fuel cells: A review,” in *International Journal of Hydrogen Energy*, Sep. 2005, pp. 1297–1302. doi: 10.1016/j.ijhydene.2005.04.016.

[55] B. G. Pollet, S. S. Kocha, and I. Staffell, “Current status of automotive fuel cells for sustainable transport,” *Curr Opin Electrochem*, vol. 16, no. i, pp. 90–95, 2019, doi: 10.1016/j.coelec.2019.04.021.

[56] P. Fisher, J. Jostins, S. Hilmansen, and K. Kendall, “Electronic integration of fuel cell and battery system in novel hybrid vehicle,” *J Power Sources*, vol. 220, pp. 114–121, Dec. 2012, doi: 10.1016/j.jpowsour.2012.07.071.

[57] Y. Wang, S. J. Moura, S. G. Advani, and A. K. Prasad, “Optimization of powerplant component size on board a fuel cell/battery hybrid bus for fuel economy and system durability,” *Int J Hydrogen Energy*, vol. 44, no. 33, pp. 18283–18292, Jul. 2019, doi: 10.1016/j.ijhydene.2019.05.160.

[58] N. Marx, D. Hissel, F. Gustin, L. Boulon, and K. Agbossou, “On the sizing and energy management of an hybrid multistack fuel cell – Battery system for automotive applications,” *Int J Hydrogen Energy*, vol. 42, no. 2, pp. 1518–1526, Jan. 2017, doi: 10.1016/j.ijhydene.2016.06.111.

[59] J. Bernard, S. Delprat, F. N. Büchi, and T. M. Guerra, “Fuel-cell hybrid powertrain: Toward minimization of hydrogen consumption,” *IEEE Trans Veh Technol*, vol. 58, no. 7, pp. 3168–3176, 2009, doi: 10.1109/TVT.2009.2014684.

[60] M. Kim, Y. J. Sohn, W. Y. Lee, and C. S. Kim, “Fuzzy control based engine sizing optimization for a fuel cell/battery hybrid mini-bus,” *J Power Sources*, vol. 178, no. 2, pp. 706–710, Apr. 2008, doi: 10.1016/j.jpowsour.2007.12.047.

[61] Y. Wang, S. J. Moura, S. G. Advani, and A. K. Prasad, “Optimization of powerplant component size on board a fuel cell/battery hybrid bus for fuel economy and system durability,” *Int J Hydrogen Energy*, vol. 44, no. 33, pp. 18283–18292, Jul. 2019, doi: 10.1016/j.ijhydene.2019.05.160.

[62] Q. Cai, D. J. L. Brett, D. Browning, and N. P. Brandon, “A sizing-design methodology for hybrid fuel cell power systems and its application to an unmanned underwater vehicle,” *J Power Sources*, vol. 195, no. 19, pp. 6559–6569, Oct. 2010, doi: 10.1016/j.jpowsour.2010.04.078.

[63] K. Çağatay Bayindir, M. A. Gözüküçük, and A. Teke, “A comprehensive overview of hybrid electric vehicle: Powertrain configurations, powertrain control techniques and electronic control units,” *Energy Convers Manag*, vol. 52, no. 2, pp. 1305–1313, 2011, doi: 10.1016/j.enconman.2010.09.028.

[64] J. S. Partridge, W. Wu, and R. W. G. Bucknall, “Investigation on the Impact of Degree of Hybridisation for a Fuel Cell Supercapacitor Hybrid Bus with a Fuel Cell Variation Strategy,” *Vehicles*, vol. 2, no. 1, pp. 1–17, Mar. 2020, doi: 10.3390/vehicles2010001.

[65] P. Atwood, S. Gurski, D. J. Nelson, and K. B. Wipke, “Degree of Hybridization Modeling of a Fuel Cell Hybrid Electric Sport Utility Vehicle,” 2001.

[66] L. Feng, T. C. Chang, G. Weiwei, Y. C. Xie, and L. P. Zheng, “Optimal system parameters and hybrid ratio for fuel cell hybrid electric vehicles,” *Sensors and Materials*, vol. 32, no. 5, pp. 1593–1607, 2020, doi: 10.18494/SAM.2020.2694.

[67] S. Grammatico, A. Balluchi, and D. Italia, *A series-parallel hybrid electric powertrain for industrial vehicles Ettore Cosoli*.

[68] M. Janulin, O. Vrublevskyi, and A. Prokhorenko, "Energy Minimization in City Electric Vehicle using Optimized Multi-Speed Transmission," *International Journal of Automotive and Mechanical Engineering*, vol. 19, no. 2, pp. 9721–9733, 2022, doi: 10.15282/ijame.19.2.2022.08.0750.

[69] B. Wu *et al.*, "Design and testing of a 9.5 kWe proton exchange membrane fuel cell-supercapacitor passive hybrid system," *Int J Hydrogen Energy*, vol. 39, no. 15, pp. 7885–7896, May 2014, doi: 10.1016/j.ijhydene.2014.03.083.

[70] D. Lanzarotto, M. Marchesoni, M. Passalacqua, A. P. Prato, and M. Repetto, "Overview of different hybrid vehicle architectures," Elsevier B.V., Jan. 2018, pp. 218–222. doi: 10.1016/j.ifacol.2018.07.036.

[71] B. O. Varga, "Electric vehicles, primary energy sources and CO2 emissions: Romanian case study," *Energy*, vol. 49, no. 1, pp. 61–70, Jan. 2013, doi: 10.1016/j.energy.2012.10.036.

[72] N. Xu *et al.*, "Towards a smarter energy management system for hybrid vehicles: A comprehensive review of control strategies," May 01, 2019, *MDPI AG*. doi: 10.3390/app9102026.

[73] R. E. Silva *et al.*, "Proton exchange membrane fuel cell operation and degradation in short-circuit," *Fuel Cells*, vol. 14, no. 6, pp. 894–905, Dec. 2014, doi: 10.1002/fuce.201300216.

[74] T. Barlow, S. Latham, I. Mccrae, and P. Boulter, "A reference book of driving cycles for use in the measurement of road vehicle emissions," *TRL Published Project Report*, p. 280, 2009.

[75] A. Esteves-Booth, T. Muneer, J. Kubie, and H. Kirby, "A review of vehicular emission models and driving cycles."

[76] M. Tutuianu *et al.*, "Development of the World-wide harmonized Light duty Test Cycle (WLTC) and a possible pathway for its introduction in the European legislation," *Transp Res D Transp Environ*, vol. 40, pp. 61–75, 2015, doi: 10.1016/j.trd.2015.07.011.

[77] R. Singh and S. Mittal, "A Simplified Method to Form a Fuel Economy Test Cycle for Test Tracks/Autonomous Vehicles," *SAE Technical Papers*, vol. 2019-Janua, no. January, pp. 1–9, 2019, doi: 10.4271/2019-26-0343.

[78] R. Nicolas, "The Different Driving Cycles," Car Engineer. Accessed: May. 07, 2025. [Online]. Available: https://www.car-engineer.com/the-different-driving-cycles/

[79] J. Son *et al.*, "COMPARATIVE STUDY BETWEEN KOREA AND UK: RELATIONSHIP BETWEEN DRIVING STYLE AND REAL-WORLD FUEL CONSUMPTION," *International Journal of Automotive Technology*, vol. 17, no. 1, pp. 175–181, 2016, doi: 10.1007/s12239−016−0017−x.

[80] E. G. Giakoumis, *Driving and Engine Cycles*. Springer, 2017. doi: 10.1007/978-3-319-49034-2.

[81] H. C. Watson, "Vehicle Driving Patterns and Measurement Methods for Energy and Emissions Assessment," *Bureau of Transport Economics*, 1978.

[82] S. M. A. Rahman *et al.*, "State-of-the-art of establishing test procedures for real driving gaseous emissions from light- and heavy-duty vehicles," *Energies (Basel)*, vol. 14, no. 14, 2021, doi: 10.3390/en14144195.

[83] EPA, “United States Environmental Protection Agency Frequently Asked Questions,” U.S. Department of Energy. Accessed: May. 07, 2025. [Online]. Available: https://www.fueleconomy.gov/feg/info.shtml#guzzler

[84] Secretariat of the United Nations, “Recueil des Traites,” *Treaty Series*, vol. 1249, pp. 20376–20402, 1981.

[85] Y. Liu, W. Zhi Xin, H. Zhou, and L. Meng Liang, “Development of China Light-Duty Vehicle Test Cycle,” *International Journal of Automotive Technology*, vol. 21, no. 4, pp. 1233–1246, 2020, doi: 10.1007/s12239-020-0117-5.

[86] G. Tsotridis, A. Pilenga, G. De Marco, and T. Malkow, “EU HARMONISED TEST PROTOCOLS FOR PEMFC MEA TESTING IN SINGLE CELL CONFIGURATION FOR AUTOMOTIVE APPLICATIONS,” 2015, doi: 10.2790/54653.

[87] DieselNet, “ECE 15 + EUDC / NEDC,” DieselNet. Accessed: May. 07, 2025. [Online]. Available: https://dieselnet.com/standards/cycles/ece_eudc.php

[88] N. T. Jeong, S. M. Yang, K. S. Kim, M. S. Wang, H. S. Kim, and M. W. Suh, “URBAN DRIVING CYCLE FOR PERFORMANCE EVALUATION OF ELECTRIC VEHICLES,” *International Journal of Automotive Technology*, vol. 17, no. 1, pp. 145–151, 2016, doi: 10.1007/s12239−016−0014−0.

[89] J. Peng, J. Jiang, F. Ding, and H. Tan, “Development of driving cycle construction for hybrid electric bus: A case study in Zhengzhou, China,” *Sustainability (Switzerland)*, vol. 12, no. 17, Sep. 2020, doi: 10.3390/su12177188.

[90] S. Samuel, L. Austin, and D. Morrey, “Automotive test drive cycles for emission measurement and real-world emission levels-a review,” 2002.

[91] H. Y. Tong and K. W. Ng, “Developing electric bus driving cycles with significant road gradient changes: A case study in Hong Kong,” *Sustain Cities Soc*, vol. 98, p. 104819, Nov. 2023, doi: 10.1016/j.scs.2023.104819.

[92] A. Fotouhi and M. Montazeri-Gh, “Tehran driving cycle development using the k-means clustering method,” *Scientia Iranica*, vol. 20, no. 2, pp. 286–293, 2013, doi: 10.1016/j.scient.2013.04.001.

[93] J. Peng, J. Jiang, F. Ding, and H. Tan, “Development of driving cycle construction for hybrid electric bus: A case study in Zhengzhou, China,” *Sustainability (Switzerland)*, vol. 12, no. 17, 2020, doi: 10.3390/su12177188.

[94] Launch UK, “X-431 Euro Pro 5 LINK,” Launch UK. Accessed: May 07, 2025. [Online]. Available: https://www.launchtech.co.uk/oem-level-vehicle-diagnostics/X-431-Euro-Pro-5-LINK-with-Smartlink-VCi/

[95] The Council of the European Communities, *Council Directive 70/220/EEC of 20 March 1970 on the approximation of the laws of the Member States relating to measures to be taken against air pollution by gases from positive-ignition engines of motor vehicles*. The Council of the European Communities, 1970.

[96] WLTP Facts, “From NEDC to WLTP: What will Change?,” WLTP Facts. Accessed: May. 05, 2025. [Online]. Available: https://www.wltpfacts.eu/from-nedc-to-wltp-change/

[97] T. Shale-Hestor, “What are the NEDC Fuel Economy Tests?,” Auto Express. Accessed: May. 07, 2025. [Online]. Available: https://www.autoexpress.co.uk/car-news/107032/what-are-the-nedc-fuel-economy-tests

[98] DieselNet, “FTP-72 (UDDS),” DieselNet. Accessed: May. 07, 2025. [Online]. Available: https://dieselnet.com/standards/cycles/ftp72.php

[99] DieselNet, “FTP-75,” DieselNet. Accessed: May. 05, 2025. [Online]. Available: https://dieselnet.com/standards/cycles/ftp75.php

[100] G. Karavalakis *et al.*, “Criteria emissions, particle number emissions, size distributions, and black carbon measurements from PFI gasoline vehicles fuelled with different ethanol and butanol blends,” *SAE Technical Papers*, vol. 2, no. April 2013, 2013, doi: 10.4271/2013-01-1147.

[101] J. Kuhlwein, J. German, and A. Bandivadekar, “Development of Test Cycle Conversion Factors Among Worldwide Light-Duty Vehicle Co2 Emission Standards,” *The International Council on Clean Transportation - ICCT*, no. September, p. 64, 2014.

[102] Mathworks, “Drive Cycle Source,” 2017, *Mathworks*: 2020a.

[103] United States Environmental Protection Agency, “PA EPA Adds Reality Driving Cycle to VEH. Certification Test,” EPA. Accessed: May. 07, 2025. [Online]. Available: https://archive.epa.gov/epapages/newsroom_archive/newsreleases/8fe4d7d91eafa23d8525646b006991da.html

[104] DieselNet, “SFTP-US06,” DieselNet. Accessed: May. 07, 2025. [Online]. Available: https://dieselnet.com/standards/cycles/ftp_us06.php

[105] DieselNet, “SFTP-SC03,” DieselNet. Accessed: May. 07, 2025. [Online]. Available: https://dieselnet.com/standards/cycles/ftp_sc03.php

[106] Earth Cars, “EPA Fuel Economy Ratings - What’s Coming in 2008,” Earth Cars. Accessed: May. 07, 2025. [Online]. Available: https://web.archive.org/web/20071008015835/http://www.earthcars.com/articles/article.htm?articleId=6

[107] DieselNet, “EPA Highway Fuel Economy Test Cycle (HWFET),” DieselNet. Accessed: May. 07, 2025. [Online]. Available: https://dieselnet.com/standards/cycles/hwfet.php

[108] Transport Policy, “Japan Light-Duty Emissions,” TransportPolicy.net. Accessed: May. 07, 2025. [Online]. Available: https://www.transportpolicy.net/standard/japan-light-duty-emissions/

[109] InterRegs, “GB/T 38146.1-2019,” InterRegs International Regulations. Accessed: May. 07, 2025. [Online]. Available: https://www.interregs.com/catalogue/details/chn-38146119/gb-t-381461-2019/automotive-test-cycle-for-light-duty-vehicles/

[110] DieselNet, “China Light-Duty Vehicle Test Cycle (CLTC),” DieselNet. Accessed: May. 07, 2025. [Online]. Available: https://dieselnet.com/standards/cycles/cltc.php

[111] H. Yu, Y. Liu, and J. Li, “Comparison of fuel consumption and emission characteristics of china VI coach under different test cycle,” *IOP Conf Ser Earth Environ Sci*, vol. 431, no. 1, pp. 1–4, 2019, doi: 10.1088/1755-1315/431/1/012062.

[112] International Council on Clean Transportation, “China’s Stage 6 Emission Standard for New Light-Duty Vehicles (Final Rule),” *International Council on Clean Transportation*, no. March 2017, 2017.

[113] X. Wang, T. Fu, C. Wang, and J. Ling, “Fuel Consumption and Emissions at China Automotive Test Cycle for A Heavy Duty Vehicle based on Engine-in-the-loop Methodology,” *J Phys Conf Ser*, vol. 1549, no. 2, 2020, doi: 10.1088/1742-6596/1549/2/022119.

[114] X-Engineer, “EV design – Energy Consumption,” X-Engineer. Accessed: May. 07, 2025. [Online]. Available: https://x-engineer.org/automotive-engineering/vehicle/electric-vehicles/ev-design-energy-consumption/

[115] EC, “Commission Regulation (EU) 2018/1832 of 5 November 2018 amending Directive 2007/46/EC of the European Parliament and of the Council, Commission Regulation (EC) No 692/2008 and Commission Regulation (EU) 2017/1151 for the purpose of improving the emission,” *Official Journal of the European Union*, vol. 1832, no. 692, p. 301, 2018.

[116] German Association of the Automotive Industry, “Global WLTP Roll-Out for More Realistic Results in Fuel Consumption,” Verband der Automobilindustrie. Accessed: May. 07, 2025. [Online]. Available: https://www.vda.de/en/topics/environment-and-climate/Global-WLTP-roll-out-for-more-realistic-results-in-fuel-consumption/WLTP-Why-a-new-test-procedure.html

[117] WLTP Facts, “Transition Timeline: From NEDC to WLTP,” WLTP Facts. Accessed: May. 07, 2025. [Online]. Available: https://www.wltpfacts.eu/

[118] DieselNet, “Worldwide Harmonized Light Vehicles Test Cycle (WLTC),” DieselNet. Accessed: May. 07, 2025. [Online]. Available: https://dieselnet.com/standards/cycles/wltp.php

[119] Drive Smart, “Speed Limits by Country,” Drive Smart. [Online]. Available: https://www.rhinocarhire.com/Drive-Smart-Blog/Speed-Limits-by-Country.aspx

[120] H. Wang, X. Zhang, and M. Ouyang, “Energy consumption of electric vehicles based on real-world driving patterns: A case study of Beijing,” *Appl Energy*, vol. 157, pp. 710–719, Nov. 2015, doi: 10.1016/j.apenergy.2015.05.057.

[121] A. Fotouhi and M. Montazeri-Gh, “Tehran driving cycle development using the k-means clustering method,” *Scientia Iranica*, vol. 20, no. 2, pp. 286–293, 2013, doi: 10.1016/j.scient.2013.04.001.

[122] Georgios. Tsotridis, Alberto. Pilenga, Giancarlo. De Marco, Thomas. Malkow, and European Commission. Joint Research Centre., *EU harmonised test protocols for PEMFC MEA testing in single cell configuration for automotive applications.* Publications Office, 2015.

[123] D. Lanzarotto, M. Marchesoni, M. Passalacqua, A. P. Prato, and M. Repetto, “Overview of different hybrid vehicle architectures,” *IFAC-PapersOnLine*, vol. 51, no. 9, pp. 218–222, 2018, doi: 10.1016/j.ifacol.2018.07.036.

[124] S. Grammatico, A. Balluchi, and E. Cosoli, “A series-parallel hybrid electric powertrain for industrial vehicles,” *2010 IEEE Vehicle Power and Propulsion Conference, VPPC 2010*, pp. 0–5, 2010, doi: 10.1109/VPPC.2010.5729045.

[125] J. Whitehead, “Here’s Why Electric Cars have Plenty of Grunt, Oomph and Torque,” The Conversation.

[126] A. Meddour, N. Rizoug, and A. Babin, “The influence of driving cycle characteristics on motor optimisation for electric vehicles,” in *2022 30th Mediterranean Conference on Control and Automation, MED 2022*, Institute of Electrical and Electronics Engineers Inc., 2022, pp. 43–48. doi: 10.1109/MED54222.2022.9837227.

[127] X. Zhao, J. Ma, S. Wang, Y. Ye, Y. Wu, and M. Yu, “Developing an electric vehicle urban driving cycle to study differences in energy consumption,” *Environmental Science and Pollution Research*, vol. 26, no. 14, pp. 13839–13853, May 2019, doi: 10.1007/s11356-018-3541-6.

[128] T. Koossalapeerom, T. Satiennam, W. Satiennam, W. Leelapatra, A. Seedam, and T. Rakpukdee, “Comparative study of real-world driving cycles, energy consumption, and CO2 emissions of electric and gasoline motorcycles driving in a congested urban corridor,” *Sustain Cities Soc*, vol. 45, pp. 619–627, Feb. 2019, doi: 10.1016/j.scs.2018.12.031.

[129] F. Borgia and S. Samuel, “Design of Drive Cycle for Electric Powertrain Testing,” in *SAE Technical Papers*, SAE International, Apr. 2023. doi: 10.4271/2023-01-0482.

[130] C. P. Lawrence, R. ElShatshat, M. M. A. Salama, and R. A. Fraser, “An efficient auxiliary system controller for Fuel Cell Electric Vehicle (FCEV),” *Energy*, vol. 116, pp. 417–428, Dec. 2016, doi: 10.1016/j.energy.2016.09.131.

[131] G. Tsotridis, A. Pilenga, G. Marco, and T. Malkow, *EU harmonised test protocols for PEMFC MEA testing in single cell configuration for automotive applications*, vol. 27632. 2015. doi: 10.2790/54653.

[132] G. Tsotridis, A. Pilenga, G. De Marco, and T. Malkow, “EU HARMONISED TEST PROTOCOLS FOR PEMFC MEA TESTING IN SINGLE CELL CONFIGURATION FOR AUTOMOTIVE APPLICATIONS,” 2015, doi: 10.2790/54653.

[133] J. Di Yang, J. Millichamp, T. Suter, P. R. Shearing, D. J. L. Brett, and J. B. Robinson, “A Review of Drive Cycles for Electrochemical Propulsion,” Sep. 01, 2023, *Multidisciplinary Digital Publishing Institute (MDPI)*. doi: 10.3390/en16186552.

[134] MATLAB, “Fuel Cell Stack,” Mathworks. Accessed: Aug. 06, 2024. [Online]. Available: https://uk.mathworks.com/help/sps/powersys/ref/fuelcellstack.html

[135] T. A. M. Suter *et al.*, “Engineering Catalyst Layers for Next-Generation Polymer Electrolyte Fuel Cells: A Review of Design, Materials, and Methods,” Oct. 01, 2021, *John Wiley and Sons Inc*. doi: 10.1002/aenm.202101025.

[136] K. Cooper, “In Situ PEMFC Fuel Crossover & Electrical Short Circuit Measurement,” *Scribner Associates*, 2008. Accessed: Aug. 06, 2024. [Online]. Available: https://www.scribner.com/files/tech-papers/Scribner-on-Crossover-Fuel-Cell-Magazine-2008.pdf

[137] Z. Rui *et al.*, “A Highly Durable Quercetin-Based Proton Exchange Membrane for Fuel Cells,” *J Electrochem Soc*, vol. 166, no. 7, pp. F3052–F3057, 2019, doi: 10.1149/2.0071907jes.

[138] C. Beasley, “Potentiostat Fundamentals,” 2024. Accessed: Aug. 06, 2024. [Online]. Available: https://www.gamry.com/assets/Uploads/Potentiostat-Fundmentals.pdf

[139] S. M. Rezaei Niya and M. Hoorfar, “Study of proton exchange membrane fuel cells using electrochemical impedance spectroscopy technique - A review,” 2013. doi: 10.1016/j.jpowsour.2013.04.011.

[140] R. J. Kang and Y. S. Chen, "Experimental study on the effect of hydrogen sulfide on high-temperature proton exchange membrane fuel cells by using electrochemical impedance spectroscopy," *Catalysts*, vol. 8, no. 10, Oct. 2018, doi: 10.3390/catal8100441.

[141] Y.-S. Kim and S. W. Roh, "Product Specification Rechargeable Lithium Ion Battery Model: INR21700 M50 18.20 Wh," 2016. Accessed: May. 07, 2025. [Online]. Available: https://www.dnkpower.com/wp-content/uploads/2019/02/LG-INR21700-M50-Datasheet.pdf

[142] Y. Zheng *et al.*, "Cell state-of-charge inconsistency estimation for LiFePO4 battery pack in hybrid electric vehicles using mean-difference model," *Appl Energy*, vol. 111, pp. 571–580, 2013, doi: 10.1016/j.apenergy.2013.05.048.

[143] I. Cho and J. Lee, "Characteristics of battery SOC according to drive output and battery capacity of parallel hybrid electric vehicle," *Applied Sciences (Switzerland)*, vol. 10, no. 8, Apr. 2020, doi: 10.3390/APP10082833.

[144] R. Zhao, R. Lorenz, and T. Jahns, "Lithium-ion Battery Rate-of-Degradation Modeling for Real-Time Battery Degradation Control during EV Drive Cycle," *IEEE Energy Conversion Congress and Exposition, ECCE* , 2018.

[145] S. Yang, C. Zhang, J. Jiang, W. Zhang, L. Zhang, and Y. Wang, "Review on state-of-health of lithium-ion batteries: Characterizations, estimations and applications," Sep. 10, 2021, *Elsevier Ltd*. doi: 10.1016/j.jclepro.2021.128015.

[146] BioLogic, "Internal Resistance series. Part I: What is internal resistance in a battery?," BioLogic. Accessed: Jan. 30, 2024. [Online]. Available: https://www.biologic.net/topics/internal-resistance-series-part-i-what-is-internal-resistance-in-a-battery/

[147] B. Liu, H. Zhang, and S. Zhu, "An Incremental V-Model Process for Automotive Development," 2016, doi: 10.1109/APSEC.2016.56.

[148] R. Luca, M. Whiteley, T. Neville, P. R. Shearing, and D. J. L. Brett, "Comparative study of energy management systems for a hybrid fuel cell electric vehicle - A novel mutative fuzzy logic controller to prolong fuel cell lifetime," *Int J Hydrogen Energy*, vol. 47, no. 57, pp. 24042–24058, Jul. 2022, doi: 10.1016/j.ijhydene.2022.05.192.

[149] X. Yang and L. Liu, "Analysis of the influence of passenger load on bus energy consumption a vehicle-engine combined model-based simulation framework," *Nature Scientific Reports*, vol. 12, no. 1, Dec. 2022, doi: 10.1038/s41598-022-18866-6.

[150] L. Barelli, G. Bidini, P. A. Ottaviano, and D. Pelosi, "Vanadium redox flow batteries application to electric buses propulsion: Performance analysis of hybrid energy storage system," *J Energy Storage*, vol. 24, Aug. 2019, doi: 10.1016/j.est.2019.100770.

[151] K. Cousins and R. Zhang, "Highly porous organic polymers for hydrogen fuel storage," Apr. 01, 2019, *MDPI AG*. doi: 10.3390/polym11040690.

[152] A. Fotouhi, N. Shateri, D. Shona Laila, and D. J. Auger, "Electric vehicle energy consumption estimation for a fleet management system," *Int J Sustain Transp*, vol. 15, no. 1, pp. 40–54, 2020, doi: 10.1080/15568318.2019.1681565.

[153] Toyota UK, "TOYOTA MIRAI TECHNICAL SPECIFICATIONS." Accessed: May. 07, 2025. [Online]. Available: https://media.toyota.co.uk/wp-content/uploads/sites/5/pdf/220203M-Mirai-Tech-Spec.pdf

[154] H. Lohse-Busch, B. Richards, and A. Loiselle-Lapointe, "Technology Assessment of a Fuel Cell Vehicle: 2017 Toyota Mirai Energy Systems Division," 2018. Accessed: May. 07, 2025. [Online]. Available: https://publications.anl.gov/anlpubs/2018/06/144774.pdf

[155] O. Bethoux, "Hydrogen fuel cell road vehicles and their infrastructure: An option towards an environmentally friendly energy transition," *Energies (Basel)*, vol. 13, no. 22, Nov. 2020, doi: 10.3390/en13226132.

[156] F. Perrotta, T. Parry, L. C. Neves, T. Buckland, E. Benbow, and M. Mesgarpour, "Verification of the HDM-4 fuel consumption model using a Big data approach: A UK case study," *Transp Res D Transp Environ*, vol. 67, pp. 109–118, Feb. 2019, doi: 10.1016/j.trd.2018.11.001.

[157] F. J. R. Verbruggen, A. Hoekstra, and T. Hofman, "Evaluation of the state-of-the-art of full-electric medium and heavy-duty trucks."

[158] J. M. Moch, "Environmental Implications and Policy Challenges for Bringing Long-Haul Electric Trucks into China The Case of the Tesla Semi," 2019. [Online]. Available: www.belfercenter.org/ENRP

[159] I. Blagojević and S. Mitić, "HYDROGEN AS A VEHICLE FUEL," *Mobility and Vehicle Mechanics*, vol. 44, no. 2, pp. 37–49, Dec. 2018, doi: 10.24874/mvm.2018.44.02.04.

[160] P. Purnima and S. Jayanti, "Optimal sizing of a fuel processor for auxiliary power applications of a fuel cell-powered passenger car," *Int J Hydrogen Energy*, vol. 45, no. 48, pp. 26005–26019, Sep. 2020, doi: 10.1016/j.ijhydene.2020.03.127.

[161] C. P. Lawrence, R. ElShatshat, M. M. A. Salama, and R. A. Fraser, "An efficient auxiliary system controller for Fuel Cell Electric Vehicle (FCEV)," *Energy*, vol. 116, pp. 417–428, Dec. 2016, doi: 10.1016/j.energy.2016.09.131.

[162] J. Kurtz, H. Dinh, G. Saur, and C. Ainscough, "Fuel Cell Technology Status: Degradation," Washington, 2017. Accessed: Apr. 17, 2024. [Online]. Available: https://www.hydrogen.energy.gov/docs/hydrogenprogramlibraries/pdfs/review17/fc081_kurtz_2017_o.pdf

[163] X. Tang, M. Yang, L. Shi, Z. Hou, S. Xu, and C. Sun, "Adaptive state-of-health temperature sensitivity characteristics for durability improvement of PEM fuel cells," *Chemical Engineering Journal*, vol. 491, Jul. 2024, doi: 10.1016/j.cej.2024.151951.

[164] B. Liu and X. Hu, "Hollow Micro- and Nanomaterials: Synthesis and Applications," in *Advanced Nanomaterials for Pollutant Sensing and Environmental Catalysis*, Elsevier, 2020, pp. 1–38. doi: 10.1016/B978-0-12-814796-2.00001-0.

[165] H. Fathabadi, "Fuel cell/back-up battery hybrid energy conversion systems: Dynamic modeling and harmonic considerations," *Energy Convers Manag*, vol. 103, pp. 573–584, Jul. 2015, doi: 10.1016/j.enconman.2015.07.010.

[166] "MX-13 EURO 6 NEW GENERATION Coach & Bus engine." Accessed: May. 07, 2025. [Online]. Available: https://www.dafcomponents.com/en/products/paccar-daf-engines/daf-mx-13-coach-and-bus-engine

6 Appendix

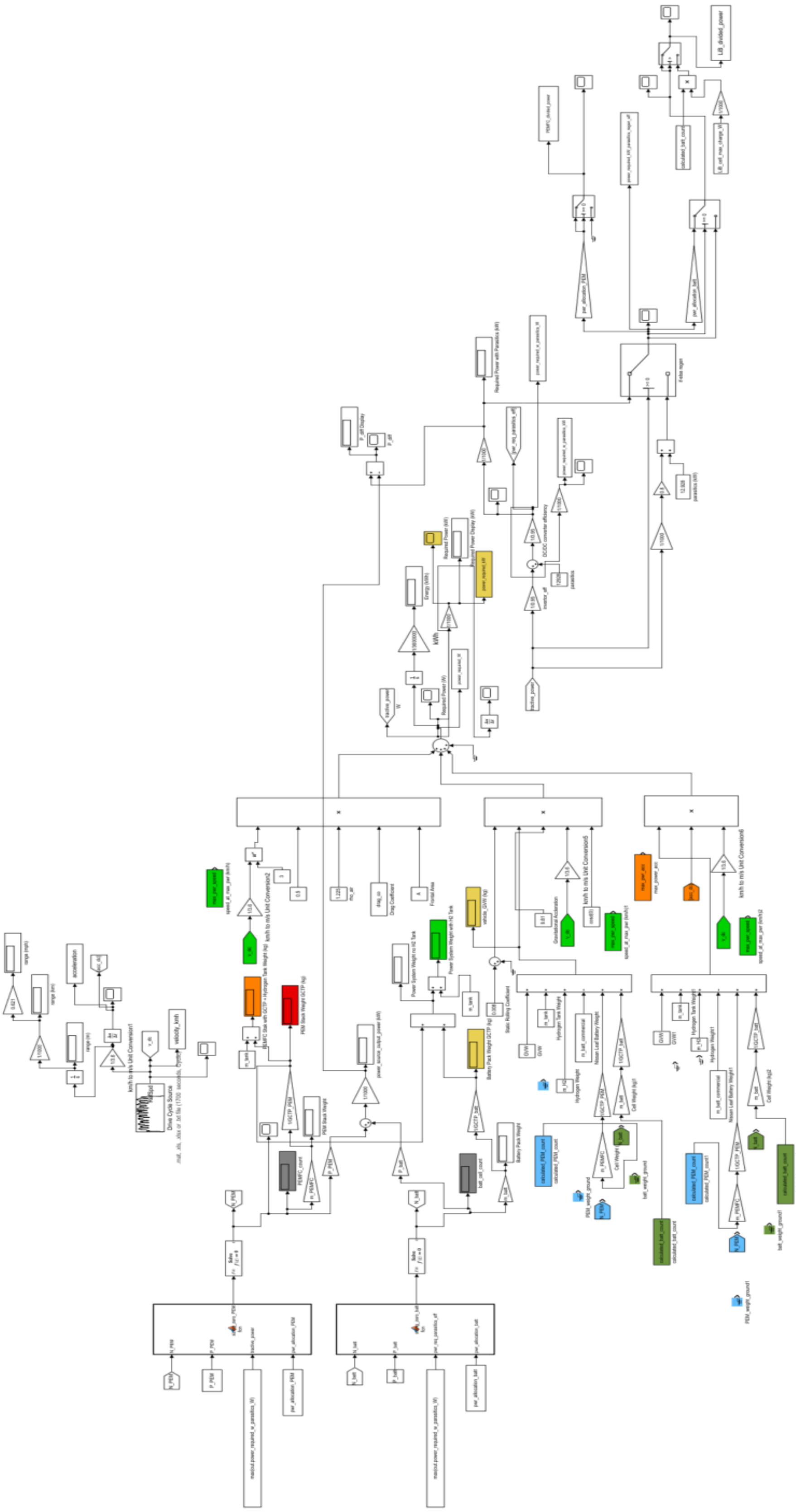

Figure 6-1: HybeMass model main system.

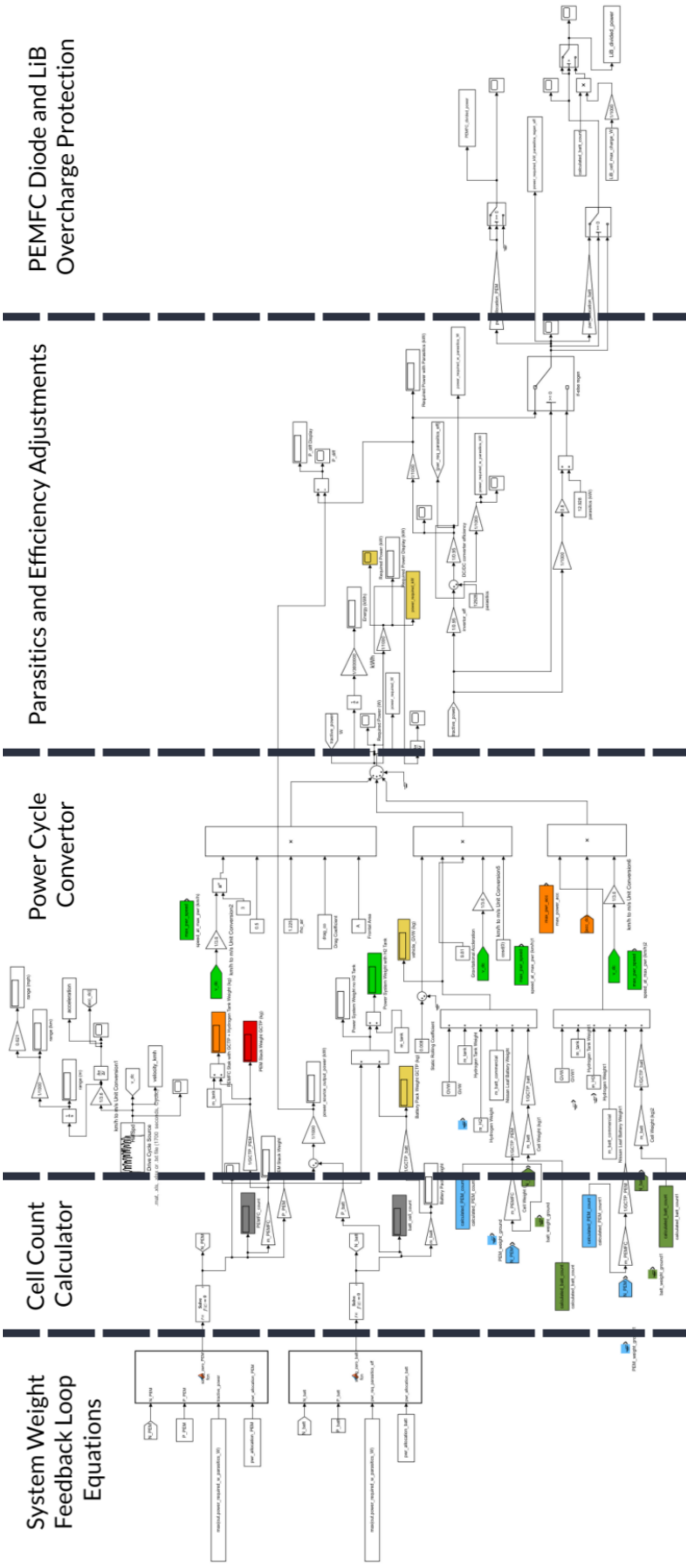

Figure 6-2: HybeMass model main system with subsystems labelled.

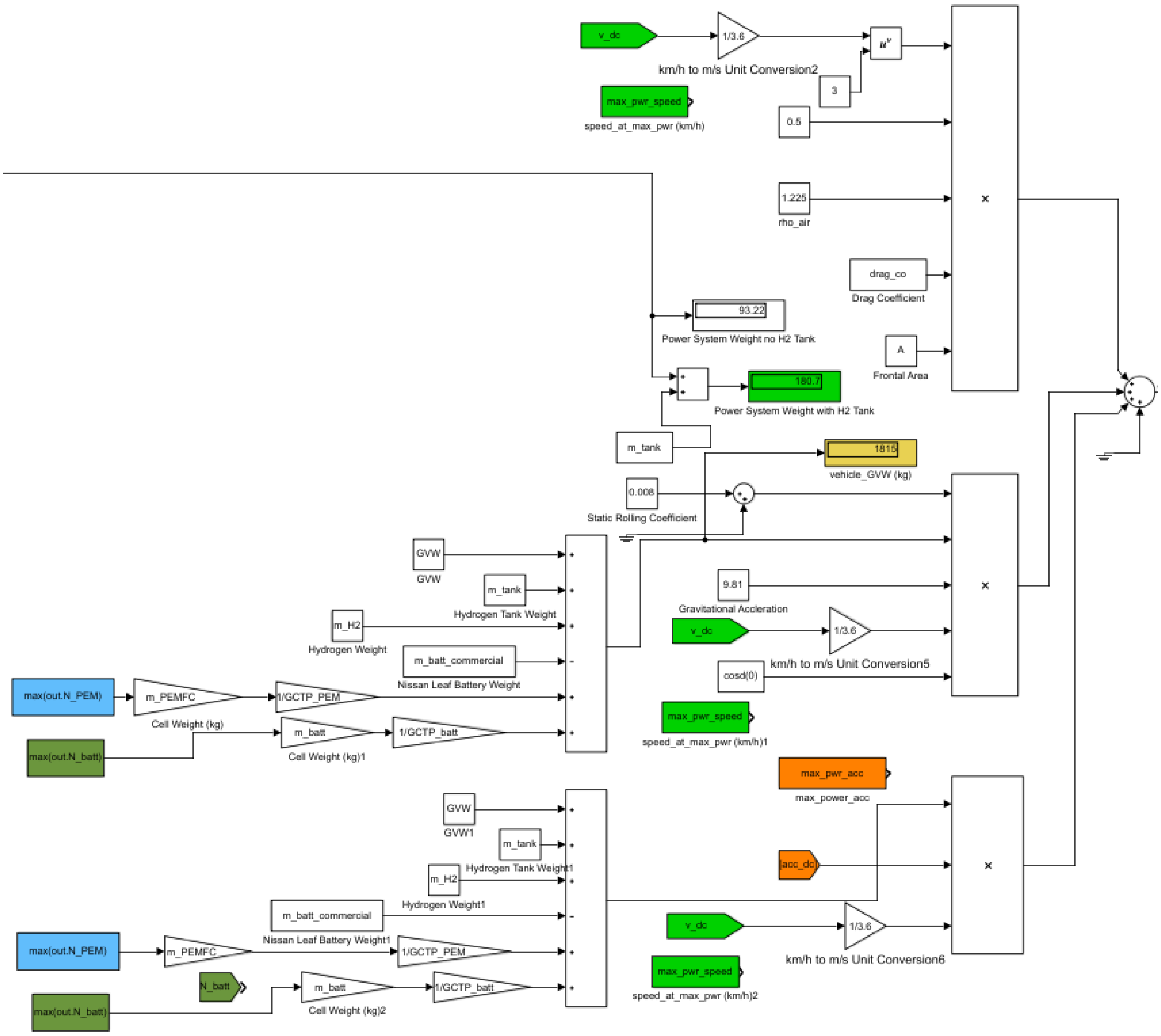

Figure 6-3: HybeMass model overview of power estimation subsystem. This subsystem converts a drive cycle to a power cycle to determine the maximum required power of the proposed vehicle.

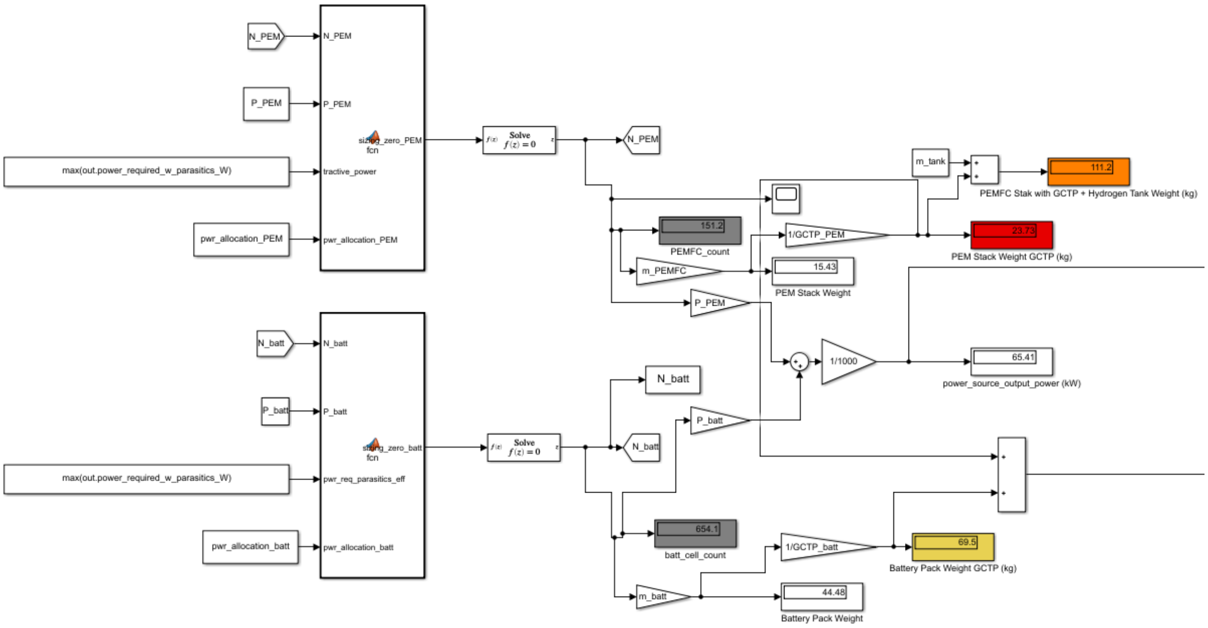

Figure 6-4: Hybemass model detailed block layout of system weight feedback loop subsystem.